



HAL
open science

Controlling the Propagation of Light in Multimode Fibers

Maxime Matthes

► **To cite this version:**

Maxime Matthes. Controlling the Propagation of Light in Multimode Fibers. Physics [physics]. Université Paris sciences et lettres, 2021. English. NNT : 2021UPSLS057 . tel-03405453v1

HAL Id: tel-03405453

<https://pastel.hal.science/tel-03405453v1>

Submitted on 27 Oct 2021 (v1), last revised 28 Oct 2021 (v2)

HAL is a multi-disciplinary open access archive for the deposit and dissemination of scientific research documents, whether they are published or not. The documents may come from teaching and research institutions in France or abroad, or from public or private research centers.

L'archive ouverte pluridisciplinaire **HAL**, est destinée au dépôt et à la diffusion de documents scientifiques de niveau recherche, publiés ou non, émanant des établissements d'enseignement et de recherche français ou étrangers, des laboratoires publics ou privés.



THÈSE DE DOCTORAT
DE L'UNIVERSITÉ PSL

Préparée à ESPCI Paris PSL

Controlling the Propagation of Light in Multimode Fibers

Contrôle de la Propagation de la Lumière dans des Fibres
Optiques Multimodes

Soutenue par

Maxime MATTHÈS

Le 12.02.2021

École doctorale n°564

Physique en Île de France

Spécialité

Physique

Composition du jury :

Sylvain GIGAN Professeur PSL Université Paris	<i>Président du jury</i>
Esben Ravn ANDRESEN Directeur de Recherche Université de Lille	<i>Rapporteur</i>
Vincent KERMÈNE Directeur de recherche Université de Limoges	<i>Rapporteur</i>
Hui CAO Professeur Yale University	<i>Examinatrice</i>
Julien de ROSNY Directeur de Recherche PSL Université Paris	<i>Directeur de thèse</i>
Sébastien POPOFF Chargé de Recherche PSL Université Paris	<i>Co-encadrant</i>

Acknowledgements

These last three and a half years of work were all but a solitary work, and my PhD would not have been possible without the support from so many people.

First of all, I would like to thank my directors, Sébastien and Julien. Sébastien, thanks for giving me the possibility to work with you on this subject: I feel lucky to have been your student. You taught me so much in Optics but also in Python or 3D printing but also in human values, and I feel glad to have been supervised by someone I could easily have a laugh with. You also sent me to conferences in very nice places in your stead which was awesome. Julien, thank you for being my PhD director. The bi-weekly meetings that we had were always a source of insights for me, and you often helped me getting the big picture of my subject which is easy to forget when most of my time was devoted to experimental work in a basement!

I would like to thank the other students of the Popoff team. It was nice to have you Clément also work on fibers for the year you were here, you came with new experimental ideas and gave a boost to my work. I was sad to see you, my work companion, leave but I hope you are enjoying your new life projects. Mathieu, I am glad that by the end of your PhD, you finally managed to fit the red and the blue curve. Joke aside, you always had ears for my experimental issues, and always were the one to answer my questions about light scattering. Louis, you always had so cool new trick to show in Python or in Mecanics, thanks for always sharing them. Noet, you always felt like the most resourceful and savvy guy in the lab, thanks for always having an idea to every problem I had!

I am happy that my PhD took place at the Langevin Institute. Having people working on different subjects in the same laboratory or in the same office forces to keep the eyes open for new ideas and approaches. I would like to thank the members of the Metheo team for the quality of the scientific discussion we had during many meetings. I was not always the most focused member, but even difficult theoretical concepts ended up percolating into my mind. I am also grateful to the PhD students that I met there at the Institute, always eager to explain what they are doing, but also going to the bar. It was nice to have Joris bring laughter to the office, and have Paul and Mons bring the society discussions to the lab. Thank you to all the others for the great time I had with you: William, Chloë, Jeanne, Margaux, Clotilde, Cassandra, Max, Elise, Léo, Gauthier, Kammel, Benjamin,

I am particularly happy that I could spend those PhD years with the smartest goofs I know, the greatest climbing partners, the coolest board games enthusiasts, and the finest beer connoisseurs Jules and Louis. Thank you guys, you are the best.

I want to thank the illustrious members of la Potée Auvergnate, you let me discuss my subject with you even if you did not understand it. Thank you to Florent, for always being ready to rebuild the world, and to Hippolyte for inviting me to awesome jazz concerts. I would also like to thank Sophie, the best lab partner I could ever have! Thanks to my family for always being supportive and treating my work like one of the most important thing that was going on in the world!

Last, nothing I did for the last 5 years would really have been possible without your unwavering support, Aliénor. Many a time, you kept me from failing. It is my greatest happiness to share the celebration of this PhD with you. I love you.

Contents

Acknowledgements	iii
Introduction.....	1
I The world of optical fibers: generalities	3
1 Optical fibers: A two century long history	4
1.1 Light guidance.....	4
1.2 Toward image transmission	6
1.3 Toward optical communications.....	7
2 Optical fiber modes	11
2.1 Vector modes.....	11
2.2 The scalar approximation.....	11
2.2.a Linearly polarized modes	12
2.2.b Orbital angular momentum modes	13
2.3 Step index and graded index fiber.....	14
2.4 Intermodal dispersion	15
2.5 Mode coupling theory	16
3 Optical fibers in telecommunications	18
3.1 Historical limitations and breakthroughs	18
3.1.a Materials and design enhancements.....	19
3.1.b Amplification of the signal	20
3.1.c Multiplexing: wavelength and polarization	21
3.1.d Modulation schemes	22
3.2 Current use of optical fibers	23
3.3 Limits of single mode fibers	24
3.3.a Chromatic and intramodal dispersion.....	24
3.3.b Polarization dispersion	25
3.3.c Non-linearities	25
4 Recent improvements	26
4.1 Non-linear methods	26
4.2 Photonic Crystal fibers	27
4.3 Space Division Multiplexing	27
4.3.a Potential advantages of SDM	28
4.3.b Challenges	28
4.3.c SDM in the weak mode coupling regime	29
4.3.d SDM in the strong mode coupling regime	29
4.3.e Principal modes.....	30
Conclusion	31
II The experimental study of Multimode Fibers.....	33
1 Modal content detection methods	34
1.1 The cross-correlation (C2) method	34
1.2 Spatially and spectrally resolved (S2) method.....	35

2	The propagation of waves in complex media	38
2.1	Aberrations and their compensation	38
2.2	Propagation of light in a complex medium	39
2.3	Spatial light modulators	41
2.4	Wavefront shaping in complex media	42
2.4.a	Focusing through a scattering medium	42
2.4.b	Digital Optical Phase Conjugation	43
2.4.c	Selective mode excitation	43
3	Measuring transmission matrices	45
3.1	The scattering matrix and the propagation channels of a system	45
3.2	The transmission matrix of scattering media	46
3.3	The mode basis TM	48
3.3.a	Direct measurement of the mode basis TM	48
3.3.b	Retrieval of the mode basis TM from the pixel basis TM	50
3.3.c	Deep learning strategies	50
	Conclusion	52
III Developing a toolbox to study fibers		53
	Introduction	54
1	Shaping and manipulating wavefronts in optical fibers	54
1.1	Wavefront shaping using a digital micromirror device (DMD) ..	54
1.1.a	Diffraction effects	54
1.1.b	Complex modulation with a DMD	58
1.1.c	Vibrations	62
1.1.d	Thermal effects	62
1.1.e	Surface curvature	62
1.2	Injecting light into fibers	62
1.3	Detection schemes	63
1.3.a	Two-polarization detection	64
1.3.b	Complex field measurements	65
1.3.c	Initial post treatments	67
2	Measurement of the pixel basis transmission matrix	68
2.1	Principles	68
2.2	Single input, single output polarization	69
2.3	Both input polarizations	71
3	Reconstruction of the mode basis TM	75
3.1	Modal projection of the TM	75
3.2	Imperfect mode conversion	76
3.3	Finding aberrations of the optical setup	78
3.3.a	Goal	78
3.3.b	Model	79
3.3.c	Cost function	81
3.3.d	Optimization	81
3.3.e	Results	82
	Conclusion	83
IV Effect of strong perturbations in multimode fibers		87
1	Introduction	88
1.1	Disorder in multimode fibers	88
1.2	Principal modes and the Wigner Smith operators	88
2	Effect of deformations on the TM	90

2.1	Experimental methods	90
2.2	Qualitative analysis of the modification of the TM	90
3	Avoiding disorder.....	94
3.1	Perturbation insensitive channels	94
3.1.a	Deformation effects on the mode basis TM.....	94
3.1.b	Generating the deformation principal modes	94
3.1.c	Study of the deformation principal modes	95
3.2	Parametrization of the deformation of the TM	96
3.2.a	The deformation matrix	96
3.2.b	Approximation of TMs under deformation.....	98
	Conclusion and perspectives	101
V	Using complex media and multimode fibers as reconfigurable linear operators.	103
1	Introduction.....	104
1.1	Context	104
1.2	Static designs	104
1.3	Programmable approaches	105
1.4	Complex medium approaches	106
2	Using complex media to perform linear optical computations	107
2.1	Objectives	107
2.2	Principle	108
2.3	Input and output projectors	108
2.4	Existence of solution with ideal modulation and theoretical limits	109
3	Experiment.....	110
3.1	Optical setups.....	110
3.1.a	Multimode fiber experiments	110
3.1.b	Scattering medium experiment.....	111
3.2	Procedure.....	112
3.2.a	Calibration	112
3.2.b	Calculation of the projections	114
3.2.c	Optical analogue computation.....	115
4	Results	117
4.1	Multimode fiber experiment	117
4.2	Scattering medium experiment	119
5	Discussion.....	120
5.1	Limits of our approximations	120
5.2	Scalability	121
5.3	Losses	121
5.4	Practical implementation	121
	Conclusion	122
	Conclusion	123
	Appendix A Mechanical stability of the DMD	127
	Appendix B Thermal effects on the DMD chip	129
	Appendix C Aberrations of the DMD	131

Appendix D Tuning the injection into the fiber	133
1 Transmitted energy through the fiber.....	134
2 Conjugation of the DMD plane and the input plane of the fiber	134
2.1 Obtaining the conjugation of the three planes	135
2.2 Adjusting the remaining parameters.....	136
Appendix E Off-axis measurements with multimode fibers	139
1 The Fourier transform of the interference pattern	139
2 Reconstruction conditions	139
3 Simulations and direct space conditions	141
Appendix F Reconstruction of the Transmission Matrix	143
1 Selecting good input patterns and singular value criterion	143
2 Quantitative assessments of reconstruction.....	144
Appendix G Numerical computation of the modes	149
Appendix H Center detection algorithm for off-axis holography	153
Appendix I Publications and Conferences	155
Bibliography.....	157

List of Figures

I.1	Illustration of light guidance in a flowing liquid.	4
I.2	General geometry of a planar waveguide.	5
I.3	Lamm's imaging experiment using a fiber bundle.	6
I.4	Process used to create glass fibers with a cladding designed by Lawrence Curtiss.	7
I.5	First description of the propagating modes inside of fibers.	8
I.6	Principle of GRIN fibers.	9
I.7	Schematic of the MCVD process used to create a preform.	9
I.8	Industrial machine design used to draw fibers.	10
I.9	Spatial profiles of the vectorial modes.	12
I.10	Spatial profiles of the LP_{ml} modes.	13
I.11	Comparison of the modes of GRIN and step index fibers.	14
I.12	Dispersion relation of step index and GRIN fibers.	15
I.13	Coupling observed in a step index MMF.	17
I.14	Capacity of optical fiber technologies over time.	18
I.15	Sources of loss in optical fibers.	19
I.16	Improvements in the design of step index fibers.	20
I.17	Wavelength distribution in WDM.	21
I.18	Advanced modulation formats.	22
I.19	Capacity as a function of SNR for different modulation schemes.	23
I.20	Evolution of the capacity of single mode fibers over time.	23
I.21	Map of the transoceanic optical cables.	24
I.22	Example of an HC-PCF design.	27
I.23	Principal modes of a complex medium.	31
II.1	Principle of the C2 method.	34
II.2	Measurements using the C2 method.	35
II.3	Principles of the S2 method.	36
II.4	Experimental results of the S2 method.	37
II.5	Illustration of the effects of simple monochromatic aberrations.	38
II.6	Principle of adaptive optics in astronomy.	39
II.7	Focusing experiment through a scattering medium using wavefront shaping.	40
II.8	Comparison of common SLM technologies.	42
II.9	Digital Optical Phase Conjugation through an MMF.	44
II.10	Modal characterization of an MMF using selective mode excitation. ...	44
II.11	Illustration of the scattering matrix formalism.	45
II.12	Measurements of the pixel basis TM using a co-propagating reference. ...	48
II.13	Measurement of the TM directly in the mode basis.	49
II.14	Measurement of the mode basis TM.	49
II.15	Setup used to measure the pixel basis TM.	51
II.16	Reconstruction of the mode basis TM with an optimization procedure. ...	52

III.1	Two possible pixel configurations.	55
III.2	Light modulation with a DMD.	55
III.3	Blazing number μ as a function of the illumination angle α	56
III.4	Diffraction patterns of two different DMDs.	57
III.5	Diffraction patterns along the diagonal.	58
III.6	Implementation of the Lee hologram.	59
III.7	Numerical simulations of the Lee hologram procedure using macropixels.	61
III.8	Schematic of the experimental setup.	63
III.9	Illustration of the degrees of freedom of the position of the fiber.	64
III.10	Experimental reconstruction of the output field with off-axis measurements.	66
III.11	Evolution of the phase correlation during an acquisition.	68
III.12	Pixel basis TM for one input and one output polarization.	70
III.13	Absolute value error of reconstruction.	70
III.14	Singular vectors of the single polarization TM.	71
III.15	Both input polarizations pixel basis transmission matrix.	72
III.16	Singular vectors of the full polarization TM.	73
III.17	Output error of the experimental reconstruction.	74
III.18	Propagation constants of graded index fiber modes.	76
III.19	Imperfect mode injection into an MMF due to misalignment.	77
III.20	Imperfect mode injection into an MMF due to wrongly estimated fiber parameters.	78
III.21	Initial mode basis TM.	79
III.22	Schematic of the model architecture used for the compensation of the aberrations.	80
III.23	Evolution of the cost function \mathcal{L} as a function of the iteration number.	82
III.24	Transmission matrix in the basis of OAM modes.	83
III.25	Corrections used to correct an input change of basis matrix.	84
III.26	Initial and corrected change of basis matrices.	84
III.27	Spatial profiles that couple into modes of the initial and corrected modes of the conversion matrix.	85
IV.1	Photography of the setup holding the fiber and schematic of the deformation system.	91
IV.2	Pixel basis TM of non-perturbed and perturbed fibers.	92
IV.3	Modal TM of non-perturbed and perturbed fibers before correction. .	92
IV.4	Modal TM of non-perturbed and perturbed fibers after correction. ...	93
IV.5	Singular value distribution of the mode basis TM.	93
IV.6	Effects of deformations on the mode basis TM.	95
IV.7	Correlation of the deformation principal modes.	96
IV.8	Output profile of the deformation principal modes.	97
IV.9	Projection of the deformation principal modes onto the basis of the propagating modes of the fiber.	98
IV.10	Singular value distribution of the global deformation operator.	99
IV.11	Fidelity between the measured mode basis TM and the approximated one.	100
IV.12	Input singular matrices of the global deformation operator.	100
IV.13	Representation of four singular components with both the input and output polarizations.	101

V.1	Energies for communications and computations inside a typical computer.	104
V.2	A multilayer slab designed to perform a specific function G	105
V.3	Mode separator with photonic crystals.	105
V.4	Principle and implementation of coherent photonic circuits.	106
V.5	Illustration of the desired system.	107
V.6	Schematic representation the submatrix $\mathbf{H}_{\mathbf{k}\perp}$	109
V.7	Schematic representation of the MMF setup.	110
V.8	Stability of the MMF experiment.	111
V.9	Schematic representation of the scattering medium setup.	112
V.10	Stability of the scattering medium experiment.	113
V.11	Step 1: Calibration of the system.	113
V.12	Step 2: Calculation of the optimal input projection.	115
V.13	Step 3: Analogue computation.	115
V.14	Comparison of the two presented methods to encode input vectors ..	116
V.15	Outputs of the MMF experiment for $\mathbf{G} = \mathbf{DFT}_{16}$	118
V.16	Comparison of experimental and target operators.	119
V.17	Response of an operator built with a scattering medium.	120
A.1	Method used to dampen the vibrations of the DMD.	127
A.2	Phase fluctuations due to vibrations of the DMD.	128
B.1	Decorrelation of the speckle pattern over time due the DMD.	129
C.1	Point spread function of the optical system.	131
C.2	Correction of the DMD surface aberrations.	132
C.3	Simulations of the correction of the aberrations of the DMD using the Lee hologram method.	132
D.1	Illustration of the degrees of freedom of the position of the fiber.	133
D.2	Coupling coefficient as a function of illumination parameters.	135
D.3	Schematic of the control setup used for alignment.	135
D.4	Incoherent speckle intensity when a defocus is present.	136
D.5	Circular symmetry of output speckles for an aligned MMF.	137
E.1	Illustration of the Fourier transform of the interference pattern of the output speckle of a fiber with a flat reference.	140
E.2	Simulations of off-axis reconstructions with different reference angles.	142
F.1	Singular value distributions of the TM for different input sets without oversampling.	144
F.2	Singular value distributions of the TM for different input sets and different oversampling ratios.	144
F.3	Reconstruction error as a function of oversampling.	146
F.4	Reconstruction error for pixel noise of different standard deviation values.	147
H.1	Operating scheme of the center detection algorithm.	154

List of Abbreviations

AIR	Achievable Information Rate
BD	Beam Displacer
BS	Beam Splitter
CCD	Charged Coupled Device
CPU	Central Processing Unit
CWDM	Coarse Wavelength Division Multiplexing
DFT	Discrete Fourier Transform
DGD	Differential Group Delay
DMGD	Differential Mode Group Delay
DMD	Digital Micromirror Device
DRA	Distributed Raman Amplification
DSP	Digital Signal Processing
FC	Fiber Coupler
FMF	Few-Mode Fiber
FPGA	Field-Programmable Gate Array
GWS	Generalized Wigner-Smith
GPU	Graphical Processing Unit
GRIN	GRaded INded
GVD	Group Velocity Dispersion
HC-PBGF	Hollow Core-Photonic BandGap Fiber
HC-PCF	Hollow Core-Photonic Crystal Fiber
HOM	Higher Order Modes
LP	Linearly Polarized
MCF	MultiCore Fiber
MDL	Mode Dependent Losses
MIMO	Multiple Inputs Multiple Outputs
MMF	MultiMode Fiber
NA	Numerical Aperture
OAM	Orbital Angular Momentum
OM	Optical Multimode
OPU	Optical Processing Unit
PBS	Polarization Beam Splitter
PSF	Point Spread Function
PSP	Principal States of Polarization
SDM	Space Division Multiplexing
SLM	Spatial Light Modulator
SMF	Single Mode Fiber
SNR	Signal to Noise Ratio
TM	Transmission Matrix
WDM	Wavelength Division Multiplexing
WP	WavePlate

Introduction

Since the middle of the XXth century, optical fibers have proved themselves to be formidable tools for light transmission. Their property to guide light for tens of kilometers with limited losses make them particularly useful for long distance telecommunications. Moreover, the process of fabrication of optical fibers has been optimized, allowing producing great lengths at low costs. Nowadays, the intercontinental information exchange relies almost exclusively on optical fibers covering up to tens of thousands of kilometers. Each fiber can carry up to tens of Tbytes/s of data.

Since the early implementations of fiber-optic communications in the 1970s, single mode fibers have played a leading role. Crucial improvements made in terms of transmission quality as well as coding efficiency have driven an increase of the achievable capacity that shows an exponential trend. Indeed, we observe that the growth of data-rates has steadily followed a ten-fold increase every four years [Richardson, Fini, and Nelson, 2013].

However, the exploitation of the degrees of freedom offered by single mode fibers, namely the wavelength, the amplitude, the phase, and the polarization of the optical field, is reaching its limits. The current technologies saturate and can no longer carry on with the trend of the previous years. Several solutions are explored to meet the growth in demand of higher data rates.

Among those, Space Division Multiplexing (SDM) is envisioned as one of the most promising and is investigated by many groups over the world. It is based on the exploitation of the different spatial channels available in multicore or multimode fibers (MMFs). Compared to single mode fiber technologies, SDM allows theoretically multiplying the capacity of fibers by the number of spatial channels. However, the implementation of SDM is hindered by the modal nature of light propagation in MMFs. Indeed, effects such as mode dependent losses, intermodal dispersion and mode coupling degrade the quality of the signal reconstruction and limit data rates. Moreover, these effects are dependent on the state of the fiber, so that changes of conformation of the fiber or external perturbations modify its modal properties that can fluctuate over time.

The characterization of the spatial channels of MMFs is not straightforward. Indeed, when monochromatic light is transmitted through an MMF, a random speckle pattern emerges at the other end, resulting from the interferences of the modes travelling at different phase velocities. This phenomenon is similar to the one affecting the propagation of light in optical scattering media. About fifteen years ago, a landmark experiment showed how spatially manipulating the electric field entering a scattering medium allowed compensating for the random nature of the propagation, allowing focusing light on a single bright spot [Vellekoop, 2008]. This first demonstration of wavefront shaping in scattering media used a spatial light modulator (SLM) that grants the ability to control the amplitude and/or phase of the electrical fields with high resolution. Since then, wavefront shaping has driven the study of the spatio-temporal properties of scattering media.

The spatial relationship between the fields entering from one side and exiting from the other side of a medium can be advantageously described by its transmission matrix. The first measurement of the optical transmission matrix of a scattering medium was performed in 2010 [Popoff et al., 2010a]. It has opened the possibility to perform the characterization of the modal content of MMFs by using transmission matrices expressed in the basis of the modes of the fiber [Carpenter, Eggleton, and Schroder, 2014; Ploschner, Tyc, and Cizmar, 2015].

During my Ph.D., we studied the modal content of MMFs by leveraging wavefront shaping techniques. To that end, our first goal was to develop a system that allows for the fast measurement of the mode basis transmission matrix of an MMF, with the requirements of being lightweight and compatible with a large range of fibers under any conformation or any source of disorder. Thanks to this setup, we surveyed the mode coupling due to external perturbations and how to tackle it.

This manuscript is divided in five chapters:

- Chapter **I** contains a historical introduction to optical fibers and to their use for telecommunications. We present the main technologies implemented in single mode fiber systems, and show how SDM is a promising method to increase the capacity of optical communication systems. We introduce the main challenges that have to be addressed to implement SDM in multimode fibers.
- Chapter **II** introduces the methods at our disposal to study optical fibers. We show how wavefront shaping has emerged and has brought efficient tools to characterize complex media. We focus our attention on the main techniques used to measure the transmission matrix in the basis of the propagating modes of a fiber.
- In Chapter **III**, we first introduce the main experimental methods we exploit to measure the transmission matrix of MMFs. We then show how, thanks to this matrix measured initially in a pixel basis, we are able to retrieve the transmission matrix in the basis of the propagating modes of the fiber using optimization algorithms.
- In Chapter **IV**, we study the effect of a mechanical stress on the transmission matrix of an MMF. We show how the measurement of the mode basis transmission matrix of the perturbed fiber allows finding an almost complete basis of wavefronts that are robust to disorder for a wide range of deformations.
- In Chapter **V**, we present an approach to take advantage of the random coupling generated by strong perturbations applied to an MMF. We show that media that scramble the spatial transmission channels, such as perturbed MMFs, can be used to perform linear operations.

Because we believe in open-science, we attempted to share our methods and procedure with the rest of the scientific community. To that end, we present several appendix sections which provide practical information. Some procedures, tutorials, and codes about our methods can also be found in our team website¹, and on our online code repositories².

¹<https://www.wavefrontshaping.net/>

²<https://github.com/MaximeMatthes> and <https://github.com/wavefrontshaping>

Chapter I

The world of optical fibers: generalities

Chapter contents:

1	Optical fibers: A two century long history	4
1.1	Light guidance.....	4
1.2	Toward image transmission	6
1.3	Toward optical communications.....	7
2	Optical fiber modes	11
2.1	Vector modes.....	11
2.2	The scalar approximation	11
2.3	Step index and graded index fiber.....	14
2.4	Intermodal dispersion	15
2.5	Mode coupling theory	16
3	Optical fibers in telecommunications	18
3.1	Historical limitations and breakthroughs	18
3.2	Current use of optical fibers	23
3.3	Limits of single mode fibers	24
4	Recent improvements	26
4.1	Non-linear methods	26
4.2	Photonic Crystal fibers	27
4.3	Space Division Multiplexing	27
	Conclusion	31

1 Optical fibers: A two century long history

From telecommunications to optical imaging in medicine, optical fibers stand as ubiquitous tools to transmit information. They allow light to travel from one end to the other one for distances up to several tens of kilometers. Moreover, they have the property of being flexible, which is required for most of their practical applications. Modern optical fibers have emerged in the middle of the XXth century and their popularity has only increased since. However, the possibility of guiding light inside solid or liquid media arose at least a century before. This section provides a chronological tour of the emergence of optical fibers, from the first implementations of optical guiding to the optical fibers as we know them today. We will introduce the key physical properties of fibers. The historical content of this section is adapted from Jeff Hecht's book *City of Light: the Story of Optical Fibers* [Hecht, 1999].

1.1 Light guidance

In 1841, Daniel Colladon, professor at the University of Geneva demonstrated for the first time light guiding. The initial objective of Colladon was to show the breaking up of water jets for a lecture. However, the audience could not see the phenomenon in the poorly lit lecture hall. In order to solve this problem, he collected sunlight and focused it through his water tank along a jet squirting out of a hole in the other side. Light arriving inside the jet seemed trapped inside the flowing liquid until the jet broke up, as shown in Figure I.1. Colladon and his audience were amazed to see that light followed the curve of the water instead of going in a straight line as they expected.

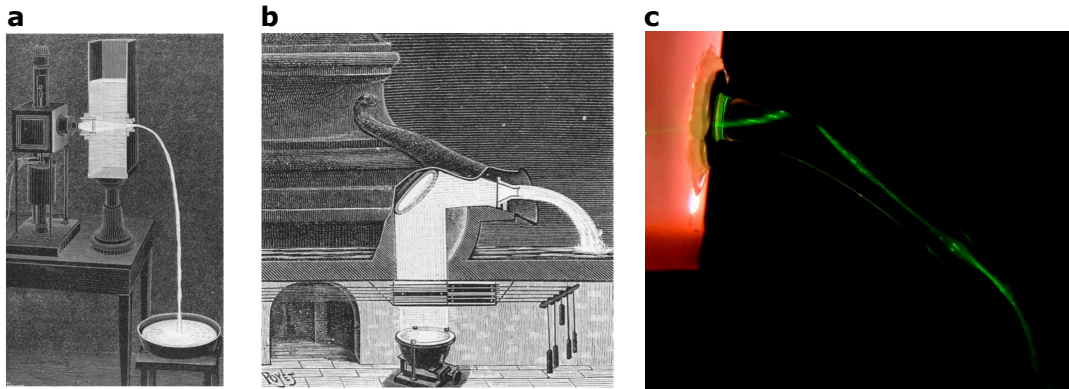


Figure I.1: Illustration of light guidance in a flowing liquid. a: Colladon's observation of light trapping. b: A mirror aimed light from an arc lamp into the center of the parabolic jet at the Universal Exposition of 1889 in Paris. c: Photography of the reproduction of Colladon's experiment of light guidance in propylene glycol. The phenomenon of successive total internal reflections can be observed in the flowing liquid. (a and b) are extracted from [Colladon, 1884], and (c) from [Bill Hammack's Videos & Audio on Engineering].

The trapping of light inside water is caused by total internal reflection. To explain the effect, we choose planar geometry for the sake of simplicity. The geometry is shown in Figure I.2. Three layers of materials are stacked. The two external ones extend infinitely in the direction orthogonal to their interface. We consider that media 1 and 3 are identical with $n_1 = n_3$, and $n_2 > n_1$. The Snell-Descartes laws of refraction allow us to observe that a ray incoming from medium 2 onto the interface between media 2 and 1 is totally reflected, and thus stays in medium 2, if the angle

of incidence r satisfies:

$$r > r_{lim} = \arcsin\left(\frac{n_1}{n_2}\right). \quad (\text{I.1})$$

It sets an upper bound for the input angle i :

$$\sin(i) < \sin(i_{lim}) = \sqrt{n_2^2 - n_1^2}, \quad (\text{I.2})$$

for the light to be totally reflected inside the medium. The *sine* of the critical angle of incidence $\sin(i_{lim}) = \sqrt{n_2^2 - n_1^2}$ is called the numerical aperture (NA) of the waveguide.

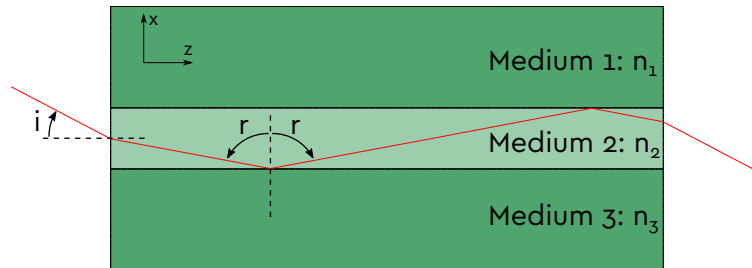


Figure I.2: General geometry of a planar waveguide.

What Colladon observed was the same phenomenon but for a cylindrical medium where air surrounds the curved cylinder of water that correspond to medium 2. We can foresee that as long as the curvature is not too large, the total internal reflection condition can still be satisfied.

The initial experiment made by Colladon used water as the guiding medium. Almost at the same time, the French optics specialist Jacques Babinet also made the same observation with water. However, he mentioned that the idea would also "work very well with a glass shaft curved in whatever manner, and [...] indicated [it could be used] to illuminate the inside of the mouth". Nevertheless, Babinet noticed that at that time the best glasses were not very clear and that propagation would not be possible for a very long distance. The applications were initially limited to artistic displays and illuminated fountains like the ones presented at the Universal Exposition of Paris in 1889 (illustration in Figure I.1.b). With Babinet's idea, it was the first time a medical application of guiding light was ever formulated.

It took many years before his idea of guiding light in glass became a reality. The glass fibers themselves were not produced before the end of the XIXth century; glass manipulation was already mastered with object of centimeter sizes, but the first documented technique allowing the fabrication of actual optical fibers was designed by Charles Vernon Boys. To do so, he heated a rod of quartz to the point it melted, attached one end to a quarrel, and shot it with a crossbow. It produced a few-meter-long thin fiber. Boys documented that he observed "a glass thread 90 feet long and 1/10,000 inch in diameter, so uniform that the diameter at one end was only one sixth more than that at the other". The threads could be as strong as steel wires of the same size, and he used them for mechanical experiments. Later on, it was observed that glass fibers meshed together had good insulating properties. It drove their production and in 1931 the Owens-Illinois glass company was able to mass produce glass wool, which is still used as an insulator today.

Using glass fiber for optical applications was still not considered at that time. However, the development of the glass industry allowed for improvements in the quality of the materials which would be crucial in the advent of optical fibers.

1.2 Toward image transmission

It was in the beginning of the XXth century that people began exploring the optical applications of glass fibers. Recalling the illuminated fountains of the Universal Exposition, some saw in thin glass fibers the possibility to carry information, images in particular. The first demonstration of image transmission was performed by Heinrich Lamm, a physician who wanted to build an apparatus to look inside the human body. One of the main challenges for physicians trying to look inside the stomach (of a living person) was that the curvature of the esophagus prevents a straight observation tool to reach the area of interest.

Lamm realized that a bundle of glass fibers could carry a discretized image if the fibers were correctly arranged at both ends. He carefully ordered glass fibers in a way that the input and output orders matched. He tried to produce at one end an image of a V-shaped incandescent filament placed at the other end of his rudimentary endoscope. He observed a faint image of the V-shaped filament, which he recorded on photographic film, as shown in Figure I.3.

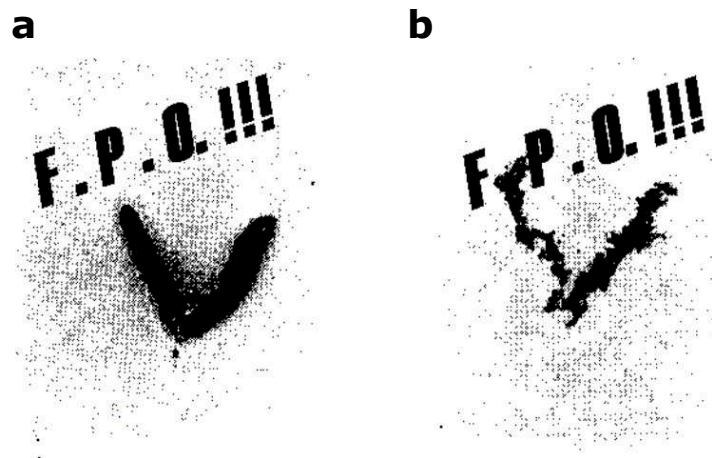


Figure I.3: Lamm's imaging experiment using a fiber bundle. **a**, Photographic negative of the bare filament used in the Lamm's experiment. **b**, Photographic negative of the image emerging from the fiber bundle. The "F.P.O.!!!" mark comes from the reproduced image. (Copyright Michael Lamm; reproduction courtesy of Corning Glass Center).

The main reason for the poor quality of the image obtained by Laam was the coupling between the fibers. Because of the proximity of the fiber cores, that effectively touch each other, coupling between the light carried by different fibers can occur. It lead to a significant degradation of the image.

To prevent coupling, about 20 years later in 1951, Brian OBrien, president of the Optical Society of America, and Abraham van Heel, president of the International Commission for Optics, considered using a cladding of a different material surrounding the fiber. By wrapping the glass fiber into another medium of lower index, it protects the fiber from the external environment, while ensuring that light remains guided by total internal reflection, thus granting the confinement of light. It made possible to use bundles of fibers as previously described.

In 1956, a physics student named Lawrence Curtiss thought of placing a rod of glass inside a tube of glass with a lower refractive index before melting them

together and drawing them with a process similar to the one still used nowadays. A schematic representation of his process is presented in Figure I.4. He waited for his professors to be away at a conference before experimenting his idea and was able to draw 40 feet of clad fiber.

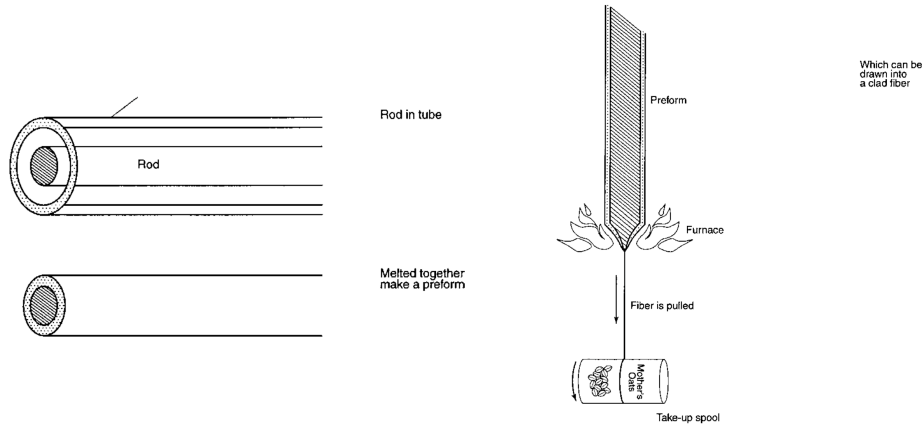


Figure I.4: Process used to create glass fibers with a cladding designed by Lawrence Curtiss.

This sets a paradigm that has not changed much since that time: the optical fiber is mainly composed of a core and a cladding both made of glass, where the cladding has a lower index than the core. In the rest of this manuscript, the cladding index is noted n_c and is constant over the whole cladding (unless specified otherwise), the index of the center of the core is noted n_1 . Similarly to equation I.2, we define the numerical aperture of optical fibers $NA = \sqrt{n_1^2 - n_c^2}$ which characterizes the maximal angle of acceptance of a fiber.

Using bundles of fiber to produce an endoscope such as Lamm's was made possible through these advances, but it was not until the creation of the laser that optical fibers were of strong industrial interest. When the first laser was invented in 1960, people started to send short pulses of light through a fiber, and scientists realized the potential of optical fibers for telecommunications.

1.3 Toward optical communications

As bundles of fibers could more easily be fabricated, and exploitable images began to be formed, people tried to reduce the size of fibers as a way to increase the resolution of those images. In the late 1950s, Will Hicks wondered how thin he could stretch optical fibers in a fused bundle. As he shrank the cores, he noticed a strange phenomenon: geometric patterns and different colors began to appear in individual fiber cores. He eventually decided it must be a waveguide effect but didn't document it further. When the dimension of the core is reduced, ray optics can no longer fully describe light propagation. Understanding how modes were exploited in microwave waveguides for telecommunications, Elias Snitzer and Will Hicks submitted a patent describing a method to do the same in optical fiber waveguides [Hicks, Elias, and Harold, 1964]. In this patent, they also described the mode structures inside optical fibers as shown in Figure I.5

Understanding that the modal propagation of light inside glass fibers was a crucial step towards optical communications. Indeed, inside a multimode waveguide, light carried by different modes do not travel at the same speed. If one sends a pulse

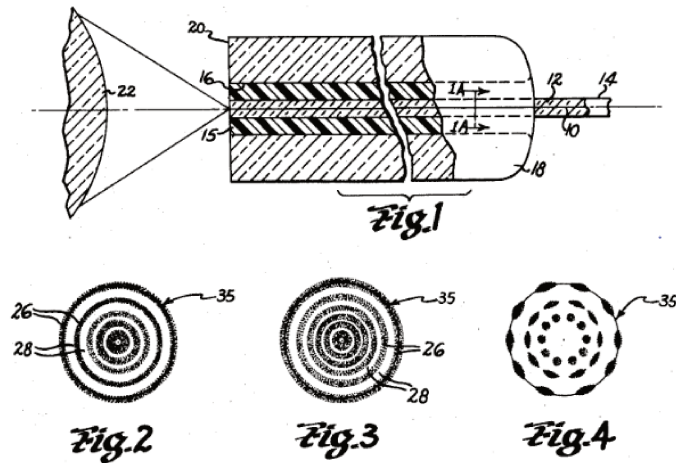


Figure I.5: First description of the propagating modes inside of fibers. Extract from the mode description of optical fibers made in [Hicks, Elias, and Harold, 1964].

into the waveguide (without being able to selectively excite a single mode) the pulse broadens and gets deformed during the propagation. This effect, called *intermodal dispersion*, limits the repetition rate achievable for which consecutive signals do not overlap. At higher rates, intersymbol interferences prevent the accurate reconstruction of the data.

One conceptually simple solution that emerged was to limit the number of propagating mode to only one. We will see that the number of propagating modes can be estimated using the so-called normalized frequency V . It is expressed as a function of the radius of the core a , the numerical aperture NA and light wavelength λ :

$$V = \frac{2\pi}{\lambda} \text{NA} a. \quad (\text{I.3})$$

For $V < 2.405$, a fiber only supports one mode per polarization, in that case the fiber is called a *Single Mode Fiber* (SMF). On the contrary, a fiber for which $V > 2.405$ supports multiple modes per polarization and is called a *Multimode Fiber* (MMF)¹.

In order to obtain SMFs with an pure silica glass core ($n_1 = 1.46$) with no cladding at $\lambda = 633 \text{ nm}$, the radius of the fiber should be $a \simeq 230 \text{ nm}$. The resulting fiber would be very fragile, the fabrication quite difficult, and injecting light inside the fiber would be difficult, leading to important injection losses. However, using a cladding with an index of refraction close to the index of the core allows for larger cores. For example, for $\text{NA} = 0.1$ and $n_1 = 1.46$ at $\lambda = 633 \text{ nm}$, the core radius for a SMF is $a \simeq 2.20 \text{ }\mu\text{m}$ which eases the use. The precise adjustments of the relative indices represented the addition of yet another fabrication constraint.

Another idea that arose to compensate for modal dispersion was the use of fibers with a varying index profile in the core; the index decreases from the center towards the cladding. These fibers are called *Graded Index fibers* (GRIN fibers) while fibers with a uniform index profile in the core are referred to as *step index fibers*. While a complete picture requires wave optics, the principle can be conceptually explained using geometrical optics: when light is injected with a small angle with respect to the normal of the input facet, light travels through high refractive index materials, reducing its speed. Conversely, for high angles, light travels a larger distance, but passes through lower indices leading to faster speeds. Both effects partially compensate

¹This threshold is valid for step index fibers (which are introduced in this section).

each other, which results in a significant reduction of the intermodal dispersion. The principle of GRIN fibers is presented in Figure I.6. GRIN fibers with parabolic index profile carry about half as many modes as step index fibers of similar radius a and indices n_1 and n_c as will be shown in section 2.3.

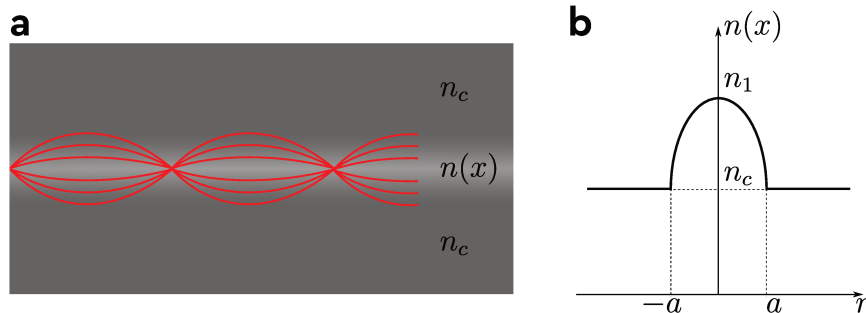


Figure I.6: Principle of GRIN fibers. a, Schematical representation of the path of light rays in a GRIN fiber. b, Example of the index profile of a GRIN fiber.

In both types of fibers, the crucial issue that remained was still about the quality of the glass and the subsequent absorption and propagation loss. In 1966, it was demonstrated that the attenuation found in glass was produced by impurities, mainly metallic ions and OH groups [Kao, 1966]. In 1969, Jones and Kao measured that pure silica glass could have absorption as low as 4 dB/km [Jones and Kao, 1969]. However, its index of refraction was quite low ($n = 1.46$), which prevented the use of a cladding with a lower refraction index. In 1970, Corning Glass Works managed

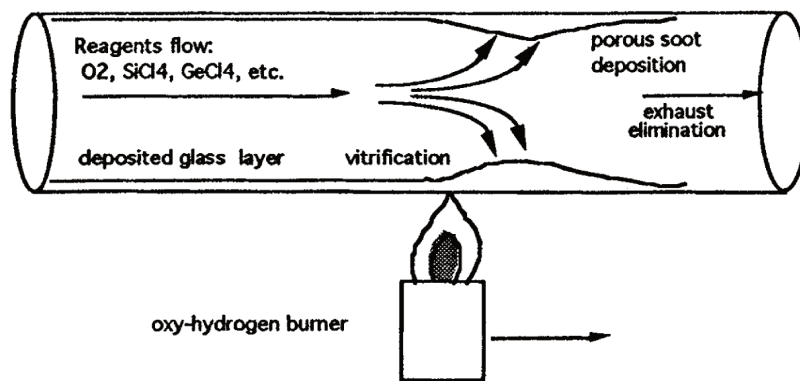


Figure I.7: Schematic of the MCVD process used to create a preform.

to produce glass optical fibers where the cladding was pure glass and the core was made of titanium doped glass. The fiber presented record losses of about 16 dB/km at 633 nm, they later demonstrated losses of 4 dB/km using Germanium doped cores. The process used nowadays is very similar to the one they used, it is called the Modified Chemical Vapour deposition (MCVD, illustrating Figure I.7); reactants are flown inside a deposition tube and are heated at around 1200°C by an oxy-hydrogen burner. Particle growth occurs at the flame position and layers are deposited in several passes. The remaining internal hole then collapses at higher temperature ($> 1800^\circ\text{C}$) and a *preform* of several centimeters of diameter is obtained [Cognolato, 1995].

With the low losses obtained by Corning, together with the control of the index of refraction of the core and cladding materials, it became possible to truly develop

optical communications with fibers. The first real-life implementation of a fiber-optic link was installed in 1975 by Dorset (UK) police after lightning knocked out their electrical communication systems.

Today, the process is automatized and machines draw and control the quality of the fiber as is shown in Figure I.8. Protective polymer coatings and sleeves are usually added during this stage to secure the fiber.

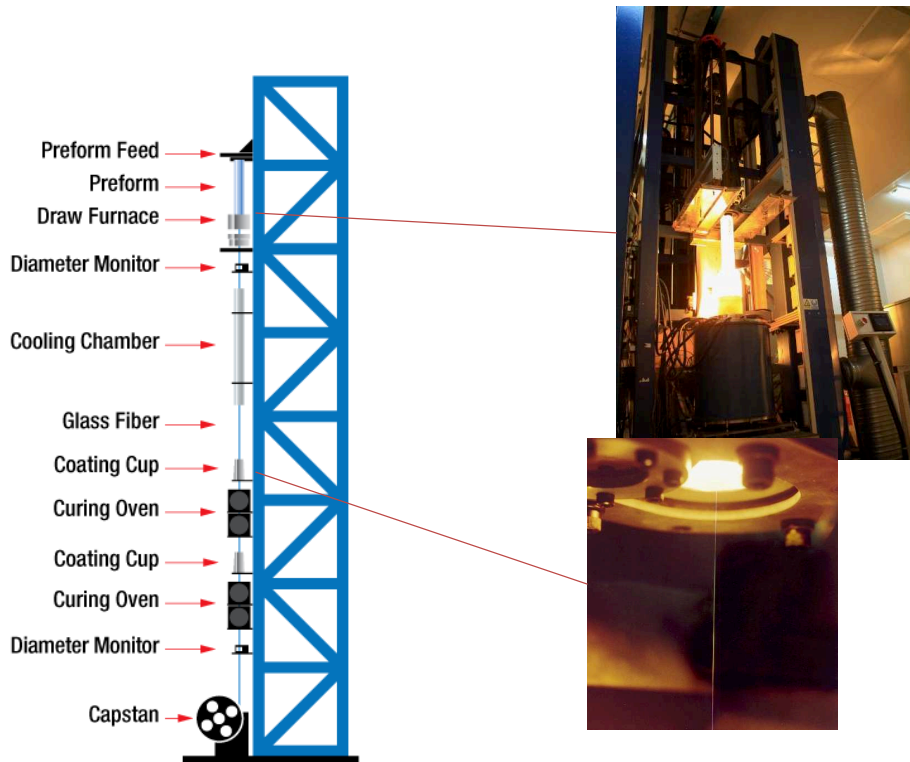


Figure I.8: Industrial machine design used to draw fibers. Schematic representation of the machine used to draw fibers. Adapted from a presentation from [Thorlabs' website](#).

2 Optical fiber modes

Optical fibers are optical waveguides. As such, light can only be propagated by a finite number of modes, which cannot be described solely using ray optics. Designing methods to encode information into light propagating through a multimode fiber must take into account the properties of modes; their number, dispersion, polarization properties, and their spatial profiles in particular. This section introduces the study of the modes of perfect fibers. We will present the different ways to describe the propagation modes and the methods to compute them. First, we will introduce the full vectorial description of the optical modes. We will then consider the weakly guided approximation and present the representation of Linearly Polarized (LP) modes. We will also introduce another description of the modes that is interesting for in telecommunications, which is the set of the Orbital Angular Momentum (OAM) modes. Finally, we will briefly introduce the mode coupling theory to describe the coupling that can occur between the modes in the presence of disorder.

2.1 Vector modes

The propagation modes of the fiber are the source-free solution of Maxwell's equation for the optical fiber waveguide geometry. Solving the vectorial wave equation leads to the emergence of three kinds of modes:

- Transverse Electric (TE) modes, for which the electric field is equal to zero along the propagation direction,
- Transverse Magnetic (TM) modes, for which the magnetic field is equal to zero along the propagation direction,
- and hybrid modes (called HE and EH), that correspond to modes where neither the electric nor the magnetic field has a zero longitudinal component.

These modes are not convenient for wavefront shaping applications. Indeed, the different modes do not have a uniform polarization across the transverse plane, as shown in Figure I.10, making them difficult to be experimentally generated.

2.2 The scalar approximation

In practice, most optical fibers have a small numerical aperture. They satisfy the *weakly guiding approximation* [Gloge, 1971], i.e. $\frac{n_1 - n_c}{n_c} \ll 1$. In this approximation, the longitudinal component of the field is neglected, we then have:

$$\vec{E}(r, \phi, z) = \vec{\psi}(r, \phi) e^{i\beta z}, \quad (\text{I.4})$$

where ϕ is the azimuthal coordinate in the transverse plane, r the radial coordinate in the transverse plane, z the longitudinal coordinate, and β is the propagation constant. $\vec{\psi}$ is the transverse optical field. $\psi(r, \phi)$ then satisfies a scalar Helmholtz equation:

$$\partial_r^2 \psi(r, \phi) + \frac{1}{r} \partial_r \psi(r, \phi) + \frac{1}{r^2} \partial_\phi^2 \psi(r, \phi) + [k_0^2 n^2(r, \phi) - \beta^2] \psi(r, \phi) = 0, \quad (\text{I.5})$$

where $k_0 = 2\pi/\lambda$ is the wavenumber with λ the wavelength. For an axisymmetric fiber, so that $n(r, \phi) = n(r)$, we can search for solution of the form:

$$\vec{\psi}(r, \phi) = \psi(r, \phi) \vec{e} = f(r) g(\phi) \vec{e} \quad (\text{I.6})$$

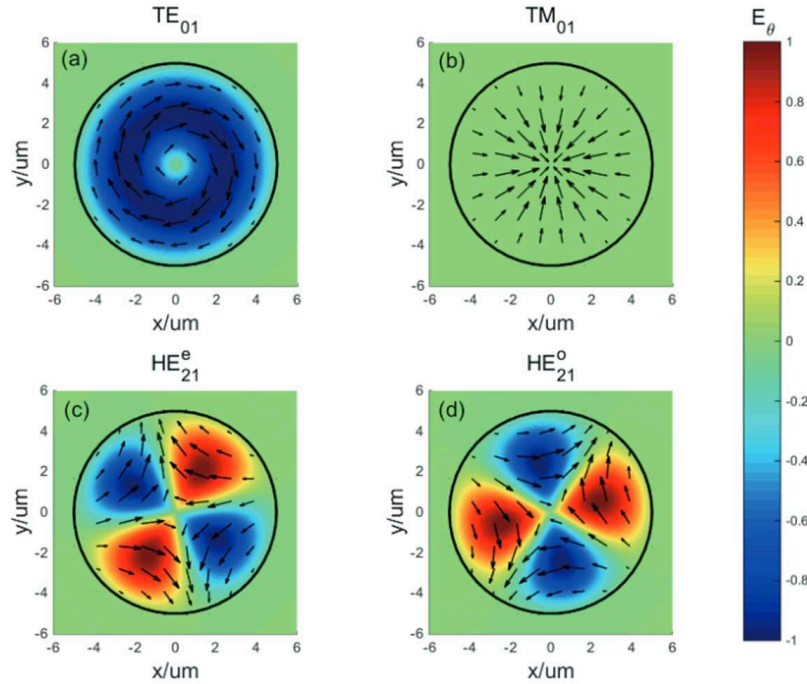


Figure I.9: Spatial profiles of the vectorial modes. Spatial profiles of the azimuthal field E_θ (in color) of the modes TE_{01} , TM_{01} , HE_{21}^e and HE_{21}^o , along with their polarizations (arrows) for an MMF. The bold black line represents the limits of the core. From [Xiong et al., 2017c].

where \vec{e} is a unit vector.

To satisfy the rotational symmetry along the longitudinal axis, we should have $g(\phi) = g(\phi + 2p\pi)$ for all integers p . Different choice of functions g and of unit vectors \vec{e} are valid and give rise to different representations of the modes. The propagation constant of each mode allows defining an effective index n_{eff} affecting light carried by the mode. The effective index is defined by:

$$\beta = k_0 n_{\text{eff}}. \quad (\text{I.7})$$

2.2.a Linearly polarized modes

Under the scalar approximation, there exists a set of orthogonal modes that are uniformly linearly polarized, called the Linearly Polarized (LP) modes. These modes are characterized by a transverse field and can take the forms:

$$\vec{\psi}^{(e)}(r, \phi) \propto f_m(r) \cos(m\theta) \vec{e}_{x/y}, \quad (\text{I.8})$$

and also, when $m > 0$

$$\vec{\psi}^{(o)}(r, \phi) \propto f_m(r) \sin(m\theta) \vec{e}_{x/y}, \quad (\text{I.9})$$

where the superscript $^{(e)}$ (resp. $^{(o)}$) indicates if the mode is *even* (resp. *odd*), which means it has a *cosine* (resp. *sine*) azimuthal dependency. When $m = 0$, the field can only take the *even* form, when $m > 0$, the field can take either the *even* or the *odd* form. \vec{e}_x and \vec{e}_y are unit vectors representing the linear polarizations along two orthogonal transverse directions x and y . These modes are indexed by a strictly positive integer

l , representing the number of oscillations of the radial dependence $f_m(r)$ ², and a positive integer m , representing the number of oscillations of the azimuthal dependence. The propagation constants β and the corresponding radial profile f are solutions of the eigenvalue problem [koshi, 1982]:

$$d_r^2 f_m(r) + \frac{1}{r} d_r f_m(r) + \left[k_0^2 n^2(r) - \beta^2 - \frac{m^2}{r^2} \right] f_m(r) = 0. \quad (\text{I.10})$$

The two modes with the same transverse profiles but with orthogonal polarizations are degenerate for axisymmetric index profiles. Similarly, for $m > 0$, the even and odd modes, that are the results of the rotation of the other one by an angle $\pi/2m$, are also degenerate.

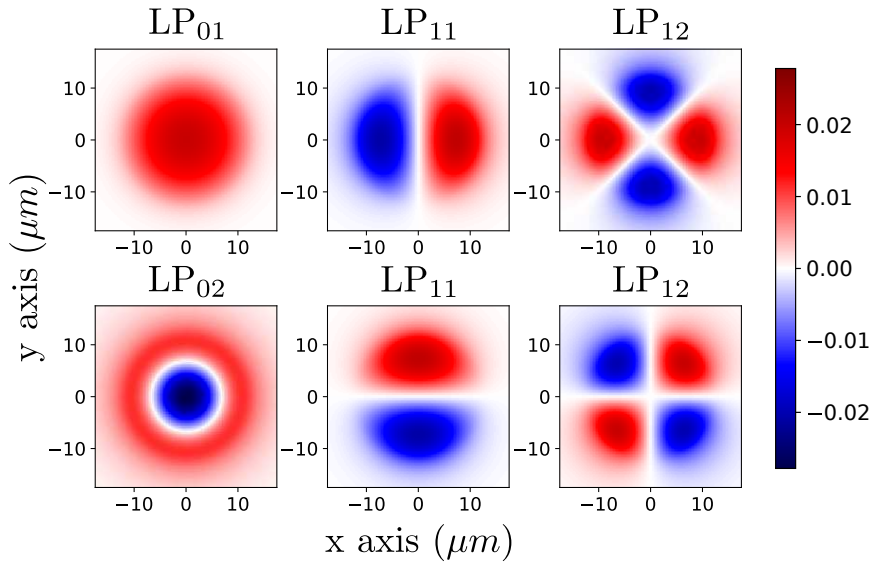


Figure I.10: Spatial profiles of the LP_{ml} modes. Real part of the mode profiles of the first 6 LP modes. Simulation performed for a 6-mode step index fiber.

2.2.b Orbital angular momentum modes

The groups of degenerate LP modes can be rearranged with linear combinations to form the so-called *Orbital Angular Momentum* (OAM) modes. The transverse component of the electric field reads:

$$\vec{\psi}(r, \phi) \propto f_l(r) e^{jm\theta} \vec{e}_{R/L}, \quad (\text{I.11})$$

where $\vec{e}_{R/L}$ is a unit vector representing either the left or right circular polarization. These modes are indexed by a positive integer l , representing the number of oscillations of the radial dependence $f_l(r)$, sometimes referred to as the radial momentum, and an integer m , that can be positive or negative, that represents the angular momentum of light. The circular polarization carries a spin σ , that is equal to -1 or 1 , associated with a spin angular momentum $\sigma\hbar$. The total angular momentum of a photon in an OAM mode is then the sum of its spin angular momentum and the orbital angular momentum of light $(m + \sigma)\hbar$ [Allen et al., 1992].

²The number l does not explicitly appear in the expression of $f_m(r)$. It is implicitly included in the propagation constants.

2.3 Step index and graded index fiber

In step index fibers, the eigenvalue problem represented by equation I.5 admits analytical solutions for the mode profiles. The radial dependence take the form of Bessel functions [Gloge, 1971]. It gives access to an analytical expression for the dispersion relation that can be solved numerically to obtain the propagation constants of the modes. No analytical expressions of the mode profiles exist in the case of GRIN fibers. Several numerical methods were developed to solve equation I.5, among which:

- the WKB (Wentzel-Kramers-Brillouin) approximation [Gloge and Marcatili, 1973],
- the Rayleigh Ritz method [Okamoto, Okoshi, and Hotate, 1979],
- the power-series expansion method [Oyamada and Okoshi, 1980],
- finite difference numerical methods.

We present in appendix G a method we developed to numerically solve equation I.5 and find the spatial profiles of the modes for GRIN fibers. The goal is to get reasonably accurate results with limited computation requirements, and to obtain the modes in a desired representation.

The index profile of a fiber strongly affects the propagation constant and the number of modes that it can support. We show in Figure I.11 the propagation constants of the OAM modes obtained for a step index and parabolic GRIN fiber with the same parameters. For the same core diameter and the same numerical aperture, a parabolic GRIN fiber supports approximately half as many modes as a step index fiber. It is common to approximate the total number of the modes, for both polariza-

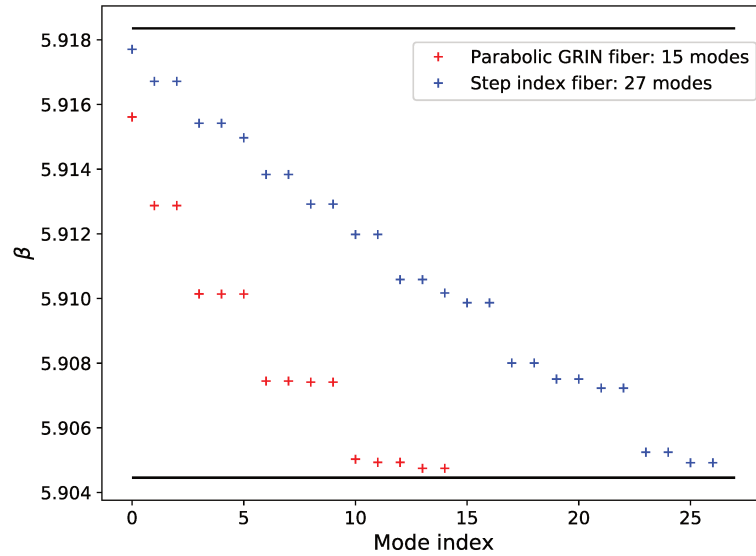


Figure I.11: Comparison of the modes of GRIN and step index fibers. Propagation constants of the modes obtained for a parabolic GRIN and step index fiber of same parameters $a = 25 \mu\text{m}$ and $\text{NA} = 0.1$. The modes are shown for a single polarization. The black lines represent the bounds of possible propagation constants $[k_0 n_c, k_0 n_1]$. Obtained using the numerical method presented in section 2.3 and detailed in appendix G.

tions, using the V-number introduced in equation I.3 [Paschotta, 2017b]:

$$\begin{aligned} N_{\text{modes}} &\sim V^2/2, \text{ for step index fibers,} \\ N_{\text{modes}} &\sim V^2/4, \text{ for GRIN fibers.} \end{aligned} \quad (\text{I.12})$$

We observe group of quasi-degenerate modes. In the case of step index MMFs, we have a four-fold degeneracy (including both polarization) for $m > 0$ and a two-fold degeneracy for $m = 0$. For GRIN MMFs, the size of the groups of degenerate modes increases for high-order modes.

In figure I.12, we show the dispersion relation for step index (a) and GRIN fibers (b). The dispersion relation exhibits the evolution of the normalized propagation constant B as a function of the normalized frequency V , where B is defined as:

$$B = \frac{n_{\text{eff}} - n_c}{n_1 - n_c}. \quad (\text{I.13})$$

We remark that for the step index fiber, only one mode is supported for $V < 2.4$.

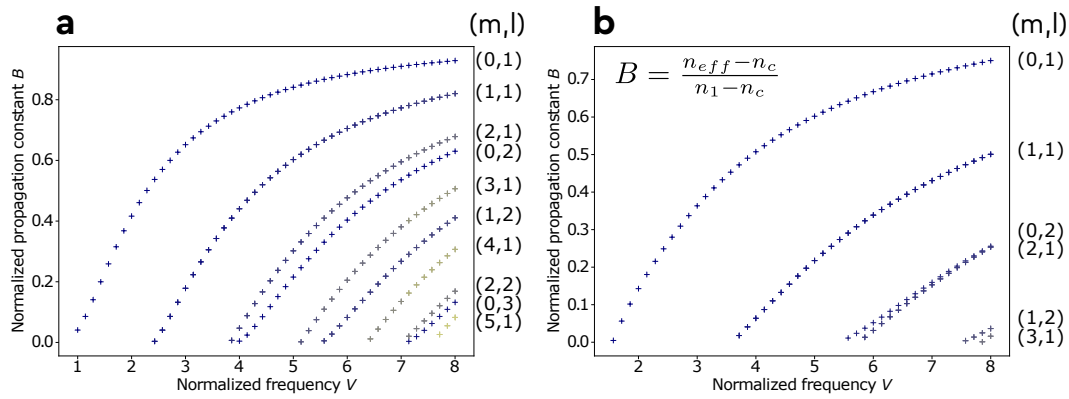


Figure I.12: Dispersion relation of step index and GRIN fibers. a, Step index fiber. b, Parabolic GRIN fiber. Simulations of the OAM modes, performed with fibers of core $a = 12.5 \mu\text{m}$, and $\text{NA} = 0.1$, using the method detailed in appendix G. The radial (l) and azimuthal (m) mode indices are displayed next to the corresponding curves.

For the parabolic GRIN, only a single mode is supported for $V < 3.6$. Below these values, a fiber is referred to as a single mode fiber (SMF), while above, it is referred to as a multimode fiber (MMF). When a MMF supports only few modes, typically less than 10 per polarization, we usually refer to them as Few Mode Fibers (FMFs).

2.4 Intermodal dispersion

The group velocity v_g of light in a medium is defined as the inverse of the derivative of the wavenumber k with respect to angular frequency ω :

$$v_g = \left(\frac{\partial k}{\partial \omega} \right)^{-1} = c \left(\frac{\partial}{\partial \omega} (\omega n(\omega)) \right)^{-1} = \frac{c}{n(\omega) + \omega \frac{\partial n}{\partial \omega}}. \quad (\text{I.14})$$

In a waveguide such as an MMF, the group velocity of a mode $v_{g,i}$ is related to its effective index $n_{\text{eff},j}(\omega)$:

$$v_{g,j} = \frac{c}{n_{\text{eff},j}(\omega) + \omega \frac{\partial n_{\text{eff},j}}{\partial \omega}}. \quad (\text{I.15})$$

The group velocities of the different modes of a fiber are generally different, which results in mode-dependent group-delays for a fiber of a given length; it means that sending a pulse that couples to multiple modes at the input results in multiple pulses with different group-delays at the output of the fiber. This phenomenon is called *intermodal dispersion*.

To quantify the intermodal dispersion of a given MMF, one typically specifies its *Differential Group Delay* (DGD) which characterizes the difference between the shortest and longest group-delays of an input pulse for a given length of fiber, or the *Differential Mode Group Delays* (DMGD) which indicate the difference between a specific mode and the fundamental mode of the fiber. The DGD is proportional to the length of the fiber in ideal MMFs with no coupling between the modes. Typical values of the DGD of MMFs can be of the order of 10 ps/m [Sillard et al., 2011; Sillard et al., 2014], while GRIN fibers can be designed to go below this value and can reach 0.1 ps/m [Paschotta, 2017a]. Having high DGDs in MMFs is a limitation to the implementation of space division multiplexing (that we will introduce in section 4.3) because it increases the complexity of the digital signal processing required to retrieve the information [Li et al., 2014].

2.5 Mode coupling theory

In ideal and unperturbed fibers, modes are invariant through propagation by definition. However, perturbations in the fiber geometry, index imperfections, mechanical stress, bends and other external effects can induce unintended coupling between the supported modes of the fiber: a fraction of energy carried by a mode is transferred to other modes.

In 1972, Gloge performed experiments where only the lower order modes of MMFs of different lengths are excited; at the output, he remarked that the longer the length, the more energy got transferred into higher order modes [Gloge, 1972]. The energy transfer is progressive, and he speculated that modes couple to *close* modes.

Most perturbations affecting optical fibers have a tendency to couple modes with close propagation constants; this effect is quantified by the longitudinal power spectrum of perturbation F , which scales as $\langle |F(\Delta\beta)|^2 \rangle \propto \Delta\beta^{-4}$ to $\Delta\beta^{-8}$ [Olshansky, 1975], with $\Delta\beta$ the propagation constant difference. The consequence is that modes with close or the same propagation constants couple over shorter lengths [Ryf et al., 2012; Kitayama, Seikai, and Uchida, 1980]. Recent studies confirmed these observations [Li et al., 2020] and demonstrated that mode coupling occurs almost isotropically in the space represented by the l and m numbers of the OAM modes. In other words, coupling between modes with the same total difference $\Delta m + \Delta l$ will couple approximately with the same amplitude. We show in Figure I.13 the measurements of the coupling observed at the output of a 754-mode step index MMF for different input modes. We notice at the output that each input mode only couples to modes with close and similar m and l indices during propagation through the fiber.

Mode coupling is governed by the following equations [koshi, 1982]:

$$\frac{dA_\mu}{dz} = -j\beta_\mu A_\mu + \sum_{v \neq \mu} C_{\mu v}(z) A_v, \quad (\text{I.16})$$

where A_μ is the amplitude of the μ^{th} mode, and $C_{v\mu}$ is the coupling coefficient between the v^{th} and μ^{th} mode. Assuming a small perturbation of the index of the form:

$$n^2(x, y, z) = n_0^2(x, y) + \delta n^2(x, y) f(z), \quad (\text{I.17})$$

then the coupling coefficients can be calculated:

$$C_{\mu v}(z) \propto \int_{-\infty}^{\infty} \int_{-\infty}^{\infty} \delta n^2(x, y) \mathbf{E}_\mu^*(x, y) \cdot \mathbf{E}_v(x, y) dx dy \cdot f(z), \quad (\text{I.18})$$

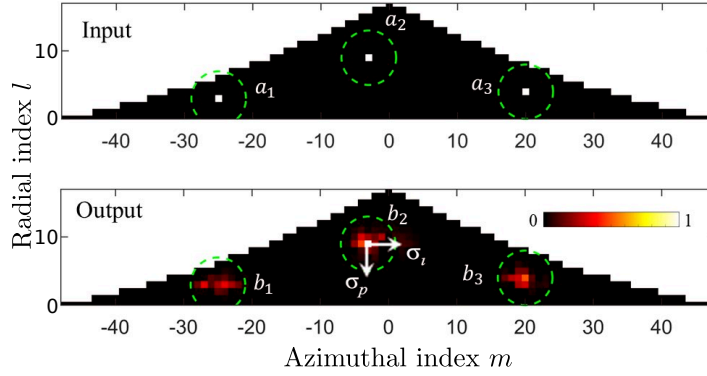


Figure I.13: Coupling observed in a step index MMF. **a**, Representation in the (m, l) -space of the 3 input OAM modes, a_1 , a_2 , and a_3 , sent into a 754-mode step index fiber. **b**, Outputs of the MMF for the 3 input modes, represented in the (m, l) -space. Extracted from [Li et al., 2020].

where $\mathbf{E}_v(x, y)$ is the vector field of the v^{th} mode. The symmetry of the disorder determines which modes will couple [Ho and Kahn, 2013].

If we inject light in a single mode ν , after a propagation length of $z = L$, the amplitude of mode $\mu \neq \nu$ is:

$$A_\mu(L) \approx e^{-j\beta_\mu L} \int_0^L C_{\mu\nu}(z) e^{-j(\beta_\nu - \beta_\mu)z} dz. \quad (\text{I.19})$$

The integral term contains a phase matching condition between the propagation constants of the modes and the longitudinal index fluctuations. Computing the conversion coefficients requires having access to the precise parameters of the fiber at all positions. This can be possible for simple cases such as periodic perturbations, but is usually out of reach.

The second approach proposed by Marcuse [Marcuse, 1972], is a power coupling model and describes coupling as a diffusion process. It describes the redistribution of energy among the modes, in this case the power coupling equations are the following:

$$\frac{dP_\mu}{dz} = -\alpha_\mu P_\mu + \sum_{\nu \neq \mu} h_{\mu\nu} (P_\nu - P_\mu), \quad (\text{I.20})$$

where $P_\mu(z) = \langle |A_\mu(z)|^2 \rangle$ is the power carried by the μ^{th} mode, α_μ is a power attenuation coefficient, and $h_{\mu\nu}$ are coupling coefficients expressed as the power spectrum of the conversion coefficient:

$$h_{\mu\nu} = \left\langle \left| \int_0^L C_{\mu\nu}(z) e^{-j(\beta_\nu - \beta_\mu)z} dz \right|^2 \right\rangle. \quad (\text{I.21})$$

In this case, we evaluate the power spectrum of the conversion coefficient over the length of the fiber in order to determine the coupling in a probabilistic manner. While it give statistically accurate results, it does not give access to the coupling properties for a given realization of disorder. Moreover, the phase is disregarded in this model, which is detrimental for applications with coherent modulation schemes.

3 Optical fibers in telecommunications

The use of optical fibers has been developing extremely fast in the field of telecommunications in the late XXth century and the beginning of the XXIst century. They are almost ubiquitous, from the transoceanic links to the home internet access. We saw in the previous section that different approaches and fiber technologies were considered, depending on the intended application, and that many improvements had to be made to the initial glass fibers to make optical communications possible.

In this section, we will first detail the main advances made in the optical fiber technology to allow for fast and robust telecommunication protocols. To that end, we will exclusively talk about SMFs, which are the preferred media of propagation of long haul links. Then, we will present the current usage of optical fibers in the telecommunications' industry. Lastly, we will discuss the current limitations and the need for a new paradigm change in order to meet the ever-increasing demand of higher data rates.

3.1 Historical limitations and breakthroughs

The 1970s' promising loss levels of tens of dBs by kilometers allowed to envision the use of fibers in short networks. As long as the distance is less than a few kilometers, the signal can be accurately retrieved and decoded at the output of the fiber. However, thousands of kilometers transmission were still out of reach. The transfer capacity of fibers was very low compared to the current ones. The maximum capacity of a channel is given by Claude Shannon's formula [Shannon, 1948]:

$$C = B \log_2(1 + \text{SNR}), \quad (\text{I.22})$$

with SNR being the signal-to-noise ratio and B the bandwidth. Increasing the information capacity can be done by increasing the SNR of the system, but it also requires to efficiently encode the information to approach this theoretical limit in practice. Figure I.14 shows the continuous improvement of the achievable capacity of optical fibers and the technologies that allowed these results.

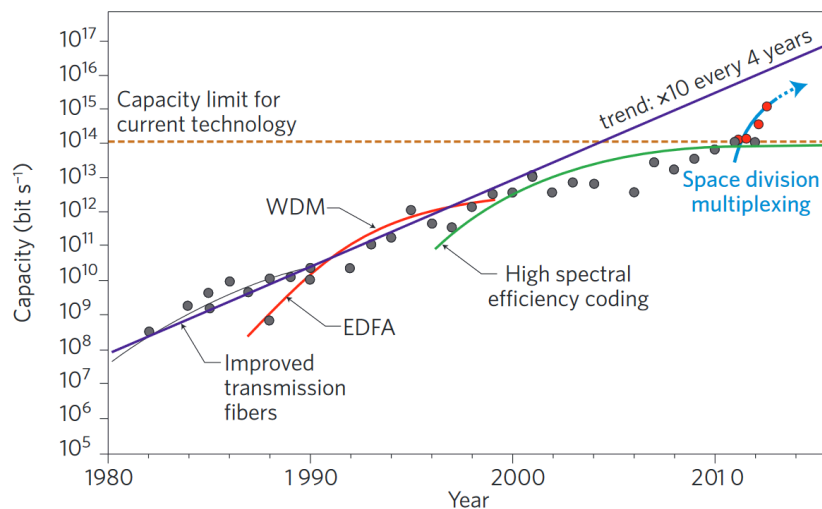


Figure I.14: Capacity of optical fiber technologies over time. Figure from [Richardson, Fini, and Nelson, 2013].

Until recently, we observed a relationship between the capacity of fiber technologies and the time that is similar to the Moore's law: the capacity is increased tenfold every 4 years since the 1980s. The next subsections detail the main improvements that lead to that trend.

3.1.a Materials and design enhancements

In the 1970s, optical fibers had very high propagation losses: most of the initial developments were aimed at reducing the absorption in the fibers. The main sources of losses in glass are caused by the presence of metal ions such as iron, copper, vanadium, and chromium [Kao, 1966]. Therefore, most of the initial efforts were made to remove these impurities, while controlling the amount of dopant (titanium then mostly germanium) to obtain the desired optical indices. In Figure I.15, we show the attenuation measured for step index silica optical fibers in 1979 [Miya et al., 1979].

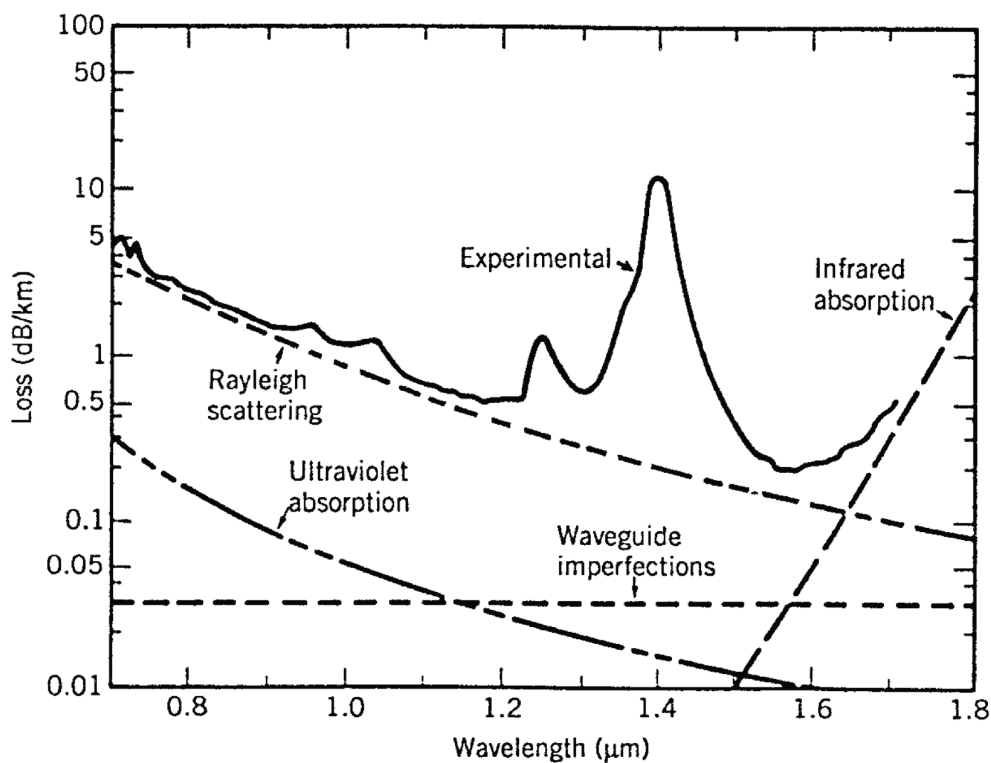


Figure I.15: Sources of loss in optical fibers. Attenuation in function of the wavelength in step index silica optical fibers. Image from [Miya et al., 1979], adapted by [Hui, 2019].

The minimal attenuation level is reached at around $\lambda = 1.55 \mu\text{m}$. A local minimum can also be observed at $\lambda = 1.30 \mu\text{m}$, between two absorption peaks that are caused by hydroxyl ions indicating the presence of water. Glass fibers can be manufactured to prevent the presence of these ions, those fibers are typically called low-OH and are suitable for visible-IR applications.

Further transmission improvements were obtained by small modifications to this scheme: geometries such as ring core [Hirano et al., 2012] or pure silica core, fluoride doped cladding [Hirano et al., 2013] were used to lower the attenuation, reaching in 2018 the lowest recorded attenuation of 0.14 dB/km at $\lambda = 1560 \mu\text{m}$ [Tamura et al., 2018] using a step design with fluoride dopants in the core and in the cladding. Some examples of these designs are presented in Figure I.16.

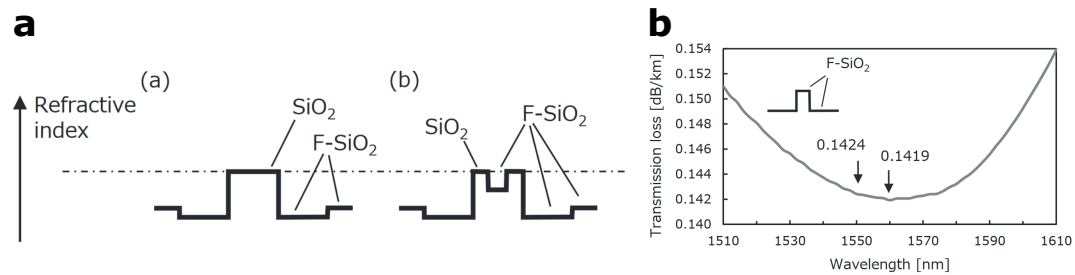


Figure I.16: Improvements in the design of step index fibers. **a**, Index profiles of fibers achieving the lowest attenuation, with step core (a) and ring core (b) fluoride doped fibers. **b**, Attenuation as a function of wavelength and design of the lowest attenuation fiber design as of 2018. Image from [Tamura et al., 2018].

3.1.b Amplification of the signal

Even with transmission attenuation as low as 0.14 dB/km, only 4% of the input light intensity comes out of the fiber after a hundred-kilometer propagation. In order to connect remote places and allow long range telecommunications, it is crucial to regenerate the signal. The initial methods relied on opto-electronic repeaters: the optical signal is converted into an electronic signal, amplified, then converted back into light and coupled into the next fiber. However, such devices are expensive, limiting the range of applications.

The invention of inline optical amplifiers, especially the Erbium doped fiber amplifier (EDFA) [Desurvire, Simpson, and Becker, 1987; Mears et al., 1987], was a major breakthrough for long range telecommunications. EDFAs rely on amplifying the signal in erbium doped fiber, thanks to a pump laser at a different wavelength ($\lambda_p = 514.5$ nm in the original work by [Desurvire, Simpson, and Becker, 1987], around 980 nm or 1480 nm today [Zyskind and Srivastava, 2011]). Light within the range $\lambda \in [1530, 1625]$ nm is amplified by stimulated emission from the excited Er^{3+} ions. The amplification is entirely optical, does not require free space conversion (the amplifier has an all-fiber design), is independent of data rate, independent of the polarization state of light and allows amplification over a large bandwidth. This technology was first implemented in the TAT-12/13 cable system in 1996, connecting the United States to the United Kingdom and France, supporting 10 Gbit/s [Trischitta et al., 1996] using undersea EDFAs.

Another scheme relies on the Raman effect to amplify the propagating signal. Contrary to EDFA, the Distributed Raman Amplifier (DRA) does not require doped sections of fibers as it exploits the stimulated Raman effect naturally occurring in fibers. The experimental principle consists in using a pump light propagating in the other direction and at different wavelength than the signal of interest. The Raman shift generates the amplification of the optical signal. The DRAs generally require higher powers than EDFAs due to smaller gain coefficients. However, they grant more spectral flexibility because the amplification is possible over a wider range of frequencies [Emori and Namiki, 1999], and is achieved with superior noise performances [Zyskind and Srivastava, 2011]. These key characteristics lead to the use of DRAs and EDFAs in hybrid setups in modern fiber architectures.

3.1.c Multiplexing: wavelength and polarization

Thanks to the optical properties of fibers links and amplifiers, a wide range of wavelengths are available for data transmission. Moreover, two orthogonal states of polarization travel through the fiber. Therefore, wavelengths and polarizations can be used to transmit information over independent telecommunication channels. The process of combining different signals into a high data rate link, e.g. the fiber here, is called multiplexing. At the end of the fiber, the signals need to be demultiplexed to be recovered. Theoretically, the transfer rate is multiplied by the number of channels used in the communication line:

$$C_{tot} = \sum_i^M C_i, \quad (I.23)$$

where C_{tot} is the total capacity of the system, M is the total number of channel, and C_i the capacity of the i^{th} channel.

Wavelength Division Multiplexing (WDM) consists in encoding individual signals with different carrier frequencies. The visible and IR spectrum is divided into several wavelength domains called bands. One or several bands are chosen for a given application, and the signals are then multiplexed into a discrete number of channels centered around different wavelengths. It is then important to ensure that the bandwidth of the channels do not overlap. WDM is typically performed with large wavelength channels (Coarse WDM: CWDM) of width about 20 nm, or small wavelength channels (Dense WDM: DWDM) of bandwidth typically of 50 GHz. Illustrations of the bands and of the CWDM technique are presented in Figure I.17.

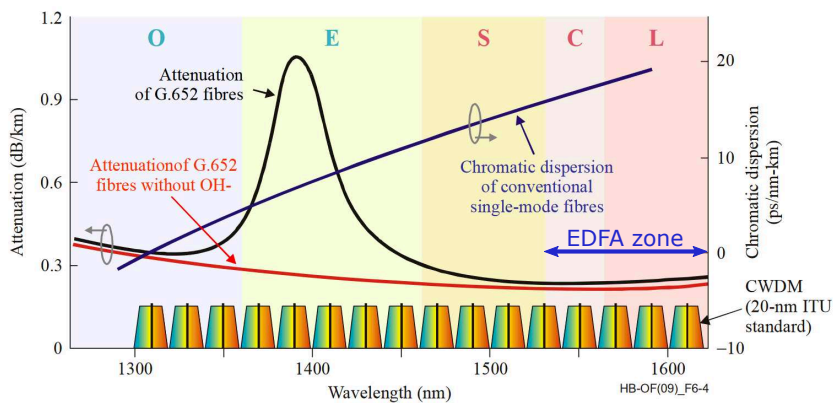


Figure I.17: Wavelength distribution in WDM. Repartition of the wavelength bands used in optical fiber telecommunications, and example of CWDM with channels 20 nm wide. Legend: O: original, E: extended-wavelength, S: short-wavelength, C: conventional and L: long bands.

In 2001, a multiplexing of 150 wavelength channels of width 25 GHz in the C-band (1530 – 1560 nm) was reported [Yamada et al., 2001], thus granting about 10 Gbit/s data rate per channel. In the same years, records of 10.9 Tbit/s were achieved [Fukuchi et al., 2001; Bigo et al., 2001].

The existence of two orthogonal states of polarization can also be used to double the number of available channels [Glance, 1987]. This technique is called Polarization Division Multiplexing (PDM). However, during propagation, coupling between polarization states occurs due to bending and imperfections. Digital signal

processing through Multiple-Input Multiple-Output (MIMO) approaches are usually required to reconstruct the input signals.

3.1.d Modulation schemes

The technological improvements in SNR contribute to increase the theoretical capacity of the channels given by Shannon's formula (equation I.22). To effectively take advantage of the increased SNR, efficient modulation strategies have to be implemented. The simplest modulation scheme relies on On-Off keying (OOK): when the signal is above a certain threshold for a certain duration, corresponding to a clock period, the receiver interprets it as a bit 1, and as a bit 0 otherwise. In this case, the modulation allows transferring as much data as the maximum bandwidth of the signal, and the spectral efficiency is $SE = 1$ (bit/s)/Hz. Other modulation schemes have to be considered to approach the theoretical capacity set by Shannon's formula I.22.

It is possible to encode more information by taking advantage of the coherent nature of light using advanced modulation formats [Winzer and Essiambre, 2006] such as Differential Phase-Shift Keying (DPSK), Differential Quadrature Phase-Shift Keying (DQPSK) or more recently Quadrature Amplitude Modulation (n -QAM, where n is the number of possible complex values called *symbols*). The symbols used in these modulation formats correspond to values of the electrical field, commonly represented in the complex plane by their *in-phase component* I and their *quadrature component* Q . Four different modulation methods are shown in Figure I.18.

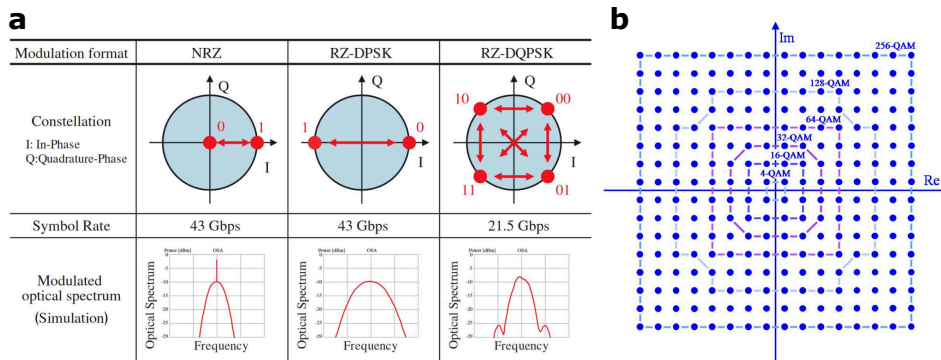


Figure I.18: Advanced modulation formats. **a**, Constellations of non-return-to-zero-OOK (NRZ-OOK), DPSK, DQPSK, and their associated spectrum from [Ohta et al., 2008]. **b**, Representation of the possible n -QAM constellations. Image from [Pfau, Hoffmann, and Noe, 2009].

With these approaches, the encoding of multiple bits of information is done with a single symbol. For instance, two bits are encoded in one complex value of the signal using DPSK modulation. Doing so increases the spectral efficiency. A given bandwidth imposes a limit on the maximal accessible symbol rate (sometimes called Baud-rate), therefore increasing the number of different symbols increases the bit-rate. Improved modulation schemes exploit more efficiently the gains in SNR that were achieved through material improvements. Figure I.19 shows how the n -QAM raises the actual capacity of optical fibers, approaching the limit imposed by Shannon's formula. Figure I.20 shows the evolution of the capacity of single mode fibers over time.

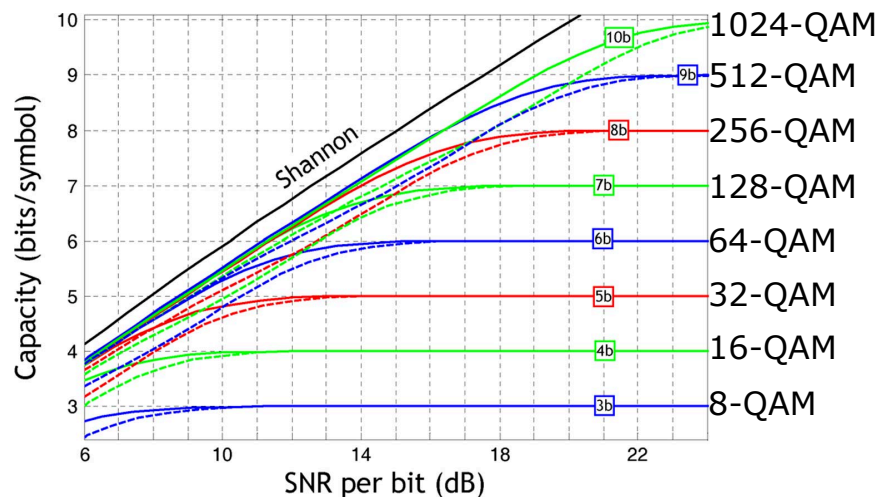


Figure I.19: Capacity as a function of SNR for different modulation schemes. Extracted from [Essiambre et al., 2010]

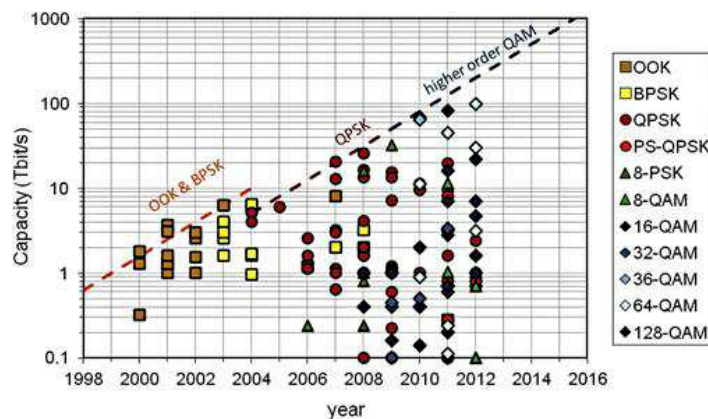


Figure I.20: Evolution of the capacity of single mode fibers over time. The maximum capacity of experimental optical communication systems has doubled every 18 months for more than a decade thanks to the use of advanced modulation formats. Extracted from [Bayvel, Behrens, and Millar, 2013].

3.2 Current use of optical fibers

As of April 2020, 406 transoceanic cables are installed around the world, their locations are presented in Figure I.21. These cables represent the largest part of the inter-continental communication infrastructure, carrying over 99% of global data transfers [Main, 2015]. With these cables and the ones covering the land, about 500 million kilometers of optical fibers are deployed around the world as of 2018 [*Optical fibre and cable industry review* | CRU]. Light is transmitted through optical fibers with very low attenuation (0.3 dB/km). In comparison, electrical copper cables show strong attenuation, ranging from a few dB/km to tens or hundreds of dB/km. Moreover, optical fibers are almost insensitive to most perturbations affecting electrical cables such as electromagnetic perturbations. These advantages make the use of optical fibers ideal for long distance information transfers. Optical fibers are also present at a smaller scale. They are increasingly used for the last mile link (fiber to the home), but also in some local networks.

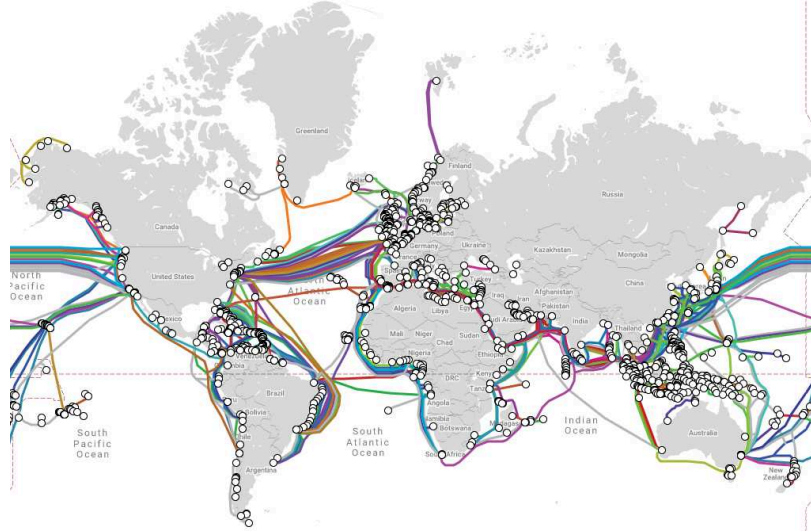


Figure I.21: Map of the transoceanic optical cables. Location of the 406 transoceanic cables present in the world as of April 2020. Map downloaded from [TeleGeography, 2020].

3.3 Limits of single mode fibers

In the recent years, a slower growth in SMF capacity was observed. The technologies presented previously in section 3.1 seem to have reached a slowdown in improvement. In this section, we present the main issues that SMF lines face.

3.3.a Chromatic and intramodal dispersion

In general, the response of a medium traversed by an electrical field depends on the optical frequency ω . The frequency dependence of the optical index $n(\omega)$ traduces the so-called *chromatic dispersion*. It is possible to approximate the index far from the resonances with the Sellmeier equation [Marcuse, 1972]:

$$n^2(\omega) = 1 + \sum_{j=1}^m \frac{B_j \omega_j^2}{\omega_j^2 - \omega^2}, \quad (\text{I.24})$$

where ω_j is the frequency of the j^{th} resonance and B_j its amplitude. The propagation constant β can thus be expressed as a Taylor series expansion around the frequency ω_0 as [Agrawal, 2002]:

$$\beta(\omega) = n(\omega) \frac{\omega}{c} = \beta_0 + \beta_1 (\omega - \omega_0) + \frac{1}{2} \beta_2 (\omega - \omega_0)^2 + \dots \quad (\text{I.25})$$

where:

$$\beta_1 = \frac{1}{v_g} = \frac{n_g}{c} = \frac{1}{c} \left(n + \omega \frac{dn}{d\omega} \right), \quad (\text{I.26})$$

and:

$$\beta_2 = \frac{1}{c} \left(2 \frac{dn}{d\omega} + \omega \frac{d^2n}{d\omega^2} \right), \quad (\text{I.27})$$

where n_g is the group index and v_g is the group velocity that quantifies the speed at which a pulse travels through the fiber. The parameter β_2 characterizes the broadening of a pulse along the propagation, this reflects the phenomenon called *Group Velocity Dispersion* (GVD).

In single mode fibers, the GVD only comes from the material dispersion and the waveguide dispersion, called *intramodal dispersion*. To quantify this broadening, the dispersion parameter $D = -\frac{\lambda}{c} \frac{d^2 n}{d\lambda^2}$, expressed in $[\text{ps} \cdot \text{nm}^{-1} \cdot \text{km}^{-1}]$ gives the temporal spread (ps) per unit of propagation distance (km), per unit pulse spectral width (nm). The dispersion parameter is equal to zero at around $\lambda = 1.27 \mu\text{m}$ for fused silica which is the zero-dispersion wavelength, and reaches about $D = 20 \text{ ps} \cdot \text{nm}^{-1} \cdot \text{km}^{-1}$ at $\lambda = 1.55 \mu\text{m}$. Similarly to intermodal dispersion, intramodal dispersion decreases the achievable data rates due to intersymbol interferences. To prevent the effects of intramodal dispersion from affecting the data-rate, the design of fiber can be adapted to produce *dispersion-shifted* fibers with a significantly decreased value of the dispersion parameter around $\lambda = 1.55 \mu\text{m}$. Values of $D = -4 \text{ ps} \cdot \text{nm}^{-1} \cdot \text{km}^{-1}$ for commercially available dispersion-shifted fiber are reported. However, intramodal dispersion is typically a few orders of magnitude weaker than intermodal dispersion in MMFs.

3.3.b Polarization dispersion

In ideal and axisymmetric optical fibers, polarizations are degenerated. For each spatial mode, there are two orthogonal polarization modes that have the same propagation constant. However, small fabrication imperfections, geometrical defects and external perturbations of the fiber result in a mixing of the two polarizations, breaking the degeneracy. The difference of the propagation constants leads to a local *birefringence*. Due to the breaking of the symmetry along the fiber the principal axes are randomly rotated along the propagation. However, for a given realization of disorder, one can find two polarization states that are associated with two distinct group velocities v_{g1} and v_{g2} . This phenomenon is referred to as *Polarization Mode-Dispersion* (PMD). Sending a pulse into a combination of these two polarization states leads to its broadening after propagation through the fiber.

PMD is quantified by the PMD parameter D_p and the pulse broadening $\Delta\tau$ can be expressed as:

$$\Delta\tau = D_p \sqrt{L}, \quad (\text{I.28})$$

where L is the propagation length. The PMD parameter D_p is expressed in $[\text{ps} \cdot \sqrt{\text{km}^{-1}}]$ and has values between 0.1 and 1 $\text{ps} \cdot \sqrt{\text{km}^{-1}}$. Due to the small values of D_p and the square root dependence, this effect is generally weak compared to GVD.

3.3.c Non-linearities

Another phenomenon that hinders telecommunication through optical fibers concerns non-linear effects. Due to the confinement of the light in the small area in the core of single mode fibers, the energy density can be high (up to $1 \text{ GW}/\text{m}^2$). This favors the manifestation of various non-linear effects.

One such effect is the change of the refractive index experienced by a medium under the influence of a high intensity electric field, called the optical Kerr effect [Kerr,

1875]. The Kerr effect can be decomposed in two parts, an *instantaneous* and a *non-instantaneous* contributions. The instantaneous part concerns the fast change of refractive index due to an intense electric field. In its simplest form its effect can be written as:

$$n(\omega, I) = n(\omega) + n_2 I, \quad (\text{I.29})$$

where I is the light intensity, and n_2 is the non-linear coefficient depending on the material properties. The two main effects resulting from this dependence are:

- The self-phase modulation, where the intensity of the optical field adds a phase shift $\phi_{SPM} = n_2 k_0 L I$, where L is the length of the fiber, responsible for the spectral broadening of ultrashort pulses [Stolen and Lin, 1978] and the formation of solitons in the anomalous dispersion region [Hasegawa and Tappert, 1973].
- The cross-phase modulation, where an optical field experiences a phase shift $\phi_{XPM} = n_2 k_0 L I_2$ due to the presence of another field (different in wavelength, polarization or direction). Cross-phase modulation is responsible for asymmetric spectral broadening of co-propagating optical pulses.

The *non-instantaneous* contribution leads to Brillouin and Raman scattering [Chraplyvy, 1988], that are not dominant in typical fiber communication systems.

4 Recent improvements

Today, SMFs are almost to their saturation in terms of Achievable Information Rate (AIR) in the linear regime because the techniques introduced in section 3.1 have been exploited up to their limit. We present here the most promising directions currently explored to improve the capacity of optical fiber communication systems.

4.1 Non-linear methods

Due to inter-channel interferences arising from non-linear effects [Essiambre et al., 2010], the maximum AIR saturates for high input powers. More precisely, the negative impact of the nonlinear signal distortion grows faster than the SNR capacity gain at high signal powers.

The AIR can be improved for high input energies using non-linear frequency division multiplexing [Yousefi and Yangzhang, 2018]. Propagation inside the fiber is governed by a non-linear Schrödinger equation:

$$j \frac{\partial q}{\partial z} = \frac{\partial^2 q}{\partial t^2} - 2s|q|^2 q + b(t, z), \quad (\text{I.30})$$

where $q(t, z)$ is the complex envelope of the signal, which is a function of the time t and the distance z along the fiber, and $b(t, z)$ is a zero-mean complex Gaussian noise. The first right hand side term corresponds to the chromatic dispersion, the second one to the non-linear Kerr effect, and the third one to the noise arising from EDFA-driven amplification along the fiber. Most conventional method of WDM disregard the second term linked to non-linear effects. The method proposed in [Yousefi and Yangzhang, 2018] consists in finding a set of frequency channels that do not suffer from interferences arising from non-linear effects using non-linear Fourier transforms.

Another studied idea concerns the use of solitons. Solitons are localized waveforms that propagate without deformation, and were observed in several domains of physics from hydrodynamics to optics [Russell, 1844; Ablowitz and Clarkson, 1991; Gardner et al., 1967; Zabusky and Kruskal, 1965]. Recent works [Dong et al., 2015; Meron, Feder, and Shtaif, 2012; Hari, Yousefi, and Kschischang, 2016] aim at implementing soliton-based channels to go beyond the limitations of linear approaches.

4.2 Photonic Crystal fibers

Hollow-Core Photonic Crystal Fibers (HC-PCF)³ are a class of fibers where light confinement is achieved thanks to a periodic structure that produces a photonic band gap. In contrast with regular fibers where the core has the highest index of the waveguide, with HC-PCF the core can be filled with air. The geometry of such a fiber is presented in Figure I.22. The propagation of light in an air-core instead of

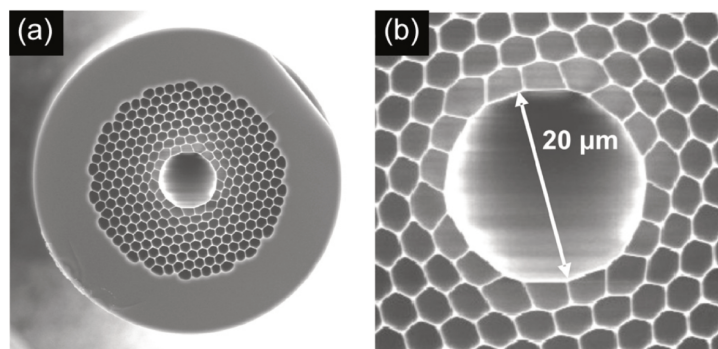


Figure I.22: Example of an HC-PCF design. a, Example of a low-loss HC-PCF, fabricated by BlazePho-tonics Ltd. b, Zoom on the core, the diameter is 20.4 μm . Extracted from [Russell, 2006]

glass-core is appealing for several reasons:

- The attenuation can be low. In 2005, attenuation as low as 1.2 dB/km was measured and theoretical models proved that an attenuation of the order of 0.1 dB/km could be achieved [Roberts et al., 2005], which is lower than the best SMFs. Recently, losses of 0.28 dB/km were reported [Jasion et al., 2020] which further reduces the gap with standard all-glass SMFs.
- Fewer non-linear effects may occur due to the medium of propagation being the air [Russell, 2006].
- Signal propagation is faster, leading to lower latencies [Zhu et al., 2020].

However, the current losses and the fabrication costs of HC-PCFs are still limiting their use for telecommunications.

4.3 Space Division Multiplexing

Arguably the next major improvements in fiber technologies will be driven by Space Division Multiplexing (SDM). To keep up with the increasing data-rate demand, network operators are required to use the *dark* fibers they previously deployed (fibers that were placed in prevision of an increase of future data rate needs but which

³Sometimes also referred to as Hollow-Core Photonic Bandgap fibers (HC-PBGF).

remained unused until now) or deploy more fibers. However, deploying parallel systems of fibers increases the cost and the energy consumption proportionally to the gain in capacity. As the demand has an exponential growth, such approach is not sustainable.

4.3.a Potential advantages of SDM

The objective of SDM is to leverage the multiple spatial channels that exist in large core optical fibers to transmit information. Increasing the number of independent channels through the same communication link would allow limiting the number of components and reduce the costs. The optical fibers put into consideration are no longer single mode fibers, but are:

- Multimode fibers (MMFs), which have larger core sizes allowing numerous modes to propagate.
- Multicore fibers (MCFs), where multiple cores are embedded in the same cladding. The cores carry either one or a few modes.

In both cases, compared to fiber bundles, the footprint is reduced for the same number of channels. For example, for a so-called OM2 fiber⁴ at $\lambda = 1550$ nm, about 50 modes per polarization are supported, giving the possibility to multiply by two orders of magnitude the capacity of the communication line with the same spatial requirements as an SMF.

Another aspect to take into account with SDM is energy density: for the same input power, the energy is spread over a larger area in multimode fibers. Consequently, non-linear effects occur for higher input powers.

4.3.b Challenges

The implementation of SDM faces challenges limiting our ability to reconstruct the signals after propagation through multimode or multicore fibers, and thus slowing their practical implementation. We discuss here the four main ones:

- Mode Dependent Losses (MDL) and mode dependent gain,
- Intermodal dispersion,
- Mode coupling,
- Spatial multiplexing and demultiplexing.

Due to MDL through the MMF communication links, and mode dependent gain in the optical amplifiers, we observe variability of the signal strength conveyed by different fiber modes [Trinel et al., 2017]. It translates into significant differences of SNR in the different channels, which hinder the efficiency of digital signal processing techniques aiming at the reconstruction of the information, and lead to lower the achievable data rates.

Intermodal dispersion, discussed in section 2.4, describes how the different spatial modes have different propagation speeds. This effect is typically few orders of

⁴OM stands for *Optical Multimode*. There are currently 5 types of OM fibers; OM1, OM2, OM3, OM4 and OM5. They are GRIN fibers and all have the same cladding diameter of 125 μm . The OM1 has a core of diameter 62.5 μm and $\text{NA} = 0.275$. The four others have a core of diameter 50 μm and $\text{NA} = 0.2$.

magnitude stronger than intramodal dispersion effects in SMFs, as discussed in section 3.3. It leads to strong group delays. MIMO approaches are considered to limit intersymbol interference. However, the complexity of the signal processing to retrieve the signals increases with the intermodal dispersion on the receiver side. Therefore, the ability to use MIMO approaches is reduced by strong intermodal dispersion.

Another significant effect is a random coupling between the propagation modes. In the case of MCFs, this effect appears when the fiber cores are close enough to allow evanescent coupling. In MMFs, it is due to fabrication imperfections and external perturbations. When using fiber modes as communication channels, it leads to a cross-talk that can forbid direct demultiplexing without signal processing.

4.3.c SDM in the weak mode coupling regime

To avoid the need for computationally demanding MIMO signal processing, one approach consists in working with fibers in which the coupling between the modes is weak. MCFs with sufficiently spaced cores fall into this category. The objective is then to maximize the density of cores while minimizing the mode coupling. In the work of [Zhu et al., 2011], 7 cores are present in a cladding of diameter 185 μm , with a distance of about 50 μm between them. Crosstalk between signals carried by the different cores is about -47 dB. It allows a record total capacity of 112 $\text{Tb}\cdot\text{s}^{-1}$ on a single 76.8-km fiber, exploiting same the techniques as the ones used with SMFs.

Few-Mode Fibers (FMF), which are MMFs that support typically less than 10 modes, were also proposed. They show a low level of mode coupling [Bigot-Astruc, Boivin, and Sillard, 2012], even over long distances, allowing long-haul communications [Ryf et al., 2012]. The level of mode coupling is improved by increasing the differential index values between the core and the cladding. These fibers can also be designed to exhibit low differential mode group delays in order to limit dispersion effects [Sillard, Molin, and Bigot-Astruc, 2015; Sillard et al., 2014]. Record transmission of 10 $\text{Pbit}\cdot\text{s}^{-1}$ were achieved by hybrid systems using multicore few mode fibers with 114 spatial channels over 11.3 km [Electric, 2017].

Fibers optimized for the propagation of orbital angular momentum (OAM) modes are also promising media to limit the coupling between channels. OAM modes refers to the helicity of the phase of the electric field as presented in section 2. Provided adequate fiber designs, the OAM modes can propagate with very limited coupling [Ma and Ramachandran, 2020]. Fiber designs such as ring core [Nejad et al., 2016], or inverse parabolic GRIN [Wang et al., 2017] allowed SDM over hundreds of meters with minimal 2×2 MIMO, or even MIMO-free [Ingerslev et al., 2018a] for 12 channels. The complexity of these approaches lies in the ability to inject, with low losses, independent signals into the different fiber modes (mode multiplexing) and to detect them (mode demultiplexing). These steps are the ones dominating the channel crosstalk [Ingerslev et al., 2018b].

4.3.d SDM in the strong mode coupling regime

A counter-intuitive approach is to work with fibers with a high level of mode coupling. Mode coupling can be beneficial in mode division multiplexing systems [Ho and Kahn, 2013] as:

- it reduces the delay spread coming from intermodal dispersion, which was observed in plastic MMF [Garito, Wang, and Gao, 1998]. The spread becomes proportional to the square root of the length of the fiber while it is proportional to the length in the weak coupling regime [Ho and Kahn, 2011],

- it tends to mitigate the mode dependent losses (and gains) [Ho and Kahn, 2014],
- and it reduces the impact of fiber non-linearities.

The main challenge then concerns the MIMO digital signal processing (DSP) complexity, that increase non-linearly with the number of modes. It then limits the number of channels that can be treated in a single MMF at reasonable costs. 72×72 MIMO has been demonstrated using 36 spatial modes in 2 polarizations [Ryf et al., 2018], but less than 10 modes can be managed in real-time⁵ [Ryf et al., 2012; Randel et al., 2015].

4.3.e Principal modes

In SMFs, due to polarization mode dispersion, the time delay of a pulse going through a fiber depends on the polarization of the input. However, there exist special orthogonal pairs of polarization at the input and output of the fiber called the *Principal States of Polarization* (PSP) [Poole and Wagner, 1986]. At the first order, these states do not change polarization at the output when the input frequency is changed. They are associated with well-defined group delays which correspond to the maximum and minimum possible time [Gordon and Kogelnik, 2000; Garnier, Fatome, and Le Meur, 2002]. Exploiting these polarization channels using 2-channel MIMO digital signal processing allows limiting the spread caused by polarization dispersion, and thus increasing the channel capacity.

In 2005, Shanhui Fan and Joseph Kahn generalized the concept of PSP to multimode waveguides [Fan and Khan, 2005]. They proved the existence of channels called *principal modes*, which do not suffer from modal dispersion to the first order in ω . These principal modes are eigenvectors of the *group delay operator*, also called the *EisenbudWignerSmith*, or *Wigner-Smith* time delay operator, defined by:

$$\mathbf{Q}(\omega) = -i\mathbf{H}^{-1}(\omega)\partial_{\omega}\mathbf{H}(\omega), \quad (\text{I.31})$$

where \mathbf{H} is an $N \times N$ unitary matrix representing lossless propagation and mode coupling⁶. It links the field on each mode at the input of the fiber to the field on each mode at the output. This matrix is referred to as the transmission matrix (TM) of the optical system, and will be extensively studied in the next chapters.

Principal Modes and PSP are not modes of the fiber *per se* as they do not maintain their shape throughout propagation in the fiber. However, they can be used as telecommunications channels for their low dispersion properties. The principal modes will be studied in more details in Chapter IV. The observation of the principal modes and a study of their spatial and dispersion properties were performed in the case of an FMF in the weak coupling regime [Carpenter, Eggleton, and Schroder, 2015] and later in an MMF in the intermediate and strong coupling regime [Xiong et al., 2016; Xiong et al., 2017a]. An illustration of the behavior of the principal modes during propagation is shown in Figure I.23.

Lately, the use of the EisenbudWignerSmith operator was generalized to study the dependence of the TM to other parameters than the frequency. The derivative

⁵Real-time MIMO with more modes was demonstrated in the weak coupling regime by using MIMO of lower dimension for different groups of modes with limited cross-talk between the groups.

⁶While the definition is true for a unitary matrix \mathbf{H} , the general definition involves the *scattering matrix* \mathbf{S} , which will be introduced in Chapter II, section 3.1. Then, the operator is $\mathbf{Q}(\omega) = -i\mathbf{S}^{-1}(\omega)\partial_{\omega}\mathbf{S}(\omega)$.

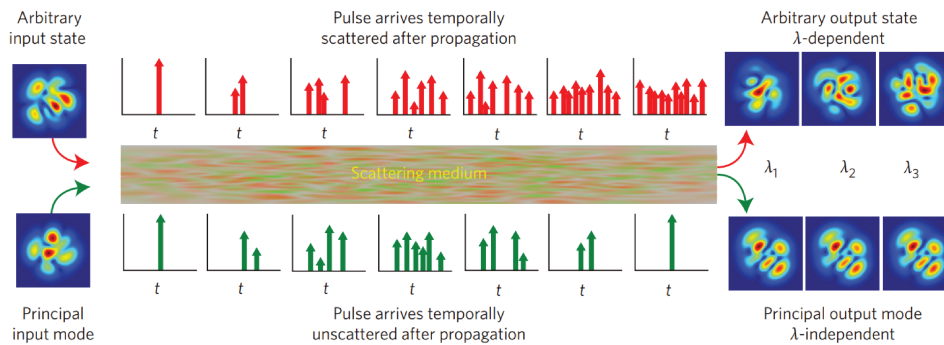


Figure I.23: Principal modes of a complex medium. Propagation of an arbitrary spatial state and a principal mode through a complex medium. Extracted from [Carpenter, Eggleton, and Schroder, 2015]

in equation I.31 can be replaced by the derivative with respect to any parameter α that affects light propagation in the optical system. This operator is called the Generalized Wigner-Smith (GWS) operator [Ambichl et al., 2017a; Horodyski et al., 2020]. The eigenstates of this operator, the *generalized principal modes*, represent channels that are insensitive to changes of the parameter α to the first order. The states associated to the highest singular values correspond to principal modes that are insensitive over the largest ranges of variations of α . Exploiting the properties of these modes allows focusing light on a specific target [Ambichl et al., 2017a] or transferring a linear or angular momentum to small objects [Horodyski et al., 2020].

Conclusion

The history of optical fibers was presented, including the key developments that lead to the modern fibers. We presented the key characteristics of the different mode families that describe the propagation of light in fibers. One basis obtained in the scalar approximation, the OAM mode basis, will be at the center of our study in Chapters III and IV. We showed the different improvements that lead to the versatile use of fibers in telecommunications and exhibited the reasons why the new paradigm of SDM is foreseen as the new technological breakthrough to carry on the exponential growth in telecommunication capacity. Finally, we presented the key challenges that SDM faces and what the two main approaches to address them are.

Chapter II

The experimental study of Multimode Fibers

Chapter contents:

1	Modal content detection methods	34
1.1	The cross-correlation (C2) method	34
1.2	Spatially and spectrally resolved (S2) method.....	35
2	The propagation of waves in complex media	38
2.1	Aberrations and their compensation	38
2.2	Propagation of light in a complex medium	39
2.3	Spatial light modulators	41
2.4	Wavefront shaping in complex media	42
3	Measuring transmission matrices	45
3.1	The scattering matrix and the propagation channels of a system	45
3.2	The transmission matrix of scattering media	46
3.3	The mode basis TM	48
	Conclusion	52

1 Modal content detection methods

MMFs offer a spatial diversity that can be exploited for telecommunications using space division multiplexing. A prerequisite is to characterize the modal content of the fiber in terms of attenuation, dispersion and spatial profiles. We present the two main standard methods to evaluate the modes properties of multimode fibers, namely the cross-correlation method, and the spatially and spectrally resolved method.

1.1 The cross-correlation (C2) method

The cross-correlation imaging, also referred to as the *C2-method*, is a technique relying on low coherence interferometry to reconstruct the modal content of an optical fiber [Schimpf, Barankov, and Ramachandran, 2011]. It uses the interferences between a reference beam and light coming out of the fiber. Interferences are measured only when the relative time delay between photons coming from the two arms is lower than the coherence time of the source, which is small as a low coherence source is used. While we continuously change the time delay between the two arms we measure the amplitude of the interferences, allowing the estimation of the temporal cross-correlation function between the signal and the reference. Using a reference arm with a low dispersion, this measure gives an estimation of the time dependence of the signal coming out of the multimode fiber.

The implementation uses a Mach-Zehnder interferometer as shown in Figure II.1.a. The cross correlation allows deducing the amplitude, weights, profiles, group delays

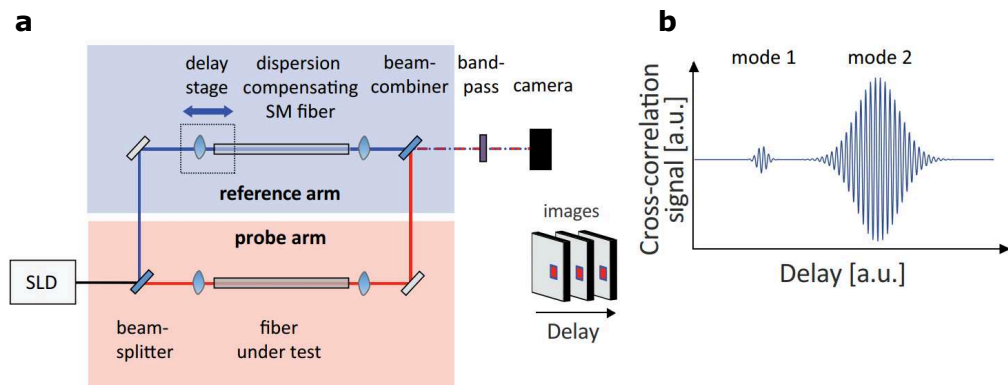


Figure II.1: Principle of the C2 method. **a**, Schematic of the experimental setup (SLD: superluminescent diode). The setup acts as a Mach-Zehnder interferometer: light propagates through the fiber under test in the probe arm, and through a dispersion compensating SMF in the reference arm. The bandpass allows tuning the temporal coherence of the source hence the spectral resolution. **b**, The cross-correlation signal at one pixel of the stack of images. Extracted from [Schimpf, Barankov, and Ramachandran, 2011].

and dispersion properties of the fiber modes. The lower the coherence, the better the group delays estimation: we show the spectrum of the source with and without a bandpass filter in Figure II.2.a, and the cross-correlation signal recorded with and without the bandpass filter in Figure II.2.b. Noticeably, the cross-correlation without the bandpass filter is more resolved and the individual contributions of the modes can be detected. At the maxima of the cross-correlation signal, the interference patterns on the camera correspond to the spatial profiles of the modes. They are measured and are shown in Figure II.2.c.

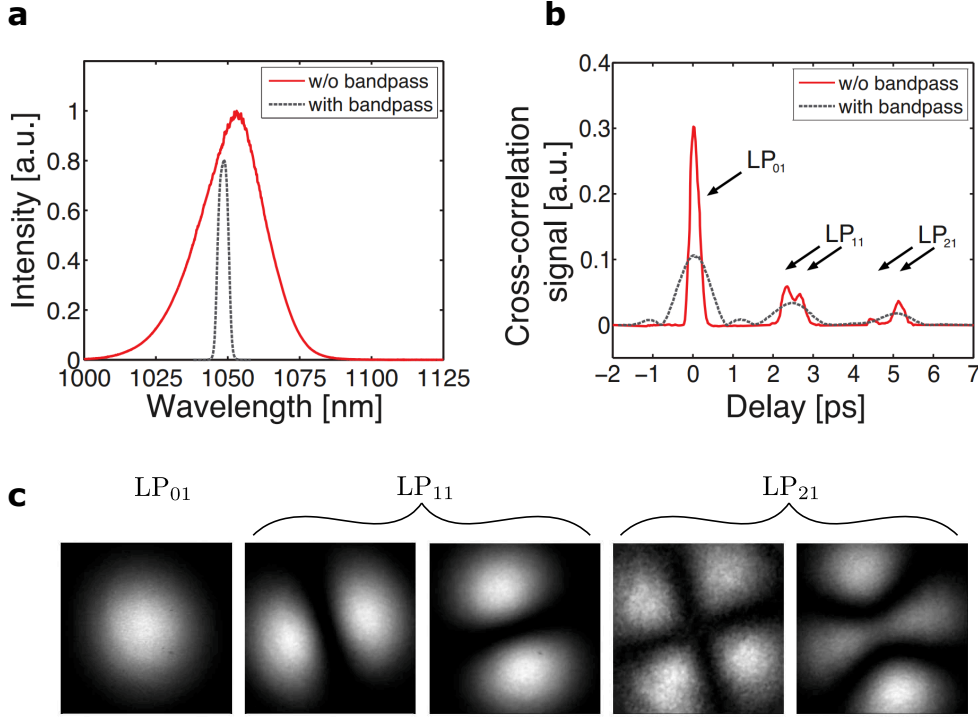


Figure II.2: Measurements using the C2 method. **a**, Spectrum of the source without and after filtering with the 5-nm bandpass of Figure II.1. **b**, Corresponding envelopes of the cross-correlation traces. **c**, Reconstructed mode profiles by order of temporal delays as shown in the cross correlation trace (b). Extracted from [Schimpf, Barankov, and Ramachandran, 2011].

1.2 Spatially and spectrally resolved (S2) method

The spatially and spectrally resolved method, also known as the *S2 method*, allows the characterization of the propagating modes of a fiber without the need for an external reference arm. It relies on the measure of the spatial and spectral interference between the different propagating modes [Nicholson et al., 2008]. The principle is to inject coherent light into an MMF in such a way that numerous modes are excited while most of the energy is still carried by the fundamental mode. This can be achieved for instance using a focused beam slightly shifted from the center of the fiber core. At the output of the fiber, the different modes interfere and form a speckle pattern which is recorded with a camera. By scanning the wavelength of the source, it is possible to extract spectral information from the modification of the speckle pattern and then use it to compute the mode profiles.

In the original article [Nicholson et al., 2008], it is assumed that the majority of the energy is carried by the fundamental mode of the MMF. We can express the field $E_j(x, y, \omega)$ of the Higher Order Modes (HOMs) as a function of the field of the fundamental mode $E_0(x, y, \omega)$ arriving at the camera using a constant $\alpha_j(x, y)$, independent of the frequency:

$$E_j(x, y, \omega) = \alpha_j(x, y) E_0(x, y, \omega) e^{i\omega\tau_j}, \text{ for } j \in [1, N_{\text{modes}}], \quad (\text{II.1})$$

where i is the imaginary unit number, τ_j is the phase delay between the j^{th} mode and the fundamental mode, given by $\tau_j = L\Delta n_g/c$ with L the length of the fiber and $\Delta n_g = n_{\text{eff},j} - n_{\text{eff},0}$ is the difference between the effective indices of the j^{th} mode and the fundamental mode. This expression is valid within small variations

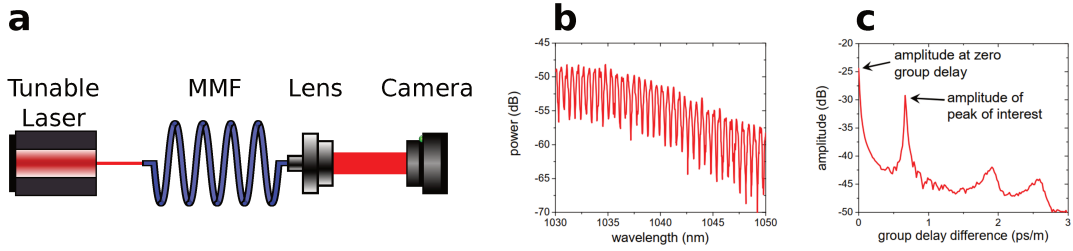


Figure II.3: Principles of the S2 method. **a**, Setup used for the S2 method using a tunable laser and a camera. **b**, Typical optical spectrum measured at an arbitrary (x, y) point. **c**, The Fourier transform of the optical spectrum in (c) showing multiple beat frequencies. Adapted from [Nicholson et al., 2008].

of the optical frequency ω . Because we assume that the intensity carried by the HOMs is low compared to the fundamental mode, the interference between HOMs is neglected and the intensity at the camera is approximated by:

$$I(x, y, \omega) = I_0(x, y) \left(1 + \sum_{j=1}^{N_{\text{modes}}} \alpha_j^2(x, y) + 2 \sum_{m=1}^{N_{\text{modes}}} \alpha_j(x, y) \cos(\omega\tau_j) \right). \quad (\text{II.2})$$

When the optical frequency is swept, the intensity oscillates due to the *cosine* terms for each point (x, y) . These oscillating terms express the beating between the fundamental mode and the HOMs. The measured oscillations are shown in Figure II.3.c. Computing the Fourier transform of the obtained spectrum gives access to the group delay differences, as shown in Figure II.3.d. The observed maxima correspond to the group delay differences between the HOMs and the fundamental mode. It is then possible to deduce the value of $\alpha_i(x, y)$ from the amplitude value of the maxima at each point (x, y) , and reconstruct the spatial profile of the different modes. The mode profiles of the fundamental mode is shown in Figure II.4.a, and the reconstructed HOM profiles are shown in Figures II.4.c-f.

Several limitations hinder the use of this method:

- Using equation II.2 is valid only if the intensities of the HOMs are small compared to the fundamental mode. However, experimentally, the beating arising from the interference between HOMs still occurs and higher order peaks can be seen in Figure II.4.b.
- If the group delay difference between two modes is too close, they can not be resolved unless a large spectral sweep is performed. Doing so would lead to the breaking of the hypothesis that the coefficients $\alpha_j(x, y)$ are independent of the frequency. This becomes a problem to resolve modes that are almost degenerate.

Methods such as principal component analysis [Sévigny et al., 2016] and independent component analysis [Sévigny et al., 2016] were developed to better isolate the contribution of interferences between HOMs, and to allow the modal characterization with a uniform excitation of the modes.

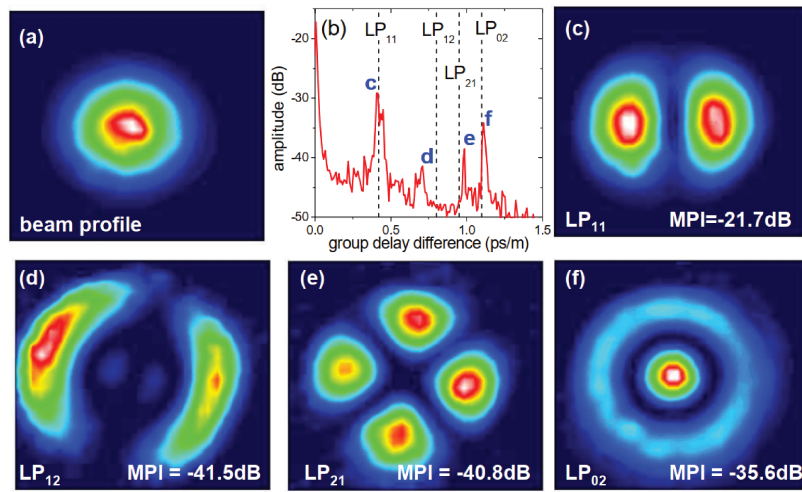


Figure II.4: Experimental results of the S2 method. **a**, Intensity profile at the output of the fiber. We observe that the profile resembles the fundamental mode. **b**, The Fourier transform of the optical spectrum showing the time delays between the fundamental mode and the higher order modes. The dashed lines represent the group delay calculated analytically. **c-f**, Mode profiles obtained for the higher order modes, and the ratio of powers of the modes compared to the fundamental (MPI) corresponding to the indicated peaks in **b**. Measurement are done on a 20 m length fiber with $a = 13.5 \mu\text{m}$ and $\text{NA} = 0.065$. Extracted from [Nicholson et al., 2008].

2 The propagation of waves in complex media

To further characterize the mode coupling properties of a fiber, we want to study the relationship between the spatial profile of the light entering the fiber and the one exiting it. The techniques and the framework to study such properties were initially introduced in the context of scattering media. We briefly introduce these approaches in scattering media and how they can be transposed to MMF characterization.

2.1 Aberrations and their compensation

Light propagation through a homogeneous medium can be described by ray optics and by the Snell-Descartes law at the smooth interface between two media. It allows determining the path of light using geometrical optics as shown in the example of a converging lens in Figure II.5.a. These laws reach their limit when the wave nature of the propagating light has to be taken into account, whether due to interferences or because of diffraction. For example, a plane wave passing through a circular converging lens is not focused to a single focal spot but forms a diffraction figure in the focal plane: an Airy disk. The characteristic diameter d of the focal spot is then:

$$d \simeq \frac{1.22\lambda}{2\text{NA}}, \quad (\text{II.3})$$

where λ is the wavelength and NA is the numerical aperture of the lens. The Airy disk is the Point-Spread Function (PSF) of a circular converging lens. The PSF is defined as the image of a point-source by an optical system, and depends on the wavelength. It allows describing how the system responds to an incoming illumination. For an isoplanetic system under coherent illumination, the observed field E_{obs} is the convolution of the geometrical image E_{geom} with the PSF [Goodman, 2005]:

$$E_{obs} \propto E_{geom} \otimes \text{PSF}, \quad (\text{II.4})$$

where \otimes is the convolution. The resolution of the optical system is defined by the width of its PSF, which is usually limited by diffraction.

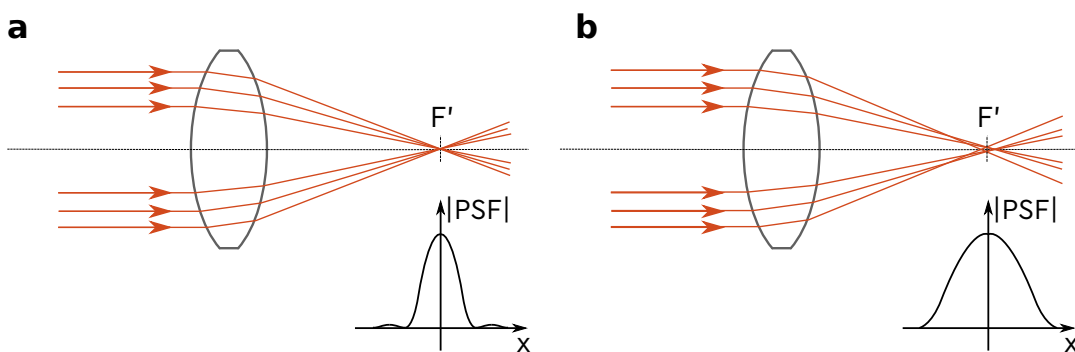


Figure II.5: Illustration of the effects of simple monochromatic aberrations. **a**, An incoming plane wave converge at focal point F' of a lens into a diffraction limited Airy disk. **b**, Due to monochromatic aberrations, the PSF is widened.

When we consider beams far away from the optical axis of a lens, they converge at different positions as shown in Figure II.5.b; the PSF is widened. We can distinguish two kinds of aberrations, the chromatic and monochromatic aberrations.

- The chromatic aberrations are produced when the properties of the optical medium depends on the wavelength. For instance, due to material dispersion,

the optical index of the medium is different for different colors. As a consequence, multiple wavelengths have different optical paths. The PSF is then wavelength dependent. Consequently, illuminating with multiple wavelength leads to an enlarged focus spot.

- The monochromatic aberrations arise when monochromatic light is distorted by the system. Spherical aberrations, astigmatism and curvature of field are examples of monochromatic aberrations. They induce a deformation of the incoming beam spatial phase. They can be modelled by Zernike polynomials of different orders [Noll, 1976].

In astronomy as well as in optical imaging, inhomogeneities of the refractive index of the medium lead to aberrations. These changes, caused by temperature fluctuations, atmospheric turbulence or imperfections of the optical systems, distort the image reconstruction of observed objects. In the middle of the XXth century, Babcock proposed a method using deformable actuators to correct the time-dependent aberrations caused by the atmosphere [Babcock, 1953]. This technique, now known as *Adaptive Optics*, is implemented in telescopes [Adaptive Optics in Astronomy 1999; Tyson, 2015] and in recent microscopy designs [Booth, 2014]. The principle consists in detecting how the wavefront coming from a reference object is perturbed by the aberrations using a wavefront sensor and compensating for these perturbations thanks to a feedback loop modifying the state of a deformable mirror. The deformable mirror locally modifies the phase of the wavefront. It allows compensating the spatial fluctuations of the phase caused by the aberrations. The principle of operation is presented in Figure II.6 in the domain of astronomy. Thanks to this method, it is possible to perform diffraction limited imaging in aberrated systems. When the

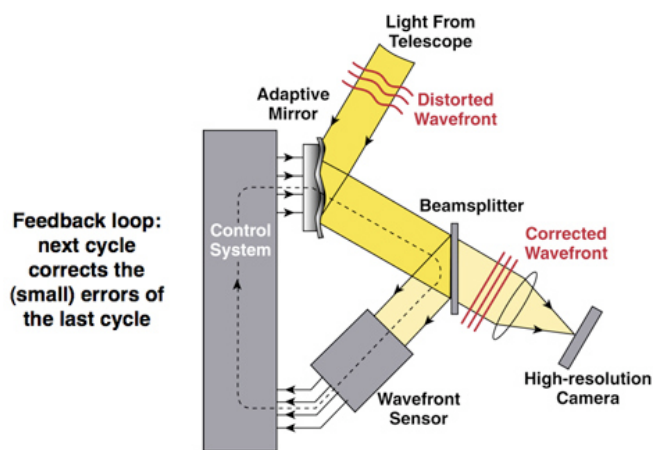


Figure II.6: Principle of adaptive optics in astronomy.

perturbations are too strong, the wavefront can no longer be corrected from such an operation. For example, the spatial information of light passing through clouds is lost. It is not possible to use adaptive optics to perform observations through them.

2.2 Propagation of light in a complex medium

The propagation of light is perturbed when it encounters an inhomogeneity, such as a dielectric particle. Due to this interaction, light gets scattered and its direction of propagation is modified. The scattering process depends on the nature of the

particle¹. An inhomogeneous medium that scatters light is typically referred to as a *scattering medium*.

We only consider the case of coherent elastic scattering: the scattered wave has the same wavelength as the incident wave. We also consider here the case of non-absorbing media. When a scattering medium is illuminated by a monochromatic source of light, the scattering events generate random optical paths and light exits the medium in different directions, and with different path length differences. The interferences of the contributions of these numerous paths give rise to a random, non-uniform, output intensity pattern, called a *speckle* pattern. The amplitude of the field at the output can be represented by the sum of random *phasors* [Goodman, 2007], as illustrated in Figures II.7.a-c. At each output point, the different phasors represent the field contributions of light coming from different input positions. The spatial distribution of the intensity follows the Rayleigh law. One remarkable property is that the fluctuation of the speckle intensity δI is equal to its average intensity $\langle I \rangle$: $\langle \delta I^2 \rangle = \langle I \rangle^2$ [Goodman, 2007].

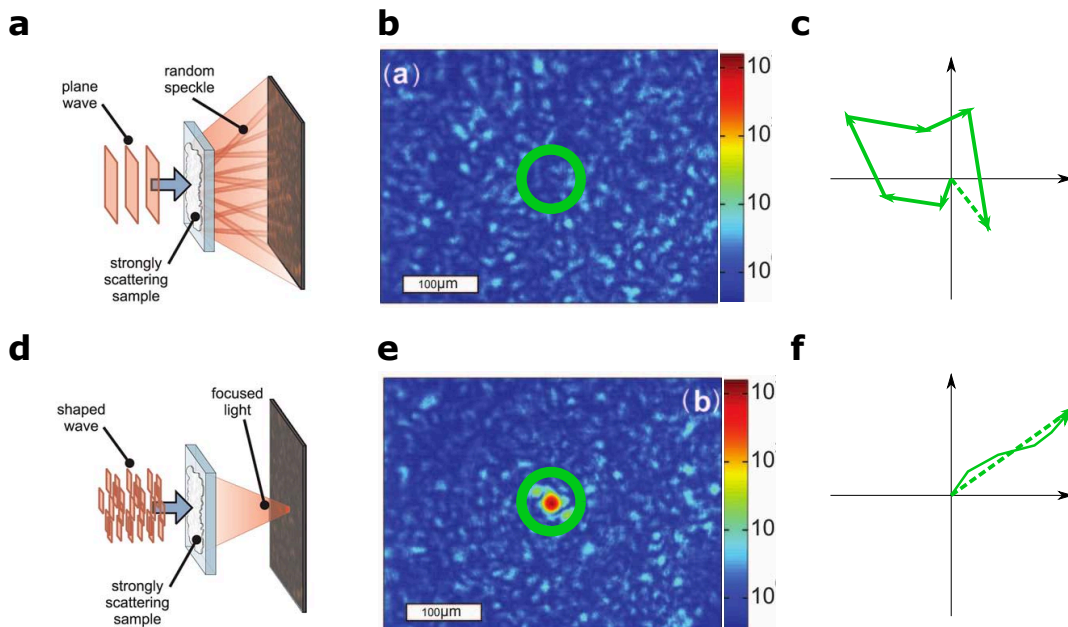


Figure II.7: Focusing experiment through a scattering medium using wavefront shaping. **a**, A plane wave illuminates a scattering medium and generates a speckle pattern at the output. **b**, Measured intensity speckle pattern. **c**, Illustration of the interference effect represented by the sum of random phasors. **d**, The input wavefront is modulated to obtain a tight focus spot in the target area at the output (green circle). **e**, Measured intensity at the output, light is focused to a spot that is 1000 times brighter than the original speckle pattern. **f**, Illustration of the coherent sum of the complex phasors to produce a constructive interference inside the green circle of **e**.

A similar phenomenon occurs in MMFs. The modes of the fiber propagate at different phase velocities due to dispersion. If we excite several input modes, they accumulate phase differences. At the output, the resulting intensity is the sum of these modes with random phase differences and a speckle pattern emerges. Similarly to the scattering medium case presented in the previous paragraph, we can use the phasor representation to illustrate the interference process. In this case, each

¹Depending on the size r of the particle relative to the wavelength of the incoming wave, the scattering process can be described by Rayleigh theory [Rayleigh, 1899] ($\lambda \gg r$), Mie theory [Mie, 1908] ($\lambda \sim r$) or Snell-Descartes law ($\lambda \ll r$).

phasor represents the contribution from a mode at a given point at the output of the fiber.

Along with chaotic cavities and scattering media, MMFs are considered *complex media*. Complex media are characterized by a seemingly random relationship between input and output fields, which translates into the generation of speckle patterns when exited with a coherent wave. In general, the scrambling of the spatial information at the output of a complex medium is considered a detrimental effect. For example, scattering occurring in biological tissue limits our ability to reconstruct images or to focus light. However, the mixing of the input information is a deterministic process, not a stochastic one; a given input spatial excitation will always give the same output speckle pattern. Using wavefront shaping, the input-output relationship can be learned and the mixing effect can be compensated for. This is the topic of the field of *wavefront shaping*, that emerged about 15 years ago, that aims at developing new applications in complex media by tailoring the input wavefront.

2.3 Spatial light modulators

Adaptive optics and wavefront shaping applications require the use of tools to spatially modify the amplitude and/or the phase of an input wavefront. These tools are grouped under the generic name of Spatial Light Modulators (SLMs). The SLMs used in astronomy to correct for the atmospheric perturbations were composed of tens of adaptive segments [Acton and Smithson, 1992]. Each segment is composed of a mirror mounted onto an actuator which controls its axial position. This allows locally changing the phase of the incoming wavefront. Nowadays, a wide range of SLMs is available to shape light [Savage, 2009]. We present the most widely used SLMs:

- Liquid Crystal on Silicon Spatial Light Modulators (LCOS-SLMs). Light is modulated on pixels of size of about $10\ \mu\text{m}$. Each pixel is composed of a liquid crystal cell trapped between two electrodes. The applied voltage changes the orientation of the crystals, thus modulating the birefringence of the medium. At a given polarization, it created a continuous phase modulation. The pixel count of SLMs can be of several millions of elements. However, they work for a single polarization, and they have a slow refresh rate due to the response time of the liquid crystals (up to 100 Hz).
- Deformable mirrors. They represent one type of Micro-ElectroMechanical-System SLMs (MEMS-SLMs). There exist segmented mirrors and mirrors with a continuous reflecting surface. Segmented mirrors consist of an array of segments which can be separately moved to control the phase. They are similar to the ones historically used for astronomy applications, but with a smaller scale (segments size of about $300 - 500\ \mu\text{m}$). Continuous surface mirrors are made with a continuous deformable reflecting surface that is deformed by an array of actuators located beneath the mirror, as shown in Figure II.8. The total number of controlled actuators is far inferior to SLMs, as only a few thousands elements can be present on a single device. Moreover, these devices are significantly more expensive. However, they work at faster frame rates ($10 - 100\ \text{kHz}$).
- The Digital Micromirror Devices (DMDs), which are another type of MEMS-SLMs. They are composed of an array of small mirrors (about $10\ \mu\text{m}$) which can be rotated into two different positions. They are fast (10 kHz) and have a high resolution ($\sim 10^6$ elements). We refer to the two states of the mirrors as *on*

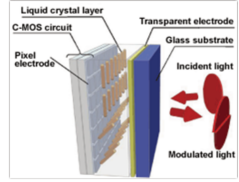

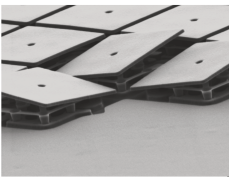
Technology	LCOS-SLM	MEMS	DMD
Illustration			
Number of pixels	10^6	10^3	10^5
Speed (Hz)	10^{1-2}	10^4	10^{4-5}
Modulation	Full-phase $0-2\pi$	Full-phase $0-2\pi$	Binary amplitude
Price	10^4 €	10^5 €	10^3 €

Figure II.8: Comparison of common SLM technologies. Extracted from [Mounaix, 2017]. Images from : Hamamatsu (LCOS-SLM), Boston Micromachine (MEMS), Texas Instrument (DMD).

and *off* depending on whether light is reflected toward a direction of interest or not. Therefore, only a binary amplitude modulation is achieved. However, several methods can be employed to increase the range of modulation such as the Lee hologram [Lee, 1978; Conkey et al., 2013] (presented in Chapter III) or the superpixel method [Goorden, Bertolotti, and Mosk, 2014] which allows obtaining an amplitude and phase modulation scheme at the price of a reduced resolution.

We show in Figure II.8 the different characteristics of the SLMs.

2.4 Wavefront shaping in complex media

In this section, we introduce the field of wavefront shaping in complex media. We present how it is now possible to focus light through complex media such as scattering layers of white paint or MMFs, thus compensating for the randomness of these media. We then present how the possibility of generating any wavefront at will allows the fine study of the modal content of MMFs.

2.4.a Focusing through a scattering medium

The apparent randomness introduced by a complex medium prevents the transmission of spatial information to the other side. This is detrimental for imaging and communication applications. Wavefront shaping techniques allow manipulating the phase and amplitude profile of the wavefront before it enters the complex medium. In 2007, a landmark experiment [Vellekoop and Mosk, 2007] demonstrates the use of wavefront shaping to focus light through a scattering medium.

In the experiment, a phase-only SLM (of $N \sim 3000$ input macropixels) is used to modulate the wavefront coming from a coherent laser source. The modulated light propagates through an opaque layer of white paint, and the output intensity pattern is imaged onto a camera. For each pixel, different phases are tested and the one that produces the highest intensity at the target position on the camera is kept. As shown in Figures II.7.d-f, the wavefront modulation allows coherently summing the contributions of the phasors, corresponding to the contributions of all the input pixels, so that they interfere constructively and produce a bright spot. For a phase only SLM, the optimal signal-to-background ratio η on a single speckle grain reads:

$$\eta \simeq \frac{\pi}{4}N. \quad (\text{II.5})$$

Experimentally, enhancement of typically 40% to 60% of this value are observed due to different effects such as the decorrelation of the medium, the limited SNR, imperfect modulation schemes, or remaining correlations between the input pixels.

2.4.b Digital Optical Phase Conjugation

Digital Optical Phase Conjugation (DOPC) is a technique to focus light through a complex media without the need for a feedback optimization. In a first step, a coherent localized source emits light inside or through a complex medium and one measures the complex output field using a camera and an interferometric setup. In a second step, the measured wavefront is numerically conjugated and generated using an SLM. The wavefront is sent toward the complex medium. The time-reversal symmetry of the wave equation guarantees that the light focuses back to its original source. It is analogue to time reversal in acoustics [Fink, 2000].

In biological imaging, MMFs are envisioned as tools to deliver light locally with a small footprint [Papadopoulos et al., 2012; Farahi et al., 2013]. In [Papadopoulos et al., 2012], the authors demonstrate the use of DOPC to focus light through a 1870-mode MMF. The setup used to implement the method is depicted in Figure II.9.a. A light source is focused at the input facet of the fiber (Figure II.9.b). The complex amplitude of the output speckle is recorded using off-axis interferometry (Figure II.9.c) and its conjugate (Figure II.9.d) is displayed on an SLM. The modulated wavefront is sent back into the fiber and the light at the input facet is recorded by a camera. We observe a focus spot at the position of the initial excitation with a contrast of 1800, as shown in Figure II.9.e.

This method allows generating a bright focus spot at the output, but requires to have access to the distal side of the fiber. As such, this method is not perfectly suited for in-vivo applications.

2.4.c Selective mode excitation

We presented in section 1 two methods usually employed to characterize the modal content of an MMF, the C2 and S2 methods. However, these techniques do not allow controlling precisely the input excitation. Using SLMs, it is possible to modulate the input wavefront so that it couples efficiently with any target guided mode of a fiber. The modal properties of the fiber may thus be assessed precisely by selectively and sequentially exciting the different modes.

In [Carpenter and Wilkinson, 2012], the authors present a method to characterize an OM2 fiber (GRIN fiber, $a = 25 \mu\text{m}$, $\text{NA} = 0.2$) thanks to selective mode excitation using a binary phase SLM. To generate the spatial profiles that best couple to the LP modes of the fiber, they use a two-state modulation. In a first step, they compute the pattern to display which produces the best overlap between simulations of the far-field and each theoretical LP mode using a numerical optimization. The wavefronts corresponding to each mode are then injected into the fiber using the setup represented in Figure II.10.a. The frequency response of the 25 modes injected is measured and the time responses are computed by performing a Fourier transform. The latter are shown in Figure II.10.b. It allows the quantitative characterization of the modal response.

This article demonstrates how wavefront shaping has grown to be an efficient tool in the characterization of MMFs for telecommunication applications. However, this initial demonstration is not suited to measure the output profile. Mode coupling effects, for example, cannot easily be assessed by the technique.

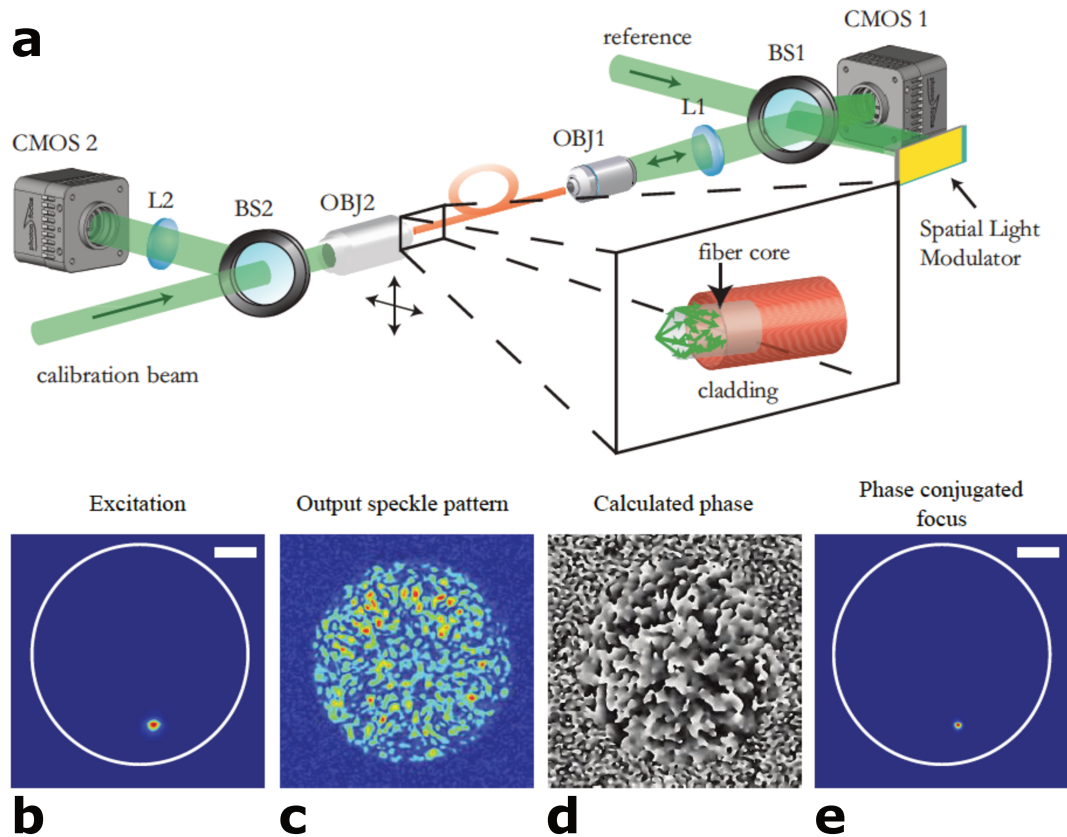


Figure II.9: Digital Optical Phase conjugation through an MMF. **a**, Experimental setup of the digital optical phase conjugation method. **b**, Injection of a focused spot. **c**, Output speckle. **d**, Hologram used for digital phase conjugation. **e**, Refocused spot. Figure extracted from [Rotter and Gigan, 2017], adapted from [Papadopoulos et al., 2012; Farahi et al., 2013]

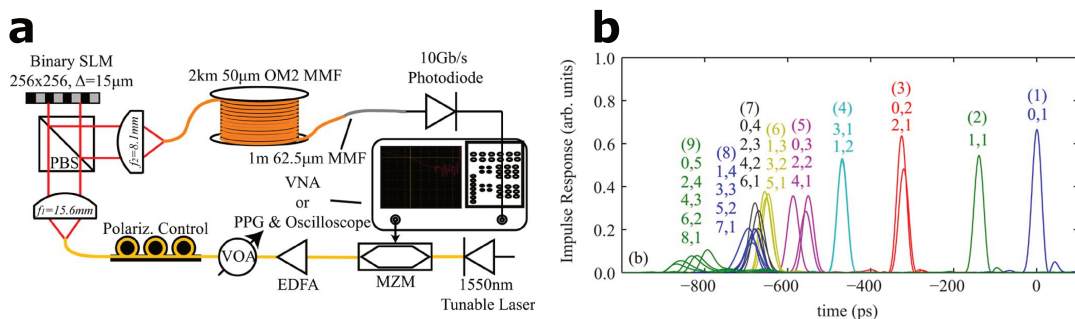


Figure II.10: Modal characterization of an MMF using selective mode excitation. **a**, Setup used to characterize a 2 km long OM2 GRIN fiber. **b**, Time response for all 25 modes of the fiber at a single polarization.

3 Measuring transmission matrices

Because SLMs give a full control over the wavefront on a discrete array of pixels, it appears possible to characterize the relationship between the input and output fields of a given linear medium. The idea is to generate a set of input excitations using an SLM and to measure the complex output field using a camera and an interferometric setup². In the following, we discuss the relationship between the inputs and the outputs of a medium with the formalism of the scattering matrix. This allows us to introduce the transmission matrix of a medium, and then the methods to measure it. In the final sections, we show that the measurement of the transmission matrix is not limited to the basis of the pixels of the equipments but can be expressed in the basis of the propagating modes of a fiber to give access to the modal properties of the propagation of light.

3.1 The scattering matrix and the propagation channels of a system

In linear media, we can express the relationship between the electric fields of the incoming light E_{in} and outgoing light E_{out} as a matrixial relationship. The scattering matrix \mathbf{S} , also called the *S-matrix*, contains the full information about the spatial propagation of light in the system, as presented in Figure II.11. The scattering matrix links the inputs and output of the medium on both sides, according to the equation:

$$E_{out} = \begin{pmatrix} \mathbf{R} & \mathbf{H}' \\ \mathbf{H} & \mathbf{R}' \end{pmatrix} \cdot E_{in} \quad \text{with} \quad E_{in} = \begin{pmatrix} E_{in}^+ \\ E_{in}^- \end{pmatrix} \quad \text{and} \quad E_{out} = \begin{pmatrix} E_{out}^- \\ E_{out}^+ \end{pmatrix}, \quad (\text{II.6})$$

where (+) (resp. (-)) refers to the propagation from left to right (resp. right to left), \mathbf{R} (resp. \mathbf{R}') is the left (resp. right) reflection matrix and \mathbf{H} (resp. \mathbf{H}') is the left to right (resp. right to left) transmission matrix (TM) of the complex medium. The dimension of the S-matrix is related to the number of propagating modes of the system. The number of modes can be different on the input and output of the system; If we note N the number of modes on the left and M the number of modes on the right, the S-matrix is of size $(N + M) \times (N + M)$. The TMs are rectangular and \mathbf{H} (resp. \mathbf{H}') is of size $M \times N$ (resp. $N \times M$). The reflection matrices are square and \mathbf{R} (resp. \mathbf{R}') is of size $N \times N$ (resp. $M \times M$). The conservation of the flux imposes

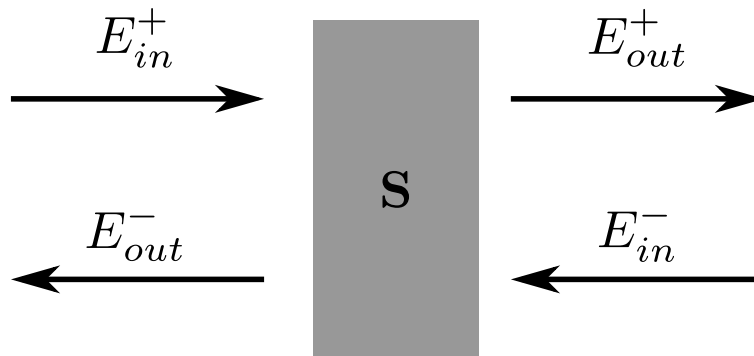


Figure II.11: Illustration of the scattering matrix formalism. The scattering matrix gives the relation between the inputs and outputs of a linear medium.

²Provided the use of an internal [Dubois et al., 2002] or external [Cuhe, Marquet, and Deppeursinge, 2000] reference.

that the S-matrix is unitary in lossless systems [Rotter and Gigan, 2017]:

$$\mathbf{S}^\dagger \cdot \mathbf{S} = \mathbf{1}, \quad (\text{II.7})$$

where \cdot^\dagger corresponds to the transpose conjugate.

Experimentally, the measurement of \mathbf{S} requires to have injection and detection on both sides and to control and measure all the modes. Moreover, the finite numerical aperture of optical systems limits the number of modes one can excite and measure. Typically, only a sub-part of fraction of the S-matrix is measured. This, in particular, is the case in scattering media where the number of modes in open systems exceed by far the number of pixels on typical SLMs and cameras [Goetschy and D. Stone, 2013; Popoff et al., 2014a]. Generally, the number of modes one can control/measure is set by the number of independent pixels on the SLM/camera. In the following, the dimensions N and M refers to the number of input pixels on the modulator and the number of output pixels on the camera. By performing the singular value decomposition of the transmission matrix, one can decompose the system into transmission channels [Rotter and Gigan, 2017]:

$$\mathbf{H} = \sum_{j=1}^N \sigma_j U_j \cdot V_j^\dagger, \quad (\text{II.8})$$

which can also be written as the Singular Value Decomposition (SVD):

$$\mathbf{H} = \mathbf{U} \cdot \mathbf{\Sigma} \cdot \mathbf{V}^\dagger, \quad (\text{II.9})$$

where $\mathbf{\Sigma}$ is a rectangular matrix with the only non-zero elements being on the diagonal: $\text{diag}(\sigma_1, \dots, \sigma_N)$. V_j and U_j are the singular input and output vectors.

The maximal (resp. minimal) singular value is associated to the channel with the maximal (resp. minimal) transmission σ_{min}^2 (resp. σ_{max}^2). Each corresponding singular vector V_j represents the input wavefront that couples light into this transmission channel, and each corresponding singular vector U_j represents the output wavefront exiting from the transmission channel. The number of non-negligible singular values represents the number of transmission channels in the system. In the remainder of this manuscript, the SVD is used as a tool to characterize and count the number of propagation channels of a system.

When studying MMFs, a negligible fraction of the energy is reflected during propagation. So, the reflection part of the S-matrix can be discarded to only take into account the TMs. Both the left-to-right and right-to-left matrices contain the same information about transmission channels since $\mathbf{H}' = \mathbf{H}^t$ due to spatial reciprocity [Rotter and Gigan, 2017]. Then, measuring the TM from a single side is sufficient to characterize the transmission channels of an MMF. In the following sections, we show how the TM measurement has emerged as a tool of choice to study the propagation of light in complex media, especially in optical fibers.

3.2 The transmission matrix of scattering media

The TM is an important tool to describe light transmission in a scattering medium. It allows in particular to characterize the statistics of the transmission channels [Popoff et al., 2014a]. It gives a lot of information about the medium, such as the transmission properties deduced from the singular value distribution of the TM [Popoff et al., 2011; Skipetrov and Goetschy, 2011].

In the following, we introduce an element h_{mn} of \mathbf{H} as the link between the field at the n^{th} pixel of the SLM and the field at the m^{th} pixel of the camera. The field at the m^{th} camera pixel is thus linked to the whole input field E^{in} according to:

$$E_m^{\text{out}} = \sum_{n=1}^N h_{mn} E_n^{\text{in}}, \quad (\text{II.10})$$

where h_{mn} is the complex amplitude of the elements of the pixel basis TM, and E_n^{in} (resp. E_m^{out}) is the input (resp. output) field at the n^{th} (resp. m^{th}) pixel. The relationship between the input and output fields thus reads:

$$E^{\text{out}} = \mathbf{H}.E^{\text{in}}. \quad (\text{II.11})$$

In 2010, Sebastien Popoff and his colleagues measured for the first time the optical monochromatic TM of a scattering medium [Popoff et al., 2010a]. In this experiment, a coherent laser source illuminates a phase-only SLM which spatially modulates the wavefront entering a multiple scattering medium (an opaque layer of ZnO). The output light is then collected by a Charged Coupled Device camera (CCD camera) as shown in the depiction of the experimental setup of Figure II.12.a. To measure the complex output field, a co-propagating reference is used, as shown in the insert of Figure II.12.a. The reference allows using the *four-phase method* [Dubois et al., 2002] to recover the complex output field. The TM is measured by sequentially sending the elements of an input excitation basis and measuring the corresponding output field.

To remove the need for interferometric measurements, numerical methods, called *phase retrieval* methods, were developed to retrieve the phase of the TM from intensity only measurements. Doing so removes the requirement for high stability of the optical system. Using a reference-less system, the measured intensity at a single camera pixel I_m^{out} reads:

$$I_m^{\text{out}} = \left| \sum_{n=1}^N h_{mn} E_n^{\text{in}} \right|^2. \quad (\text{II.12})$$

We indeed see that intensity measurements do not allow direct access to the complex coefficients of the TM. Using phase retrieval methods, the lack of direct phase measurements is compensated by adding redundancy. Instead of sending each element of an output basis, these methods rely on using a large amount of random input fields [Dremeau et al., 2015; Metzler et al., 2017]. Typically, one sends a number of random input patterns displayed on an SLM which is several times the number of controlled input pixels.

These works were then extended to measure the TM of different systems, such as MMFs [Florentin et al., 2018; Cizmar and Dholakia, 2012], as shown in Figure II.12b with a similar setup. We also note that TM measurements were performed outside the monochromatic regime, with multispectral measurements [Mounaix et al., 2015], and also in the quantum regime of light [Defienne et al., 2014; Defienne et al., 2016; Wolterink et al., 2015]. The measurement of the TM has applications for imaging through scattering media [Popoff et al., 2010b; Kim et al., 2015], for MMF image transmission [Cizmar and Dholakia, 2012], with potential applications in endoscopy [Choi et al., 2012], and for micromanipulation through MMFs [Leite et al., 2017].

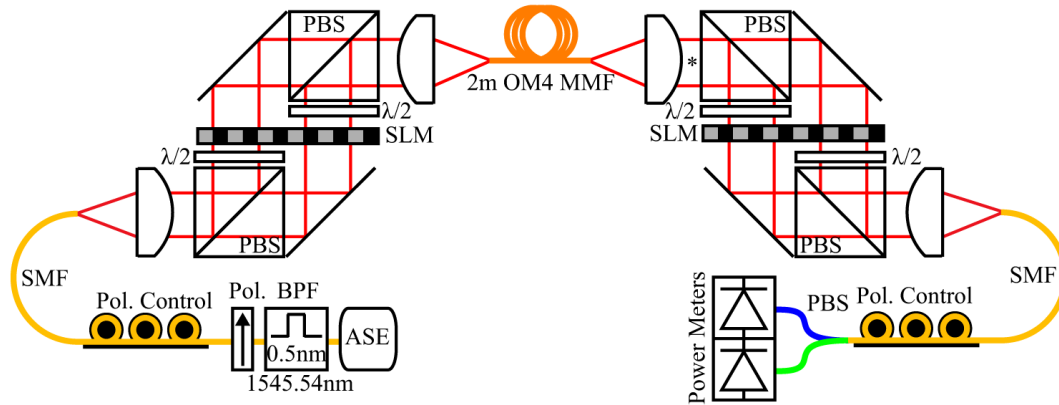


Figure II.13: Measurement of the TM directly in the mode basis. Extracted from [Carpenter, Eggleton, and Schroder, 2014].

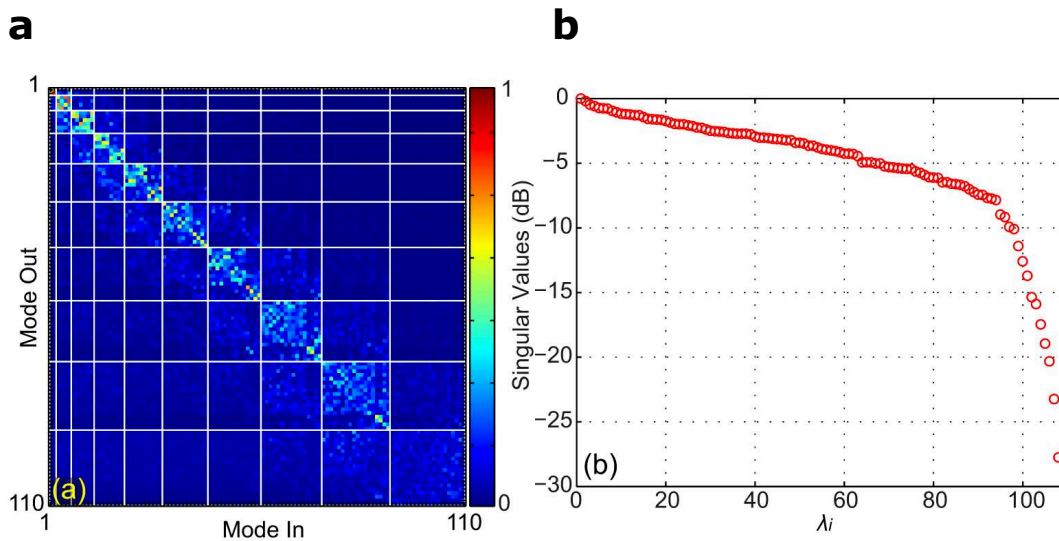


Figure II.14: a, Amplitude of the mode basis TM for all the 110 modes of an OM4 GRIN fiber. **b**, Singular values distribution of the mode basis TM. Extracted from [Carpenter, Eggleton, and Schroder, 2014].

Schroder, 2014]. The last channels have a sharp decrease in transmission. It corresponds to modes with propagation constants close or smaller than the cutoff, meaning that they are not efficiently confined in the fiber core. Theoretically, the studied fiber supports 110 modes, however, the measured value is lower.

By measuring the mode basis TM at different wavelengths, the quantitative characterization of the spatial and spectral properties of the fiber is possible. Using the same setup, the same authors present in [Carpenter, Eggleton, and Schroder, 2016] the measurement of a mode basis TM of high dimension for multiple wavelengths. They measured mode basis TMs of 420 modes, for 32768 different wavelengths in the range [1525, 1566.7] nm, of an OM1 fiber (GRIN, $a = 36.25 \mu\text{m}$, $\text{NA} = 0.275$). They demonstrate that the knowledge of this stack of matrices gives the ability to generate any spatial/polarization state at the output of the fiber at any wavelength, as well as to predict the temporal response of any spatial/polarization input state.

Building the mode basis TM, one element at a time, requires the precise calibration of the SLMs to accurately inject a single mode at the input and measure the overlap of the output with a single mode of the fiber. If the system is not accurately

aligned, the displayed pattern on the SLM at the input may excite more than one mode, and, similarly, the measurement of the overlap may be incorrect. This method imposes a careful tuning of the optical setup.

3.3.b Retrieval of the mode basis TM from the pixel basis TM

To avoid the issue arising from improper calibration, another method introduced in [Ploschner, Tyc, and Cizmar, 2015] uses the information contained in the pixel basis TM to reconstruct the mode basis TM. The underlying idea is to use change of basis matrices that allows the passage from the pixel basis to the mode basis and *vice versa*. The change of basis matrices at the input and output $\mathbf{M}_{\text{in/out}}$ project the measured pixel basis TM \mathbf{H} into the basis of propagating modes $\mathbf{H}_{\text{modes}}$ according to equation:

$$\mathbf{H}_{\text{modes}} = \mathbf{M}_{\text{out}}^{\dagger} \cdot \mathbf{H} \cdot \mathbf{M}_{\text{in}}. \quad (\text{II.13})$$

The columns of $\mathbf{M}_{\text{in/out}}$ represent the modes of the fiber expressed in the initial pixel basis in which \mathbf{H} is measured.

They measure the TM of a short segment (≤ 30 cm) of a fiber supporting approximately 500 modes (step index, $a = 25$ μm , $\text{NA} = 0.22$). To do so, the input facet of the fiber is scanned by focusing light on diffraction limited spots using the setup depicted in Figure II.15.a, and shown schematically in Figure II.15.b. The output far-field is measured on the pixel basis of a camera using an off-axis reference carried by an SMF as shown in Figure II.15.a. The resulting pixel matrix \mathbf{H} is shown in Figure II.16.a. To build the change of basis matrices, the mode profiles are computed with the parameters of the studied MMF. These matrices allow building an initial mode basis TM using equation II.13, the resulting projected mode basis TM is shown in Figure II.16.b.

The fiber segments under study are very short (up to 30 cm). In principle, little coupling occurs between the modes. However, the mode basis TM is not diagonal as would be expected. Indeed, the initial pixel basis TM does not only represent the propagation in the MMF, but also the free space propagation from the SLM to the input facet and from the output facet to the camera. In these part of the optical setup, light is affected by monochromatic aberrations. These aberrations are not taken into account to generate the initial change of basis matrices. Moreover, any misalignment will also affect the change of basis matrix. Another detrimental effect arises from the fact that the mode profiles and effective indices are computed from an ideal index profile of the fiber. The uncertainty on the fiber parameters leads to an incorrect estimation of the modes and thus of the change of basis matrices. The authors developed an algorithm to correct these different sources of errors to maximize the diagonality of the reconstructed matrix $\mathbf{H}_{\text{modes}}$. We further discuss the operation principle and the optimization scheme in Chapter III, section 3.3. The results of their method is shown in Figure II.16.c. A diagonal matrix accurately representing the propagation of the modes inside the fiber is obtained. Using the knowledge of the mode basis TM, the authors used the MMF to illuminate samples in a controlled fashion. They are thus able to accurately reconstruct images of objects using a 30 cm long fiber endoscope, without calibration.

3.3.c Deep learning strategies

Recently, several attempts have been made to use numerical methods to guess the modal content contained in the output speckle of a fiber [An et al., 2018; Rothe et al.,

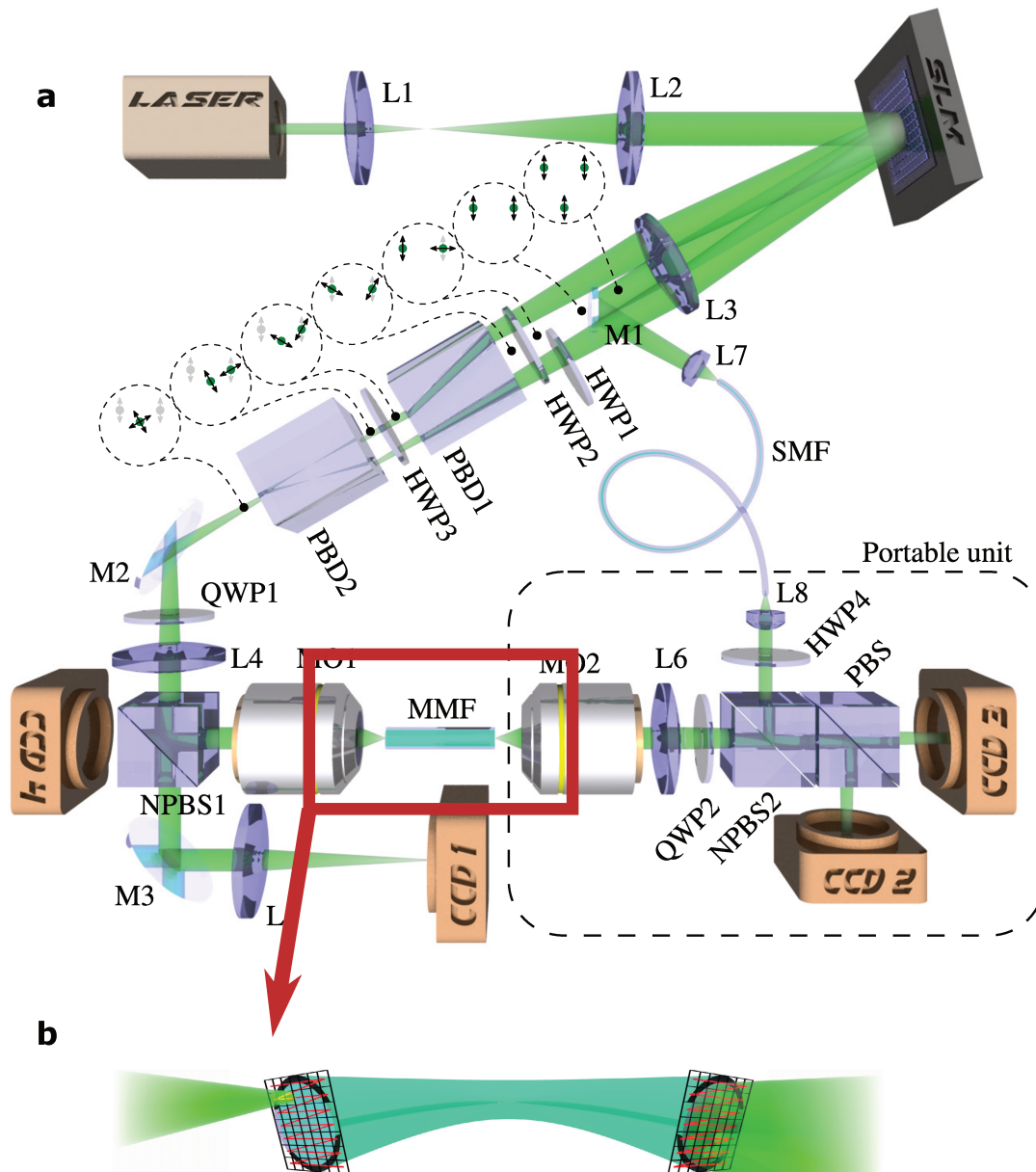


Figure II.15: Setup used to measure the pixel basis TM. **a**, Full setup used in [Ploschner, Tyc, and Cizmar, 2015] to measure the pixel basis TM of an MMF. **b**, Illustration of the measurement process: the input facet of the fiber is scanned while the complex output speckles are recorded. Extracted from [Ploschner, Tyc, and Cizmar, 2015].

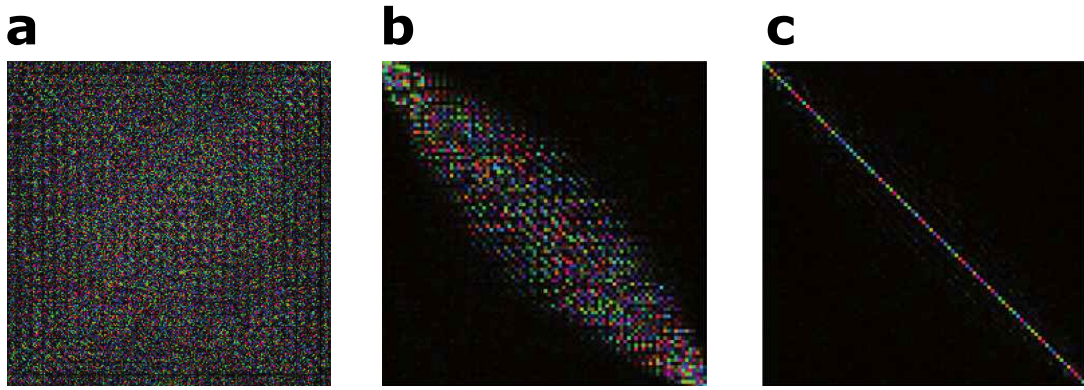


Figure II.16: Reconstruction of the mode basis TM with an optimization procedure. **a**, Complex representation of the pixel basis TM of the MMF. **b**, Mode basis TM without correction of the aberrations and of the parameters of the fiber. **c**, Mode basis TM after correction. Only a single input and output polarization is shown. Extracted from [Ploschner, Tyc, and Cizmar, 2015].

2020]. These methods use deep learning methods to train neural networks architectures to guess correctly the contribution of modes to form speckle patterns.

The principle is to train a neural network to predict the amplitude and phase of each mode interfering in an intensity speckle pattern using mode profiles obtained through numerical simulations. The training is performed for a specific fiber with a given number of modes. Then, intensity speckle patterns from experiments using a fiber of the same type as the one used in simulation are given to the neural network which predicts the amplitude and phase of each mode. Successful demonstrations for a 3-mode fiber are presented in [An et al., 2018] using a convolutional neural network. These methods have the advantage of not relying on interferometric measurements. However, they require heavy computational efforts for the training and are limited to few-mode fibers up to this date.

Conclusion

In this chapter, we presented the main methods used to characterize the modal content of MMFs: the spectral and spatial content of FMFs can be probed using the S2 and C2 methods. These methods are adapted for FMFs, but do not easily allow the study of coupling inside MMFs. Thanks to wavefront shaping, it is possible to manipulate the field at the input of a medium and to generate profiles that selectively couple light into the propagating modes of an MMF to study their temporal response. Moreover, the measurement of the mode basis TM of an MMF gives access to the transmission values of spatial channels and to the coupling between the modes. The wavefront shaping methods presented in this chapter are at the starting point of the work of this Ph.D. In Chapter III, we present how we implemented the measurement of the pixel basis TM and how we retrieved the mode basis TM from it.

Chapter III

Developing a toolbox to study fibers

Chapter contents:

Introduction.....	54
1 Shaping and manipulating wavefronts in optical fibers	54
1.1 Wavefront shaping using a digital micromirror device (DMD) ..	54
1.2 Injecting light into fibers	62
1.3 Detection schemes	63
2 Measurement of the pixel basis transmission matrix	68
2.1 Principles	68
2.2 Single input, single output polarization	69
2.3 Both input polarizations	71
3 Reconstruction of the mode basis TM	75
3.1 Modal projection of the TM	75
3.2 Imperfect mode conversion	76
3.3 Finding aberrations of the optical setup	78
Conclusion	83

Introduction

As we detailed in Chapter II section 2.2, even in the absence of disorder, the illumination of an MMF with a coherent source of light will result in the observation of a speckle pattern at the output, due to the existence of intermodal dispersion. Thus, unlike scattering media, the observation of a speckle is not in itself a signature of disorder. As a consequence, measuring the TM of an MMF does not allow to easily assess the level of disorder if the basis in which we measure the matrix is not carefully chosen. The TM measurement has to be performed in the basis of the propagating modes of the fiber to capture the propagation properties of the MMF.

In a context of telecommunication applications, another constraint is speed. Manipulating light inside fibers and data acquisition need to be performed quickly to reduce potential downtime of the system occurring during measurements. For the same reasons, the system should require little effort for the alignment in order to minimize the handling time and to be compatible with real-life implementations.

The goal of this chapter is to present the tools we developed and used to meet the requirements for a fast and efficient measurement of the mode basis TM of MMFs:

1. a fast and precise modulation of the input wavefront (sections 1.1 and 1.2),
2. the complex measurement of the output field for both polarizations (section 1.3),
3. the recovery of the TM in the basis of the pixels of the DMD and of the camera (section 2),
4. the projection of the pixel basis TM into the mode basis TM using adapted change of basis matrices (section 3)
5. a fast and easy to use post-processing procedure to cancel the effects of aberrations and misalignments (section 3.3).

1 Shaping and manipulating wavefronts in optical fibers

1.1 Wavefront shaping using a digital micromirror device (DMD)

As introduced previously in 2.3, DMDs are able to shape an incoming wavefront by switching their mirrors between two different orientations (that we name *on* if they direct light in the direction of interest the optical system and *off* if their contribution is blocked) at speeds up to few tens of kHz, effectively achieving a binary amplitude modulation. As such devices were not originally designed for the manipulation of complex coherent fields, their use in such a context requires tackling a few technical but important issues that could otherwise severely alter experimental results.

1.1.a Diffraction effects

Liquid crystals phase modulators, traditionally used in wavefront shaping experiment, exhibit a reasonably flat surface. Ideally, the modulator only alters the phase of the reflected light by modulating the refractive index at a given polarization. The finite size of the pixels and their repetition make the array acts as a flat grating. If all the pixels are in the same state, e.g. with no phase modulation, when illuminated with a coherent plane wave with an incident angle α , we observe multiple orders of diffraction. Those orders do not all have the same intensity and the maximum of

the envelope is always centered around the zeroth order, which corresponds to the reflected beam at the angle $-\alpha$ (see figure III.1).

With DMDs, the states of the pixels correspond to two positions of the micro-mirrors, none of which is aligned with the surface of the array. If all the pixels are in the same state, the angle of the pixels makes the system act as a blazed grating. The consequence is that the envelope modulating the amplitude of the orders of diffraction is shifted by twice the angle of the pixels. The maximum of this envelope may not coincide with an order of diffraction anymore. By selecting one order for the modulation, this could lead to a significant loss of energy and modulation efficiency. Therefore, it is important to choose a combination of incident angle and pixel pitch that maximizes the energy transmitted in the diffraction order of interest at a chosen wavelength.

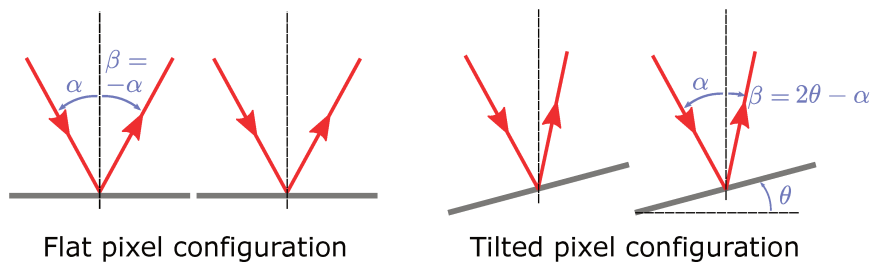


Figure III.1: Two possible pixel configurations. The flat pixel configuration corresponds to a flat grating, the tilted pixel configuration corresponds to a blazed grating. α is the incident angle and β is the reflected angle with respect to the normal of the surface of the array.

Simple 1D criterion The DMDs produced by Texas Instruments have the rotation axis of the mirrors in their diagonal direction as previously shown in Chapter II, Figure II.8.

In our experiments, we inject light in a plane direction normal to the rotation axis in order to have the output beam in the direction normal to the surface of the DMD. An illustration of the light injection is shown in Figure III.2. Therefore, as mirrors

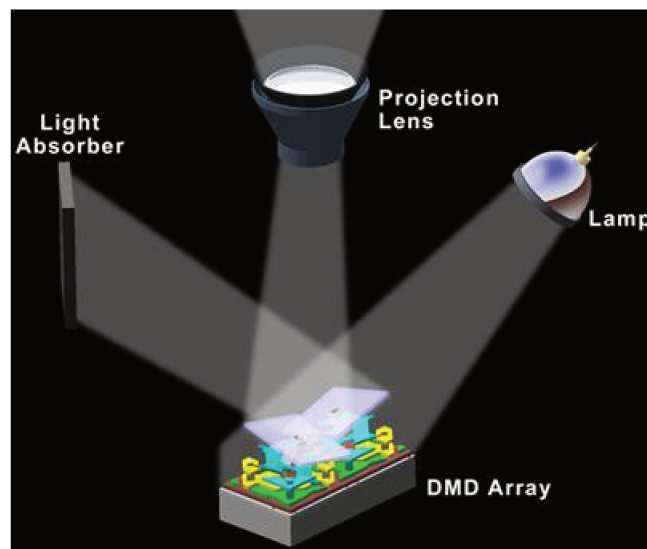


Figure III.2: Light modulation with a DMD. In this configuration, light is injected at an angle $\alpha \simeq 2\theta$ so that the modulated beam normal to the surface of the DMD.

are square, projecting the problem in the X or Y axis is equivalent: it is possible to consider a 1D problem like represented in Figure III.1.

In 1D, the angles of incidence α' and of tilt θ' correspond to the projection of α and θ along the X -axis or the Y -axis:

$$\sqrt{2}\sin(\alpha') = \sin(\alpha) \text{ and } \sqrt{2}\sin(\theta') = \sin(\theta), \quad (\text{III.1})$$

We place the optical axis of our system in the direction corresponding to $\beta = 0$. We want to ensure that this direction corresponds to an order of diffraction of the grating, thus guarantying the maximal intensity of the modulated field. To do so, we have to match the grating equation:

$$\sin(\alpha') + \sin(\beta') = \frac{m\lambda}{d}, \quad (\text{III.2})$$

where $\beta' = 2\theta' - \alpha'$ is the angle of reflection on a single pixel in the on orientation (see Figure III.1).

When m is close or equal to an integer, we are at the blazing condition, and a local maximum of the energy is indeed sent into the reflection direction. When m is close or equal to a half integer, only a fraction of the energy is sent in the direction of the reflection angle, where we collect the modulated beam, as it corresponds to a local minimum of the total collected intensity in this direction. To determine the optimal angle to illuminate the DMD, we need to find the incident angles for which m is an integer or close to an integer.

In Figure III.3, we show the blazing number $\mu = |(m\%1) - 0.5|$, where $\%$ is the modulo operator, as a function of the angle of incidence α when illuminating two DMDs of pitch values equal to $7.6 \mu\text{m}$ and $10.8 \mu\text{m}$, at $\lambda = 1.55 \mu\text{m}$. These two values are the most common ones in DMDs produced by Texas Instruments. When μ is close to 0.5, we are in the blazing condition and when it is close to 0, we are in a dim state.

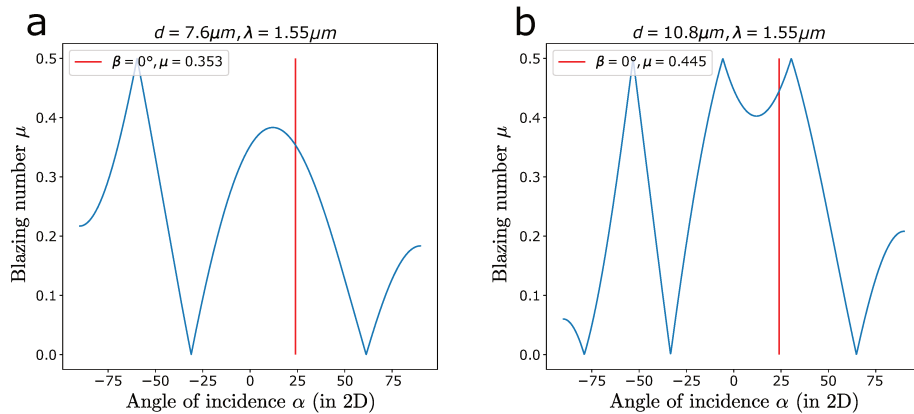


Figure III.3: Blazing number μ as a function of the illumination angle α . **a**, $7.6 \mu\text{m}$ DMD, **b**, $10.8 \mu\text{m}$ DMD. The red line indicates the angle for which the reflection is normal to the plane of the DMD, $\beta = 0^\circ$. It corresponds to the desired configuration when the light is reflected with a direction normal to the surface of the DMD.

For small incident angles, we obtain a better modulation efficiency (m closer to an integer) for the $10.8 \mu\text{m}$ -pitch device compared to the $7.6 \mu\text{m}$ -pitch one.

2D simulations To examine the diffraction profiles of the different DMDs, we perform a 2D simulation of the system by representing the array of pixels, where two neighboring pixels have a phase difference of $\frac{2\pi}{\lambda}d[\sin(\alpha') + \sin(\beta')]$. Then, we can observe the directions of the diffracted orders by computing the 2D-Fourier transform of the complex field, centered around the direction of the reflected beam at angle $\beta = 0^\circ$. The phase of the optical field on the DMD surface and its Fourier transform for the two pitch values are presented in Figure III.4. We observe that in both cases, several diffraction orders carry a significant fraction of the energy:

- In the $7.6 \mu\text{m}$ -pitch DMD, four beams of equivalent energy exit the DMD at angles around the reflection angle. This situation is not optimal as we intend to use a single order of diffraction,
- In the $10.8 \mu\text{m}$ -pitch DMD, one beam is close to the reflection angle and is a global maximum. This is the preferred configuration for maximizing the available power of the modulated field.

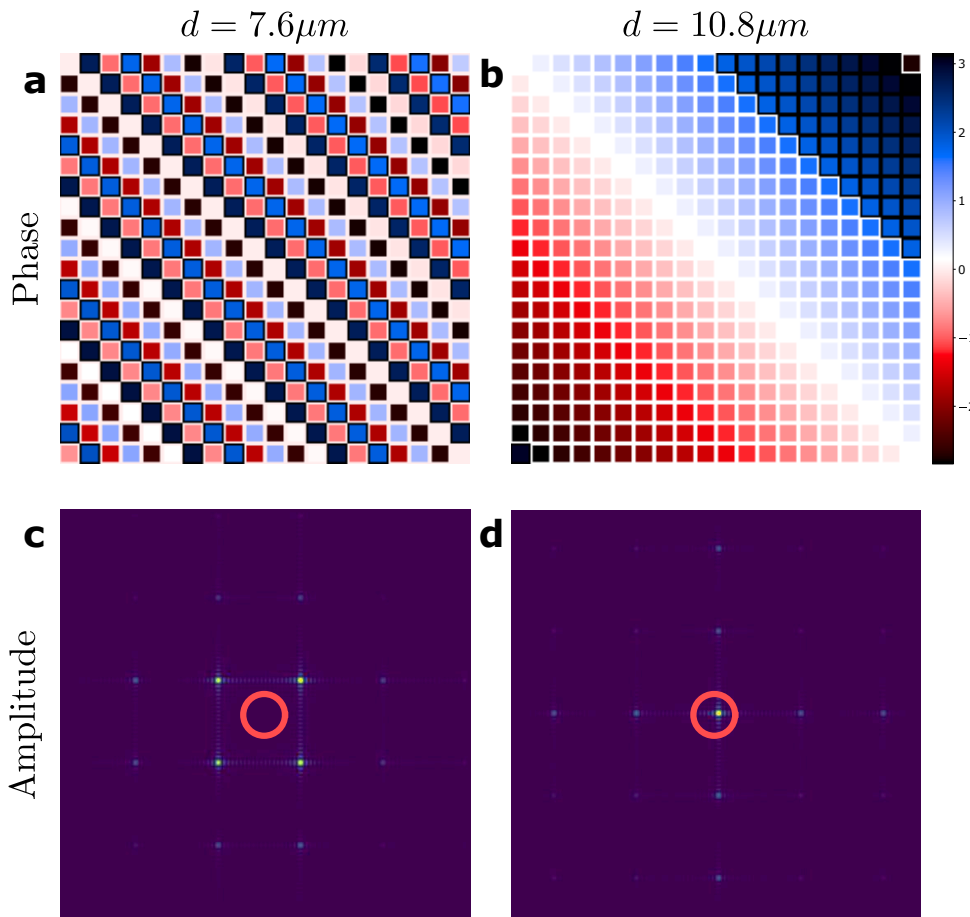


Figure III.4: Diffraction patterns of two different DMDs. **a, b**, Phase of the near-field. **c, d**, Amplitude in the far-field for a configuration where all the pixels are *on*, with pitch values $7.6 \mu\text{m}$ (**a, c**) and $10.8 \mu\text{m}$ (**b, d**). The illumination comes from the angle $\alpha = 24^\circ$. The far field image is centered around the reflection angle $\beta = 0^\circ$ (red circle).

Off-pixel diffraction To use a DMD as an ideal binary amplitude modulator, one needs to discard light diffracted by pixels in the *off*-state. When pixels are in their *off*-state, the reflection angle is $-2\theta - \alpha$. The envelope is shifted and the diffraction

order in the optical axis of the setup has low energy. When a pattern contains both *on* and *off*-pixels, most of the energy comes from the *on*-pixels, but a small fraction also comes from the *off* pixels. This effect may deteriorate the quality of the modulation, especially for masks where only a few pixels are in the *on* state.

We simulated the diffraction patterns of the all-*on* and all-*off* configurations and represented in Figure III.5 the amplitude of the far field along the diagonal orthogonal to the axis of rotation of the pixels for both 7.6 μm and 10.8 μm DMDs. For

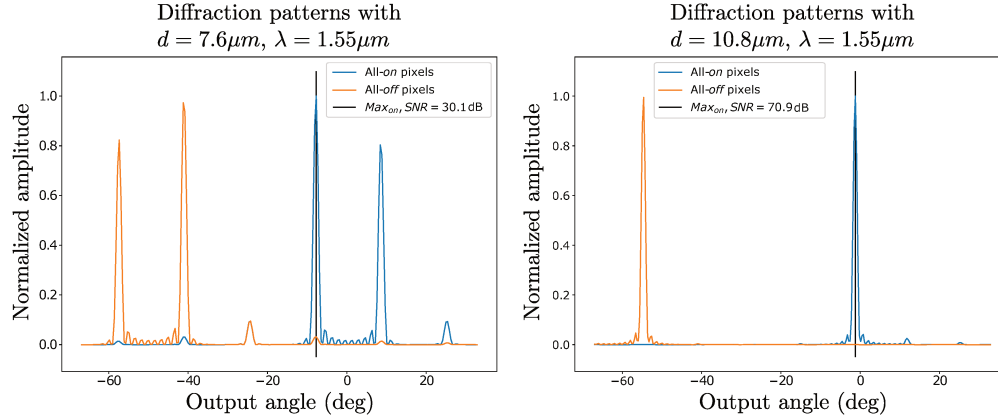


Figure III.5: Diffraction patterns along the diagonal. Amplitude of the diffracted profile, measured in the diagonal orthogonal to the axis of rotation of the pixels, for mirrors of pitches 7.6 μm and 10.8 μm at $\lambda = 1.55 \mu\text{m}$. The SNR is computed for the intensity and expressed in dB.

both DMDs, we choose the optical axis so that it coincides with the maximum of the energy of the *on*-state. In this direction, the ratio of intensity between the all-*on* and all-*off* states is about 40 dB higher in the 10.8 μm case than in the 7.6 μm case as shown in Figure III.5. It means that when modulating light, a non-negligible spurious contribution is added to the desired one in the case of the 7.6 μm -pitch DMD. Therefore, the 10.8 μm -pitch DMD allows reducing the unwanted influence of the *off* pixels when displaying complex patterns.

In the following experiments, we use the 10.8 μm DMD because it has a better modulation efficiency and because it presents a minimum of unwanted energy from the *off*-pixels in the direction $\beta = 0^\circ$.

1.1.b Complex modulation with a DMD

As DMDs can only physically perform a binary amplitude modulation. In wavefront shaping applications, it is often necessary to perform a phase modulation of the field. A joint amplitude and phase modulation can also be required to improve the performances. A first method allowing performing phase modulation is the Lee-hologram method [Lee, 1978], which was used on DMDs for wavefront shaping applications in complex media for the first time by the team of Raphael Piestun [Conkey, Caravaca-Aguirre, and Piestun, 2012].

Lee holograms for phase modulation The principle of the Lee-hologram method is to encode the desired complex modulation in amplitude fringes, and perform a spatial filtering in the Fourier plane with a 4-f system. Without loss of generality, we will present the method in 1D.

Let's consider we want to display a phase pattern $e^{i\phi(x)}$ using an amplitude only wavefront modulator. The Lee method consists in displaying the amplitude pattern (the so-called Lee hologram):

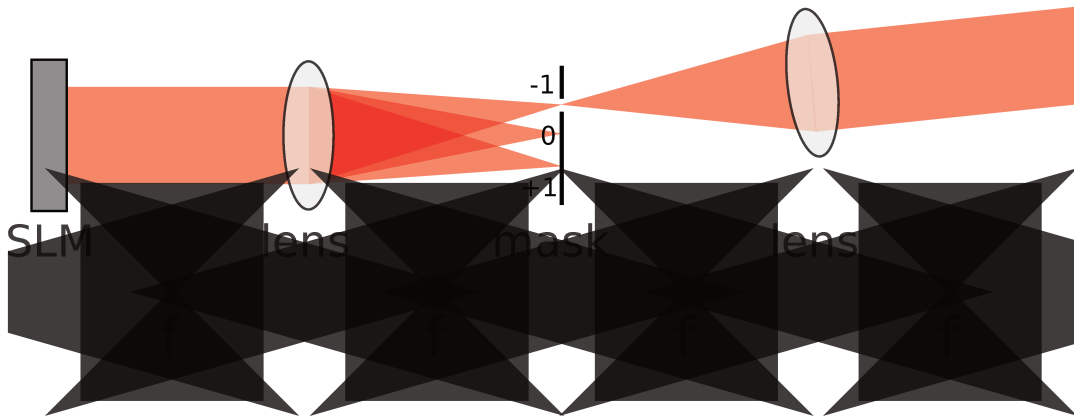
$$f(x) = \frac{1}{2}[1 + \cos(2\pi x\nu_0 - \phi(x))] \quad (\text{III.3})$$

where ν_0 is the Lee modulation spatial frequency that corresponds to the spatial frequency of the fringes. This expression can also be written:

$$f(x) = \frac{1}{2} + \frac{1}{4}e^{i2\pi x\nu_0}e^{-i\phi(x)} + \frac{1}{4}e^{-i2\pi x\nu_0}e^{i\phi(x)} \quad (\text{III.4})$$

It presents three terms of central spatial frequencies ($\nu_x = 0$), ($\nu_x = \nu_0$) and ($\nu_x = -\nu_0$). If ν_0 is larger than the highest spatial frequency of $\phi(x)$, then the three terms of $f(x)$ represent three spatially separated diffraction orders in the far field. We call these orders 0 , 1 and -1 . The term $e^{-i2\pi x\nu_0}e^{i\phi(x)}$ corresponds to the desired phase modulation tilted by an angle resulting from the diffraction off the fringes at the Lee modulation frequency.

We want to only conserve this term and remove the other ones. To do so, we can use a 4-f system with a diaphragm in the Fourier plane centered around the $-\nu_0$ frequency as presented in Figure III.6.a. The resulting complex field modulation in



$e^{i\phi(x)}$.

DMDs can only perform binary amplitude modulation, it is not possible to display the amplitude pattern described in equation III.3. To generate a modulation using a binary amplitude modulator, we generate a hologram by thresholding the previous amplitude pattern III.3 to approximate it by:

$$g(x) = \begin{cases} 1 & \text{if } f(x) > 1/2 \\ 0 & \text{otherwise} \end{cases} \quad (\text{III.5})$$

We show an implementation of the Lee hologram method in Figures III.6.b and c.

Experimental implementation We group pixels into square macropixels like shown in Figure III.7.a. The key parameters to tune are the spatial carrier frequency ν_0 , the spatial sampling (which is the number of pixels per macropixel), and the size and position of the pinhole at the Fourier plane. A careful choice allows the best trade-off between resolution and fidelity. In Figure III.7, we show the result of a simulation representing the Lee hologram method. A sampling of 8 periods per macropixel is used, we observe in Figures III.7.g, h, i that the phase and intensity of the field at the final plane of the 4-f accurately approximates the desired pattern.

A beneficial side effect of the 1st order filtering is the removal of specular reflections and other unmodulated contributions; those perturbations and are filtered in the Fourier plane of the first lens.

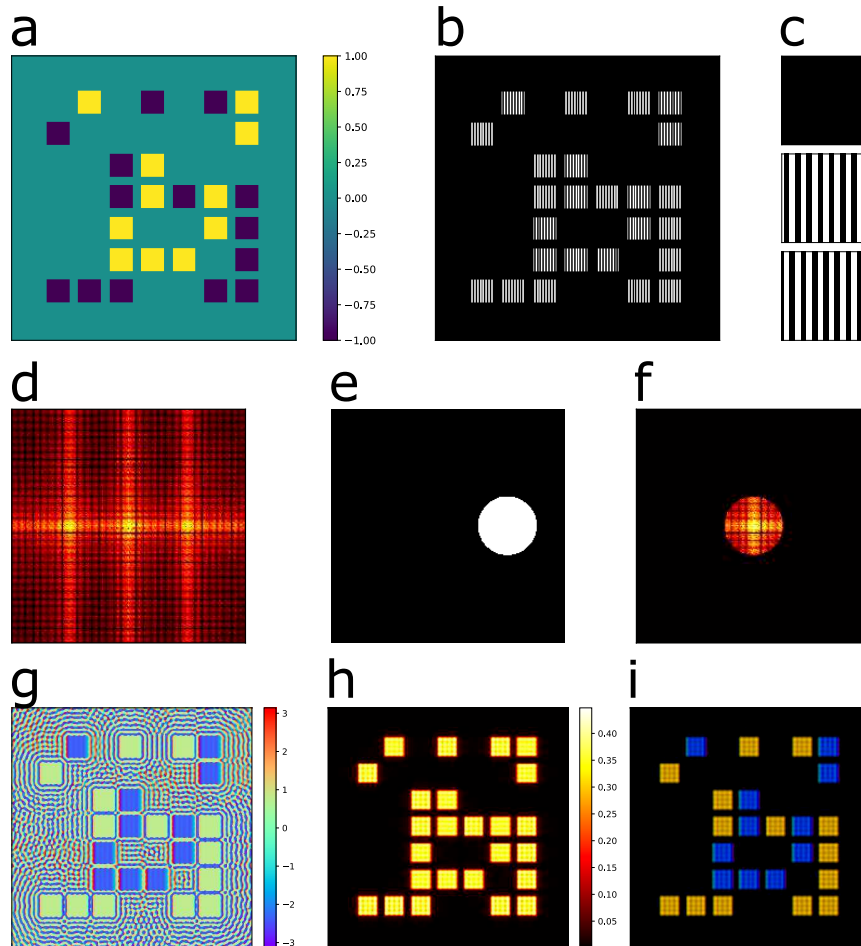


Figure III.7: Numerical simulations of the Lee hologram procedure using macropixels. **a**, A desired three level (0, -1 and 1) optical field modulation. **b**, Corresponding patterns displayed on the DMD. **c**, Close up view of the three macropixel patterns corresponding to a modulation value of 0, -1 and 1 respectively. The -1 and 1 macropixels have fringes that are shifted by half a period, thus creating a π phase shift. **d**, Fourier transform of **b** (log scale), mimicking the effect of a lens. **e**, Filtering mask used to keep the first order of diffraction, simulating the experimental spatial frequency filtering by a diaphragm. **f**, Selected first order shifted to be centered around the 0 spatial frequency (log scale). **g** and **h**: Phase and amplitude of the inverse Fourier transform of **f**. **i**, Representation of the complex optical field in the modulation plane. The field is colored in the Hue, Saturation, Value color scheme where the amplitude is encoded into the value and the phase is encoded into the hue. The blue color corresponds to a phase of 0 and yellow to a phase of π .

1.1.c Vibrations

The controller board of the DMD is cooled thanks to a heat sink and fan. The controller is connected to the DMD thanks to a rigid ribbon cable that transmits vibrations, they produce fast random temporal fluctuations of the modulated field which negatively impact the reproducibility of the measurements. In appendix A, we present the impact of the vibrations on the modulation field over time and a method to attenuate them. It allows us to obtain improved mechanical stability over time.

1.1.d Thermal effects

After turning on the controller board and the DMD, there is a transitional regime during which the DMD heats up before reaching a thermal equilibrium. It creates slow unwanted fluctuations of the phase of the modulated field which are detrimental to our measurements. In appendix B, we present the impact of the transitional heating regime on intensity measurements coming out of an MMF and a method to identify and stay in the stationary regime. We adapted the design of our experiments to always work in the stationary regime to allow the best reproducibility.

1.1.e Surface curvature

If we display a uniform disk on a DMD, we observe in the Fourier plane of a lens a pattern that deviates from the expected Airy disk. Indeed, the surface of the DMD is not perfectly flat which adds unwanted phase perturbations to the displayed pattern. We present in appendix C a method to measure and compensate for the curvature of the DMD surface. The calibration of the DMD surface prior to the experiments allows to experimentally obtain the desired wavefront or to correct the data in a post-processing step.

1.2 Injecting light into fibers

We want to study the spatial and modal properties of the light propagation inside MMFs by measuring their transmission matrices. To do so, it is crucial that the light injection respects several criterions:

- it has to maximize the coupling between free-space and fiber propagation to ensure sufficient output power,
- the field at the input facet of the fiber has to be known for each input mask on the DMD,
- the light source and the optical setup have to remain stable over time.

Our optical setup is presented in Figure III.8. The light source is a continuous linearly polarized fiber laser at $\lambda = 1550 \text{ nm}$ ¹. It is sent into a 90:10 polarization maintaining fiber coupler². The 90% arm is collimated and expanded to illuminate a DMD³ composed of 1280 by 800 pixels with a pitch of 10.8 μm working at a maximum frame rate of 10.7 kHz. A quarter waveplate (WP), mounted onto a motorized precision rotation mount⁴, allows converting the light into circular left or right polarization.

¹TeraXion NLL, high stability (frequency variation of less than 30 MHz over 8 hours of operation), ultra-narrow linewidth ($< 5 \text{ kHz}$), and low intensity noise ($< -130 \text{ dBc/Hz}$ up to 1 GHz).

²1 \times 2 polarization maintaining coupler, 1550 nm with 90 : 10 split, Thorlabs PN1550R2A1.

³Vialux V-650L.

⁴Thorlabs PRM1/MZ8.

The plane of the DMD is conjugated to the input facet of the fiber through the 4-f system used for the Lee-hologram technique.

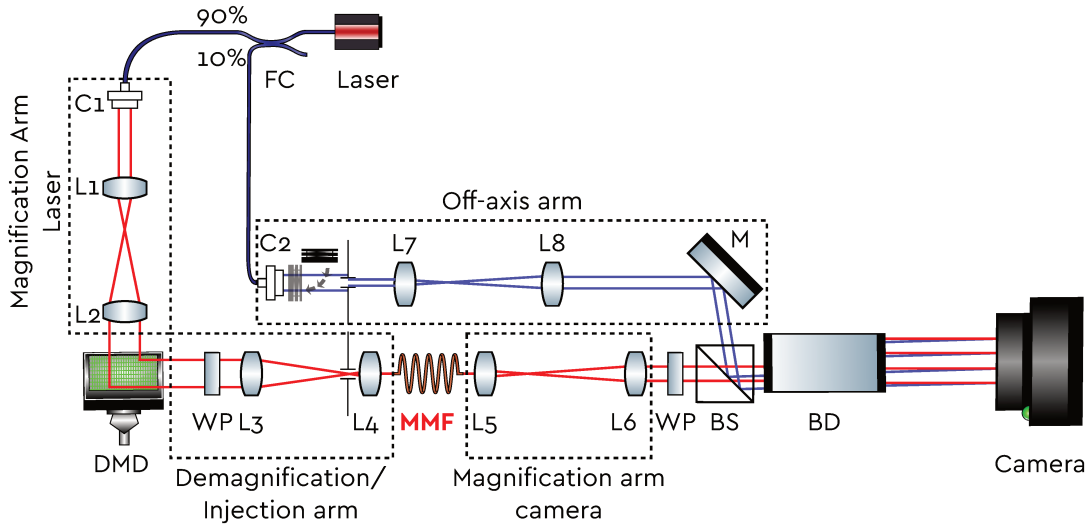


Figure III.8: Schematic of the experimental setup. The red rays designate the path of the light going into the fiber, the blue rays designate the path of light in the reference arm. Legend: FC: Fiber Coupler C: Collimator, L: Lens, WP: Quarter WavePlate, BS: Beam Splitter, BD: Beam Displacer, M: Mirror)

To use the full height of the DMD array to modulate the light on the input facet of MMFs of core radii up to $a = 50 \mu\text{m}$, we used a demagnification of $\gamma = -\frac{1}{96.8}$. It is achieved thanks to two lenses, L_3 ⁵ of focal length $f_3 = 300 \text{ mm}$ and L_4 ⁶ of focal length $f_4 = 3.10 \text{ mm}$. The MMF input facet is held by a fiber connector⁷ and a bare fiber terminator⁸, and is mounted onto a 5-axis translation stage⁹ which allows for fine translations along the x , y and z axis and allows the tuning of the pitch and yaw tilt of the fiber. The output facet is positioned into a V-groove¹⁰ and held by magnetic clamps. Using this setup allows us to conveniently switch between fibers while granting a precise control over the parameters of light injection.

In Figure III.9, we show an illustration of the five main geometrical degrees of freedom that exist when trying to couple light into an optical fiber. We explain in appendix D the method we used to tune the injection parameters using light that is reflected at the input facet of the fiber.

1.3 Detection schemes

In order to fully describe the spatial and polarization effects occurring in MMFs, the detection of the output light must allow the measurement of the field for both orthogonal polarizations.

⁵Thorlabs plano-convex lens LA1484-C-ML.

⁶Thorlabs aspheric lens C330TMD-C.

⁷Thorlabs B30128C3.

⁸Thorlabs BFT1.

⁹Thorlabs APY001/M and MAX311D/M.

¹⁰Thorlabs HFV002.

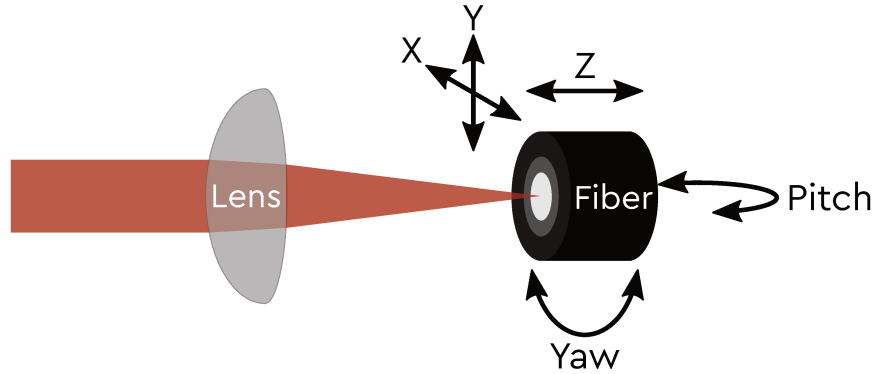


Figure III.9: Illustration of the possible degrees of freedom of the position of the fiber.

The output magnification arm was shown previously in Figure III.8. The output facet of the fiber is imaged with a 4- f system onto a fast InGaAs camera¹¹. The 4- f system achieves a magnification $|\gamma| = 68$ with lenses L_5 and L_6 of focal lengths $f_5 = 6.24$ mm and $f_6 = 428$ mm¹² respectively.

1.3.a Two-polarization detection

To measure the vectorial light field, one convenient method consists in measuring the two orthogonal linear polarizations of light, either sequentially (by rotating a polarizer for instance), or simultaneously, by using an optical component that separates the polarization contributions. We used a beam displacer¹³ that has the property to conveniently separate an incoming beam into two parallel beams of orthogonal linear polarizations.

The beam displacer we use separates the two polarization beams by a distance $D = 4$ mm. In order to prevent the two beams emerging from the beam displacer to overlap, the magnification γ of the output beam is constrained. An image of the two recorded polarizations was previously shown in Figure D.5, the magnification is chosen to maximize the width of the speckle while preventing any overlap between the two polarizations.

The number M of pixels that can be measured for each polarization is limited by the pixel pitch d of the camera and the maximal illuminated area is limited by the beam splitter displacement D . M scales as $(D/d)^2$, which gives, for $D = 4$ mm and $d = 20$ μm in our experiment, a maximum of about 40,000 pixels. This upper bound is thus high enough to allow us to envision the characterization of fibers commonly used in telecommunication applications which typically support up to 300 modes (OM1 fibers at $\lambda = 1.55$ μm) with our setup.

If larger fiber cores are to be studied, we list a few methods that can be used to lift the aforementioned limitations:

- a polarizer mounted on a rotation stage: doing so has the advantage of allowing to use the whole array of the camera. However, it requires the rotation of the polarizer to measure both polarizations,

¹¹Xenics Cheetah 640-CL 400Hz.

¹²Obtained by coupling two lenses of focal lengths 1000 mm and 750 mm.

¹³Thorlabs BD40.

- the use of two cross-polarized off-axis references simultaneously (single off-axis will be explained in the following paragraph) to measure the field of both polarizations with a single measurement [Han et al., 2017],
- a custom setup designed to act as a beam displacer could be envisioned using a polarizing beam splitter. However, organizing the optical elements correctly might be cumbersome.

1.3.b Complex field measurements

To retrieve the complex output field, we implement the off-axis holography method presented in the work of [Cuche, Marquet, and Depeursinge, 2000].

Principles The method uses the interference pattern created at the sensor array between the signal field $A_O(x, y)$ and a known reference field $A_R(x, y)$. We consider as the reference field a plane wave tilted by an angle θ with respect to the optical axis. Without loss of generality, we consider an angle along the x direction so that $A_R(x) = \sqrt{I_R}e^{-iks\sin(\theta)x}$, where $I_R = |A_R|^2$ is the intensity of the reference, uniform over the observation plane. We observe interference fringes along the y axis. The intensity of the interference pattern at the camera reads:

$$I_{tot}(x, y) = I_R + |A_O(x, y)|^2 + \sqrt{I_R}e^{-iks\sin(\theta)x}A_O(x, y) + \sqrt{I_R}e^{iks\sin(\theta)x}A_O^*(x, y). \quad (\text{III.6})$$

The Fourier transform of the interference pattern $I_{tot}(x, y)$ gives:

$$\begin{aligned} \tilde{I}_{tot}(u, v) = & I_R\delta(u, v) + (\tilde{A}_O \otimes \tilde{A}_O)(u, v) + \sqrt{I_R}\delta\left(u + \frac{\sin\theta}{\lambda}, v\right) \otimes \tilde{A}_O(u, v) \\ & + \sqrt{I_R}\delta\left(u - \frac{\sin\theta}{\lambda}, v\right) \otimes \tilde{A}_O(-u, -v), \end{aligned} \quad (\text{III.7})$$

where $\tilde{f}(u, v)$ is the Fourier transform of the function $f(x, y)$, (u, v) are the spatial frequencies in the x and y direction, \otimes is the cross-correlation, and \circledast is the convolution.

The last two terms of equation III.7 are the ones we are interested in as they hold the information about the complex field A_O (we call them replicas).

$$\tilde{A}_{O, -\frac{\sin\theta}{\lambda}}^+ = \delta\left(u + \frac{\sin\theta}{\lambda}, v\right) \otimes \tilde{A}_O(u, v) \quad \text{on the left,} \quad (\text{III.8})$$

$$\tilde{A}_{O, \frac{\sin\theta}{\lambda}}^- = \delta\left(u - \frac{\sin\theta}{\lambda}, v\right) \otimes \tilde{A}_O(-u, -v) \quad \text{on the right.} \quad (\text{III.9})$$

The first one as has the exact same spectral content A_O as the signal but is translated in the Fourier domain by $-\frac{\sin\theta}{\lambda}$. By isolating the replica $\tilde{A}_{O, \frac{\sin\theta}{\lambda}}^+$, recentering it in the Fourier space and performing an inverse Fourier transform, we retrieve the signal A_O . These operations are performed numerically from the interference images collected by a discrete sensor of pixel pitch d .

In the off-axis technique with discretized sensors, the angle θ has to be carefully chosen so that the replicas do not overlap while allowing a correct spatial sampling

of the signal. An illustration of these limits is presented in Figure E.1 of appendix E. When working with multimode fibers, the output field is constrained in a given spatial frequency range by the numerical aperture of the fiber. Therefore, it is possible to express the range of angles θ which allows reconstructing the output field without loss of information:

$$\begin{cases} \sin\theta/\lambda \geq 3\Delta f/(2\gamma) & \text{(No overlap condition)} \\ \sin\theta/\lambda + \Delta f/(2\gamma) \leq 1/(2d\gamma) & \text{(Shannon condition)} \end{cases} \quad (\text{III.10})$$

where γ is the magnification of the output arm and d the pitch of camera pixels. The demonstration of the equations III.10 is presented in appendix E. With an OM2 GRIN fiber ($\text{NA} = 0.2$ and $a = 25 \mu\text{m}$) and a magnification $|\gamma| = 68$ like the ones in our setup, the bounds are $\theta \in [0.50^\circ, 2.55^\circ]$.

Implementation The reference is created from the 10% output of the polarization maintaining fiber coupler. Its polarization is at 45° with respect to the orientation of the beam displacer in order to have a balanced distribution of energy in both polarizations at the camera. The light is collimated and illuminates a diaphragm. The plane of the diaphragm is imaged onto the camera through the beam displacer. It generates two orthogonal polarization beams that overlap with the two polarization contributions of the signal beam. The reference path is indicated in blue in Figure III.8.

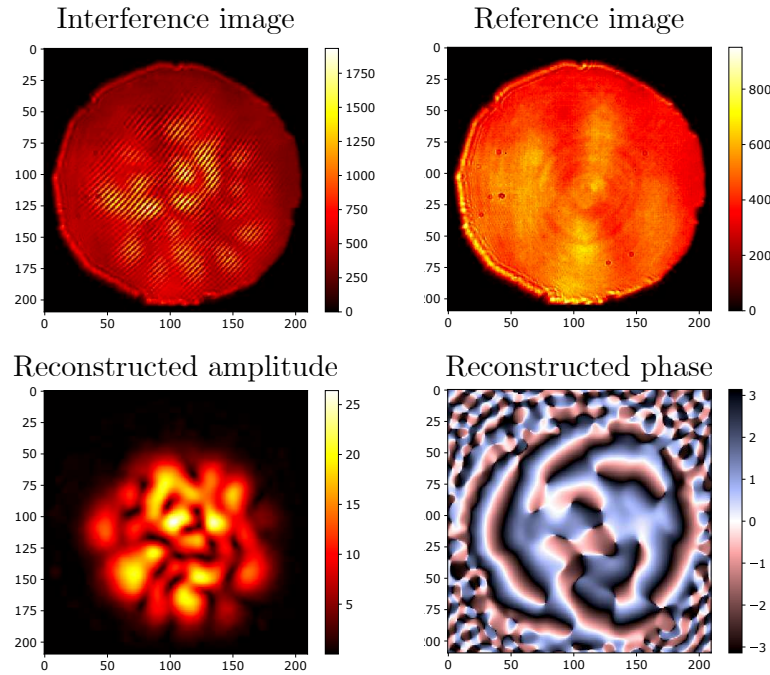


Figure III.10: Experimental reconstruction of the output field with off-axis measurements. Off-axis interference image, reference intensity and reconstructed amplitude and phase.

The amplitude of the reference field is not perfectly homogeneous. To compensate for this effect, we measure the amplitude map of the reference field and then divide each complex measurement by this term.

Automated field recovery To retrieve the correct phase out of off-axis measurements, we designed a method to precisely determine the center of the replica. Indeed, a wrong estimation of the center of the replica leads to an incorrect phase estimation in the direct real plane. The algorithm is presented in Appendix H. It is applied on the stack of the Fourier transforms of the interference patterns and allows the reconstruction of complex fields as presented in Figure III.10.

1.3.c Initial post treatments

Reducing data footprint To avoid manipulating the huge amount of data to the next steps of the post-treatments, we want to reduce the data footprint of the images. The off-axis replica we chose to keep has a bounded spatial frequency bandwidth which occupies a small fraction of the available spatial frequency space. We crop the spatial frequency domain around the replica and keep only a fraction of the frequency domain before performing the inverse Fourier transform. Doing so, we removed unused information from the images.

Centering of the speckles In order to estimate the modal content of the fiber, we want to precisely know the position of the center of the fiber. Previously described algorithm 1 allows to find the center with ease when applied to the stack of complex valued speckles.

Phase decorrelation During our experiments, we sometimes observe a global phase decorrelation occurring throughout acquisitions. This phenomenon can be caused by local temperature gradient that affect the optical path of the light in the two arms of the interference setup. To evaluate the magnitude of this effect, a specific reference pattern is periodically sent on the DMD and the corresponding output speckles are recorded. After reconstruction of the output fields, we can measure the complex correlation between these speckles throughout a full acquisition¹⁴. We can observe fluctuations in the correlation as shown in the red curve of Figure III.11.

To compensate for these fluctuations, each time we send the reference input mask, we estimate the relative global phase variation of the output field compared to the first time we sent the reference mask. We then subtract this value from all following measurements until we repeat the operation for the next occurrence of the reference mask. We show in Figure III.11 the decorrelation of the field as a function of the time before and after this correction.

After correction of the whole sequence, we computed the correlation on the second sequence of repeated speckles unused for the calibration, the results are presented in the blue curve of Figure III.11. We remark that the corrected images suffer from fewer phase fluctuations.

Rearranging of the data We collect the phase corrected complex speckles that correspond to the sequence of inputs. We want to reshape them in a form to manipulate them easily later on, so we express the inputs and outputs as the 1D vectors x and y . After reshaping the input and output images of the sequence of acquisition, we stack them in the second dimension. The input (resp. output) sequence of vectors is arranged in a 2D matrix \mathbf{X} (resp. \mathbf{Y}) where the 1st dimension N (resp. M) represents

¹⁴The correlation is computed for pixels with an amplitude value greater than 20% of the maximum to reduce the influence of noise.

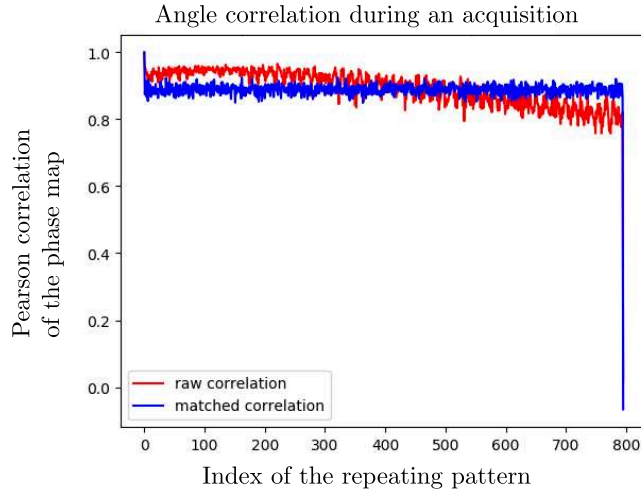


Figure III.11: Evolution of the phase correlation during an acquisition. Comparison of the decorrelation of the corrected and raw signal over time. The total time of the acquisition is 16 seconds.

the size of individual vectors, i.e. the total number of input (resp. output) macropixels, and the 2nd dimension represents the total number of elements p in a sequence. The input and output matrices are represented in the following way:

$$\mathbf{X} = (x_1, x_2, \dots, x_p) \text{ and } \mathbf{Y} = (y_1, y_2, \dots, y_p). \quad (\text{III.11})$$

2 Measurement of the pixel basis transmission matrix

In this section, we present the methods used to measure the transmission matrix that links the field on the pixels of the SLM (in our case a DMD) to the field on the pixels of the camera. This TM describes the propagation of the light in the full optical setup i.e. between the plane of the SLM and the one of the camera. Consequently, it does not represent only the propagation inside the fiber, but also takes into account the optical system between the modulator and the input facet of the fiber, and between the output facet of the fiber and the camera.

2.1 Principles

By definition of the TM, if we send an input mask represented by a vector x , we measure the output field y that reads:

$$y = \mathbf{H}.x. \quad (\text{III.12})$$

We note \mathbf{H} the transmission matrix which link the pixels, or macropixels¹⁵, of an SLM to the pixels of a camera. It is referred to as the pixel basis TM. When multiple input vectors are sent into the system, the previous equation becomes:

$$\mathbf{Y} = \mathbf{H}.\mathbf{X}, \quad (\text{III.13})$$

where \mathbf{X} and \mathbf{Y} are the matrix representation of the sequence of input and output vectors.

¹⁵From there to the end of Chapter IV, we will only consider the input and output macropixels. The term *pixel* will thus be employed to refer to the macropixels.

To give an estimation $\hat{\mathbf{H}}$ of the pixel basis TM of the system, one can send each vector of the canonical basis so that $\mathbf{X} = \mathbb{1}_n$. In that case, we directly obtain an estimation of the TM: $\mathbf{Y} = \hat{\mathbf{H}}$. To increase the input power sent into the system, one can also use the Hadamard basis [Popoff et al., 2010a]. The TM is retrieved by inverting the input matrix: $\hat{\mathbf{H}} = \mathbf{Y}.\mathbf{X}^\dagger$, with \cdot^\dagger representing the Hermitian (transpose conjugate) of a matrix. In this case, we have as many measurements as there are input pixels: $N = p$.

In the presence of noise, the quality of the estimated TM can be severely diminished. It is also the case if one measurement, corresponding to one vector of the input basis, fails. It is then desirable to have redundancy in the measurements to compensate for possible faulty measurements and to mitigate the effect of the measurement noise. We use a sequence of random inputs where $p > N$ and estimate the matrix using:

$$\hat{\mathbf{H}} = \mathbf{Y}.\mathbf{X}^+ , \quad (\text{III.14})$$

where \mathbf{A}^+ is the so-called *Moore-Penrose* pseudo inverse of matrix \mathbf{A} ¹⁶.

Not all random sequences of random input patterns obey the condition which allows the existence of the pseudo-inverse of \mathbf{X} . To get an idea of the reconstruction quality, one method consists in directly simulating the reconstruction of a TM from complex output fields \mathbf{Y} in the presence of measurement noise. In appendix F, we perform such simulations to choose an appropriate input sequence to display with the DMD.

We choose x to be random patterns where the modulation on each macropixel can take the value 0, -1 or 1. The corresponding masks are then generated using the Lee-hologram technique. For each pattern, on average, 60% of pixels are *off*, i.e. taking the value 0. The *on* pixels can take the value 1 or -1 in an even distribution.

2.2 Single input, single output polarization

We performed the experiments using a square grid of $35 \times 35 = 1225$ input macropixels of size 20×20 pixels of the DMD. The output field is measured on the camera in a region of interest of size 200×200 for each polarization. The images are then reduced to $41 \times 41 = 1681$ macropixel images by filtering and downsampling. We study here a 30 cm OM2 fiber (GRIN fiber, NA = 0.2, $a = 25 \mu\text{m}$), which supports theoretically 55 modes per polarization at $\lambda = 1550 \text{ nm}$. We measure the pixel basis TM of the system. We show in Figure III.12 the amplitude of the pixel basis TM for one input and one output polarization.

To assess the quality of our reconstructions, we compute the test error between the experimental output \mathbf{Y}^{test} corresponding to a number p_{test} of input patterns \mathbf{X}^{test} , that are not used for the estimation of the TM, and the simulated output of the estimated TM $\mathbf{Y}^{\text{simu}} = \hat{\mathbf{H}}.\mathbf{X}^{\text{test}}$. For each output point j , we measure the absolute value error defined as:

$$\epsilon_j = \frac{\sum_{i=1}^{p_{\text{test}}} |y_{ji}^{\text{test}} - y_{ji}^{\text{simu}}|}{\sum_{i=1}^{p_{\text{test}}} |y_{ji}^{\text{simu}}|} . \quad (\text{III.15})$$

It allows building maps of the output error as shown in the left of Figure III.13. In the right part of the Figure, we show the error as a function of the oversampling ratio defined as $\frac{p}{N}$. We observe that the error is quite high (about 10% in the core region), which would indicate theoretically performance. However, this error measurement

¹⁶When \mathbf{A} has linearly independent rows, then \mathbf{A}^+ is a right inverse such as $\mathbf{A}.\mathbf{A}^+ = \mathbb{1}_n$. If this condition is valid for the matrix \mathbf{X} , then equation III.14 is verified.

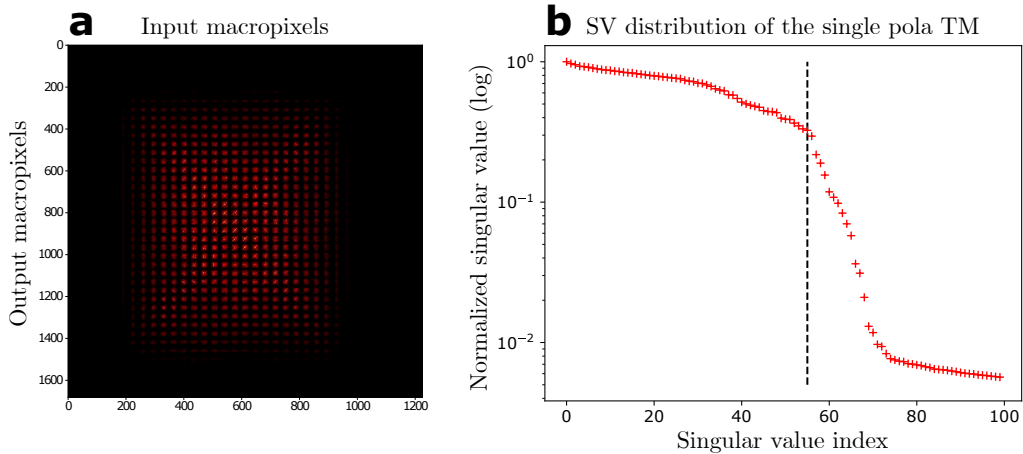


Figure III.12: Pixel basis TM for one input and one output polarization. **a**, Absolute value of the pixel basis TM recorded for a single polarization both in input and output. **b**, Associated singular value distribution. The dashed vertical line indicates the theoretical number of supported modes per polarization of the fiber, here 55.

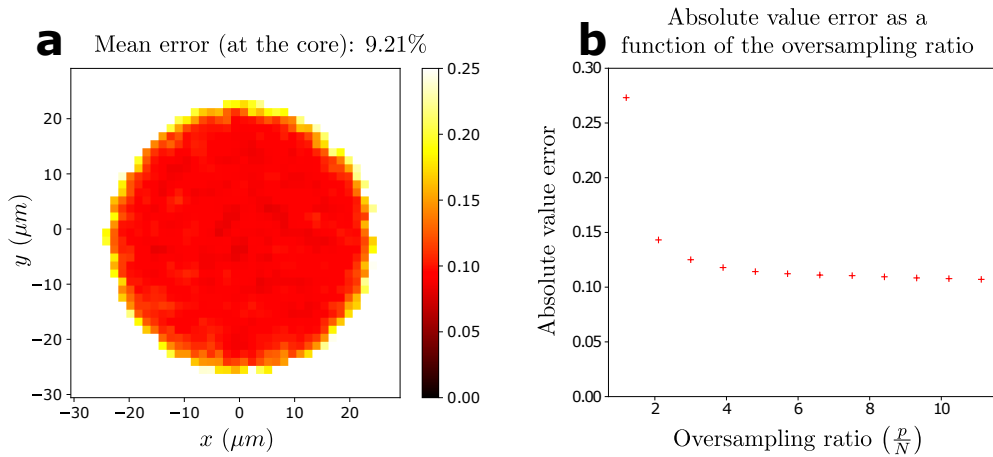


Figure III.13: Absolute value error of reconstruction. **a**, Absolute test error measured for a TM reconstructed with an oversampling ratio of 5). **b**, Experimental absolute value error of reconstruction averaged over the center output zone for different oversampling ratios p/N .

is a strongly biased evaluation of the quality of the TM. We present in appendix F how high error values can be caused by measurement noise, and how the fidelity of the matrix can be excellent even for high test errors. When evaluating the reconstruction error by using test vectors like we did, we mostly evaluate the measurement noise of the setup. However, those errors are mostly mitigated in the TM estimation thanks to the redundancy of information as detailed in the previous section. From the conclusions of our simulations and the error values of the experimental reconstruction, we chose $p/N = 6125/1225 = 5$ as the reference oversampling value to act as a trade-off between acquisition time and reconstruction error. The output speckles are recorded at a framerate of 1 kHz¹⁷, the acquisition takes about 6 seconds

¹⁷The framerate is limited by the camera due to the size of the region of interest (ROI), a smaller ROI allows for faster acquisitions.

The singular value distribution of the TM is displayed in the right part of Figure III.12. We observe that the distribution shows three regimes, the first one before the mode cut-off (corresponding to 55 modes per polarization) where the distribution is approximately flat; then a quick drop, then a plateau corresponding to the noise level. The fact that we have a sharp transition (more than 10 dB) between high singular values, corresponding to high transmission channels, and a continuum of low values, means that we can effectively observe the modal content of the fiber. It validates the spatial discretization parameters and the number of input images chosen for the reconstruction of the TM.

Moreover, as the drop occurs at the cut-off, we validate that we have correctly estimated the number of modes and that the experiments seem to fit our theoretical model so far. The input and output singular vectors associated to four singular values are shown in Figure III.14. We note that the first one does not resemble a theoretical mode, while the 50th looks like an LP mode. The 70th singular vectors still

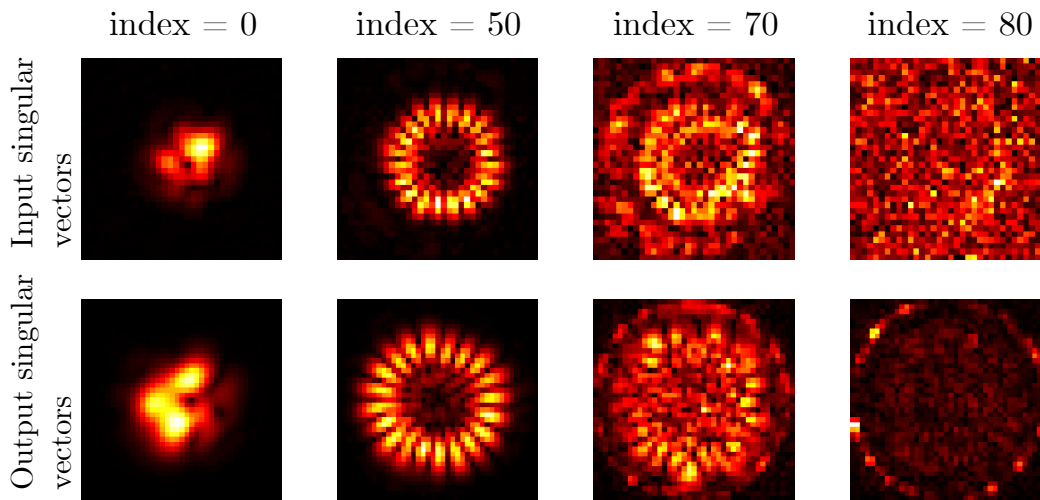


Figure III.14: Singular vectors of the single polarization TM. Absolute values of the input (top) and output (bottom) singular vectors for different singular values for a pixel basis TM recorded at a single polarization both in input and output.

shows a profile which looks like a linear combination of modes which indicates that it still contains information about the fiber modes. The singular vectors after the 80th are associated to noise and can be discarded.

2.3 Both input polarizations

To estimate the full pixel basis TM, we concatenate the four TMs obtained for two orthogonal input polarization states by rotating the quarter waveplate in the injection arm by 90°, and two orthogonal output polarizations recorded thanks to the beam displacer. Because of the quarter-wave plates, each input and output polarization state corresponds to the left or the right circular polarization. We show a full TM in Figure III.15. The submatrices corresponding to the TM for one input and one output polarization are separated by blue dashed lines. In the following of this work, we will sometimes refer those submatrices as *quadrants* of the full polarization TM.

We note that the diagonal block seems to hold more energy than the off-diagonal ones, we confirmed this observation by measuring a ratio $\frac{\|\hat{\mathbf{H}}_{\text{diag}}\|^2}{\|\hat{\mathbf{H}}_{\text{offdiag}}\|^2} = 2.5$. This

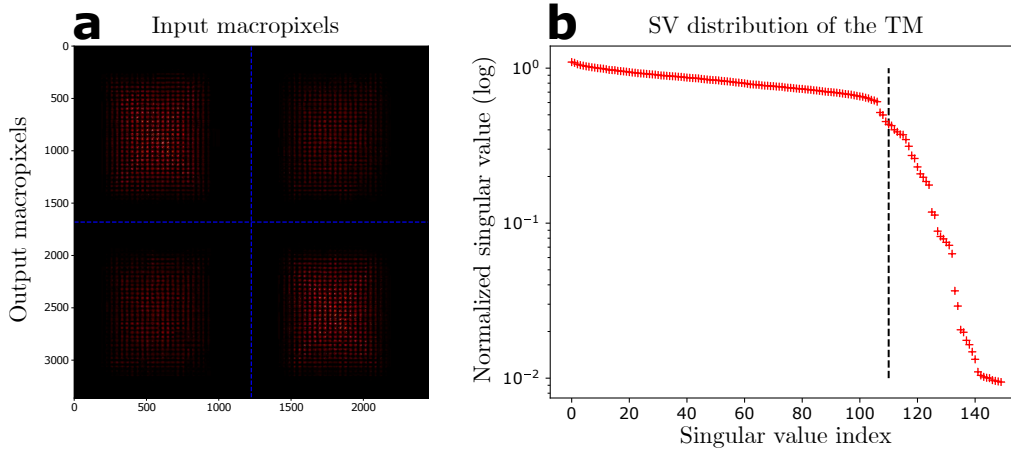


Figure III.15: Both input polarizations pixel basis transmission matrix. a, Absolute value of the pixel basis TM recorded for both circular polarizations. **b,** Associated singular value distribution.

behavior is expected in unperturbed multimode fibers as circular polarization states are known to be robust [Ploschner, Tyc, and Cizmar, 2015].

The distribution of the singular values also displays a flat plateau and a sharp decay, occurring slightly before the 110 modes cut-off (at the 105th singular value). The plateau is flatter than for a single polarization, and we have $s_0 = 1.8 s_{105}$. The drop is also deeper with $s_{105} = 56.7 s_{141}$, corresponding to 17 dB. The singular vectors are shown for both polarizations in Figure III.16. The spatial profiles of the absolute test error for full mode basis TM are presented in Figure III.17. We observe that the four quadrants present a flat error profile in the center of the outputs, they also have the same levels of error. Finally, we observe that the input singular vectors appear to be shifted with respect to the center of the image. Once again, to recenter the inputs of the TM, we use the center detection algorithm presented in Appendix H.

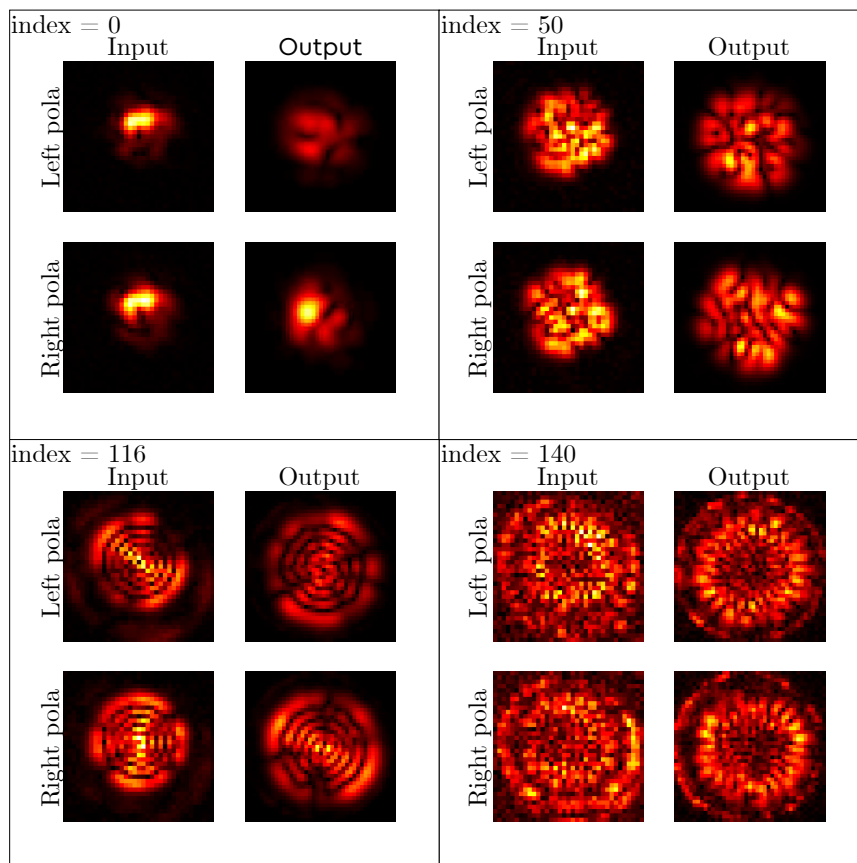


Figure III.16: Singular vectors of the full polarization TM. Absolute value of the input and output singular vectors for both polarizations for the full pixel basis TM for several singular values. The colormap is adjusted relative to the maximal amplitude of each image.

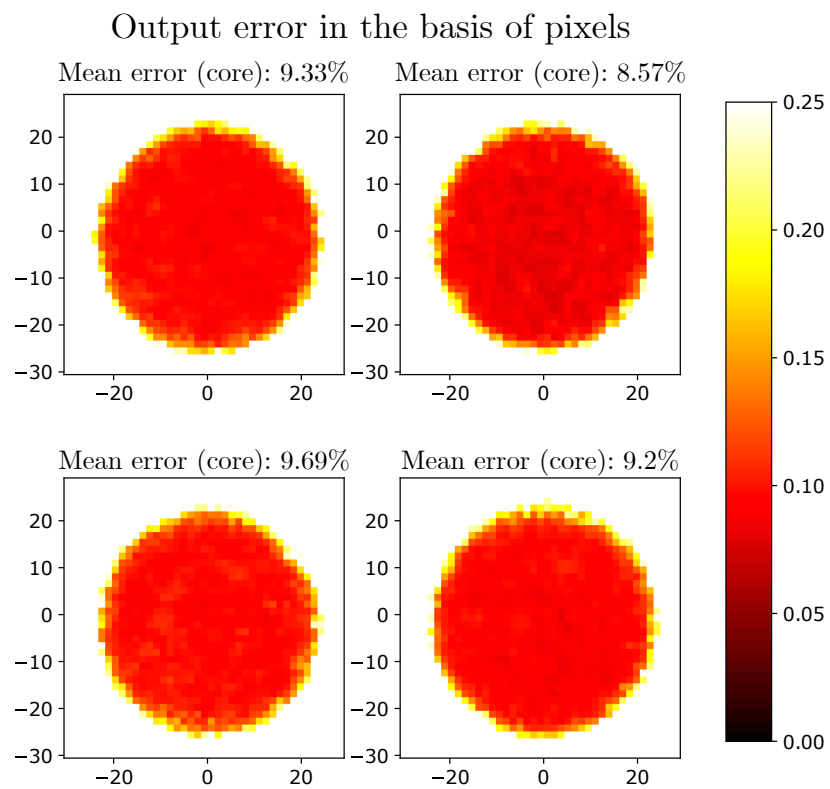


Figure III.17: Output error of the experimental reconstruction. Spatial profile of the experimental reconstruction error computed at the output, for each quadrant of the full pixel basis TM.

3 Reconstruction of the mode basis TM

Our goal is to measure the TM of MMFs in the fiber mode basis to study their transmission properties that are not directly accessible in the pixel basis TM. In an ideal optical system, the planes of the DMD and the camera are perfectly conjugated with the input and output facets of the fiber. The pixel basis TM measured then represents the TM of the fiber. By computing the spatial profiles of the fiber modes, we can then numerically project this matrix in the mode basis.

However, when the optical setup is not perfect, such as in the presence of aberrations and misalignments, the change of basis matrices between the pixel and modal representations cannot be inferred only from the calculation of the theoretical modes. To retrieve the accurate mode basis TM, we need to numerically compensate for the imperfections of the system.

In this section, we describe the procedure we designed to project accurately the TM in the basis of the propagating modes of the MMF. We first present the formalism for the conversion between the pixel and modal representations. We then present how to numerically estimate the ideal conversion basis between the pixel basis and the mode basis (i.e. in the situation where the optical system is perfect). Next, we briefly describe the negative effect of the experimental system imperfections. Finally, we present the original procedure we developed for the numerical compensation of the aberrations and misalignments using a model-based optimization taking advantage of deep learning frameworks.

3.1 Modal projection of the TM

First, we discuss the sets of spatial profiles that we used for the conversion from the measured pixel basis TM \mathbf{H} to the modal basis TM $\mathbf{H}_{\text{modes}}$. To go from pixels at the input facet of fibers to modes, we use the change of basis matrices \mathbf{M}_{in} . \mathbf{M}_{out} represents the change of basis matrix between the pixels of the camera and the propagating modes of the fiber. A vector $e_{\text{in/out}}^{\text{pixel}}$ representing the discretized electric field at the input or the output is converted into the mode representation $e_{\text{in/out}}^{\text{modes}}$ according to the relation:

$$e_{\text{in/out}}^{\text{pixel}} = \mathbf{M}_{\text{in/out}} \cdot e_{\text{in/out}}^{\text{modes}} \quad (\text{III.16})$$

the rows of $\mathbf{M}_{\text{in/out}}$ represent the complex spatial profiles of the modes (expressed in 1D as explained in 1.3). We convert the pixel basis TM into the mode basis representation using:

$$\hat{\mathbf{H}}_{\text{modes}} = \mathbf{M}_{\text{out}}^\dagger \cdot \hat{\mathbf{H}} \cdot \mathbf{M}_{\text{in}} \quad (\text{III.17})$$

The next step consists in estimating the theoretical mode profiles of the fiber we are studying. This gives access to the change of basis matrices in the case of a perfect optical setup (no aberration or misalignment).

Due to symmetries, there exist groups of degenerate modes in typical multimode fibers as shown in Chapter I section 2. Therefore, different representations exist to describe those modes. Graded-index fiber mode profiles and dispersion relation do not have a closed-form analytical expression. Finite difference methods are easy to implement numerically, but the 2D discretization of the field leads to high memory requirement and computation time, and could lead to inaccuracies for high order modes. Because we consider axisymmetric index $n(r)$ profiles, we want to simplify the system to solve a 1D problem that only depends on the radial coordinate r , allowing us to increase the accuracy and decrease the computation time. Because the refractive index only depends on the radial coordinate r for a perfect graded-index

fiber, we can separate the variables r and ϕ . We are then looking for modes of the form:

$$\phi_{ml}(r, \theta) = e^{im\theta} f_l(r), \quad (\text{III.18})$$

with l the radial order and m the azimuthal order, which also corresponds to the orbital angular momentum. We inject it in the 2D scalar Helmholtz equation defined in Chapter I, section I.5, we obtain:

$$d_r^2 f_l(r) + \frac{1}{r} d_r f_l(r) + \left[k_0^2 n^2(r) - \beta^2 - \frac{m^2}{r^2} \right] f_l(r) = 0. \quad (\text{III.19})$$

The details of the numerical resolution of this equation are presented in appendix G. This procedure has been implemented in the Python module pyMMF [Popoff, 2020] that was created during my PhD. The obtained propagation constants are shown in Figure III.18 and compared to the propagation constants obtained with the vectorial finite element solver Comsol.

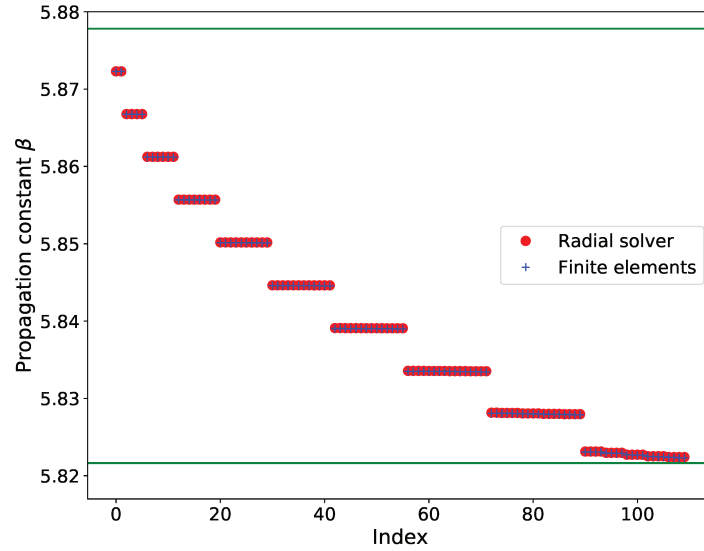


Figure III.18: Propagation constants of graded index fiber modes. Propagation constants obtained by numerically solving the equation III.19 (red) and obtained with the finite element solver Comsol (blue) for a OM2 GRIN fiber of radius $a = 25 \mu\text{m}$ and $\text{NA} = 0.2$. The green lines correspond to $k_0 n_1$ and $k_0 n_c$, i.e. the upper and lower bounds for the propagation constants of guided modes. The propagation constants obtained with our numerical method are almost identical to the ones obtained with the finite element resolution.

The numerical solutions give access to the spatial mode profiles that correspond to the Orbital Angular Momentum modes (OAM modes) when the polarization is circular, as presented in Chapter I section 2.2.b. After obtaining the complex mode profiles, we build the conversion matrices $\mathbf{M}_{\text{in/out}}$.

3.2 Imperfect mode conversion

In the presence of imperfections in the optical setup, the resulting aberrations and misalignments modify the change of basis matrices $\mathbf{M}_{\text{in/out}}$ between the pixel basis and the mode basis.

Let's consider a simple example in which the only imperfection is a misalignment corresponding to a lateral shift in the transverse plane. If we send the mask corresponding to one mode of the fiber on the DMD, the overlap between the excitation field and the target mode of the fiber is not perfect. Not all the energy is transmitted to the desired modes, and a fraction of the light is also injected in other modes.

The coupling between the injected field $E(x, y)$ and the modes $\phi_i(x, y)$ supported by the fiber reads:

$$C = \sum_{i=1}^{N_{modes}} \left| \int \Phi_i(x, y) E(x, y)^* dx dy \right|^2 \quad (\text{III.20})$$

In the example of Figure III.19, we send a mode with a lateral shift of $2.7 \mu\text{m}$. We observe that only 95.5% of the light intensity is transmitted to the fiber, and that several modes are excited. In actual experiments, other types of perturbation occur;

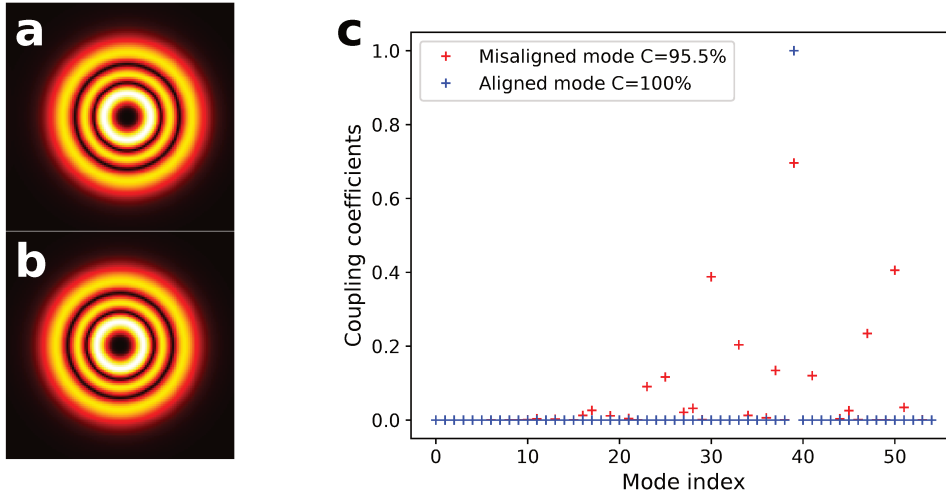


Figure III.19: Imperfect mode injection into an MMF due to misalignment. **a**, Misaligned ($2.7 \mu\text{m}$ shift) and **b**, Ideal intensity profile of a fiber mode. **c**, Associated coupling coefficients.

defocus, misalignment of the optical axis or aberrations in various planes along the propagation. In particular, we show in section 1.1 (and in appendix C) that the DMD used for the modulation introduces a significant amount of aberrations due to the curvature of its modulation plane.

Similarly, uncertainties about the fiber parameters introduce errors on the change of basis matrices. An error about the radius, the numerical aperture or the mode profile, changes the computed mode profiles compared to actual ones of the fiber. We illustrate this phenomenon in Figure III.20. In this simulation, we convert the spatial profile of a mode obtained for a fiber of parameters $\text{NA} = 0.205$ and of radius $a = 24 \mu\text{m}$ using the conversion matrices computed for an ideal OM2 fiber of parameters $\text{NA} = 0.20$ and of radius $a = 25 \mu\text{m}$. We observe that 97% of the energy of the input profile is coupled into the corresponding mode of the fiber, but a fraction of energy of about 3% is coupled into another one. We also lost about 1% of the total energy which does not couple to the fiber.

Using change of basis matrices that do not take into account the aberrations or that are generated using incorrect fiber parameters introduces mode conversion artifacts when computing the mode basis TM. In the presence of perturbations, we

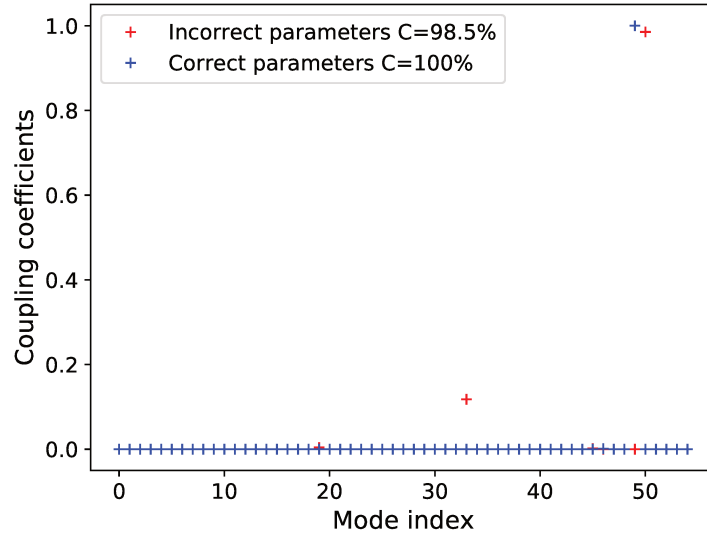


Figure III.20: Imperfect mode injection into an MMF due to wrongly estimated fiber parameters. Coupling coefficients between a mode computed with incorrect parameters $NA = 0.205$ and of radius $a = 24 \mu\text{m}$ (red), and a mode computed with the correct parameters and the modes of an ideal OM2 fiber (blue). Fewer modes are supported by the fiber of incorrect parameters, which explains why the coupling maxima are not for the same index.

expect the resulting mode basis TM to display the same behavior as the one observed in the simpler examples of Figures III.19 and III.20: a global loss of energy after conversion, and an artificial coupling between modes that does not represent the physics of propagation. We show in Figure III.21 the estimated mode basis TM after conversion of the pixel basis TM with the initial conversion matrices. Even though the fiber on which the TM was measured was straight and unperturbed, the mode basis TM appears random. This mode basis TM does not represent the propagation properties of the optical fiber. We also measure that the total energy of the modal TM is only 49% of the energy of the pixel basis TM, which indicates that the change of basis was not correct. Indeed, the basis of modes is not a complete basis in free-space, it does not allow the perfect description of the transformations generated by the aberrations and misalignments.

3.3 Finding aberrations of the optical setup

3.3.a Goal

At this state, the change of basis matrices $\mathbf{M}_{\text{in/out}}$ do not allow to accurately obtain the mode basis TM. For a given pixel basis TM, we want a method which allows correcting the change of basis matrices to take into account the imperfections of the system. Tomas Cizmar and his team [Ploschner, Tyc, and Cizmar, 2015] introduced a method to correct those matrices. In their work, they ran an optimization procedure which aims at maximizing the intensity of the diagonal elements of the mode basis TM by modifying the change of basis matrices. The new change of basis matrices are computed by numerically applying transformations to the initial ones, which corresponds to modifying the x , y and z positions, pitch and yaw tilt of the fiber (geometrical degrees of freedom) as well as the parameters of the fiber used for

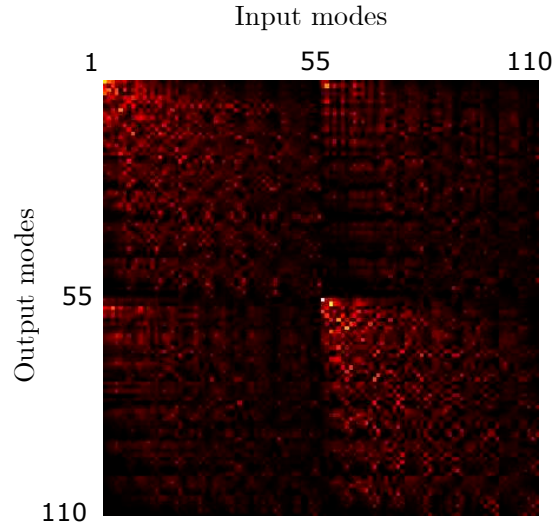


Figure III.21: Initial mode basis TM. Absolute value of the mode basis TM obtained with the initial change of basis matrices that do not take into account the aberrations.

the computation of the modes. The optimization procedure accurately corrects the change of basis matrices in a few hours for a fiber of about a hundred modes.

However, this technique presupposes the fact that the mode basis TM is diagonal, which is true for a short and unperturbed fiber. It limits applications for long fiber or for the study of disorder, where the mode basis TM is not expected to be diagonal, such as in the experiment we present in Chapter IV. Moreover, the optimization takes about 5 hours for a 520 mode fiber with 12 degrees of freedom for the aberrations and misalignments (6 for the input, 6 for the output). Such computation time limits real-life applications where one wants to limit downtimes.

We then seek to develop a technique fast and general enough to work for any kind of fiber, regardless of the degree of disorder.

3.3.b Model

We designed a numerical procedure based on the neural network framework PyTorch [Paszke et al., 2019], taking advantage of Graphics Processing Units (GPUs) for optimized computational times. Unlike neural networks, that consists of generalist layers, typically dense or convolutional layers, we use a model-based approach. Similarly to the previous work by the team of Tomas Cizmar, the general principle is to apply to the change of basis matrices $\mathbf{M}_{\text{in/out}}$ a set of transformations that mimics the effect of aberrations and misalignments to compensate for the experiment's imperfections. The schematic of the model is presented in Figure III.22

The key parts of our approach are the layers that mimic the effect of aberrations represented by Zernike polynomials. The effect of a layer Z_k , corresponding to the k -th Zernike polynomial, is to add, to each 2D image, a phase contribution. It amounts to transforming each input image K_{pq} , $(p, q) \in [1, N_{pix}] \times [1, N_{pix}]$ into a modified one K'_{pq} using:

$$K'_{pq} = K_{pq} e^{i\alpha_k F_k(r_{pq}, \phi_{pq})}, \quad (\text{III.21})$$

where i is the unit imaginary number, $F_k(r, \phi)$ is the k -th Zernike polynomial, r_{pq} and ϕ_{pq} are the polar coordinates corresponding to the pixel indexed by p and q , and α_k is

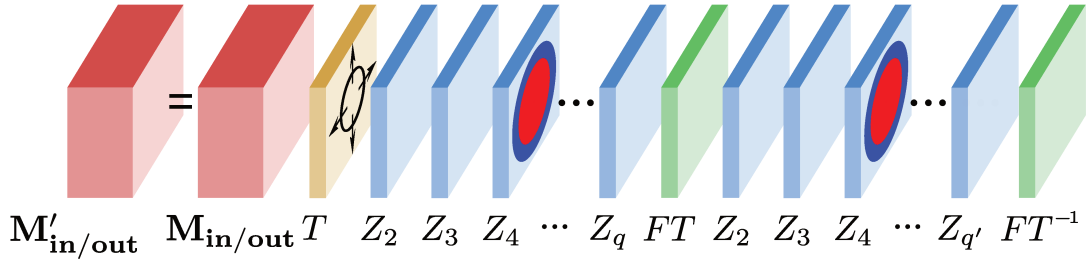


Figure III.22: Schematic of the model architecture used for the compensation of the aberrations. The matrices $\mathbf{M}_{\text{in/out}}$ are modified by differentiable and trainable layers representing a homothety (yellow layer) and phase aberrations characterized by Zernike phase polynomials (blue layers). The Fourier transforms (green layers) allow applying aberrations in the direct and the Fourier planes. The models for the two input and output mode conversions are trained simultaneously against a cost function that maximizes the energy in the projected matrix $\hat{\mathbf{H}}_{\text{modes}}$.

the weight of the aberration. α_k is the only trainable parameter of the layer. The layer automatically calculates and stores the derivative of the output tensor with respect to this parameter, as required for the training process (backpropagation). By adding multiple Zernike layers, we simulate the effect of a high level of aberrations. We perform a Fourier transform in the spatial dimensions and add other Zernike layers to simulate aberrations in the Fourier plane as shown in Figure III.22. The first Zernike polynomials correspond to phase slopes in the x and y directions and to a parabolic phase. When applied in the Fourier plane, they introduce spatial shifts in the x and y directions and a defocus. It allows compensating for misalignments in the x , y and z directions. Finally, we add a transformation T that applies a global scaling in the spatial dimensions. The scaling parameter is the only trainable parameter of this layer. We use 9 layers corresponding to the corrections in the Fourier plane, 14 layers for the direct plane, and one homothety T . It makes a total of 24 layers to optimize for each side of the fiber.

We treat separately each combination of input and output polarizations. For each optimization, we train simultaneously two models, one for the input and one for the output change of basis matrix. The input data corresponds to the matrices \mathbf{M}_{in} and \mathbf{M}_{out} of respective size $N^{\text{modes}} \times N$ and $N^{\text{modes}} \times M$ that we compute using the approach detailed in the previous section. We convert and reshape them as PyTorch tensors¹⁸ of sizes $N^{\text{modes}} \times N_x^{\text{in}} \times N_y^{\text{in}} \times 2$ and $N^{\text{modes}} \times N_x^{\text{out}} \times N_y^{\text{out}} \times 2$, with $N^{\text{modes}} = 55$ the number of modes per polarization, $N_x^{\text{in}} = N_y^{\text{in}} = \sqrt{N} = 35$, and $N_x^{\text{out}} = N_y^{\text{out}} = \sqrt{M} = 41$. The first dimension is treated as the batch size in conventional neural networks. The two models return new input and output change of basis matrices \mathbf{M}'_{in} and \mathbf{M}'_{out} . We use the change of basis matrices as input and output projectors on the pixel basis TM:

$$\hat{\mathbf{H}}_{\text{modes}} = \mathbf{M}'_{\text{out}}{}^\dagger \cdot \mathbf{H} \cdot \mathbf{M}'_{\text{in}}, \quad (\text{III.22})$$

where $\hat{\mathbf{H}}_{\text{modes}}$ is the mode basis TM estimated with the modified change of basis matrices.

¹⁸Complex tensors are not natively supported by the PyTorch framework we use. To do so, we add a dimension to our data structure of size 2 to encode the real part and the imaginary part of the complex values. We then create a set of elementary operations: complex conjugation, element-wise, and matrix multiplications. The models and algorithms are available in the repository: [Github.com/wavefrontshaping/article_MMF_disorder](https://github.com/wavefrontshaping/article_MMF_disorder).

3.3.c Cost function

In the previous work by the team of Tomas Cizmar, the fibers studied have a step index profile, and are kept straight during the acquisition with minimal external perturbation. In this case, we expect low coupling between the modes: the mode basis TM is expected to be diagonal. For this reason, the optimization goal of their algorithm is to maximize the diagonality of the mode basis TM, using a cost function of the form:

$$\mathcal{L} = \frac{\|\hat{\mathbf{H}}_{\text{modes}}\|}{\|\text{diag}(\hat{\mathbf{H}}_{\text{modes}})\|}, \quad (\text{III.23})$$

where $\|\cdot\|$ represents the L_2 norm (Frobenius norm) of a matrix. The parameters are trained to minimize the cost function.

In our work, we work with 30 cm long segments of GRIN fibers. Longer lengths imply that the modes may display stronger coupling between them, thus leading to a non-diagonal matrix. Furthermore, we want to be able to study the effect of disorder, in which case the mode basis TM is not expected to be diagonal due to the mode coupling induced by perturbations. The previous cost function is not suitable for our study. Instead, we train the model parameters to maximize $\|\mathbf{H}_{\text{modes}}\|$. Energy conservation imposes that the input and output projections performed in equation III.17 lead to $\|\mathbf{H}_{\text{modes}}\| \leq \|\mathbf{H}\|$. Since the light can only be transmitted through the fiber by the propagating modes, these two quantities are equal when the matrices \mathbf{M}_{in} and \mathbf{M}_{out} correctly compensate for the aberrations and misalignments. We choose as the cost function to minimize:

$$\mathcal{L} = \frac{\|\mathbf{H}\|}{\|\hat{\mathbf{H}}_{\text{modes}}\|}, \quad (\text{III.24})$$

Unlike neural networks, we do not need a large training set. Indeed, we feed to the network only one experimentally measured matrix \mathbf{H} .

3.3.d Optimization

Finally, we run an optimizer based on a stochastic gradient descent approach. We use the Adam optimizer¹⁹ [Kingma and Ba, 2017] to find the set of parameters (weights of the Zernike polynomials and the global scaling factors in input and output) that minimizes the cost function \mathcal{L} defined in equation III.24.

The evolution of the cost function during the optimization is shown in Figure III.23: We notice that the cost function quickly reaches a state of quasi-stationarity, punctuated only by small ripples. We end the optimization after 500 iterations.

We perform the optimization on the two diagonal quadrants of the full polarization pixel basis TM. We obtain two pairs of change of basis matrices (one for the input and one for the output of each possible polarization). Using this change of basis matrices on the other quadrants, it allows obtaining the full polarization mode basis TM²⁰. Because of the low number of trainable parameters, $2 \times 24 = 48$ corresponding to as much Zernike polynomials plus one for a global scaling on each facet,

¹⁹The advantage of this method over standard gradient descent is that ADAM adapts the learning rate during the learning phase. It keeps *momentum* of previous gradients to help climb local minima while adding *friction* to prevent from overshooting the potential global minimum. Educational notes about gradient descent methods written by Sebastian Ruder can be found at [Ruder, 2016]

²⁰We use the results to correct the two quadrants that were not used during the optimization.

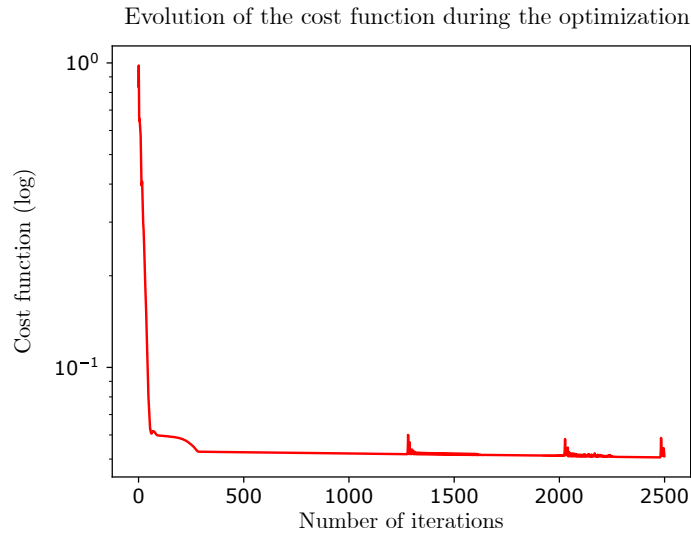


Figure III.23: Evolution of the cost function \mathcal{L} in function of the iteration number.

the optimization takes only a few seconds to converge for a 110 mode fiber on our GPU²¹.

3.3.e Results

The corrected mode basis $\hat{\mathbf{H}}_{\text{modes}}$ is obtained with the corrected change of basis matrices. We show in Figure III.24 the intensity (square of the absolute value) of the mode basis TM of a straight 30 cm OM2 fiber. The total energy of the corrected TM is about 94% of the energy of the initial pixel basis TM. Similarly to what was observed in [Ploschner, Tyc, and Cizmar, 2015], optimizing the index profile to better account for the real geometry of the fiber may help increase the total energy in the corrected mode basis TM. We remark that the mode basis TM has a very strong diagonal. Indeed, about 53% of the total energy of the matrix is localized in the main diagonal. This figure rises to 92% for the energy contained in the block diagonal (white contours), representing the groups of degenerate modes.

The final state of the optimization coefficients is shown for the input in Figure III.25. We notice that the corrections in the Fourier space are limited to the first 4 coefficients, meaning that there is little perturbation coming from the optics, mostly the misalignments in the transverse and longitudinal directions are corrected. On the contrary, we observe that all the coefficients in the direct space have a significant weight, mostly due to perturbations caused by the DMD (and possibly the surface of the fiber).

We show the initial and corrected input change of basis matrices in Figure III.26. For better visualization of the effects of the corrections, we display how the aberrations transform the raw modes by showing some corrected modes in Figure III.27. We remark that the aberrations heavily modify the wavefronts that couple to the modes.

²¹NVIDIA GeForce RTX 2080.

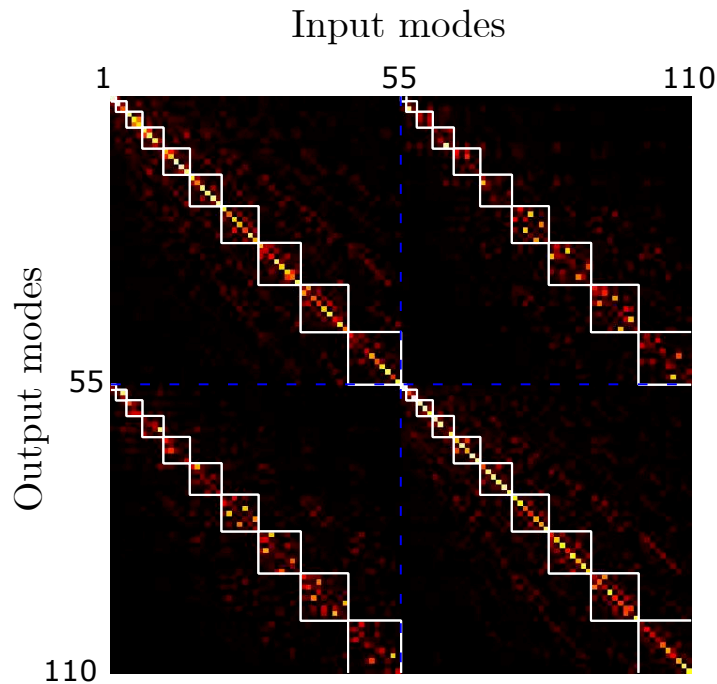


Figure III.24: Transmission matrix in the basis of OAM modes. Intensity of the transmission matrix in the basis of OAM modes of a OM2 GRIN fiber. The white contour delineates the groups of degenerate modes.

Conclusion

We presented in this section the tools we developed to measure the mode basis TM of MMFs. A DMD is used with the Lee hologram method to produce a few level phase modulation that illuminates the MMF, both orthogonal polarizations are sequentially sent into the MMF thanks to a rotating quarter waveplate. The control of both polarizations in the input and output and the precise measurement of the output fields thanks to automated off-axis measurements allow us to build the pixel basis TM. This matrix represents the transmission properties of the system between the plane of the DMD and the plane of the camera.

We developed an approach leveraging deep learning frameworks to correct the aberrations and misalignment of the input and output parts of the optical setup. This allows us to recover precisely the mode basis TM of MMFs in a matter of minutes. The complexity of handling the effects of aberrations is rejected on the numerical post-processing. This approach is robust to any system imperfections *a priori*, allowing *plug-and-play* operations. It unlocked the possibility to work on many fiber samples and measure their mode basis TMs in a few minutes.

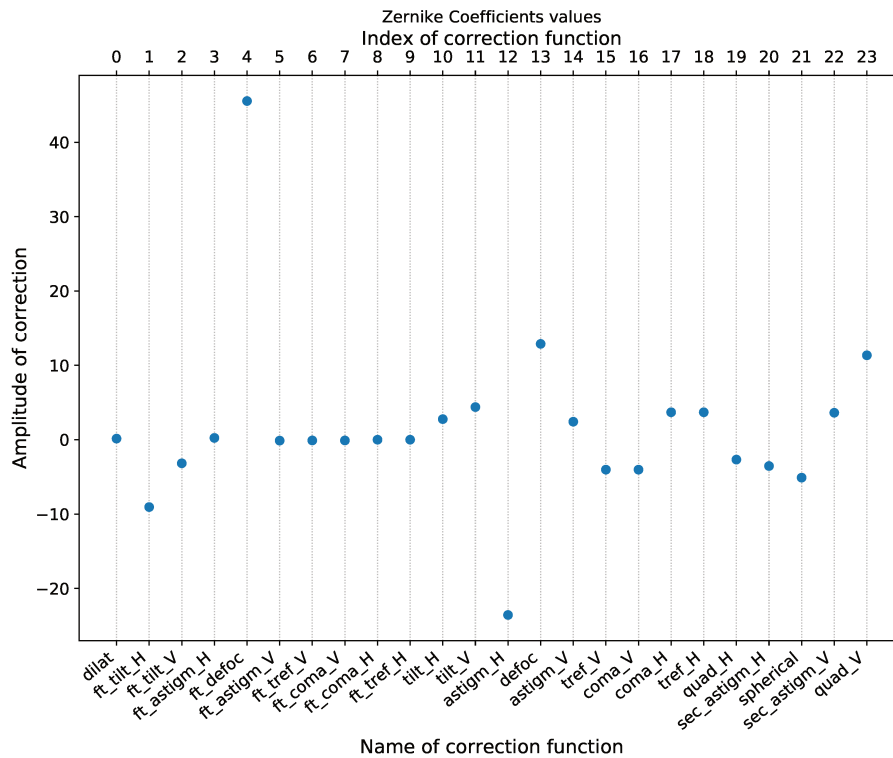


Figure III.25: Corrections used to correct an input change of basis matrix. Zernike coefficients obtained with the optimization procedure for the input of the top left quadrant.

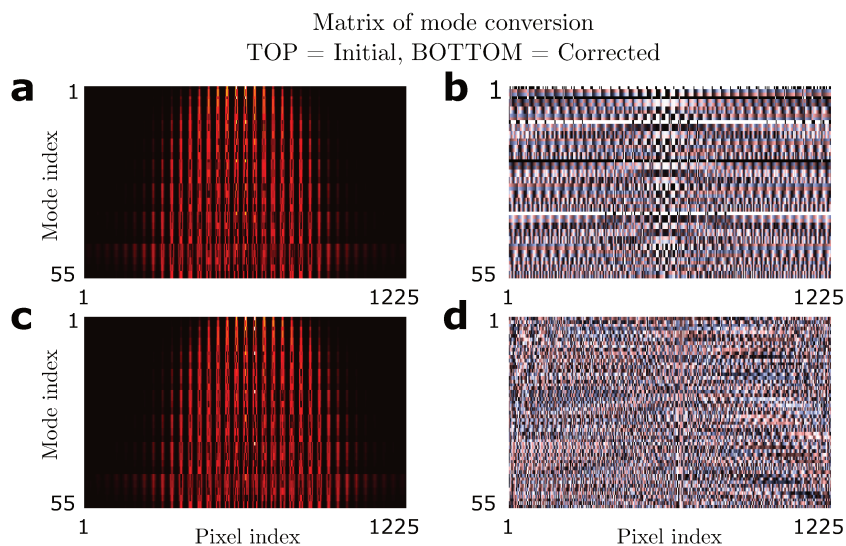


Figure III.26: Initial and corrected change of basis matrices. **a, c**, Absolute value and **b, d**, Phase of the initial (**a, b**) and corrected (**c, d**) change of basis matrices.

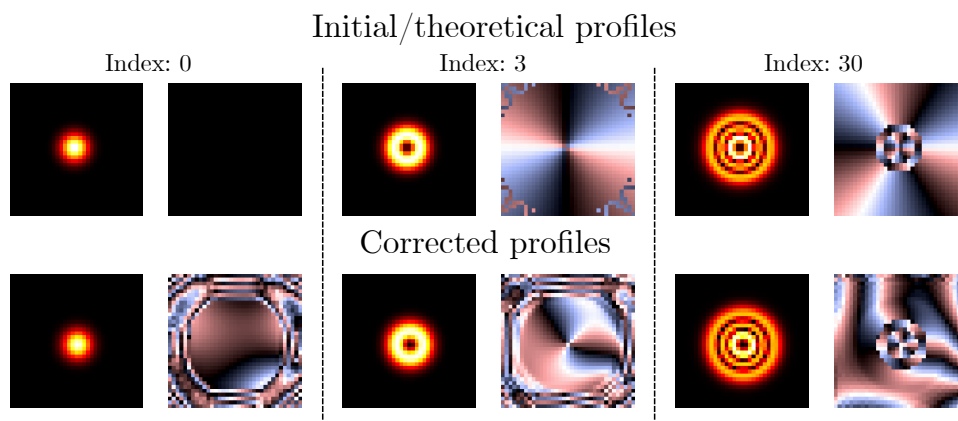


Figure III.27: Spatial profiles that couple into modes of the initial and corrected modes of the conversion matrix. Intensity and phase of three of the initial spatial profiles (top) and corrected profiles (bottom) of the conversion matrix.

Chapter IV

Effect of strong perturbations in multimode fibers

Chapter contents:

1	Introduction.....	88
1.1	Disorder in multimode fibers	88
1.2	Principal modes and the Wigner Smith operators	88
2	Effect of deformations on the TM	90
2.1	Experimental methods	90
2.2	Qualitative analysis of the modification of the TM	90
3	Avoiding disorder.....	94
3.1	Perturbation insensitive channels	94
3.2	Parametrization of the deformation of the TM	96
	Conclusion and perspectives	101

1 Introduction

1.1 Disorder in multimode fibers

The description of light transport in Multimode Fibers (MMFs) has been widely studied since the '70s, with a complete analytical understanding available in the case of an ideal straight fiber [Marcuse, 1974]. However, fabrication imperfections, geometrical deformations, or changes of the environmental conditions introduce randomness that drastically modifies their transmission properties. When light injected in one mode statistically explores all the other modes with the same probability, i.e. in the *strong coupling regime*, some average properties can be predicted [Ho and Kahn, 2011]. However, from a few centimeters to a few kilometers, typical MMF systems are neither in the no coupling nor in the strong coupling regime; disorder strongly influences light propagation but some aspects of the ordered behavior survive [Gambling, Payne, and Matsumura, 1975; Ryf et al., 2012; Ryf et al., 2015]. This intermediate regime has been little investigated so far due to the difficulty to experimentally characterize the effect of disorder on the modal content of the fibers. Understanding the transition between these two regimes remains an important challenge for optical telecommunications, endoscopic imaging, and micromanipulation applications.

It is well known that injecting coherent light into an MMF results in the observation of a random pattern of bright and dark spots at the output, called *speckle pattern*. However, unlike scattering media, the observation of a speckle is not in itself a signature of disorder. Indeed, perfect straight fibers also exhibit this property due to the existence of intermodal dispersion [Ploschner, Tyc, and Cizmar, 2015] as we discussed in Chapter I, section 2.4. As long as multiple modes are excited, they quickly accumulate seemingly random relative phases leading to such complex interference patterns.

In the previous chapter, we explained how the TM expressed in the basis of pixels of a DMD and a camera does not directly allow quantifying disorder inside an MMF due to its seemingly random aspect. Only when represented in the basis of the propagating modes does the TM allow us to fully capture the spatial propagation properties of the MMF.

1.2 Principal modes and the Wigner Smith operators

One of the main challenges of practical applications of multimode fibers is not only to understand the effect of disorder, but to avoid it altogether. In this context, the time-delay operator introduced in quantum mechanics by E. Wigner and F. Smith [Wigner, 1955; Smith, 1960], and also called the Wigner-Smith operator, has recently attracted renewed interest among the complex media community. For a lossless optical system characterized by its scattering matrix \mathbf{S} , which links all input channels to all output ones, the Wigner-Smith operator is constructed using the frequency derivative of \mathbf{S} , and defined as $\mathbf{Q} = -i\mathbf{S}^{-1}\partial_\omega\mathbf{S}$. Interestingly, the eigenstates of this operator, also called *principal modes*, are insensitive to small variations of the frequency. The possibility to use wavefront shaping techniques to generate those input states opened new applications to improve some properties of light transport, such as to generate particle-like wave packets in chaotic cavities [Rotter, Ambichl, and Libisch, 2011] and in scattering media [Gérardin et al., 2016; Böhm et al., 2018], or to optimize energy storage in scattering media [Durand et al., 2019].

We presented in Chapter II section 3.1, how, in MMFs, the scattering matrix can be approximated by the TM, which measurement give access to the principal modes.

In the context of telecommunications, they are particularly attractive as they do not suffer from modal dispersion to the first order [Fan and Khan, 2005]. Their ability to be stable over a large bandwidth was observed in weak disorder regime [Carpenter, Eggleton, and Schroder, 2015], with hundred-meter fibers of 6 and 72 modes. In this demonstration, the best principal mode consistently exhibits a significant suppression of mode dispersion compared to the propagating modes of the fiber. The Wigner-Smith operator was calculated in a 2 nm range. However, the bandwidth of the principal modes largely exceed this range, and can be stable over tens of nanometers. This observation was also made in the strong coupling regime for a 120-mode step index fiber [Xiong et al., 2017b]. They show a stability over a bandwidth larger than for random inputs, but perform worse than their weak-coupling regime counterpart.

The possibility to find channels invariant to small modifications can be extended to other parameters than the frequency using the Generalized Wigner-Smith (GWS) operator [Ambichl et al., 2017a; Horodyski et al., 2020] defined as:

$$Q_\alpha = -i\mathbf{S}^{-1}\partial_\alpha\mathbf{S}, \quad (\text{IV.1})$$

where α is an arbitrary parameter of the system, and i is the unit imaginary number. The eigenstates of Q_α are invariant with respect to a small parametric shift of α . In [Ambichl et al., 2017a], α is the position of one scatterer in a multiple scattering medium embedded in a planar waveguide. By moving this precise scatterer, the GWS operator can be estimated. Its eigenmodes, the *generalized principal modes*, are used to focus light onto the scatterer or to create light channels that avoids the scatterer. The parameter α can also be chosen to be the angle of a scattering object [Horodyski et al., 2020]. The corresponding principal modes can be used to transfer an angular momentum and rotate a target.

In the case of MMFs, we measure the transmission matrix that approximate the scattering matrix \mathbf{S} , as detailed in Chapter II, section 3.1. The TM is not perfectly unitary due to injection losses, mode losses and estimation errors. Therefore, the operator defined by $-i\mathbf{H}^{-1}\partial_\alpha\mathbf{H}$ is not Hermitian and its eigenvalues are complex. However, this non-Hermitian operator inherits the property that its eigenvalues are invariant with respect to changes of the parameter α from its Hermitian counterpart Q_α [Ambichl et al., 2017a]. It was shown in the case of the Wigner-Smith operator that its Hermitian part is sensitive to dispersion whereas its non-Hermitian is not [Durand et al., 2019]. For this reason, we define the GWS operator computed with TMs as its Hermitian part [Durand et al., 2020]:

$$Q_\alpha = -\frac{i}{2} \left[\mathbf{H}^{-1}\partial_\alpha\mathbf{H} - \left(\mathbf{H}^{-1}\partial_\alpha\mathbf{H} \right)^\dagger \right]. \quad (\text{IV.2})$$

In this chapter, we demonstrate the ability to use the knowledge of the TM for small deformations to find an almost complete set of channels using the GWS operator that are insensitive to strong perturbations. We call this set of channels the *deformation principal modes* and show their properties in section 3.1. To understand the ability of deformation principal modes to avoid the effect of large deformations, we show in section 3.2 that all across the deformation range, the evolution of the TM can be characterized by only a few parameters that account for the mode coupling between close-by propagating modes. The contents of this chapter are the subject of an article [Matthès et al., 2020] to be published in a scientific journal.

2 Effect of deformations on the TM

In this section, we first describe how we apply controlled perturbations on MMFs. While a fiber undergoes these perturbations, we measure its mode basis TM thanks to the methods developed in Chapter III. We qualitatively show that a change of regime of coupling happens when a strong deformation is applied on a fiber.

2.1 Experimental methods

To experimentally estimate the pixel basis and mode basis TMs of a MMF, we use the setup presented in the previous chapter, in section 1.2. The OM2 fibers we use¹ are composed of a glass core and a glass cladding of total diameter 125 μm , with an acrylate coating of diameter 242 μm . Only two centimeters are stripped of their coating at both ends. The fiber is held approximately straight, maintained by a fiber terminator at the input end and by magnetic clamps at the output end. Roughly at half the length, we place a V-groove to support the fiber and hold it in place where we introduce a deformation as shown in Figure IV.1.b. The perturbation is applied on the fiber by pressing on it on a direction orthogonal to the axis of the fiber, using a 50 nm precision DC servo motor actuator². Magnetic clamps are placed on both sides of the servo motor to prevent the fiber from slipping when the deformation increases. We note Δx the translation value of the actuator from the contact position³. The coating absorbs a significant part of the deformation of the fiber. Indeed, the Young modulus of the acrylate coating is several orders of magnitude larger than the one of the core and cladding, which are made of glass⁴. We assume that the deformation applied to the fiber core and cladding $\Delta x'$ is proportional but smaller than the translation value Δx . We show a schematic of the effect of the deformation in Figure IV.1.b.

2.2 Qualitative analysis of the modification of the TM

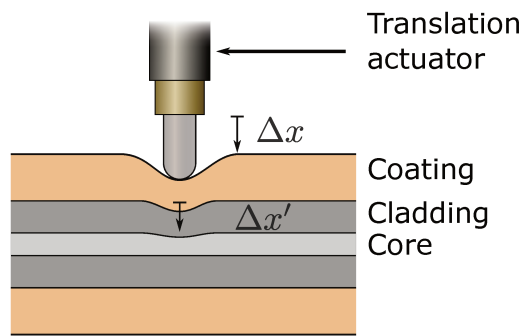
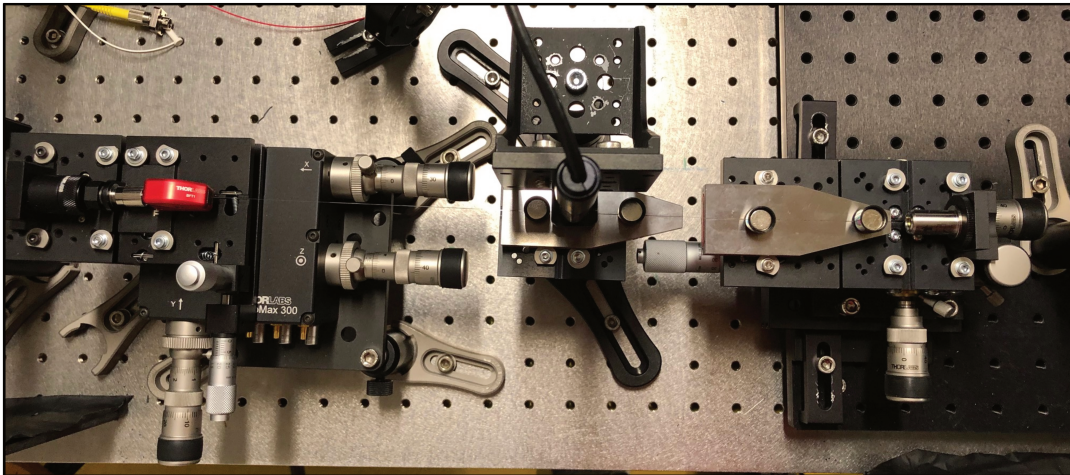
First, we qualitatively assess the effect of the perturbation on the fiber. To that end, we measure the pixel basis TM of an OM2 fiber (GRIN, $a = 25 \mu\text{m}$, $\text{NA} = 0.20$) with and without a 70 μm deformation. Both TMs are shown in Figure IV.2. They appear random, even for no perturbation. A straight fiber of this length is expected to act close to an ideal fiber [Boonzajer Flaes et al., 2018]. It is then difficult to analyze the effect of deformation in this pixel basis representation. We now convert the TMs in the mode basis representation using the knowledge of the mode profiles, computed using the approach detailed in chapter III, section 3.3. The resulting mode basis TMs are represented in Figure IV.4. Despite these changes, the matrices in the unperturbed and perturbed cases are seemingly random. This is the results of an imperfect mode conversion due to the presence of aberrations and misalignments, as qualitatively studied in Chapter III section 3.2.

¹Thorlabs GIF50C.

²Thorlabs Z812.

³To give an *a priori* estimation of the position at which the actuator touches the fiber, we measure the correlation of an output speckle as the function of the position of the actuator. We observe a fast drop as soon as contact is made.

⁴Values of 72.0 GPa are reported in the literature for the glass parts [Wierzba and Kosmowski, 2003] and values between 6 MPa to 1.0 GPa for the acrylate coating [Padilla Michel et al., 2015].



Small text block, likely a reference or copyright notice.

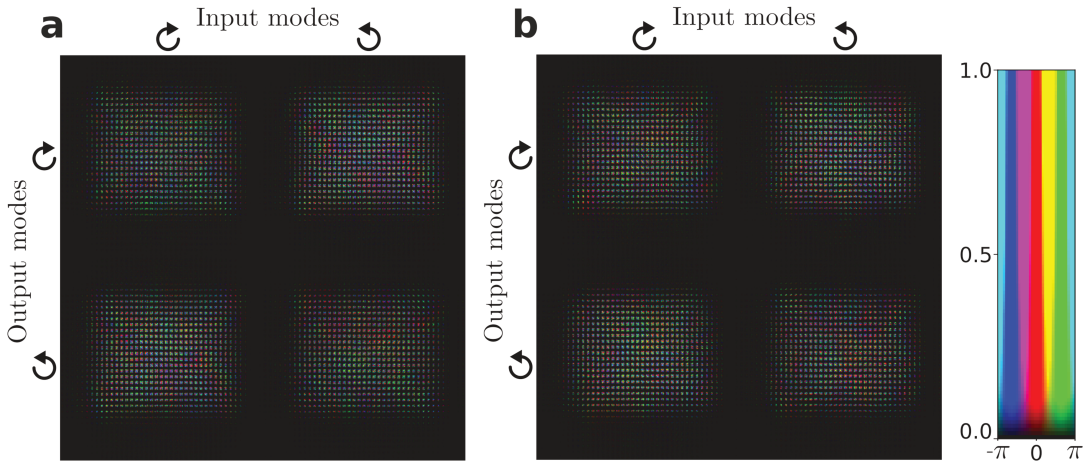


Figure IV.2: Complex representation of the TM in the pixel basis. **a**, For a non-perturbed OM2 MMF. **b**, For a strongly perturbed fiber corresponding to the maximal deformation $\Delta x = 70 \mu\text{m}$. The brightness of the image was enhanced for easier visualization as represented in the colormap.

group of degenerate modes holds 92% of the energy of the TM. In the perturbed TM, we observe that the energy of the diagonal blocks decreases to 21.3%. Now a significant part of the energy is in the off-diagonal components.

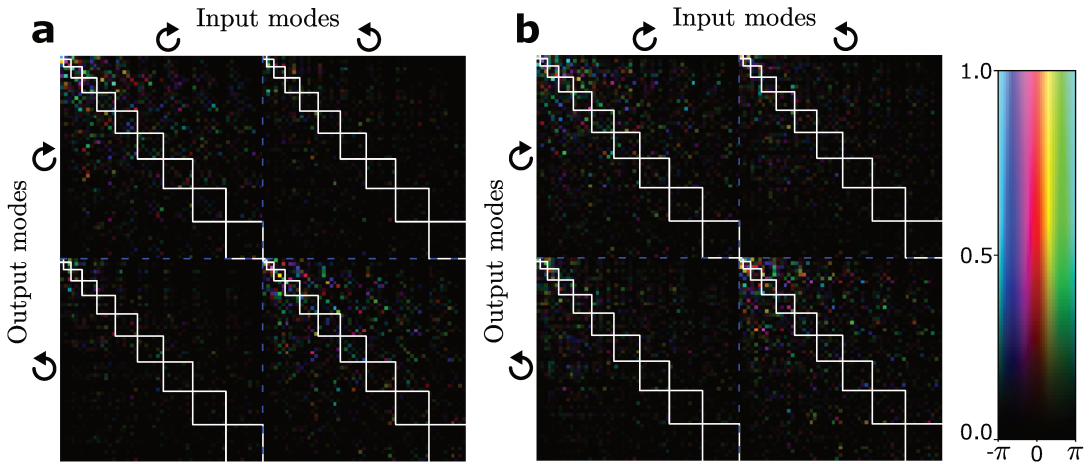


Figure IV.3: Complex representation of the mode basis TMs before correction. **a**, For a non-perturbed OM2 MMF. **b**, For a strongly perturbed fiber corresponding to the maximal deformation $\Delta x = 70 \mu\text{m}$.

We compute the singular value decomposition of the different matrices we measured. We showed in Chapter II, section 3.1 that the singular values correspond to the transmission coefficient of the spatial transmission channels. The corresponding singular vectors represent the input and output wavefronts associated with those channels. We present in figure IV.5 the distributions of the singular values of the pixel basis TM (red), of the uncorrected (cyan) and of the corrected (blue) mode basis TM. We observe a plateau of close-to-unity singular values for the unperturbed, corrected mode basis TM. This plateau is shorter for the perturbed corrected mode basis TM. In the unperturbed case, we observe high transmission values ($> 60\% s_0$, with s_0 the highest singular value), up to the 100th singular value. In the perturbed case, only the first 80 singular values are significant. This behavior means that the

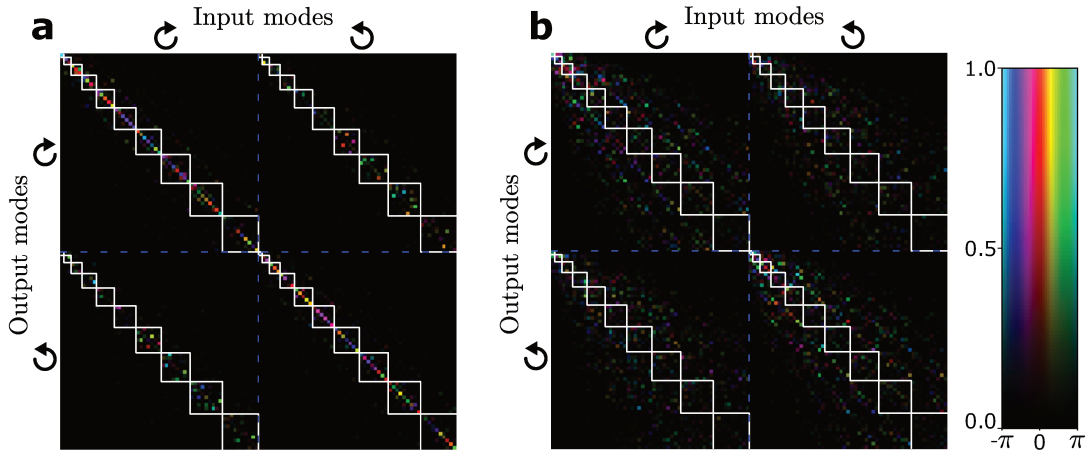


Figure IV.4: Complex representation of the mode basis TMs after correction. **a**, For a non-perturbed OM2 MMF. **b**, For a strongly perturbed fiber corresponding to the maximal deformation $\Delta x = 70 \mu\text{m}$.

deformation reduces the number of available transmission channels: we have fewer low-loss channels due to the perturbation. We cannot observe this behavior without the compensation of the aberration as both distributions of the uncorrected TMs show a similar aspect (shown in cyan in Figure IV.5). This further proves the efficiency of the correction algorithm. The observation of the singular vectors shows that the most attenuated channels are mainly composed of higher order modes as was predicted for curvature induced deformations [Marcuse, 1976].

In the rest of this chapter, the mode basis TM $\mathbf{H}_{\text{modes}}$ refers to the aberration corrected TM.

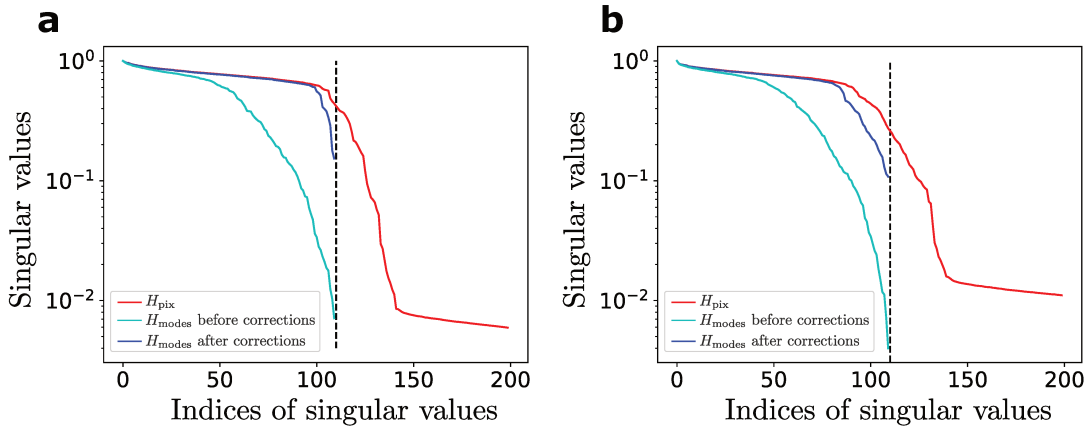


Figure IV.5: Singular value distribution of the mode basis TM. Distributions of the singular values of the pixel basis TM (red), of the uncorrected (cyan) and of the corrected (blue) mode basis TM. **a**, No deformation. **b**, A transverse deformation $\Delta x = 70 \mu\text{m}$ is applied to the fiber.

3 Avoiding disorder

In this section, we discuss how the measurements of the mode basis TM at different levels of perturbation allow finding spatial channels that are robust to disorder. These channels form an almost complete orthogonal basis that avoids the effect of disorder. We show that, even though we find these modes by exploiting measurements performed for small deformations, these channels are still robust to strong deformations. We show how these channels exploit numerous modes to *avoid* disorder. To justify these properties, we show how the perturbations can be characterized by a few number of parameters that represent the physical behavior of the modes, even for large amplitudes of deformations.

3.1 Perturbation insensitive channels

To learn how to be insensitive to disorder, we characterize the full mode basis TM of the MMF when we introduce and gradually increase the deformation. We use the translation actuator that presses on the fiber with increments of 4 μm before the contact position and increments of 2 μm afterwards. We measure the mode basis TM for each position of the translation actuator.

3.1.a Deformation effects on the mode basis TM

Qualitatively, strong deformations have the effect of progressively populating the off-diagonal elements of the TM while reducing the energy in the diagonal. Thanks to the precise modal projection, we observe the crossover from a nearly diagonal TM (weak coupling) [Ploschner, Tyc, and Cizmar, 2015] as shown in Figure IV.6.b, to a seemingly random TM (strong coupling) [Xiong et al., 2017b] as shown in Figure IV.6.e.

We estimate the fidelity between the matrix of the deformed fiber $\mathbf{H}_{\text{modes}}(\Delta x)$ and the reference matrix for the unperturbed configuration $\mathbf{H}_{\text{modes}}(\Delta x = 0)$, from:

$$F = \frac{\text{Tr}(|\mathbf{H}_{\text{modes}}(\Delta x = 0) \cdot \mathbf{H}_{\text{modes}}(\Delta x)^\dagger|^2)}{\sqrt{\text{Tr}(|\mathbf{H}_{\text{modes}}(\Delta x = 0)|^2) \text{Tr}(|\mathbf{H}_{\text{modes}}(\Delta x)|^2)}}. \quad (\text{IV.3})$$

We show in Figure IV.6.a how the fidelity decreases quickly as the displacement Δx increases.

3.1.b Generating the deformation principal modes

While the transmission properties are strongly altered for large deformations, our goal is to find a set of channels that are little affected by them. In the present work, the parameter of interest is the applied displacement Δx , we then study the GWS operator defined as:

$$\mathbf{Q}_{\Delta x} = -\frac{i}{2} \left[\mathbf{H}_{\text{modes}}^{-1} \cdot \partial_{\Delta x} \mathbf{H}_{\text{modes}} - \left(\mathbf{H}_{\text{modes}}^{-1} \cdot \partial_{\Delta x} \mathbf{H}_{\text{modes}} \right)^\dagger \right]. \quad (\text{IV.4})$$

We estimate the GWS operator for a small deformation $\Delta x = 14 \mu\text{m}$. The derivative in the expression of the GWS operator in equation IV.4 is numerically estimated using the approximation:

$$\partial_{\Delta x} \mathbf{H}_{\text{modes}} \approx \frac{\mathbf{H}_{\text{modes}}(\Delta x_0 + \delta x) - \mathbf{H}_{\text{modes}}(\Delta x_0 - \delta x)}{2\delta x}. \quad (\text{IV.5})$$

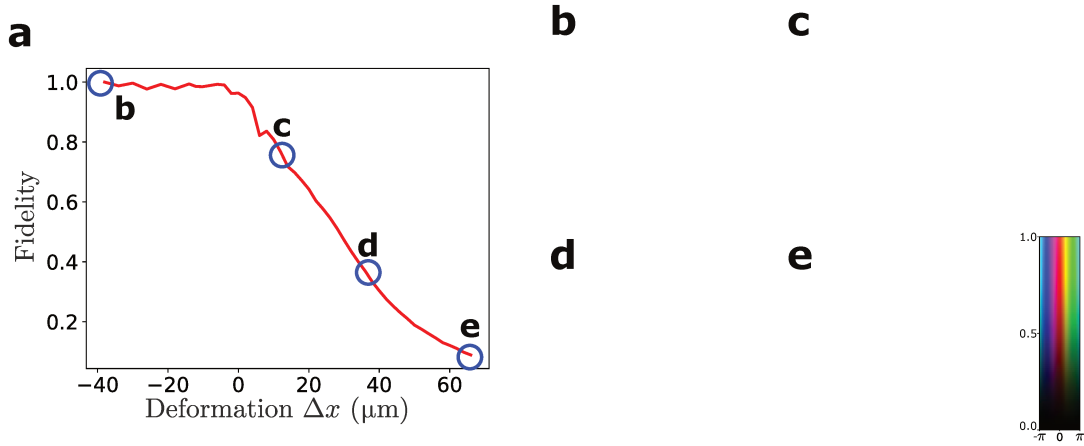


Figure IV.6: Effects of deformations on the mode basis TM. **a**, Fidelity between the TM of the deformed fiber and the unperturbed one as a function of Δx . **b**, Reference mode basis TM for no deformation. **c**, **d**, **e**, Mode basis TM for transverse deformations $\Delta x = 16 \mu\text{m}$, $42 \mu\text{m}$, and $70 \mu\text{m}$ (maximal deformation) respectively.

We choose $\delta x = 8 \mu\text{m}$. This value is chosen to be a trade-off between two competitive effects. Indeed, too small differentiation steps δx make the numerical system sensitive to noise fluctuations, while taking too large values leads to an incorrect estimation of the derivative. The eigenmodes of the GWS, the deformation principal modes, are theoretically insensitive to the deformation parameter Δx to the first order [Fan and Khan, 2005; Ambichl et al., 2017a]. We perform the eigendecomposition of $\mathbf{Q}_{\Delta x}(14 \mu\text{m})$ to obtain the deformation principal modes v_j :

$$\mathbf{Q}_{\Delta x}(14 \mu\text{m}) \cdot v_j = \zeta_j v_j, \quad j \in [1, N_{modes}], \quad (\text{IV.6})$$

where ζ_j are the eigenvalues of $\mathbf{Q}_{\Delta x}(14 \mu\text{m})$, and $N_{modes} = 110$. We obtain the input profiles of the principal modes from the eigenvectors v_i .

3.1.c Study of the deformation principal modes

To test the stability of the deformation principal modes, we numerically inject them in the TM for each deformation value and compute the corresponding output intensity profiles. We then compute the Pearson correlation coefficient between the outputs obtained at the reference deformation $\Delta x = 14 \mu\text{m}$ ($\mathbf{H}_{modes}(\Delta x = 14 \mu\text{m}) \cdot v_j$)

and the outputs for each deformation ($\mathbf{H}_{modes}(\Delta x) \cdot v_j$). The stability of the deformation principal modes is shown in Figure IV.7 as a function of Δx . For comparison, we also test the injection of the fundamental mode, which is less affected by disorder than the other modes [Marcuse, 1976], and random wavefronts (the correlation is averaged over 20 different random input wavefronts).

The correlation between the outputs of the best principal mode without defor

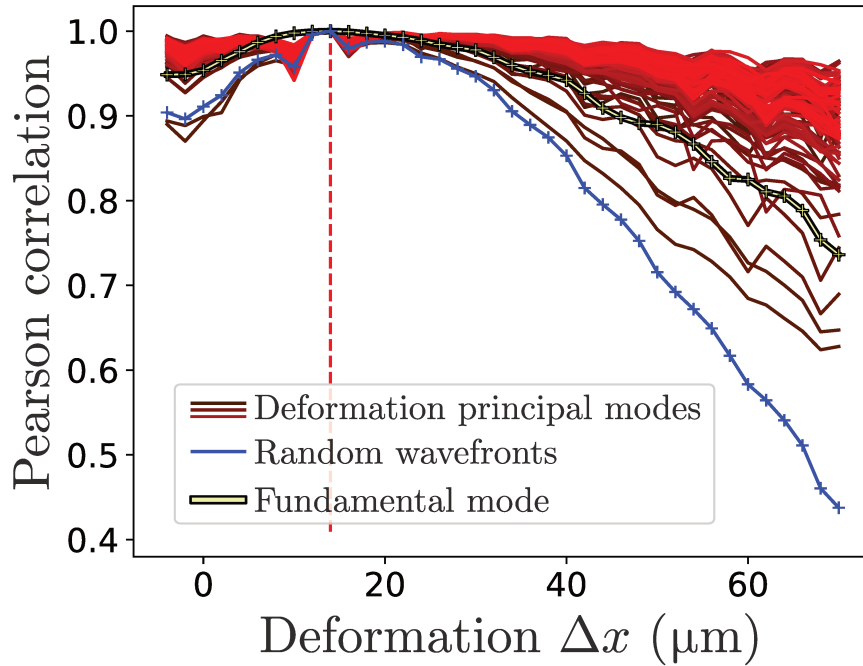


Figure IV.7: Correlation of the deformation principal modes. Pearson correlation coefficient between the output intensity pattern at Δx and the one at $\Delta x = 14 \mu\text{m}$ for all the deformation principal modes (shades of red), the fundamental mode (yellow with black stroke), and after averaging over 20 random input wavefronts (blue).

attributed to some fiber modes close to the cutoff being greatly attenuated as shown previously in Figure IV.5.

We show in Figure IV.8.a-c the profiles of the outputs corresponding to the best, the 12th best and the last deformation principal modes respectively, in d the fundamental mode and in e a random profile, without deformation and under a deformation of $\Delta x = 70 \mu\text{m}$. We observe in that the output intensity patterns of the deformation principal modes do not resemble any modes of the perfect fiber. In Figure IV.9, we show the absolute values of the coefficients of the decomposition of the input deformation principal modes that were shown in Figure IV.8, in the basis of the modes of the fiber⁵. We observe that the deformation principal modes are indeed composed of a wide range of fiber modes, including even the highest order modes which are the most affected by the deformation. Exploring a wide range of modes of the fiber is a behavior also observed in the case of the standard principal modes, that are the modes robust to changes of the light frequency [Ambichl et al., 2017b; Xiong et al., 2017b]. We remark that the last principal mode is mostly composed of higher order modes which are the most affected by the effects of disorder.

3.2 Parametrization of the deformation of the TM

3.2.a The deformation matrix

To further investigate how the deformation principal modes, computed from the TMs for small deformations, can efficiently cancel the effect of large deformations, we study the deformation matrix defined as:

⁵To obtain the output profiles $v_{j,pix}$ of the deformation principal modes that were shown in Figure IV.8, we use here the change of basis matrix \mathbf{M}_{out} that does not take into account the aberrations (i.e. the one presented in Chapter III section 3). The output profiles are then $v_{j,pix} = \mathbf{M}_{\text{out}} \cdot v_j$.

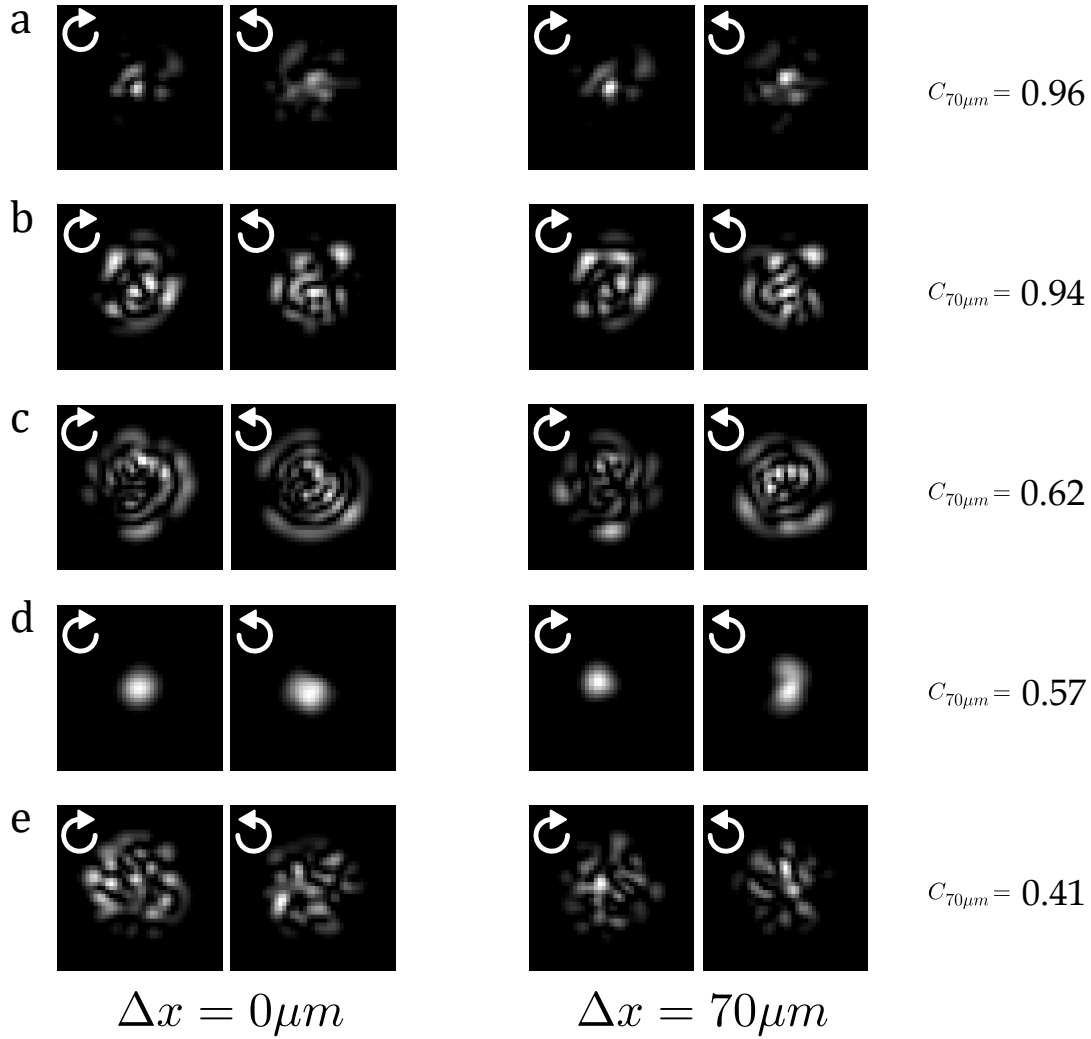


Figure IV.8: Output profile of the deformation principal modes. **a-c**, The best, the 12th and the last deformation principal mode output profiles intensity. **d**, The fundamental mode output intensity. **e**, Output intensity of a random input. The left column corresponds to the output under no deformation of the fiber, the right column corresponds to the output when the translation actuator is at $\Delta x = 70 \mu\text{m}$. The values $C_{70\mu\text{m}}$ correspond to the Pearson correlation coefficient between the output intensity profiles without deformation (left column) and for the maximal deformation (right column).

$$\mathbf{D}_j = \mathbf{H}_{\text{modes}}^{-1}(\Delta x = 0) \times \mathbf{H}_{\text{modes}}(\Delta x_j) - \mathbf{I}. \quad (\text{IV.7})$$

This matrix quantifies how $\mathbf{H}_{\text{modes}}(\Delta x)$ deviates from $\mathbf{H}_{\text{modes}}(\Delta x = 0)$. It is equal to 0 if the TM remains unchanged. We want to determine the main characteristics that best describe how the TM is modified when the perturbation is applied. To do so, we first build an operator that links a deformation Δx_j to the corresponding deformation matrix \mathbf{D}_j . To do so, we first reshape the stack of the matrices \mathbf{D}_j as a 2-dimensional matrix $\bar{\mathbf{D}}$ of size $N_{\text{modes}}^2 \times N_{\Delta x}$, where $N_{\Delta x}$ is the number of deformations, and $N_{\text{modes}} = 110$ the number of propagating modes. We call the matrix $\bar{\mathbf{D}}$ the *global deformation operator*. It links each deformation, indexed by j , to all the elements of the matrix \mathbf{D}_j , indexed by the composite index $\{kl\} \in [1 \dots N_{\text{modes}}^2]$. The range $[1 \dots N_{\Delta x}]$ of the index j corresponds to deformations between $\Delta x = 0 \mu\text{m}$ and the maximal deformation $\Delta x = 70 \mu\text{m}$. The expression of the global deformation

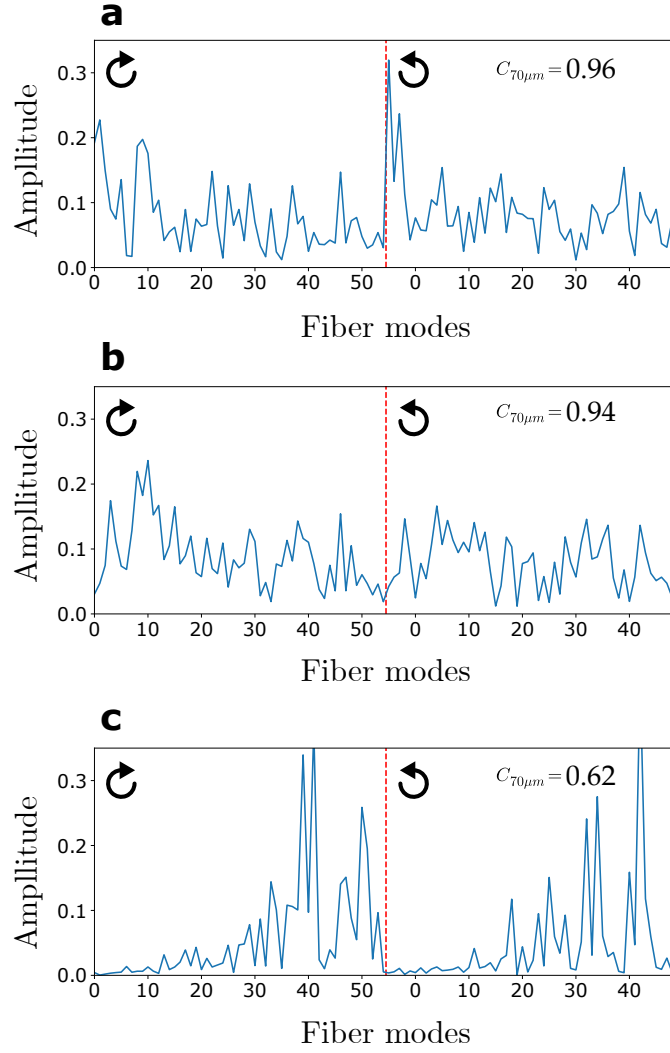


Figure IV.9: Representation of the deformation principal modes in the basis of the propagating modes of the fiber. a-c, Representation of the best, the 12th and the last deformation principal modes in the mode basis.

operator reads:

$$\bar{\mathbf{D}} = \begin{pmatrix} d_{kl=1, j=1} & d_{kl=1, j=2} & \cdots & d_{kl=1, j=N_{\Delta x}} \\ d_{kl=2, j=1} & d_{kl=2, j=2} & \cdots & d_{kl=2, j=N_{\Delta x}} \\ \vdots & \vdots & \vdots & \vdots \\ d_{kl=N_{modes}^2-1, j=1} & d_{kl=N_{modes}^2-1, j=2} & \cdots & d_{kl=N_{modes}^2-1, j=N_{\Delta x}} \\ d_{kl=N_{modes}^2, j=1} & d_{kl=N_{modes}^2, j=2} & \cdots & d_{kl=N_{modes}^2, j=N_{\Delta x}} \end{pmatrix}. \quad (\text{IV.8})$$

3.2.b Approximation of TMs under deformation

We first perform the singular value decomposition of the global deformation operator:

$$\bar{\mathbf{D}} = \mathbf{U} \cdot \mathbf{\Lambda} \cdot \mathbf{V}^\dagger. \quad (\text{IV.9})$$

$\mathbf{\Lambda}$ is a diagonal matrix of size $N_{\Delta x} \times N_{\Delta x}$ containing the singular values, which distribution is represented in Figure IV.10. The first two singular values amount to more than 96% of the total energy of the operator. It means that if we only keep the first

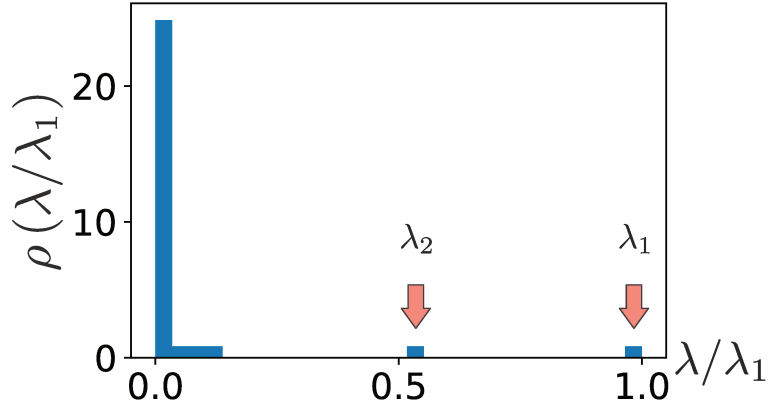


Figure IV.10: Singular value distribution of the global deformation operator. 96% of the total energy of the operator is contained in the first two singular values λ_1 and λ_2 .

singular values, 96 % of the output energy is conserved compared to the full matrix. It implies that the other singular vectors do not play an important role in the transmission properties of the system. \mathbf{V} is a matrix containing the corresponding input singular vectors V_j of size $N_{\Delta x}^2$, $j \in [1 \dots N_{\Delta x}]$. \mathbf{U} is a matrix containing the corresponding output singular vectors U_j of size N_{modes}^2 , $j \in [1 \dots N_{\Delta x}]$. They can be reshaped as 2-dimensional matrices \mathbf{U}_j of size $N_{\text{modes}} \times N_{\text{modes}}$.

To test here if the TM of a fiber under strong deformations can be parametrized by only a few parameters, we approximate the deformation matrix using only the first two components \mathbf{U}_1 and \mathbf{U}_2 according to the equation:

$$\hat{\mathbf{D}}_j = \alpha_j \mathbf{U}_1 + \beta_j \mathbf{U}_2 . \quad (\text{IV.10})$$

where the coefficients α_j and β_j are expressed by:

$$\alpha_j = \lambda_1 V_{1j}^* , \quad (\text{IV.11})$$

$$\beta_j = \lambda_2 V_{2j}^* . \quad (\text{IV.12})$$

It is equivalent to replace $\mathbf{\Lambda}$ in equation IV.9 by $\tilde{\mathbf{\Lambda}}$ defined by $\tilde{\Lambda}_{11} = \Lambda_{11} = \lambda_1$, $\tilde{\Lambda}_{22} = \Lambda_{22} = \lambda_2$ and $\tilde{\Lambda}_{kl} = 0$ for all other values.

We show in Figure IV.11 the fidelity between the estimated matrix $\hat{\mathbf{H}}_{\text{modes}}(\Delta x_j) = \mathbf{H}_{\text{modes}}(\Delta x = 0) \cdot [\hat{\mathbf{D}}_j + \mathbf{I}]$ and the measured one. All across the range of deformations, the TM can be estimated using only two parameters with a fidelity above 93%. We can give a qualitative interpretation of the two significant components; the matrices \mathbf{U}_1 and \mathbf{U}_2 are shown in Figure IV.12.a and b. We remark that \mathbf{U}_1 is close to identity, traducing the loss of energy in the diagonal compared to the reference TM at $\Delta x = 0$. It is equivalent to the decay of the ballistic light in the presence of a scattering environment in free space. We note that this first component is qualitatively identical to the first component identified in [Yammine et al., 2019] to parametrize the temporal fluctuations of an MMF over several hours; a matrix close to a block identity matrix. The second vector \mathbf{U}_2 shows a well-defined symmetric pattern that corresponds to an energy conversion between modes with close-by radial and angular momenta l and m . To support that interpretation, we show in Figure IV.12.c a matrix representing the coupling between modes with a radial order l difference equal or lower than 1 and an orbital momentum m difference equal or lower than

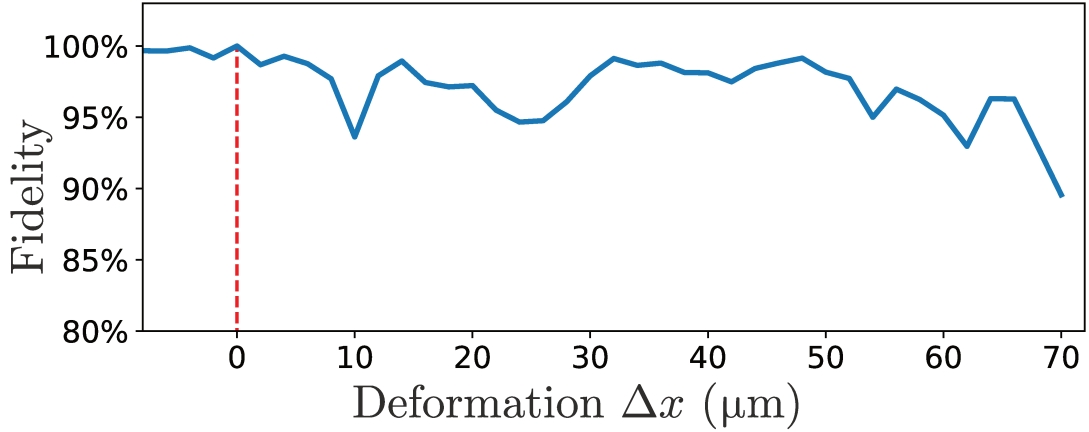


Figure IV.11: Fidelity between the measured mode basis TM and the approximated one. We use equation IV.10 to approximate the TM at a given deformation, and we compute the fidelity between this approximated TM and the measured one.

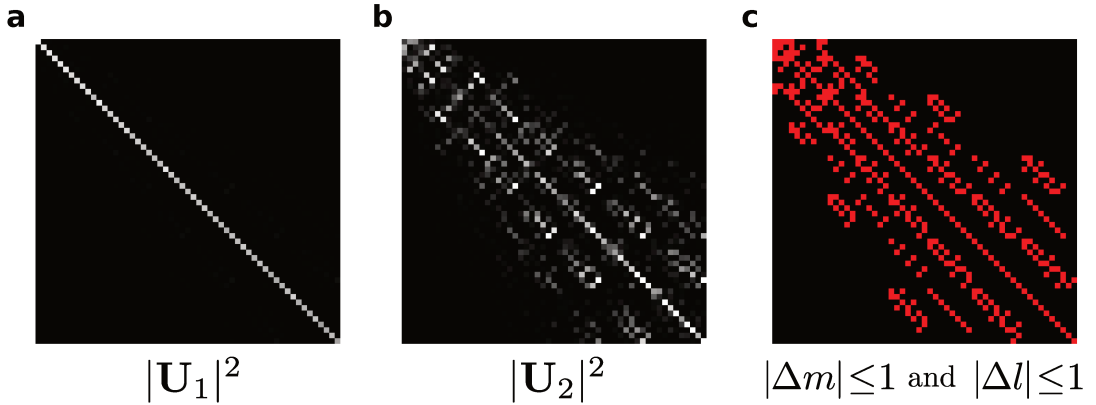


Figure IV.12: Input singular vectors of the global deformation operator. **a, b,** First two input singular vectors of $\bar{\mathbf{D}}$ rearranged as 2D matrices for a single polarization both at the input and output. **c,** Matrix representing the coupling between close-by modes, i.e. with a radial order l difference equal or lower than 1 and an orbital momentum m difference equal or lower than 1.

1. The two arrays show similar patterns. This is consistent with the previous observations that show that mode coupling occurs mostly between neighboring modes in the l and m space [Li et al., 2020]. This is analogous to the conversion between ballistic and single scattered photons in scattering media.

The fact that the TM can be estimated precisely using only two terms, only one of them accounting for mode coupling, is counter-intuitive considering the fact that $\mathbf{H}_{\text{modes}}$ shows a seemingly random aspect for high order modes at large deformations (see Figure IV.6.e). Coupling between modes further away in the l and m space can occur, it is the equivalent of multiple scattered photons in scattering media. We show in Figure IV.13 the higher order singular components \mathbf{U}_j , $j \in [2, 5]$. The singular components after the first two involve coupling effects between modes further away in the l and m space and include cross polarization coupling that is not taken into account by \mathbf{U}_1 and \mathbf{U}_2 . However, these contributions are associated to a small weight in the singular value decomposition. The fact that the same component \mathbf{U}_2 dominates the mode coupling effect for the whole deformation range explains how the deformation principal modes, estimated for low deformations, are still valid for strong deformations.

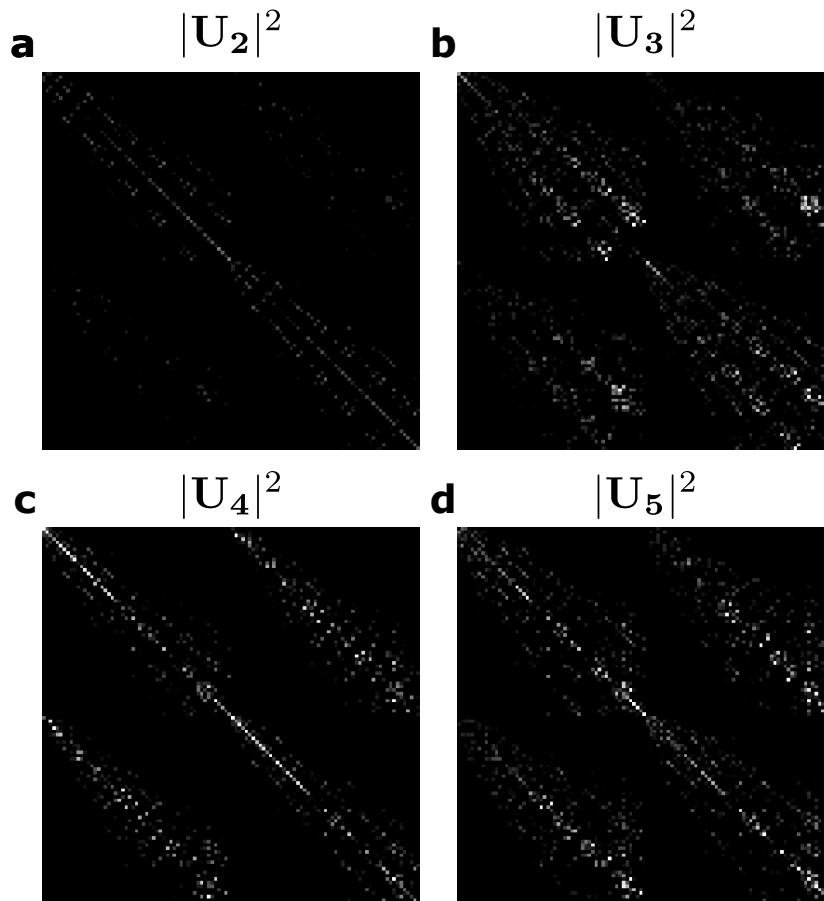


Figure IV.13: Representation of four singular components with both the input and output polarizations. Intensity of singular components \mathbf{U}_j , $j \in [2, 5]$, represented as 2d arrays for both polarizations in input and output.

Conclusion and perspectives

We presented how the reliable measurement of the mode basis TM allows observing the effect of a deformation on the TM. We showed how the TMs measured for low deformations allow building the deformation principal modes by computing the eigenmodes of the generalized Wigner-Smith operator. These modes are robust against strong deformations. Indeed, the corresponding fiber outputs almost all stay correlated over the whole range of deformations. They are found by only using the knowledge of the fiber properties for small deformations. This can be explained by the predominance in the transmission properties of the coupling between nearby modes, even for large deformations.

In our work, we studied the effect of a single type of local disorder. The framework we developed is general and is suited to study the effect of other kinds of disorders and perturbations that are common in telecommunications. Those may include splicing imperfections when connectorizing two fibers, bending, temperature fluctuations, vibrations or the effect of the natural disorder of the fiber affecting propagation after longer lengths. One can then characterize how they contribute to the mode coupling by studying the singular vectors of the global deformation operator as we did in section 3.2.b.

Chapter V

Using complex media and multimode fibers as reconfigurable linear operators.

Chapter contents:

1	Introduction.....	104
1.1	Context	104
1.2	Static designs	104
1.3	Programmable approaches	105
1.4	Complex medium approaches	106
2	Using complex media to perform linear optical computations	107
2.1	Objectives	107
2.2	Principle	108
2.3	Input and output projectors	108
2.4	Existence of solution with ideal modulation and theoretical limits	109
3	Experiment.....	110
3.1	Optical setups.....	110
3.2	Procedure.....	112
4	Results	117
4.1	Multimode fiber experiment	117
4.2	Scattering medium experiment	119
5	Discussion.....	120
5.1	Limits of our approximations	120
5.2	Scalability	121
5.3	Losses	121
5.4	Practical implementation	121
	Conclusion	122

1 Introduction

1.1 Context

In 1965, Intel’s co-founder Gordon Moore made the prediction that the number of transistors in an integrated circuit would double every two years. That prediction, the Moore’s law, has proven accurate during the past four decades¹. This exponential growth allowed the booming of the computing capacity of electronic devices. Reducing the size of the transistors allows integrating more of them while reducing the energy required to treat each information bit. However, heat becomes a problem when transistor density and clock speed get too large. Most of the energy is not consumed by the components performing operations but during communications and transfers across chips by Joule heating [Miller, 2017]. In Figure V.1, we show the main source of energy consumption in communications and computations inside a typical computer. As is highlighted in red, we observe two to five orders of magnitude between the switching of a transistor and the communication in the chip.

ENERGIES FOR COMMUNICATIONS AND COMPUTATIONS

Operation	Energy per bit	
Wireless data	10 – 30 μ J	
Internet: access	40 – 80nJ	
Internet: routing	20nJ	
Internet: optical WDM links	3nJ	
Reading DRAM	5pJ	
Communicating off chip	1 – 20 pJ	x100 to x10,000
Data link multiplexing and timing circuits	~ 2 pJ	
Communicating across chip	600 fJ	←
Floating point operation	100fJ	
Energy in DRAM cell	10fJ	
Switching CMOS gate	~50aJ – 3fJ	
1 electron at 1V, or	0.16aJ	
1 photon @1eV	(160zJ)	

Figure V.1: Main sources of energy consumption for communications and computations inside a typical computer. Adapted from [Miller, 2017]

Substituting photons for electrons is one promising way around these limitations. Nevertheless, electronic circuits are made of silicon which is a poor substrate for photonic devices [Hitz, 2009]. As a consequence, research in this domain aims at designing new devices to perform computations using light and implementing them into optical processing units.

1.2 Static designs

Similarly to how an electronic computing unit is composed of elementary elements designed to perform one specific operation, a photonic device is typically designed to perform one given operation [Borel et al., 2007; Jensen and Sigmund, 2011; Silva and Engheta, 2014; Shen et al., 2015; Piggott et al., 2017]. To illustrate this principle, we take the broader picture of electric field manipulation. In the example of

¹This law is often used for other domains of technology such as optical fiber telecommunications as was presented in Chapter I.

the work by [Silva and Engheta, 2014] in the microwave domain, the authors show how a multilayered metamaterial slab can be designed in order to exhibit a chosen transversal green's function $G(y)$, which traduces the operation that is performed on a signal encoded into an input beam. The authors developed a method to determine the optimal arrangement of materials and their properties to realize the target function as shown in Figure V.2.

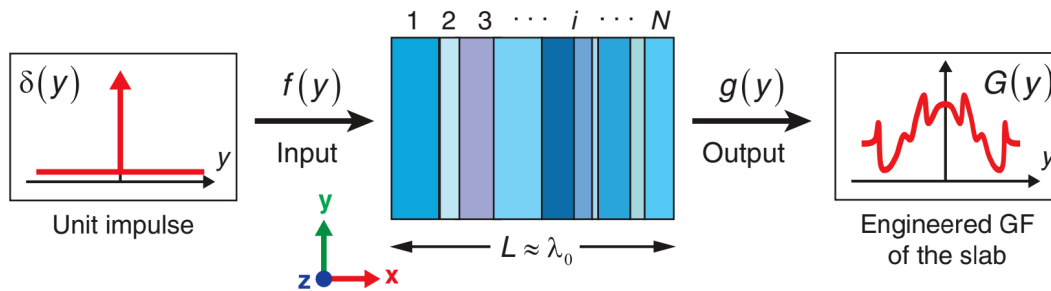


Figure V.2: A multilayer slab designed to perform a specific function G . Extracted from [Silva and Engheta, 2014]

In photonics, we take the example of the optimization method developed in [Jiao, Fan, and Miller, 2005] to design a mode demultiplexer using photonic crystals. The idea is to use a numerical algorithm to optimize the geometry of the photonic structure. The result of the optimization, shown in Figure V.3.b, provides a seemingly disordered structure that accurately performs the desired function. In these works, the conformation of the devices is directly linked to their intended functions. As a consequence, fabrication imperfections and changes of environmental conditions negatively impact their performance, limiting the range of operation of the device. Furthermore, such inverse-design approaches inherently prohibit reconfigurability.

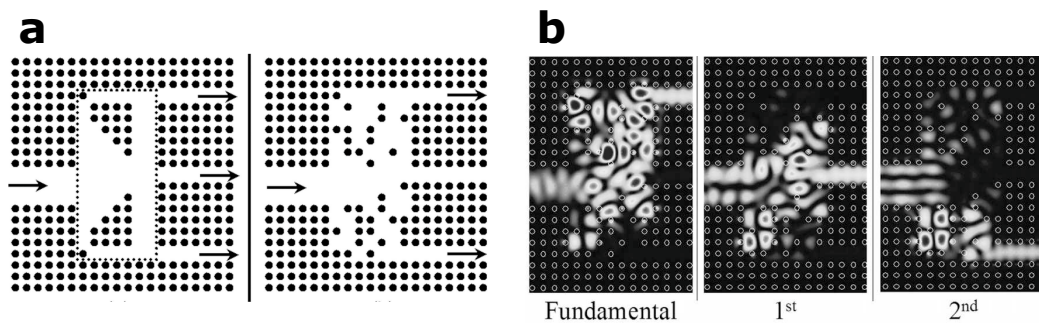


Figure V.3: Mode separator with photonic crystals **a**, Initial and optimized photonic crystal structure. **a**, Mode separator in action: the light carried by the modes of the incoming multimode waveguide is directed towards the corresponding output waveguides. Extracted from [Jiao, Fan, and Miller, 2005].

1.3 Programmable approaches

Trying to perform an optical linear operation means to figure out an optical system with a proper defined TM. One approach introduced conceptually for free space optics [Reck et al., 1994] consists in using a set of n^2 optical controllable partial reflectors and phase shifters [Miller, 2013a] as represented in Figure V.4. It was demonstrated that this structure theoretically allows performing any linear operation. Recent advances in silicon photonics enabled the implementation of the concept in integrated

designs [Miller, 2013b; Carolan et al., 2015; Ribeiro et al., 2016; Annoni et al., 2017; Shen et al., 2017a; Mennea et al., 2018]. These approaches allow the device to be configured quickly without optimization schemes, and to be robust to potential drifts as the device can be reconfigured on the fly.

Several experimental demonstrations of this approach have produced promising results. However, for a target operation described by a matrix of size $n \times n$, the number of elements to control in these architectures scales as n^2 , which limits the overall scalability of the approach. The authors successfully demonstrate a high fidelity, reprogrammable 6×6 optical circuit, using 30 thermo-optic phase shifters. A schematic of their implementation is shown in Figure V.4.b.

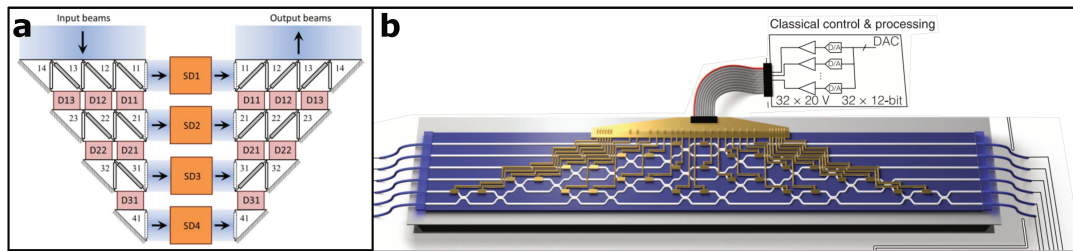


Figure V.4: Principle and implementation of coherent photonic circuits. **a**, Representation of the theoretical programmable linear photonic device. **b**, Implementation of the design on silicon photonics. Adapted from [Miller, 2013b] and [Carolan et al., 2015].

Alternatively, the idea of controlling the mode coupling inside a multimode waveguide to shape the output wavefront was demonstrated using silicon-on-insulator planar waveguides whose index profile can be tuned using femtosecond laser pulses [Bruck et al., 2016]. Another approach using multi-plane modulation was proposed [Morizur et al., 2010] and was at first successfully utilized for few mode manipulations [Labroille et al., 2014]. In this method, the field is successively modulated at different planes along the propagation. It is done using a reflection SLM placed in front of a mirror. The SLM can be reconfigured at will to allow changing the operation performed by the system. Recently, a device that supports 1035 Laguerre-Gaussian modes using 14 planes of modulation was demonstrated [Fontaine et al., 2020]. However, this system exhibits no reconfigurability because the phase modulation is achieved using static phase plates.

While small transformations may suffice for optical communications, the increasing complexity of the physical system may hinder the implementation of the high rank reconfigurable transformations required for optical analogue computation. There are currently few solutions for performing optical linear operations involving a high number of channels. Such objective is particularly attractive for the development of optical artificial neural networks [Shen et al., 2017b; Zuo et al., 2019], for which such operations are one of the main building blocks.

1.4 Complex medium approaches

Controlling wave propagation in complex media to perform linear transformations has been considered, using wavefront shaping to tune the response of the optical system. The literature contains reports on implementations of two-port beam-splitters in white paint and opaque materials [Huisman et al., 2014; Huisman et al., 2015], with applications to control quantum interferences in mind [Defienne et al., 2016; Wolterink et al., 2015], as well as on spatial mode sorting [Fickler and Boyd, 2016].

In particular, the possibility of implementing large reconfigurable linear transformations as required for optical neural networks has remained unexplored until recently.

Lately, the use of the large number of degrees of freedom provided by SLMs combined with the randomness of complex media was exploited to perform large scale random projections. These operations are interesting, for example for classification and reservoir computing [Dong et al., 2020; Saade et al., 2015]. Noticeably, LightOn, a recently born French company, has begun exploiting this principle to produce Optical Processing Units specialized in machine learning tasks².

Building on recent works that demonstrated wave-based analogue computation in a chaotic microwave cavity [Hougue and Lerosey, 2018], we explored during my thesis the possibility of performing complex-valued linear operations in optical complex media. This chapter details the principle and experiments we performed and published in [Matthès et al., 2019].

2 Using complex media to perform linear optical computations

2.1 Objectives

We want a system able to perform a given complex linear operation \mathbf{G} of size $m \times n$ on an input signal represented as a vector x

$$y = \mathbf{G}.x. \quad (\text{V.1})$$

We schematically represent the desired operation in Figure V.5. We want our sys-

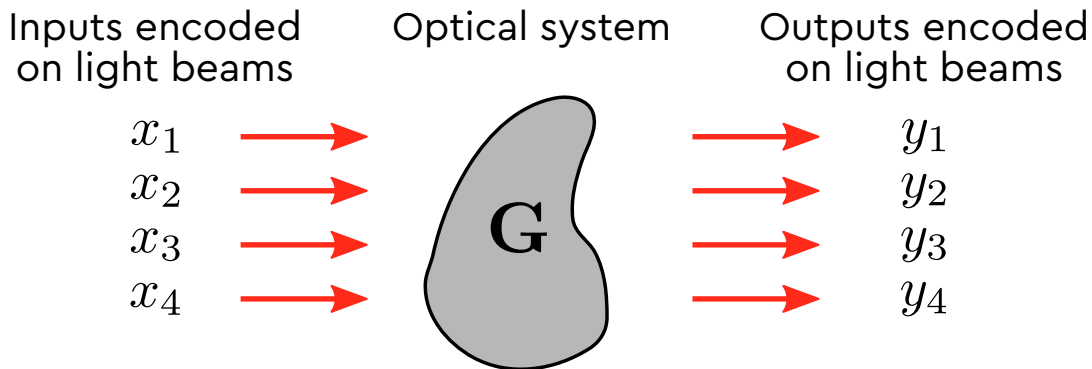


Figure V.5: Illustration of the desired system. An input vector x , encoded into n light beams, enters the optical system. The optical system can be represented by a TM \mathbf{G} . The output of the system is a vector $y = \mathbf{G}.x$, encoded into m light beams. Here, $n = m = 4$.

tem to meet the criteria for real-life implementation. These include reconfigurability in a short time, robustness to fabrication imperfections, low cost, and low stability requirements. To fulfil the latter point, we wish to avoid the use of interferometric measurements to retrieve the field at the fiber output.

DMDs, presented in Chapter II section 2.3, are tools of choice in this regard. Not only are they able to change state at speeds of tens of kHz, but the chips also cost very little as they are mass-produced to equip most video-projectors.

²The company LightOn born in 2015 is hosted in ESPCI Paris startup incubator PCUP.

2.2 Principle

Usually, in a random medium, only a small subset of the input and output modes are controlled and measured. In this case, the TM has the statistical properties of an ideal Gaussian random matrix [Goetschy and D. Stone, 2013; Popoff et al., 2014b]. If one controls N input modes and measures M output modes, \mathbf{H} is represented by a $M \times N$ matrix. Let's say we seek to create a system performing a linear operation represented by the matrix \mathbf{G} of size $m \times n$ with $m < M$ and $n < N$. Once the TM of the complex medium \mathbf{H} is measured, we want to identify adequate input and output projections so that the optical system acts on an input signal x , encoded in the incoming wavefront, as the operator \mathbf{G} following equation V.1. These projections are represented by $N \times n$ and $M \times m$ input and output matrices \mathbf{P}_{in} and \mathbf{P}_{out} , that satisfy:

$$\mathbf{G} = \mathbf{P}_{\text{out}}^\dagger \cdot \mathbf{H} \cdot \mathbf{P}_{\text{in}}. \quad (\text{V.2})$$

The goal of the following is to show how to find and physically generate those projectors to perform the linear operation \mathbf{G} on input signals using a disordered system represented by its matrix \mathbf{H} .

2.3 Input and output projectors

We limit ourselves to input projectors \mathbf{P}_{in} that can be created by modulating the optical field at a given input plane, i.e. using an SLM. We divide the SLM into n groups of N/n macropixels on which we control the amplitude and/or the phase of the optical field, as shown in Figure V.6 in the case of $n = 4$. The output projection \mathbf{P}_{out} is performed by measuring m speckle grains at the output plane³.

For illustration purposes, we take here $n = m = 4$. The corresponding projectors \mathbf{P}_{in} and \mathbf{P}_{out} have the following matrix representations:

$$\mathbf{P}_{\text{in}} = \begin{bmatrix} p_{1,1} & 0 & 0 & 0 \\ \vdots & \vdots & \vdots & \vdots \\ p_{N/4,1} & 0 & 0 & 0 \\ 0 & p_{1,2} & 0 & 0 \\ \vdots & \vdots & \vdots & \vdots \\ 0 & p_{N/4,2} & 0 & 0 \\ 0 & 0 & p_{1,3} & 0 \\ \vdots & \vdots & \vdots & \vdots \\ 0 & 0 & p_{N/4,3} & 0 \\ 0 & 0 & 0 & p_{1,4} \\ \vdots & \vdots & \vdots & \vdots \\ 0 & 0 & 0 & p_{N/4,4} \end{bmatrix}, \quad \mathbf{P}_{\text{out}} = \begin{bmatrix} 1 & 0 & 0 & 0 \\ 0 & 1 & 0 & 0 \\ 0 & 0 & 1 & 0 \\ 0 & 0 & 0 & 1 \\ 0 & 0 & 0 & 0 \\ \vdots & \vdots & \vdots & \vdots \\ 0 & 0 & 0 & 0 \end{bmatrix}, \quad (\text{V.3})$$

where $p_{k,l}$, for $(k,l) \in \llbracket 1, N/4 \rrbracket \otimes \llbracket 1, 4 \rrbracket$, represents the modulation on the k^{th} pixel of the l^{th} segments of the modulator. For the sake of simplicity, the output projection is done here by taking the first 4 elements of the output basis which corresponds to taking only the field on four speckle grains. We define the submatrix $\mathbf{H}_{\mathbf{k}\perp}$ of \mathbf{H} that links the field on each pixel of the k^{th} part of the SLM to the field on the m selected pixels of the camera. The schematic representation of the submatrix $\mathbf{H}_{\mathbf{k}\perp}$ is shown in Figure V.6. We will then focus our effort on finding the optimal input projection \mathbf{P}_{in}

³Directly taking the individual output speckle grains is the most straightforward method to construct the output projection. However, it could also be constructed by performing a linear combination of the field measured on different speckle grains.

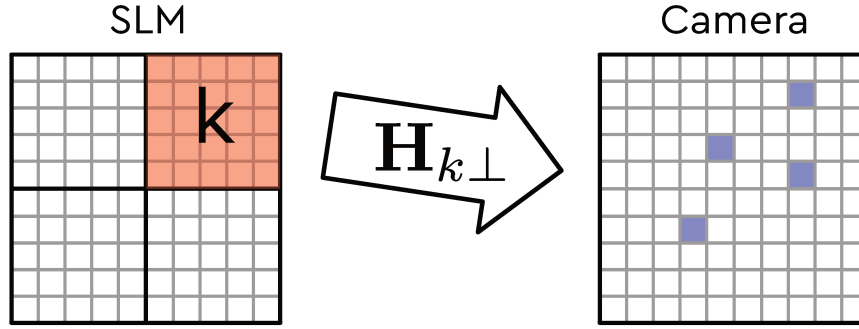


Figure V.6: Schematic representation the submatrix $\mathbf{H}_{k\perp}$. The submatrix $\mathbf{H}_{k\perp}$ links the k^{th} group of pixels of the SLM (represented in red), to the m selected pixels of the camera (represented in blue).

2.4 Existence of solution with ideal modulation and theoretical limits

We assume the ideal case of \mathbf{H} being a Gaussian random matrix measured with negligible noise and the spatial modulation scheme being able to control with a high fidelity the amplitude and the phase of the field. The Gaussian matrix approximation is known to be valid when one controls and measures a fraction of the total number of modes [Goetschy and D. Stone, 2013]. Satisfying the equality of equation V.2 requires that the coefficients of the projector \mathbf{P}_{in} corresponding to the k^{th} subdivision of the SLM satisfy a system of m linear equations corresponding to the matrix equation:

$$\mathbf{H}_{k\perp} \cdot \begin{bmatrix} p_{1,k} \\ p_{2,k} \\ \vdots \\ p_{N/n,k} \end{bmatrix} = G_k \quad \text{for } k \in [1, n], \quad (\text{V.4})$$

G_k is the k^{th} column of the target matrix \mathbf{G} . We are interested in the particular solution:

$$\begin{bmatrix} \hat{p}_{1,k} \\ \hat{p}_{2,k} \\ \vdots \\ \hat{p}_{N/n,k} \end{bmatrix} = \mathbf{H}_{k\perp}^+ \cdot G_k, \quad (\text{V.5})$$

with $\hat{p}_{i,k}$ the estimated coefficients of the input projector, $\mathbf{H}_{k\perp}^+$ the Moore-Penrose inverse (pseudo-inverse) of $\mathbf{H}_{k\perp}$. Such a solution exists if $\mathbf{H}_{k\perp}$ has linearly independent rows, which makes $\mathbf{H}_{k\perp}^+$ a left inverse for $\mathbf{H}_{k\perp}$:

$$\mathbf{H}_{k\perp}^+ \cdot \mathbf{H}_{k\perp} = \mathbf{1}. \quad (\text{V.6})$$

Because $\mathbf{H}_{k\perp}$ is a Gaussian random matrix with independent identically distributed elements, it can be eigendecomposed and its singular value distribution follows the Marceko-Pastur law [Marcenko and Pastur, 1967]. It shows that the probability of having a zero singular value vanishes when the number of columns is larger than the number of rows, i.e for $N/n > m$. It ensures that equation V.6 is verified, and that $\mathbf{H}_{k\perp}^+ \cdot G_k$ is a solution of equation V.4. If one can independently control the amplitude and the phase of the optical field, the complex mask corresponding to equation (V.5) can be implemented. This procedure can be done for each value of k , i.e. for each subdivision of the SLM. It amounts to solving n independent systems of equations described by equation V.4.

If a full modulation of the complex field is possible, controlling $M = n \times m$ independent channels of the complex system, i.e. independent SLM pixels, allows to

correctly simulate the target matrix \mathbf{G} . While other types of media may allow equation V.2 to be satisfied, the random nature of complex media ensures the existence of a trivial solution regardless of the complexity of the target operator \mathbf{G} .

Note that no hypothesis has been made on the operator \mathbf{G} . It demonstrates the universality of the approach to perform any linear transformation. Experimentally, the passive modulation of the SLM imposes $|p_{k,l}| < 1 \quad \forall (k,l) \in \llbracket 1, N/n \rrbracket \times \llbracket 1, n \rrbracket$. It limits the applications to operators with transmission values below unity. However, for any operator \mathbf{G} of maximum singular value s_0 , the experimental system we present can simulate the transformation corresponding to the operator $\mathbf{G}' = \alpha \mathbf{G}$ with $\alpha \leq 1/s_0$, chosen so that the largest transmission value of \mathbf{G}' is smaller than 1.

3 Experiment

We saw in the previous section that a solution can be found when the TM of the system is a random Gaussian matrix. Complex media typically show this type of behavior [Popoff et al., 2010a; Sebbah, 2001]. To illustrate the versatility of our approach, we test two different complex media, namely a ground glass diffuser, also referred to as a scattering medium in the following, and an MMF with random mode coupling, and show that we can use them as optical processing units. We present here the two experimental setups used.

3.1 Optical setups

3.1.a Multimode fiber experiments

For the MMF experiment, we use a 1 meter-long segment of a step index fiber of numerical aperture $NA = 0.22$ with a core radius of $a = 52.5 \mu\text{m}$ supporting approximately 1000 guided modes⁴.

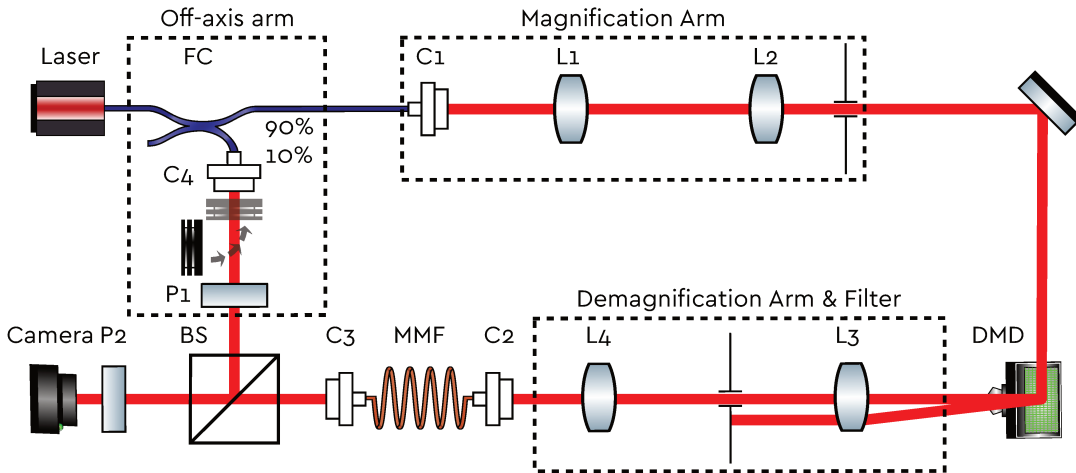


Figure V.7: Schematic representation of the MMF setup. An expanded laser beam is modulated after reflection off a DMD and injected into an MMF. One polarization of the output light is recorded by a camera. A reference arm is used only to measure the complex optical field for the final estimation of the fidelity. FC: fiber coupler, C_i (with $i \in [1..4]$): fiber collimator, L_i (with $i \in [1..4]$): planoconvex lens, BS: beam splitter, P1 and P2: polarizers.

⁴Thorlabs M43L01. The fiber is sold within a protective jacket and is already connectorized.

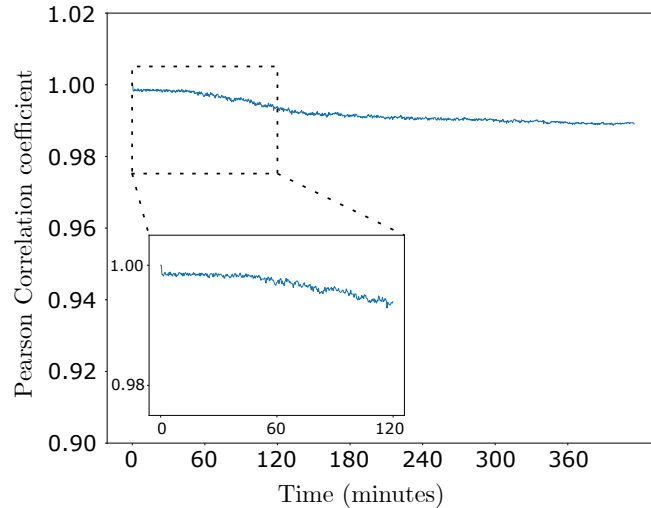


Figure V.8: Stability of the MMF experiment. Pearson coefficient over time between a reference speckle intensity measured at $t = 0$ and a speckle measured after a time t at the output of the MMF, both for the same input wavefront.

We use the same light source as in the experiments presented in chapters III and IV; a 1.55 μm telecom narrow-band laser⁵. We use a DMD⁶ of 1920 by 1200 pixels with a maximum framerate of 16 kHz for the modulation. We divide the DMD into $N = 1568$ macropixels. The horizontal output polarization intensity pattern is recorded onto a fast InGaAs camera of maximum framerate of 100 kHz⁷. The fiber is compressed at four different locations to ensure strong mode coupling [Xiong et al., 2017a].

We measure the stability of the experiment by sending a specific pattern into the fiber and observing the decorrelation of the output intensity over time. We measure the Pearson correlation coefficient between the reference speckle at $t = 0$ and the speckle recorded at a time t . The results are shown in Figure V.8. We note that the experiment stays stable for more than two hours (the correlation remains higher than 99%).

3.1.b Scattering medium experiment

The scattering medium experiment uses a simpler version of the setup which is shown in Figure V.9. We use a ground glass diffuser⁸ with a 632.8 nm laser source⁹ modulated by a DMD¹⁰ of resolution 2560 by 1600 pixels and maximum framerate 13 kHz. We divide the DMD into $N = 2304$ macropixels. The outputs are recorded on a CCD camera¹¹ of resolution 2336×1752 pixels of framerate 29.3 Hz at full resolution. The stability of the scattering medium experiment is shown in Figure V.10. Even if the system is slightly less stable than in the MMF experiment, the output speckle pattern of the system stays correlated for more than two hours.

⁵Teraxion PS-NLL.

⁶Vialux V-9601

⁷Xenics Cheetah 640CL, 640 by 512 pixels. A 100 kHz framerate can be achieved by reducing the resolution of the camera down to 32×4 pixels.

⁸Thorlabs DG20-1500.

⁹JDSU 1137/P.

¹⁰Vialux V-9001

¹¹Allied Vision Prosilica GT2300.

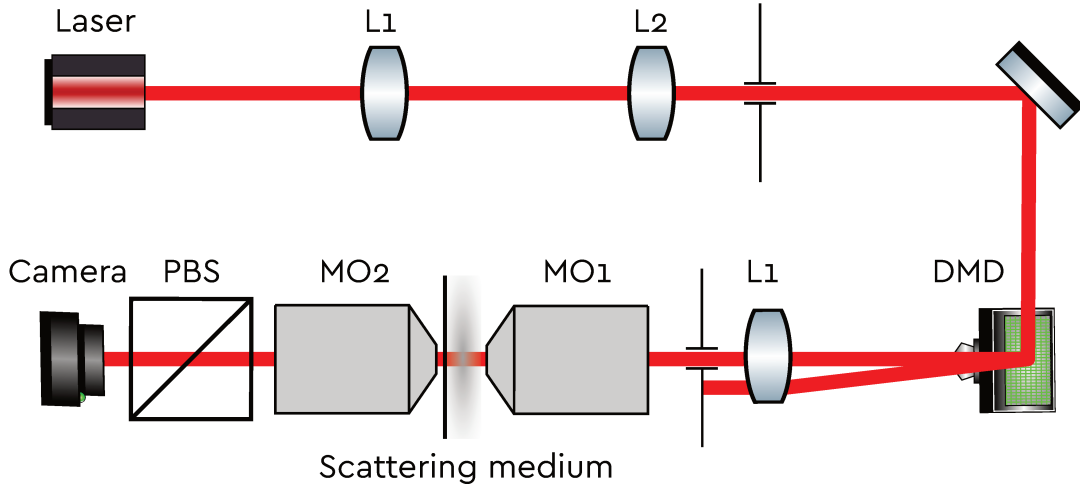


Figure V.9: Schematic representation of the scattering medium setup. A free space polarized laser beam is expanded and is modulated after reflection off a DMD and is injected into a scattering medium. One polarization of the output light is recorded by a digital camera. L1: planoconvex lens, MO1 and MO2: microscope objectives, PBS: polarizing beam splitter.

3.2 Procedure

A first calibration step consists in learning the TM of the complex propagation medium. The second step consists in numerically finding the optimal projectors \mathbf{P}_{in} and \mathbf{P}_{out} that best satisfy equation (V.2) for a given operator \mathbf{G} , knowing the TM \mathbf{H} . Finally, by displaying the corresponding masks onto the SLM and measuring the output field, the system acts as the target operator \mathbf{G} on the incident field.

3.2.a Calibration

We first estimate the TM \mathbf{H} of the system. To remove the need for interferometric measurements, which requires high mechanical stability, therefore limiting the versatility of the approach, and to mitigate the effect of measurement errors, we use a phase retrieval algorithm. It allows recovering the full TM from intensity-only measurements [Dremeau et al., 2015; Metzler et al., 2017] as already evoked in Chapter II, section 3.2. These algorithms use statistical learning to reconstruct the phase information that was lost in the non-linear process of recording only the intensity. We divide the pixel array of the DMD into N macropixels. We then send a learning set of $7N$ random binary vectors x (entries have zero or unity amplitude). The stack of input vectors x is expressed as a matrix \mathbf{X} of size $N \times 7N$. We then measure on the camera the corresponding output intensity patterns. These patterns are projected onto an output basis of macropixels of size corresponding to a speckle grain, we thus measure $|\mathbf{Y}|^2 = |\mathbf{H}\mathbf{X}|^2$. The inputs \mathbf{X} and the absolute value of the obtained data $|\mathbf{Y}|$ are sent into the phase retrieval algorithm prVAMP [Metzler et al., 2017]. The results are further refined using a gradient descent optimization to better account for the non-linearity of the camera response¹². We estimate matrices $\hat{\mathbf{H}}$ of size 100×1568 for the MMF experiment and 100×2304 for the scattering medium one.

¹²It is possible to perform the phase retrieval using a gradient descent, however, this method is not efficient in regard to the computation time compared to the dedicated prVAMP algorithm. We also remark that the gradient descent had no incidence on the result of the MMF experiment because the InGaAs camera was manually calibrated. We therefore use it only for the scattering medium experiment.

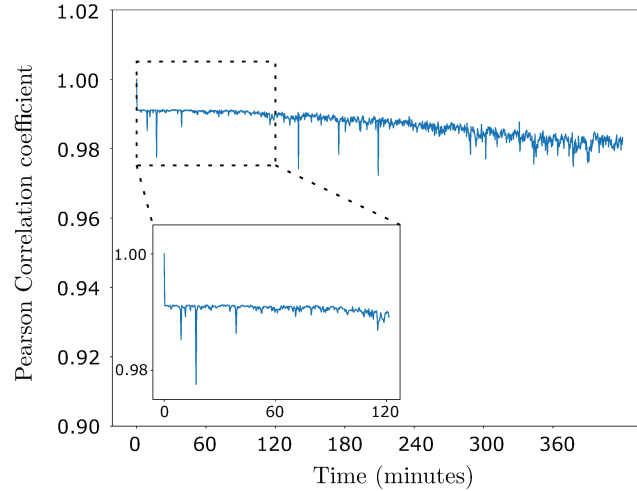


Figure V.10: Stability of the scattering medium experiment. Pearson coefficient over time between a reference speckle intensity measured at $t = 0$ and a speckle measured after a time t at the output of the scattering medium, both for the same input wavefront.

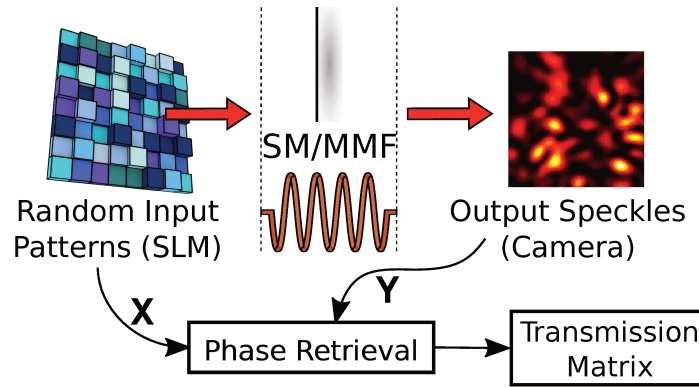


Figure V.11: Step 1: Calibration of the system. Acquisition of the complex TM by measuring a set of input patterns and output intensity speckles and using a phase retrieval algorithm.

The computation is accelerated through parallelization with a graphical processing unit (GPU)¹³ and is completed in under two minutes. Using a GPU allows us to divide the processing time by a factor of 20 to 40 compared to the same calculations done with the central processing unit only.

We evaluate the quality of the reconstructed TM using a number p_{test} of test input wavefronts \mathbf{X}^{test} that have not been used for the learning procedure. To do so, we record the corresponding intensity patterns $|\mathbf{Y}^{test}|^2$ and compare them to the simulated intensity patterns $|\mathbf{Y}^{simu}|^2 = |\hat{\mathbf{H}} \cdot \mathbf{X}^{test}|^2$ from the estimated TM. To quantify the similarity, we compute the normalized root-mean-square error (RMSE) on the absolute value of the signals, for each output point $i \in [1, 100]$ according to the formula:

$$\epsilon_i = \frac{\sum_{j=1}^{p_{test}} \left| |Y_{ij}^{test}| - |Y_{ij}^{simu}| \right|^2}{\sum_{j=1}^{p_{test}} |Y_{ij}^{test}|^2}, \quad i \in [1, 100]. \quad (\text{V.7})$$

We obtain the following errors for both experiments:

¹³NVIDIA GTX 1050 Ti

- We measure an average error of 7%, with a standard deviation of 6% and a median value of 5% for the MMF experiment. No improvement is achieved using the gradient descent optimization.
- We measure an average error of 15.7%, with a standard deviation of 7.9% and a median value of 14.4% for the scattering medium experiment. This value is improved to an average error of 11.6%, with a standard deviation of 7.3% and a median value of 7.9% when performing an additional gradient descent optimization after the phase retrieval.

However, we presented in Chapter III and in appendix F how computing the error this way can give values that underestimate the quality of the measured TM, due to the noise of the camera.

3.2.b Calculation of the projections

The output projection \mathbf{P}_{out} is performed by selecting m output speckle grains. The optical fields in these areas correspond to the outputs of our operator. We choose the output points that give the lowest reconstruction error during the calibration step. We then obtain the output projection as represented in equation V.3, where rows are ordered from the lowest to the highest error. Performing the output projection amounts to selecting the corresponding rows of the TM.

We demonstrate that for a full amplitude and phase modulation, the input masks corresponding to the optimal input projectors \mathbf{P}_{in} can readily be calculated from the TM using the relation V.5. Using binary amplitude modulators, we achieve a few-level modulation of the optical phase using Lee holograms as shown in Chapter III, section 1.1.b. This means that we cannot directly generate the amplitude and phase for any value of the optical field. With the setup parameters we use, we can obtain 2 levels of phase (0 and π) giving 3 total levels $\{-1, 0, 1\}$. The modulated beam is then projected onto the complex medium. Identifying an input mask on the DMD that approximates the equality in equation V.2 for a given target matrix \mathbf{G} is an ill-posed problem since we do not have full control over the complex wavefront.

Numerically, we try to find the projector \mathbf{P}_{in} that satisfies:

$$\mathbf{P}_{\text{in}} = \underset{\mathbf{P}}{\operatorname{argmin}} \left\| \mathbf{P}_{\text{out}}^\dagger \cdot \mathbf{H} \cdot \mathbf{P} - \mathbf{G} \right\|_2, \quad (\text{V.8})$$

where $\|\cdot\|_2$ is the quadratic norm¹⁴. In practice, we try to solve the n sub-problems defined in equation V.4. We use a multiplicative constant γ to tune the average value of the expected signals. The final problem consists in solving the n sub-problems:

$$\mathbf{P}_{\text{in},k} = \underset{\mathbf{P}_{k,\gamma}}{\operatorname{argmin}} \left\| \mathbf{P}_{\text{out}}^\dagger \cdot \mathbf{H} \cdot \mathbf{P}_k / \gamma - \mathbf{G}_k \right\|_2, \quad k \in [1, n]. \quad (\text{V.9})$$

It amounts to minimizing a least-square cost function to perform a linear regression, which is a convex problem. We can thus use convex optimization algorithms. We use CVXPY, a convex optimization framework for Python [Diamond and Boyd, 2016] which allows us to express in simple terms the problem and to add the discrete value constraint to the elements of \mathbf{P}_{in} . Gurobi [Gurobi Optimization, 2018] is the backend solver we use for CVXPY as it allows the resolution of mixed integer problems, e.g. finding a solution with discrete values. The value of γ is set to have the mean output

¹⁴Sometimes referred to as the Froebenius norm

of the operator to match the mean intensity of the speckle grains at a given camera exposure time. This choice empirically gives the best experimental results.

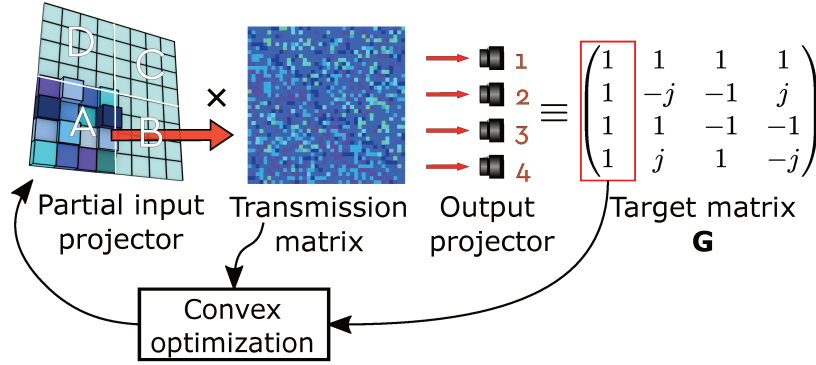


Figure V.12: Step 2: Calculation of the optimal input projection. For a DFT operation of size 4 ($n = m = 4$ and $\mathbf{G} = \text{DFT}_4$), we illustrate the procedure by showing how to find one subpart of the input mask. The computation is done independently for each subpart of the SLM, using a convex optimization solver and using the TM and the corresponding column of the target matrix \mathbf{G} as inputs.

We estimate the quality of this step by computing the fidelity F_c , defined in Chapter V by equation IV.3, between the desired operator \mathbf{G} and the operator $\tilde{\mathbf{G}}_{\text{num}} = \mathbf{P}_{\text{out}}^\dagger \cdot \mathbf{H} \cdot \mathbf{P}_{\text{in}}$ obtained after applying numerically the computed projectors \mathbf{P}_{in} and \mathbf{P}_{out} to the TM \mathbf{H} . We consistently measured $F_c(\mathbf{G}, \tilde{\mathbf{G}}_{\text{num}}) > 0.99$, demonstrating the efficiency of the numerical optimization. The computation of the input projector \mathbf{P}_{in} takes less than 20 minutes for 16×16 operators and under 5 minutes for 8×8 operators on a computer with an Intel i7-7700 CPU with 32GB of RAM, equipped with an Nvidia GTX 1050Ti GPU¹⁵ and running on Windows 10.

3.2.c Optical analogue computation

Once the appropriate input mask, corresponding to the input projector \mathbf{P}_{in} , is calculated and displayed on the DMD, the system is ready to act like the desired linear operator \mathbf{G} .

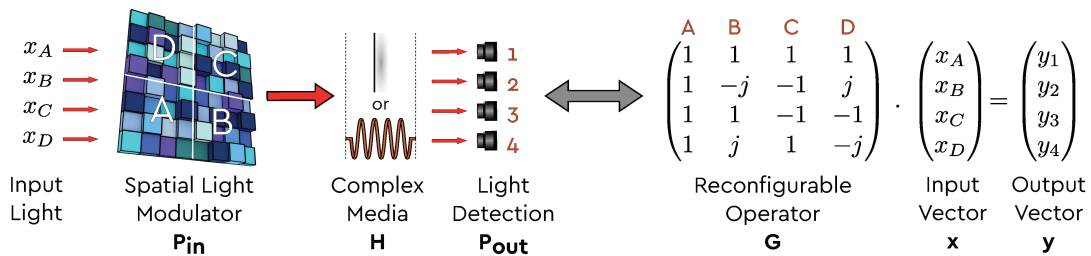


Figure V.13: Step 3: Analogue computation. The proposed optical processing unit is composed of an SLM and a complex medium. The SLM and the output detection take the role of the projectors \mathbf{P}_{in} and \mathbf{P}_{out} , converting the given TM \mathbf{H} of the complex medium into a desired linear transformation \mathbf{G} (see equation V.2).

In an ideal implementation, the input information is encoded into the optical field values impinging on the different segments of the DMD as shown in Figure V.14.a. This approach is compatible with an integration into a larger optical processing unit. In potential applications, it is possible to collect the output field to carry it to the next

¹⁵The GPU is not used to find the projectors.

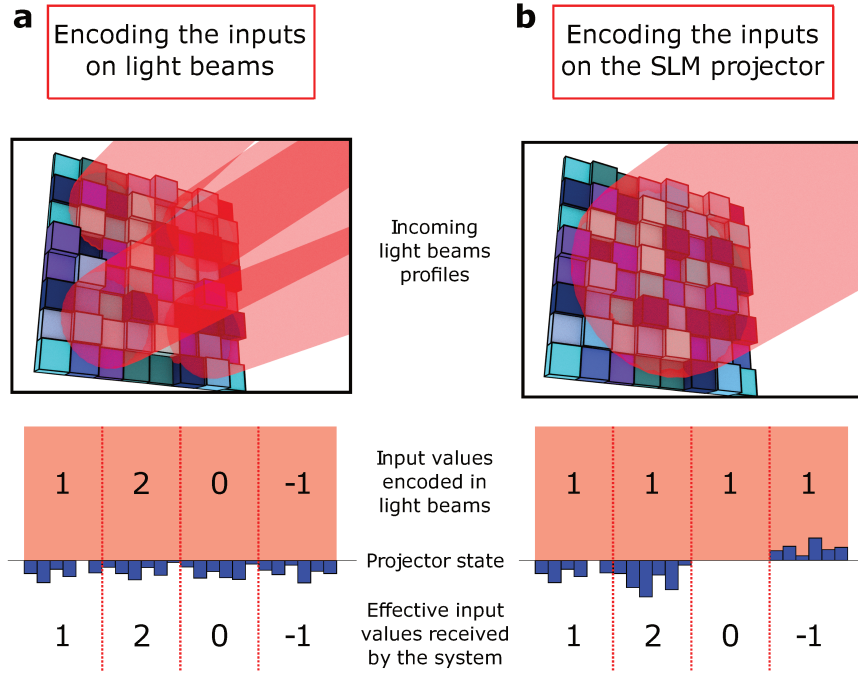


Figure V.14: Comparison of the two presented methods to encode input vectors in the case of a 4×4 operator. **a**, The input vector is represented by the optical field of 4 light beams previously modulated to carry the signal information. The input projector obtained in the optimization procedure is then applied to the whole incoming field. **b**, A single plane wave illuminates the SLM. The input vector is built by modulating each sub-part of the projector according to the respective input vector value. The actual mask displayed on the SLM thus changes for each different input vector.

optical processing unit instead of measuring it and therefore converting it to electric signals.

To limit the complexity of the experimental setup, input vectors are directly encoded using the DMD. To do so, each subpart of the input projection is modulated by the value of the corresponding component of the incoming input vector x as shown in Figure V.14.b. This allows us to work with a single incoming light beam. However, as the DMD allows for a limited number of modulation states per macropixels, we are then limited to only a few input levels. Using this method, equation V.2 is rewritten as:

$$\begin{aligned}
 y &= \mathbf{G} \cdot x \\
 &= \mathbf{P}_{\text{out}}^T \cdot \mathbf{H} \cdot \mathbf{P}_{\text{in}} \cdot x \\
 &= \mathbf{P}_{\text{out}}^T \cdot \mathbf{H} \cdot \mathbf{P}_{\text{in}} \cdot \mathbf{diag}(x) \cdot e \\
 &= \mathbf{P}_{\text{out}}^T \cdot \mathbf{H} \cdot \tilde{\mathbf{P}}_{\text{in}}(x) \cdot e
 \end{aligned} \tag{V.10}$$

where $\mathbf{diag}(x)$ is a square matrix, its diagonal elements are equal to x and the off-diagonal equal to 0. $e = (1)_n$ a n -size vector of elements all equal to 1, representing the plane wave and $\tilde{\mathbf{P}}_{\text{in}}(x) = \mathbf{P}_{\text{in}} \cdot \mathbf{diag}(x)$ is the actual mask displayed on the DMD for each individual input vector x . In essence, instead of encoding the vector x in the input wavefront, it is directly encoded in the projector $\tilde{\mathbf{P}}_{\text{in}}(x)$ and the system is always excited by a plane wave, represented by the vector e . Using this method, we can express any input vector x as long as its values are within the amplitude depth of our modulation scheme.

4 Results

We illustrate the reconfigurability of the presented scheme by experimentally implementing two linear transformations very common in computer and physical science, namely the discrete Fourier transform and the Hadamard matrix. They are represented by the matrices \mathbf{DFT}_n and \mathbf{Ha}_n respectively. Their general expressions read:

$$\mathbf{DFT}_n = \frac{1}{n} \left[\omega_n^{jk} \right]_{j,k=0..n-1} \quad \text{with } \omega_n = e^{-2\pi i/n}, \quad (\text{V.11})$$

and

$$\mathbf{Ha}_{n^2} = \frac{1}{\sqrt{n}} \begin{bmatrix} \mathbf{Ha}_{(n-1)^2} & \mathbf{Ha}_{(n-1)^2} \\ \mathbf{Ha}_{(n-1)^2} & -\mathbf{Ha}_{(n-1)^2} \end{bmatrix} \quad \text{with } \mathbf{Ha}_1 = [1], \quad (\text{V.12})$$

with n the size of the operator. We experimentally perform all optical operations according to the presented principle. A high number of input signals is prepared and sent to the setup for computation. The inputs are random vectors with values taken in $\{-1, 0, 1\}$, which is the modulation range of our system.

4.1 Multimode fiber experiment

We show in Figure V.15 the inputs and outputs of the MMF experiment, configured to perform a discrete Fourier transform of size 16, in single shot realizations (Figure V.15.b), and averaged 10 times (Figure V.15.c). The quality of our results is assessed by the Pearson correlation coefficient C between the absolute values of the experimental and the ideal output vectors. The results show good agreement, as emphasized by the correlation coefficients exhibiting average values over 90% for these realizations.

In order to also assess the phase quality, we carry out off-axis holographic measurements as was presented previously in chapter III, section 1.3. Note that the reference arm was not part of the procedure of implementing the linear operator, it is solely used to monitor the effective complex-valued operator $\hat{\mathbf{G}}$ afterwards. Moreover, when recording the output values, a single image allows measuring the complex value output of the operator. Therefore, interferometric stability over times longer than the integration time of the camera is not required. We quantify the quality of the operation by estimating the operator's fidelity F_c between the ideal operator and the effective one. To characterize the effective operation $\hat{\mathbf{G}}$ performed by our experimental system, we sequentially send vectors from an input basis and measure the corresponding outputs fields. We sequentially send each element of the canonical basis for the input x .

In Figure V.16, we show the real and imaginary parts of the estimated experimental operators $\hat{\mathbf{G}}$ after normalization, and of the target operator \mathbf{G} , both for the Hadamard transform (a) and the discrete Fourier transform (b) of size 16×16 . The results presented are obtained without averaging

A summary of the measured quality estimators for the MMF experiment is presented in table V.1 with and without averaging for operator sizes of $n = m = 8$ and $n = m = 16$. A good agreement between the experimental data and the ideal operations outputs is observed for the different sizes tested, even without averaging. It demonstrates the possibility of performing *one shot* operations through an MMF. When we perform single shot transformations, the outputs are perturbed by the noise of the camera. The fidelity of the actual optical computation is higher, as

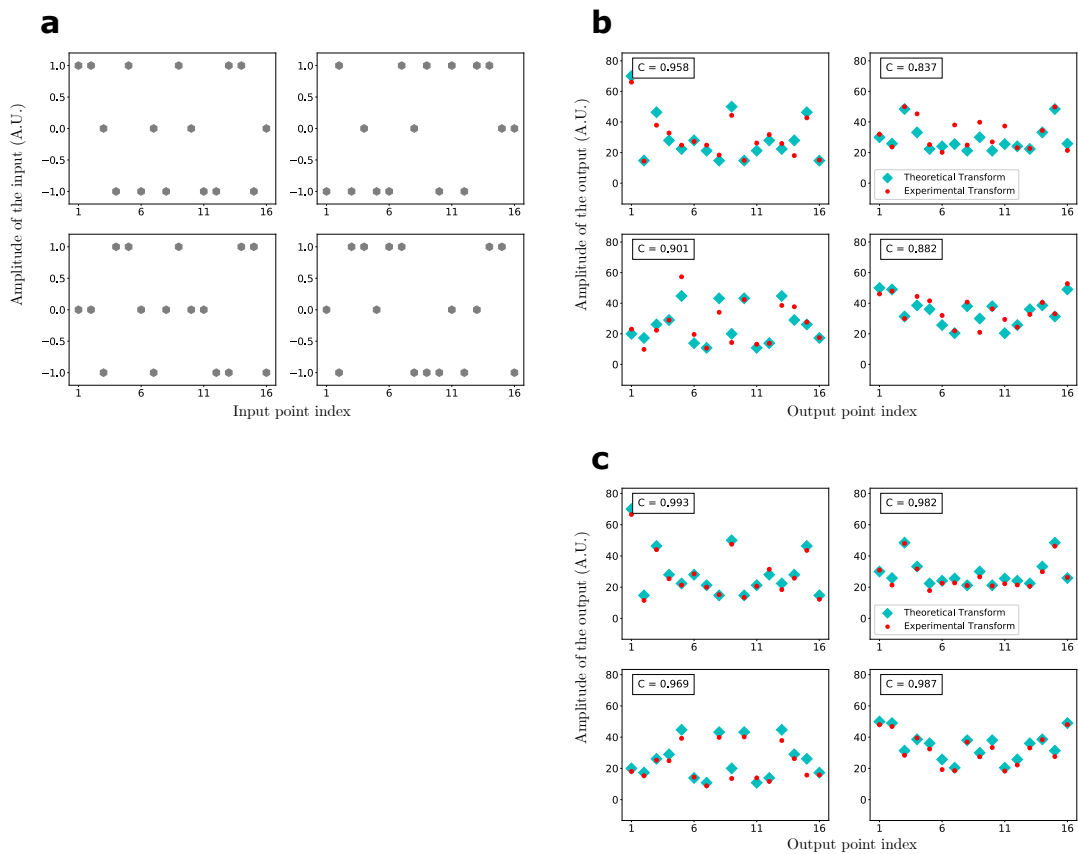


Figure V.15: Outputs of the MMF experiment for $G = \text{DFT}_{16}$. **a**, Random input vectors drawn from $\{-1, 0, 1\}$. **b**, Absolute values $|y|$ of the recorded output vectors in a single shot. **c**, Average over 10 realizations of the absolute values of the recorded output vectors. We give the correlation between the experimental and expected results in the top left inserts of each graph.

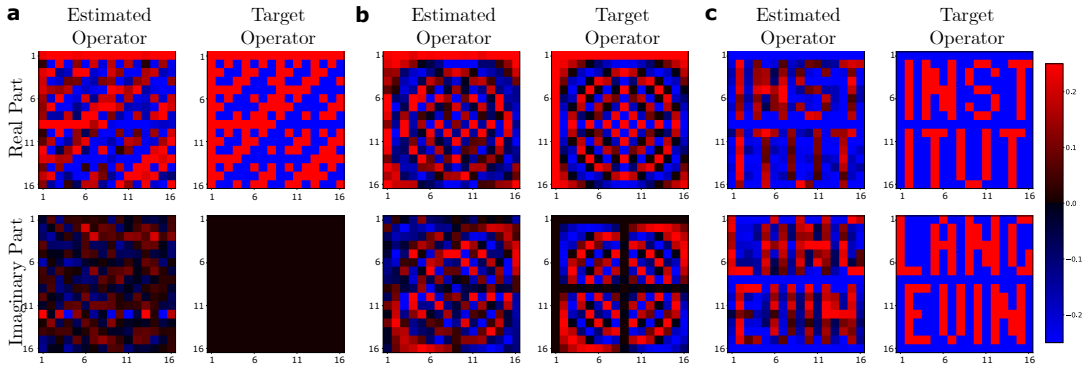


Figure V.16: Comparison of experimental and target operators. **a**, Hadamard transform \mathbf{H}_{16} , measured fidelity: $F_c = 0.785$. **b**, Discrete Fourier transform \mathbf{DFT}_{16} , measured fidelity: $F_c = 0.818$. **c**, Operator with no physical meaning representing the name of our host institution.

Size	Averaging	C	F_c
$n = m = 8$	1	0.977 ± 0.009	0.973 ± 0.014
$n = m = 8$	10	> 0.99	0.996
$n = m = 16$	1	0.912 ± 0.027	0.792 ± 0.027
$n = m = 16$	10	> 0.99	0.968

Table V.1: Summary of the efficiency results for the MMF experiment. C stands for the correlation between the absolute value of the experimental and expected signals, F_c stands for the experimental fidelity between the effective experimental operators and the target ones. The values are averaged over the Hadamard and the discrete Fourier transforms.

shown by the measurement of a fidelity of $F_c = 0.968$ when averaging over 10 estimations of the \mathbf{DFT}_{16} matrix.

To further illustrate the possibility to create any desired operator, we show in figure V.16.c an experimental implementation of a matrix with no physical meaning, displaying the name of our host institution by encoding information independently in the real and imaginary part of the matrix \mathbf{G} .

4.2 Scattering medium experiment

The ground glass diffuser experiment is more prone to errors in the operator reconstruction, we therefore only present results for operators of size 8. In Figure V.17 we show the raw amplitude of 4 different outputs for the \mathbf{DFT}_8 operator. We measure $C = 0.948 \pm 0.018$ on average over a wide range of outputs of the operator. We estimate that the sources of the errors are the lower laser stability and the non-linear response of the CCD camera pixels. By comparing the obtained correlation values of the results with the ones obtained in the MMF experiments, we can argue that the results are qualitatively similar but more noisy. It demonstrates the capacity of the approach to work with relatively cheap and off-the-shelf equipments, namely a HeNe laser and a standard CCD camera.

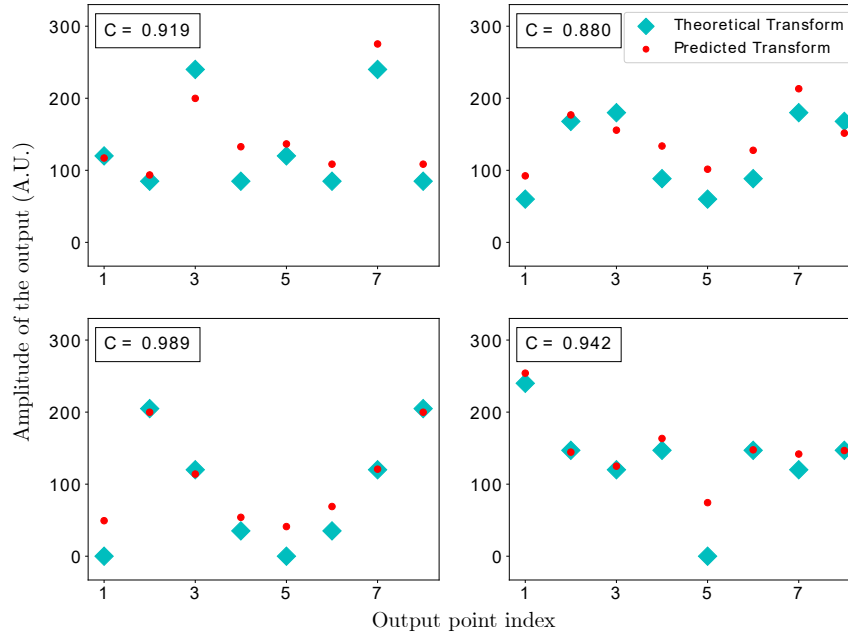


Figure V.17: Response of an operator built with a scattering medium. Amplitude of the output vectors corresponding to four different random inputs for operator $\mathbf{G} = \text{DFT}_8$, obtained using a ground glass diffuser as a complex medium. Cyan diamonds correspond to the theoretical outputs and red dots to the experimental data. Inserts in the top left corners give the correlation between the experimental and the expected results.

5 Discussion

5.1 Limits of our approximations

We demonstrated the possibility of using cheap and common media as optical processing units to perform linear operations using wavefront shaping. The attractiveness of such an approach is linked to its ability to be scaled up for larger operations. While we report the implementations of operators of size 16, much larger operations can be performed, provided an increased control over the input field and a reduced noise level. Noticeably, equation V.5 was only satisfied approximately because of the limited modulation scheme that allows for only three values of the complex field. The search for such approximation requires computation efforts. Moreover, we used a number of input macropixels that far exceeds the theoretical scaling of the system, that would ideally only require $16^2 = 256$ independent input pixels (we used 1568 in experiment). Once again, this is due to the discrete input modulation that does not allow the direct implementation of the theoretical ideal solution presented in section 2.4.

While averaging over realizations mitigates the error, a single shot operation is usually wanted. For an ideal amplitude and phase modulation, equation V.5 can be satisfied exactly with a simple matrix pseudo-inversion. A complete independent amplitude and phase modulation can be obtained using a couple of liquid crystal spatial light modulators encoding the phase and the amplitude respectively, for example. Another approach is, after characterization of the medium, to print phase plates to fix the input mask. While limiting the reconfigurability of the system, it reduces the final cost of the processing unit. It is to be noted that contrary to multi-plane approaches like the ones presented in section 1.3, the SLM performs only a

single modulation of the incoming fields. In this case, the complex medium is crucial to mix the spatial information.

5.2 Scalability

As we demonstrated in section 2.4, for a square target matrix \mathbf{G} , the largest size for which one can find a solution for a fixed number M of controlled modes is $n = m = \sqrt{M}$. We have a quadratic power law between the number of controlled optical channels N and the size $n = m$ of the operation. The scalability is the same as in the designs using a cascade of beam splitters presented in section 1.3. However, our method provides more room for maneuver. Indeed, in the beam-splitter approach, increasing the size of the operator requires increasing the number of beam-splitters, phase shifters and the complexity of the required electronics. Our scheme uses modulators (SLMs) that are typically composed of millions of independent pixels. Thus, while the scaling is the same, reaching higher operator sizes is easier in the approach we present. Using an MMF as a complex medium, the limiting factor is the number of modes supported by the fiber; for a typical large core step index fiber (550 μm diameter core, $\text{NA} = 0.22$), $M \approx 30,000$ at $\lambda = 1.55 \mu\text{m}$, corresponding to maximal operator dimensions $n = m \approx 170$. In contrast, in scattering media such as glass diffusers, the number of degrees of freedom available given by the number of propagating modes is quasi unlimited. Thus, the number of independently controlled modes is limited by the number of pixels on the modulator, typically of the order of one million. Note that this remains true in the multiple scattering regime as long as the number of transmission channels is large compared to the number of input pixels. Hence, this would allow creating linear operators of size $n = m \approx 1000$. These operator sizes match the order of magnitude of the size needed for optical neural networks.

5.3 Losses

It is important to note that our approach, due to intrinsic losses and the absence of gain in the system, can perform any linear operation only up to a constant multiplier as explained in section 2.4. In particular, it cannot perform operations with above unity singular values. However, using disordered gain media, it may be possible to overcome this limitation. Such a restriction can be detrimental to quantum optics applications where losses can modify the optical state of light. Our apparatus based on DMDs cause more than 50% of the light to be lost upon modulation. However, using a phase only SLMs based on deformable mirrors or a phase plate together with a careful injection into an MMF, close to unitary operations can be achieved. MMFs have the potential to outperform integrated photonics based platforms in terms of losses, with insertion losses of the order of 0.3 dB and propagation losses below 1 dB/km, compared to values above 1 dB and 0.1 dB/cm respectively for photonic integrated circuits [McNab, Moll, and Vlasov, 2003].

5.4 Practical implementation

The presented method requires computational efforts during its calibration but once the TM is retrieved and the projectors are calculated, the operations are performed in a single shot ($O(1)$ operations) on a passive system. No further calibration is needed as long as the system is stable. MMFs up to 100 meters are stable enough to be used as accurate optical instruments [Redding, Popoff, and Cao, 2013]. Stability

over multiple days can be obtained by ensuring a controlled environment and good laser stability. Thin diffusers are only limited by the stability of the input source and thus are very stable. The approach we present offers the possibility to implement large optical linear transformations without elaborate fabrication techniques as well as to reconfigure the desired operator without further measurements. Moreover, it opens the opportunity to drastically reduce the energy consumption compared to classical electronic components while increasing the computation speed [Shen et al., 2017a; Hougne and Lerosey, 2018]. These characteristics may enable the presented technique to play a role in the advent of optical analogue computation and machine learning.

Conclusion

Performing computations with light is promising because it allows reducing the energy consumption currently limiting the growth of silicon electronics computation capacities. The method we designed consists in using complex media together with DMDs, which are fast and have numerous controllable elements. Complex media, such as heavily perturbed MMFs or scattering media, display very large Gaussian random TMs. We exploit this randomness to create linear operators. We use input and output projectors which project the random TM into a smaller subspace where its effect is represented by a target linear operator. The projectors are physically generated by the modulation achieved by a DMD and the precise selection of outputs on a camera.

We showed that a lightweight system can be used to measure the TM of a complex medium without the need for interferometric measurements, but by using numerical phase retrieval algorithms. This TM is used to compute the projectors thanks to convex optimization.

The system we build is able to perform any computation of size 16×16 with good accuracy and fidelity, and to switch between operations at will. The method can be scaled up for larger operation sizes, and is limited only by the number of spatial channels of the system and the number of controlled pixels on the modulator. Indeed, the number of required channels scales as the square of the size of the operations, like previously implemented methods. However, provided a large depth of modulation, we can expect to outperform existing approaches. With MMFs, we can envision operations of size 170×170 , and with scattering media, operations of size 1000×1000 .

Conclusion

Multimode fibers are a promising medium for the next generation of optical communication networks. Thanks to their high mode density, many spatial channels can be exploited to increase data rates and face the ever-increasing demand in capacity. However, effects such as intermodal dispersion, mode dependent losses/gains and mode coupling make it challenging to retrieve the input information. Multiple Input Multiple Output (MIMO) strategies can be used to counteract the effects of mode coupling. However, because their numerical complexity is very high, their real-time implementation is limited. As a consequence, fiber-optic systems have to be designed to relax the constraints on the digital signal processing required to retrieve the transmitted signals. Typically, this involves paying a particular attention to the modal content of the MMFs.

Techniques, such as the cross-correlation method, or the spatially and spectrally resolved method, described in Chapter II, can be used to measure the temporal and spatial properties of modes. These methods are especially adapted to the study of few-mode fibers but are not perfectly suited to characterize mode coupling. The recently born field of wavefront shaping has brought a change of paradigm in the study of MMFs. Thanks to the control of the phase and amplitude of the field provided by spatial light modulators, it has become possible to measure the transmission matrix of a MMF. Moreover, its measurement in the basis modes allows fully describing the coupling properties.

This was the starting point of the study performed during my Ph.D. In Chapter III, we presented the tools and methods we developed for these last three and a half years. In a first step we perform reliable measurements of the pixel basis TMs of MMFs. To express the mode basis TM, we used change of basis matrices from the pixel basis to the modal basis. However, because of the imperfections of the system and the optical aberrations, the resulting TM is not representative of the propagation inside the fiber. We developed an optimization method to correct these aberrations by physically modeling them into layers of a deep learning framework. This method has the advantage of requiring a single TM measurement, does not make any assumption about the disorder inside the fiber, and can be adapted to any type and level of aberrations.

Because the measurement of the mode basis TM is fast and reliable, we are able to perform multiple measurements successively. In Chapter IV, we used a translation actuator to apply controlled deformations onto a fiber, and for each of them we measured the mode basis TM. Using this stack of TMs, we studied the effect of perturbations onto the transmission channels of fibers. We observed that mode coupling increases as the perturbation gets stronger. In order to design spatial wavefronts robust to the deformation, we studied the generalized Wigner-Smith (GWS) operator, which has been popular in wavefront shaping activities in recent years. In the continuity of the studies presented about this operator, we computed it with respect to the level of induced deformation on a fiber. The eigenvalues of this GWS

operator, called the *deformation principal modes*, form an almost complete basis of transmission channels of the fiber which are robust to deformations. One of their key characteristics is that they are insensitive to disorder within a wide range of deformation intensities, even though they are computed for small deformations. We observed that the best channels are composed of a broad range of modes of the fiber, thus exploiting mode diversity to obtain robustness.

We investigated why the GWS operator computed for a small range of deformations produces channels robust to a large range of deformation. Introducing the global deformation operator, we characterized the main coupling mechanisms induced by the perturbation. We showed that two mechanisms are responsible for most of the changes of the TMs. These mechanisms show that modes couple significantly with groups of modes that are close in the momentum space, as previously observed.

In Chapter V, we presented an approach to use the random coupling between the spatial channels of a medium to perform optical operations. From the large-size-pixel basis TM of a complex medium, we can generate smaller size linear operators using adapted projections. By using an SLM and a camera to generate the appropriate projections, and using an MMF in the strong coupling regime, or a scattering medium such as a ground glass diffuser, we showed that it is possible to create an optical processing unit. Implementing this system does not require phase measurements, and can be reconfigured at will by changing the displayed pattern of the SLM. We managed to build complex operators of size 16×16 using a DMD together with a high mode-count MMF.

A significant part of this work consisted in designing a system that is easy to use, versatile and fast for the study of MMFs. Measuring the mode basis TM of an MMF is a matter of tens of minutes, which includes handling the fiber, performing the measurements and computing the matrix. From this state, it is possible to envision several subjects of study:

Studying a wider range of deformations. In Chapter IV, we studied a single perturbation of increasing intensity affecting the fiber. In the scope of telecommunication applications, the study of multiple perturbations is the key to designing channels of transmission adapted to arbitrary perturbations. Using the global deformation operator introduced in Chapter IV may prove beneficial to study the coupling mechanisms associated to other types of perturbation of interest in the scope of telecommunication applications, for example incorrect splicing of fiber sections, temperature gradients, bends, and natural imperfections of the fibers.

The improvement of the optimization process to include mode adjustments. In previous works done by the team of Tomas Cizmar, the optimization procedure includes corrections to the parameters of the fiber to refine the quality of the change of basis operation. This operation may be required to perform more in depth studies of the coupling effects in unperturbed fiber. Alternatively, it seems possible to implement an optimization on the spatial profiles of the modes to maximize the energy conservation between the pixel basis and mode basis TMs. Doing so may alleviate the requirement for the precise knowledge of the index profile of the fiber.

Adapting the optimization procedure to the study of other types of waveguides. To obtain the mode basis TM of an MMF, our optimization method only require the knowledge of its mode profiles. Therefore, provided we know the spatial

profile of the propagating modes of any other waveguide, it appears possible to obtain its mode basis TM by using the same procedure. Doing so could allow studying the modal behavior of light in silicon waveguides for example.

Appendix A

Mechanical stability of the DMD

The field-programmable gate array (FPGA) of the controller board of the DMD is cooled by fan associated to a heat sink. This system generates vibrations that are transmitted by a rigid ribbon cable to the DMD. They contribute to vibrations of the surface of the DMD. To quantify the effect of this perturbation, we inject light in the MMF with all the pixels of the DMD in the on state. We measure the output complex field on one point of the InGaAs camera, and track the value of its phase over time using off-axis measurements. We show in Figure A.2 that we observe periodic fast phase fluctuations as well as a slow drift¹.

To limit this effect, we use a system to dampen the vibrations. We attached the ribbon to the optical table using foam and clamps as shown in Figure A.1. Thanks to this method, we observed the attenuation of the fast fluctuations and also limit the slow drift of the phase as shown in blue in Figure A.2.

We applied this technique to all ribbons and cable susceptible to transmit mechanical vibrations to the optical elements to maximize the stability of the setup.



Figure A.1: Method used to dampen the vibrations of the DMD. The rigid orange ribbon cable is attached with foam and clamps in the top of the image.

¹A movie of the observed phenomenon, its correction, and a tutorial of our method can be found at <https://www.wavefrontshaping.net/post/id/25>.

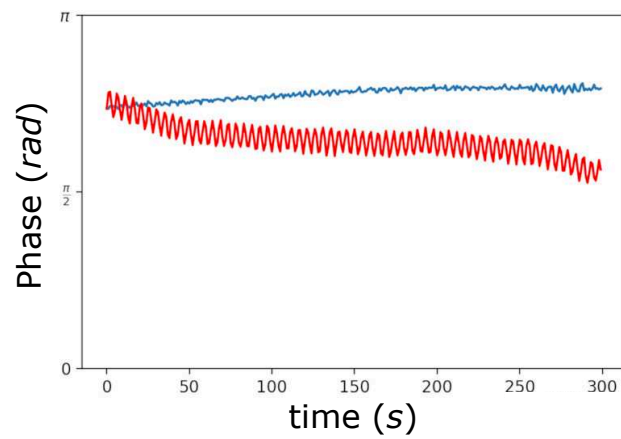


Figure A.2: Phase fluctuations due to vibrations of the DMD. Evolution of the phase of one point of the complex measured field as a function of time (in seconds) without (red) and with (blue) isolation.

Appendix B

Thermal effects on the DMD chip

When we turn on the DMD, it heats up during a transitional regime before reaching a stable temperature. For a fixed displayed pattern the modulated field changes as the temperature rises. After injection through a MMF, we observed that the output speckle pattern changes over time. The fluctuations of the modulation affects only the phase of the field, as the intensity of the modulated pattern does not fluctuate over time. We attribute this effect to the presence of a protective glass layer on top of the DMD chip. When the temperature changes, so does the index of refraction of the material, changing the phase of the reflected field.

We monitored the changes by computing the correlation between intensity speckles $I(t)$ and a reference speckle $I(t = 0)$ taken shortly after turning on the DMD. We used the Pearson correlation coefficient defined as

$$C(t) = \frac{\sum_{i=1}^n \left(I(0)_i - \overline{I(0)} \right) \left(I(t)_i - \overline{I(t)} \right)}{\sqrt{\sum_{i=1}^n \left(I(0)_i - \overline{I(0)} \right)^2} \sqrt{\sum_{i=1}^n \left(I(t)_i - \overline{I(t)} \right)^2}}, \quad (\text{B.1})$$

where the index i refers to the individual pixels of the images, and $\overline{I(t)}$ represents the average of the image at time t . The results are presented in Figure B.1.

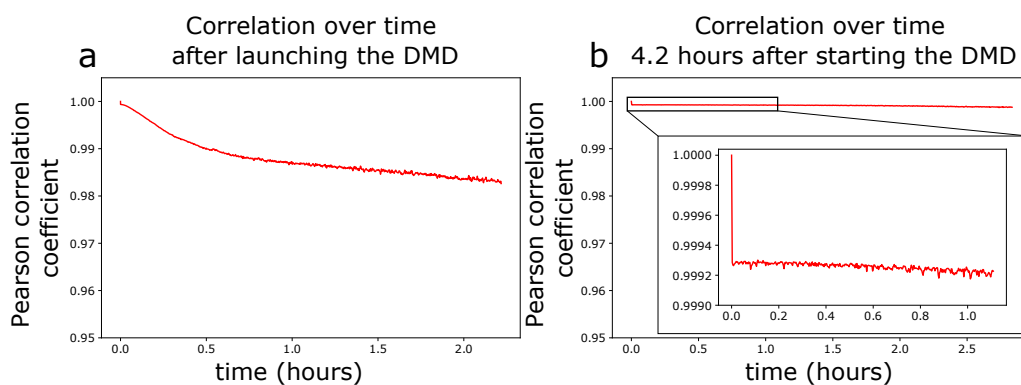


Figure B.1: Decorrelation of the speckle pattern over time due to the DMD. **a**, Pearson correlation of the speckle intensity with respect to an image taken right after readying up the DMD. **b**, Same experiment performed 4.2 hours after launching the DMD.

In the transitional regime, the speckle modifications over time are similar to the ones observed when changing the input pattern. About one hour after turning on the DMD, the change of speckle at the output of the fiber ceases and the correlation stabilizes. We computed the correlation of speckles in the stationary regime with a reference taken after one hour. We observed a high stability over several hours, granting enough time to perform acquisitions. To prevent the fluctuations caused

by the thermal effects, we simply wait at least one hour before performing an experiment with the DMD.

Appendix C

Aberrations of the DMD

The DMD surface is not perfectly flat. When illuminating the DMD with a plane wave, and sending a pattern corresponding to a flat phase mask, we observe in the Fourier plane of a lens an intensity pattern. It corresponds to the Point Spread Function (PSF) of the optical system that we show in Figure C.1.a, which deviates from an expected Airy disk.

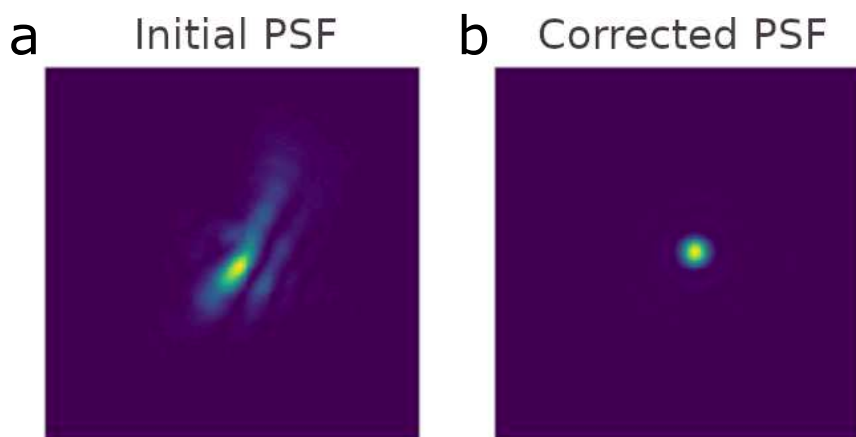


Figure C.1: Point spread function of the optical system. **a**, Intensity of the PSF of the DMD. **b**, Intensity of the PSF of the DMD after correction of the aberrations.

To estimate the curvature of the DMD surface, we can use the Lee hologram and learn to compensate for this effect. Using a feedback optimization, we find the phase mask that correct the PSF of the system measured by the camera. The phase mask is composed of Zernike polynomials which coefficients are the variables of the optimization procedure.

The obtained phase correction allows to have a map of the curvature of the DMD surface which can be used to compensate the wavefront in post-treatment. The final phase map produces a intensity response which resembles an Airy disk shown in Figure C.1.b. We are able to reconstruct the correct PSF using the first nine Zernike polynomials which coefficients are shown in Figure C.2.a. The curvature has slow spatial fluctuations, they are represented in Figure C.2.b. A tutorial on the aberrations effects and the codes used to correct the phase profile of the DMD can be found on the website of our team at wavefrontshaping.net/post/id/23. Using the Lee hologram technique with a DMD we achieve only discrete values of phase modulation. However, decent corrections can be obtained with limited number of phase values. We present simulations performed with different number of phase values used for the correction of the surface aberrations in Figure C.3. We are above 94 % correlation between the corrected PSF and the ideal Airy disk PSF with only 4

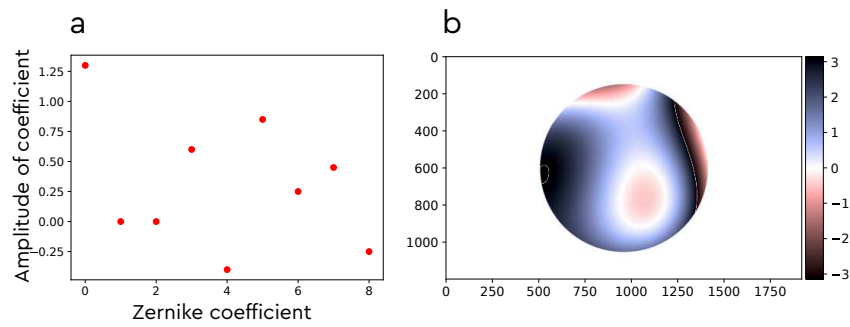


Figure C.2: Correction of the DMD surface aberrations. a, Contribution of each Zernike polynomial to the correction. **b,** Corresponding phase profile on the DMD.

phase values. Having a low number of phase values implies that the Lee modulation frequency is low and thus the spatial resolution of the DMD is maximal. This ensures that a good trade-off between correction of the surface curvature and spatial resolution of the modulation can be achieved.

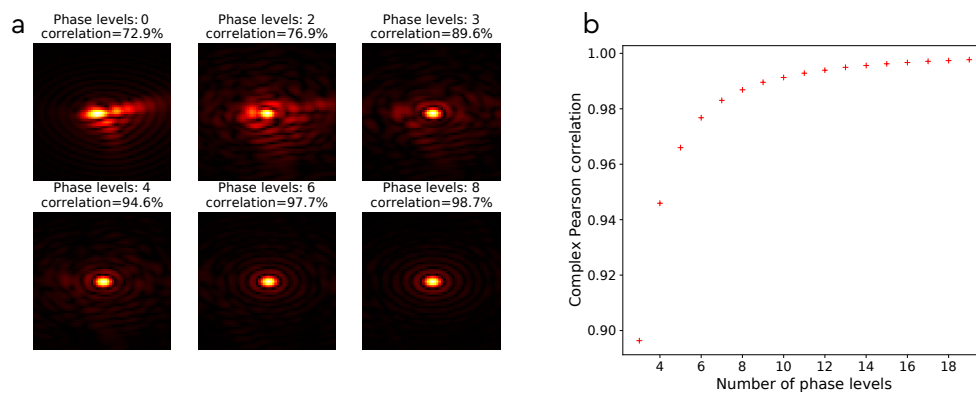


Figure C.3: Simulations of the correction of the aberrations of the DMD using the Lee hologram method. a, Intensity of the PSF of the DMD with corrections performed with increasing numbers of accessible phase levels. **b,** Complex Pearson correlation between the ideal Airy disk PSF and the corrected PSF as a function of the number of phase levels.

Appendix D

Tuning the injection into the fiber

Due to the strong demagnification and the small focal length f_4 of lens L_4 of the setup (presented in Figure III.8 of Chapter III), several experimental limitations are encountered when setting up the injection arm.

- The small dimensions of lens L_4 makes it hard to correctly center the incoming light beam. Moreover, its small clear aperture of 3.84 mm may lead to a truncated beam,
- The initial positioning of the optical fiber is made difficult by the low to null coupling happening before reaching a correct alignment. This difficulty may be overcome by initially aligning the setup with an MMF with a very large core (a fiber of square core of side $150\ \mu\text{m}$ ¹ was used due to availability and good results),
- Vertical position is hard to change at the injection platform, therefore it has to be set up correctly beforehand. Minor adjustments are performed by changing the pitch tilt of lens L_3 .

In Figure D.1, we show an illustration of the five main geometrical degrees of freedom that exist when trying to couple light into an optical fiber.

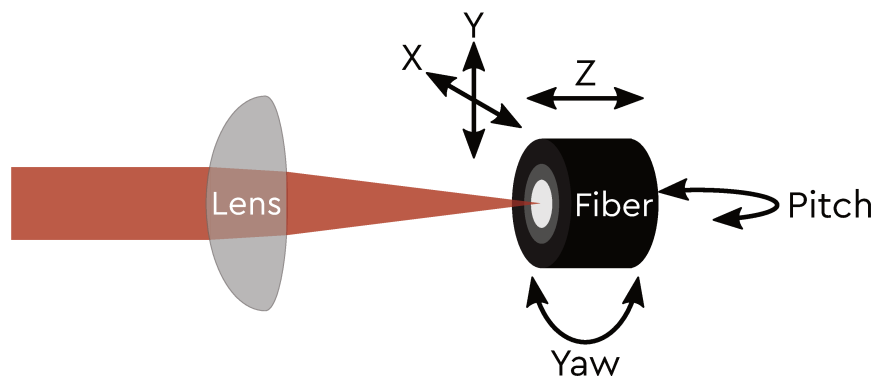


Figure D.1: Illustration of the possible degrees of freedom of the position of the fiber.

As our equipment allows adjusting the presented degrees of freedom, we want to develop a procedure to correctly tune the position of the fiber in order to achieve the conjugation between the planes of the DMD and the plane of the fiber input. The initial procedure we employed consisted in maximizing the power at the output, which we measured with a power-meter. We demonstrate first why this method is not reliable when working with MMFs. Instead, we collect light that is reflected

¹Thorlabs M101L02.

by the input facet of the fiber. We explain in the second section how we collect the reflected light and how the measurement of the field at the input facet of the fiber allows tuning the injection parameters.

1 Transmitted energy through the fiber

Tuning the geometrical degrees of freedom of the injection is a complicated task: one needs to find the parameters which allows the best coupling efficiency to all the of propagating modes. When working with single mode fibers, light propagating in free space can only couple to a single mode. In order to perform the alignment, gradually maximizing the power coming out of the fiber is generally sufficient to optimize the injection.

In MMFs, more than a single mode can be coupled to: the energy can be carried by several modes with different spatial profiles. Therefore, the modification of one injection parameter may change the energy distribution between the modes. Local maximas of transmission corresponding to selective excitation of the modes may appear. Gradually increasing the total transmission does not guarantee to converge to the optimal set of parameters.

To illustrate these observations, we define the coupling coefficient $\mathcal{C}(A_{ill})$ between an incoming illumination of amplitude A_{ill} and a fiber of mode amplitudes M_i by

$$\mathcal{C}(A_{ill}) = \frac{\sum_i \left| \int A_{ill} \cdot M_i^* \right|^2}{|A_{ill}|^2}, \quad (\text{D.1})$$

which values varies between 0 in the case of an absence of coupling, to 1 when a perfect coupling is achieved. The Figure D.2 shows how the coupling coefficient varies when a disk illumination of $23.9 \mu\text{m}$ is sent onto the input facet of a step index fiber of radius $a = 25 \mu\text{m}$ and $NA = 0.2$ (which guides approximately 103 modes at $\lambda = 1.55 \mu\text{m}^2$), with several coupling imperfections.

In Figure D.2:a, the illumination is offset by $3.41 \mu\text{m}$ with respect to the axis of the fiber, and the angle of the fiber with respect to the incoming wavefront is scanned in the range $\pm 2^\circ$ in both directions. We observe a global maximum corresponding to an angle of 0° while secondary maximas exist for a non-zero angle. In Figure D.2:b, the illumination comes with an imperfect angle of 5.73° and is transversally scanned around the axis of the fiber. This time, we notice no sharp maximum at the center of the fiber and the existence of wide plateau.

These two examples of coupling efficiency indicate that the maximization of the coupling is not convex with respect to the parameters. Moreover, only the simplest levels of aberrations were considered for this simulation. We can conclude by arguing that a criterion solely based on gradually maximizing the transmitted intensity is not efficient to achieve the best coupling parameters.

2 Conjugation of the DMD plane and the input plane of the fiber

Instead of relying on the transmitted energy to adjust the injection, we use a method where we observe the pattern illuminating the input plane of the fiber. To do so, we use a camera which collects the light reflected at the input plane of the fiber.

²Estimated with $M = V^2/2$ where $V = 2\pi a NA/\lambda$.

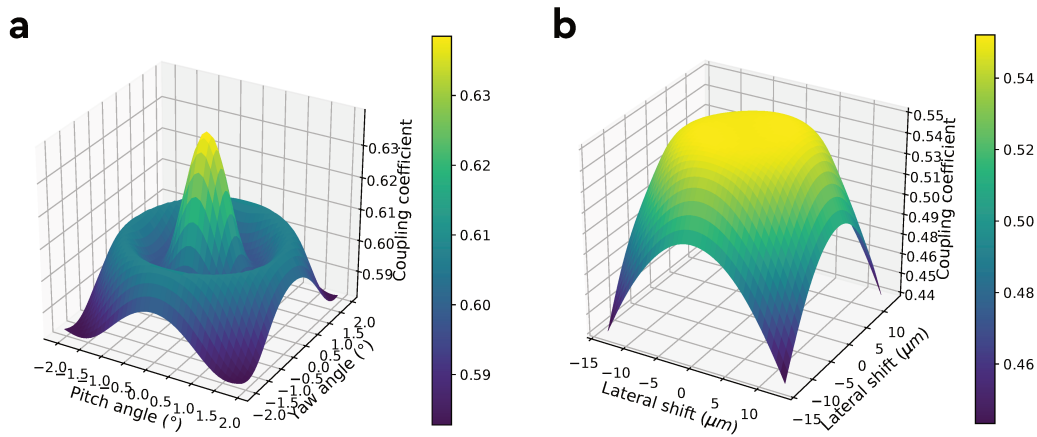


Figure D.2: Coupling coefficient as a function of illumination parameters. **a**, Coupling coefficient as a function of the pitch and yaw angle, for a fiber of misaligned center ($3.42 \mu\text{m}$ shift). **b**, Coupling coefficient as a function of the lateral shift, with an illumination coming from an angle $\alpha = 5.73^\circ$.

2.1 Obtaining the conjugation of the three planes

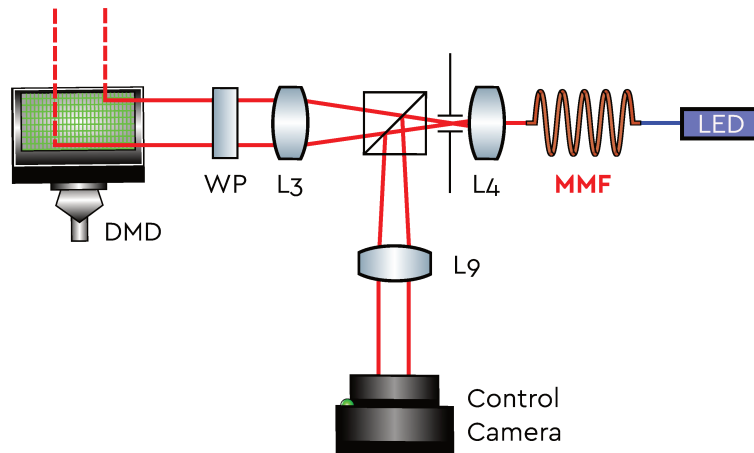


Figure D.3: Schematic of the control setup used for alignment. An LED is used on the back of the fiber to provide an incoherent illumination.

We want a method to conjugate both the DMD and the control camera to the input facet of the fiber as presented in Figure D.3 to record the intensity of the light at the plane of the fiber. To conjugate the fiber to the control camera, we use an incoherent light-emitting diode to inject light from the output side of the fiber. Light couples into a high number of modes. After propagation through the fiber, the excited modes are incoherently summed on the control camera. If a sufficiently high number of modes are excited we observe a flat intensity profile. When the input fiber facet is correctly conjugated to the control camera, we observe a sharp decrease of the intensity at the core-cladding interface, as is presented in blue in Figure D.4. Conversely, when the two planes are not conjugated, for example due to a defocus, the intensity at the core-cladding interface decreases more slowly, as is presented in green in Figure D.4. When tuning the z-position of the camera, maximizing the

sharpness at the interface allows reaching the conjugation between the fiber and camera planes.

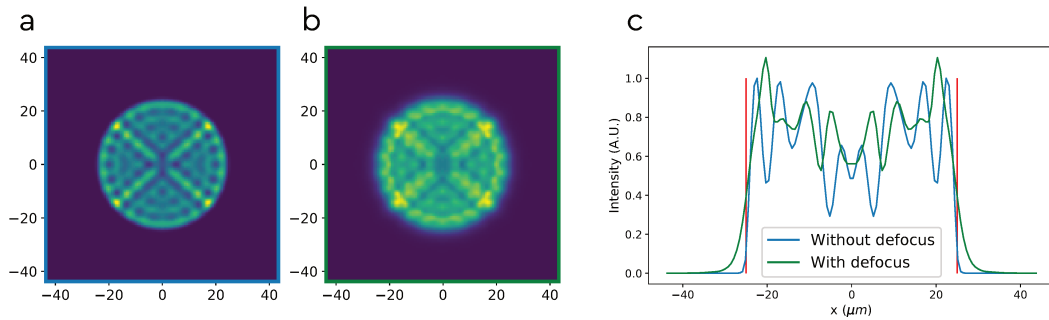


Figure D.4: Incoherent speckle intensity when a defocus is present. **a**, Intensity of an incoherent speckle recorded after a 4-f system. **b**, Intensity of an incoherent speckle recorded after a 4-f system with lateral translation of the fiber facet. **c**, Projection of the speckle intensity along the horizontal in both cases.

We then have to perform the conjugation between the DMD and the facet of the fiber. To do so, a pattern is displayed on the DMD while the LED is still illuminating the other side of the fiber. The position of the camera and of the fiber are simultaneously adjusted to observe the displayed pattern and to conserve the sharpness of the incoherent light on the control camera. Further adjustments of the L_3 lens may be necessary to reach the best axial position of the injection elements.

When the conjugation of the three planes is reached, observing the distinctive pattern on the control camera is sufficient to calibrate the axial position of the fiber in future experiments. It means that if the fiber needs to be changed, there is no need to use an LED to reach fiber-camera conjugation; readjusting the position of the fiber so that the DMD and the camera are conjugated guarantees that the DMD and the fiber are conjugated as well.

When performing these steps, an additional speckle coming from the reflection on the output glass-air interface may be observed. To prevent the observation of this speckle and its interference with the pattern of interest, we use a fiber optic light trap³: it forces light to couple away from the fiber into a medium which index matches the one of the core⁴.

2.2 Adjusting the remaining parameters

We want to use the observation of the pattern arriving at the input facet of the fiber to tune the other degrees of freedom of the injection. Thanks to the backreflected speckle, we know the position of the core of the fiber with respect to the DMD illumination. We adjust the transverse position of the fiber to maximize the overlap between the core and the illumination while monitoring the transmitted intensity. The intensity at the output of the fiber should increase when the overlap increase, otherwise it means that the incidence pitch and yaw angle are tilted. The pitch and yaw error at the proximal fiber facet can be assessed by rocking the fiber back and forth while a pattern is displayed on the DMD and its reflection observed onto the control camera. Observing which side of the pattern gets blurred by the defocus effect allows to correct the angle of the fiber with respect to the optical axis.

³Thorlabs FTFC1.

⁴Thus performing an optical impedance matching.

Once the geometrical degrees of freedom of the fiber are tuned, we have to check those of lens L_3 . The most important parameters for this lens are the pitch and yaw position, to assess them we display a centered ring pattern on the DMD and record the output speckle on a camera. A correct tuning of the injection arm corresponds to observing a centro-symmetric output. Correcting the pitch and yaw of the lens leads to observe axisymmetric patterns like the ones shown in Figure D.5, indicating good adjustment of the injection arm.

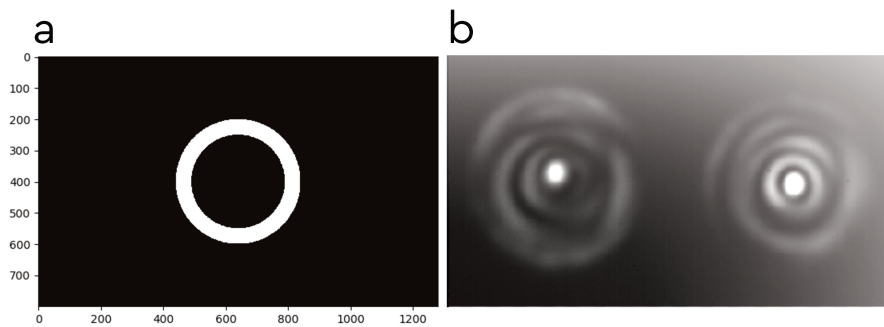


Figure D.5: Circular symmetry of output speckles for an aligned MMF. **a**, Pattern displayed on the DMD. **b**, Resulting speckles for the two linear polarizations at the output of a correctly aligned MMF. We observe the central symmetry of the output speckles.

Appendix E

Off-axis measurements with multimode fibers

In this appendix, we explain how the off-axis method presented in chapter III is implemented to measure the complex output field of MMFs.

1 The Fourier transform of the interference pattern

We want to compute the range of acceptable off-axis angle that can be used when working with a given multimode fiber. We work with equation III.6:

$$I_{tot}(x, y) = I_R + |A_O(x, y)|^2 + \sqrt{I_R} e^{-iks\sin(\theta)x} A_O(x, y) + \sqrt{I_R} e^{iks\sin(\theta)x} A_O(x, y)^* . \quad (\text{E.1})$$

And its Fourier transform III.7

$$\begin{aligned} \tilde{I}_{tot}(u, v) = I_R \delta(u, v) + (\tilde{A}_O \otimes \tilde{A}_O)(u, v) + \sqrt{I_R} \delta\left(u + \frac{\sin\theta}{\lambda}, v\right) \otimes \tilde{A}_O(u, v) \\ + \sqrt{I_R} \delta\left(u - \frac{\sin\theta}{\lambda}, v\right) \otimes \tilde{A}_O(-u, -v) , \end{aligned} \quad (\text{E.2})$$

In figure E.1, we schematically show the four terms of the Fourier transform of the interference pattern $\tilde{I}_{tot}(u, v)$ when the signal comes from an MMF.

The first term of equation III.7 is the yellow dot at the center. The second term is the centered wide red spot of width $2\Delta f$. We note Δf the spatial spectral width of A_O , the MMF output field that we try to retrieve¹. The width double that of the signal is due to the auto-correlation operation on \tilde{A}_O ².

2 Reconstruction conditions

When we perform the reconstruction, we need to isolate the field $A_O(x, y)$ from other contributions to be able to filter them using a diaphragm in the Fourier plane of a lens. The conditions for which this is the case can be derived from the observation of the Fourier space. From the Figure E.1, we remark that the correct selectivity is

¹Note in off-axis measurements, the observed object is not necessarily bounded in spatial frequencies. Limited numerical aperture and diffraction are often the limiting factors. In the case of MMFs the frequency range is limited by the numerical aperture of the fiber.

²While the frequency footprint of $\tilde{A}_O \otimes \tilde{A}_O$ is $2\Delta f$, the correlation product leads to a fast decrease in amplitude: in practice we do not observe such wide spots because they are strongly attenuated on the side.

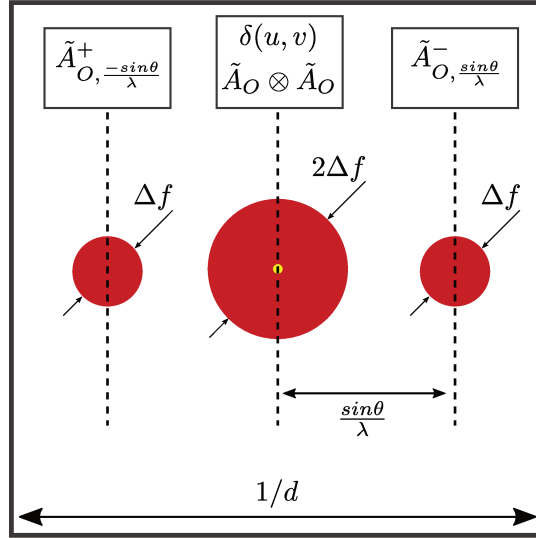


Figure E.1: Illustration of the Fourier transform of the interference pattern of the output speckle of a fiber with a flat reference. For simplicity, the reference intensity is $I_R = 1$.

achieved when there is no overlap between the replicas and the center spots. Moreover, the maximal spatial frequency of I_{tot} should be lower than $1/2d$ to satisfy the Shannon-Nyquist sampling theorem. It amounts to having the replica inside the window in figure E.1.

This is achieved when:

$$\begin{cases} \sin\theta/\lambda - \Delta f/2 \geq \Delta f & \text{(No overlap condition)} \\ \sin\theta/\lambda + \Delta f/2 \leq 1/(2d) & \text{(Shannon condition)} \end{cases} \quad (\text{E.3})$$

As we magnify the image at the facet of the fiber onto the camera by a factor γ , this condition becomes:

$$\begin{cases} \sin\theta/\lambda \geq 3\Delta f/(2\gamma) & \text{(No overlap condition)} \\ \sin\theta/\lambda + \Delta f/(2\gamma) \leq 1/(2d\gamma) & \text{(Shannon condition)} \end{cases} \quad (\text{E.4})$$

Because we work with multimode fibers, we know that the maximal spatial frequency Δf reads:

$$\Delta f = \frac{2NA}{\lambda} \quad (\text{E.5})$$

Thus, the general conditions written in equation E.3 can be re-written:

$$\begin{cases} \sin\theta/\lambda \geq 3NA/(\gamma\lambda) & \text{(No overlap condition)} \\ \sin\theta/\lambda + NA/(\gamma\lambda) \leq 1/(2d\gamma) & \text{(Shannon condition)} \end{cases} \quad (\text{E.6})$$

In most of our experiments, we work at $\lambda = 1.55 \mu\text{m}$ with OM2 fibers of numerical aperture $NA = 0.2$, magnification of $|\gamma| = 68$ and a pixel pitch at the camera plane of $d\gamma = 20 \mu\text{m}$. The previous conditions allow us to deduce the range of admissible angles for the off-axis reference beam:

$$\theta \in [0.50^\circ, 2.55^\circ] \quad (\text{E.7})$$

3 Simulations and direct space conditions

We verify the theory with simulations of the off-axis method. We generate speckles coming from an OM2 fiber (GRIN, $NA = 0.2$, $a = 25 \mu\text{m}$) using the method presented in Appendix G, and have them interfere with references coming from different angles θ . Simulations of off-axis experiments for three different illumination angles are presented in Figure E.2, they are below, in, or beyond the range of acceptable angles. We obtain good reconstructions both in phase and amplitude only when the illumination angle respects the conditions E.6.

Careful consideration of the different sampling rates are necessary when designing the experiment to ensure that the complex field is correctly retrieved and that no spectral content is lost.

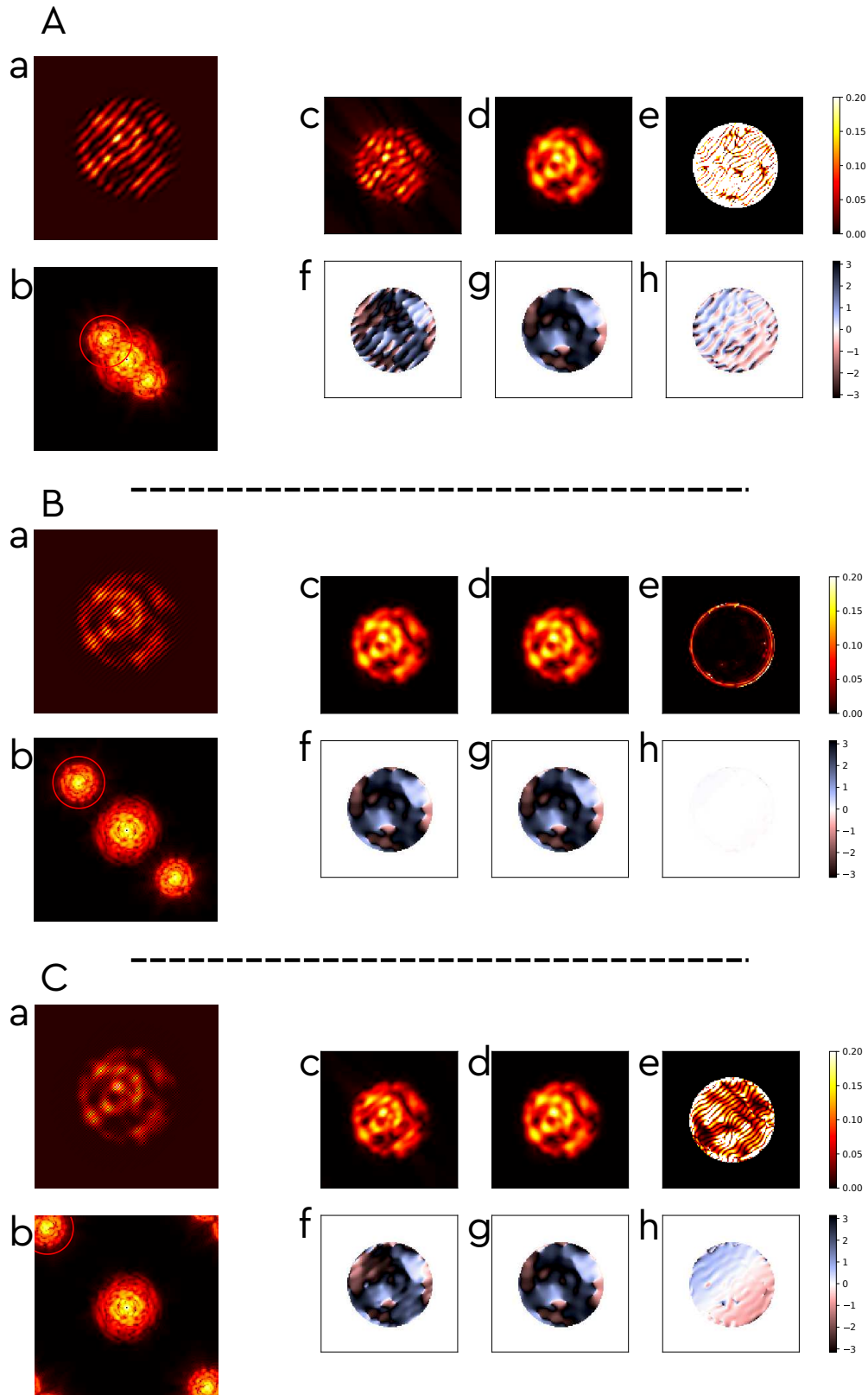


Figure E.2: Simulations of off-axis reconstructions with different reference angles. A, Off-axis angle too small; **B,** Angle in the admissible range; **C,** Angle too high (Shannon-Nyquist theorem not satisfied). **a,** Interference pattern observed on the camera. **b,** Fourier transform of the pattern with circled in red the selected zone of interest. **c,** reconstructed intensity. **d,** expected speckle. **e,** relative error between the two intensity (capped to 20%). **f,** reconstructed phase. **g,** expected phase. **h,** phase difference between the expected and reconstructed phase.

Appendix F

Reconstruction of the Transmission Matrix

In this appendix, we study simulations of the reconstruction of the transmission matrix. The objective is to assess if our method allows an accurate reconstruction of the pixel basis TM.

1 Selecting good input patterns and singular value criterion

First, we run simulations where we generated outputs \mathbf{Y} from several sets of input matrices \mathbf{X} and a TM corresponding to the propagation in a perfect 6-mode step index MMF. The input excitation consists in a square array of $N = 2^6$ square pixels mimicking the effect of an SLM excited with a coherent plane wave. We consider that the SLM sends $p \in \{N, 6N, 12N\}$ different input vectors in the system. The outputs consist of $M = N$ elements that simulate camera pixels. The different random input approaches are the following:

The *random* inputs are a uniform distribution of -1 and 1 . The *permuting* inputs come from a vector where -1 and 1 are in equal number, this vector is then randomly permuted for each column of the input matrix. The *custom vec* inputs are a distribution of $-1, 0$ and 1 with the proportion of active elements (-1 and 1) varies and the proportion of -1 and 1 also varies within active elements. The last approach is an attempt at creating inputs that excite a wider range of fiber modes. The value p is one of significant importance; we call the ratio $\frac{p}{N}$ the input oversampling.

The goal is to verify whether these input sets are efficient at reconstructing the TM, using equation F.1 previously presented in Chapter III:

$$\hat{\mathbf{H}} = \mathbf{Y} \cdot \mathbf{X}^+, \quad (\text{F.1})$$

where \cdot^+ designates the Moore-Penrose invert of a matrix. We also want to assess if a high oversampling allows a better reconstruction of the TM. In Figure F.1, we show the singular value distributions of TMs obtained from noisy measurements emerging from different kind of input patterns in the case of the oversampling ratio equal to $p/N = 1$ (no effective oversampling). Using the singular value distribution is a qualitative criterion the reconstruction quality because it shows if the transmission channels are correctly measured. In this case, we observe that the distributions are not physical, the reconstructions fail. This is due to the fact that the pseudo inverse of the matrix \mathbf{X} corresponding to the stack of inputs does not have linearly independent rows, it thus cannot be inverted using the Moore-Penrose pseudo inverse.

In Figure F.2, we show the singular value distributions of TMs obtained with the same methods but with oversampling of $p/N = 6$ and $p/N = 12$.

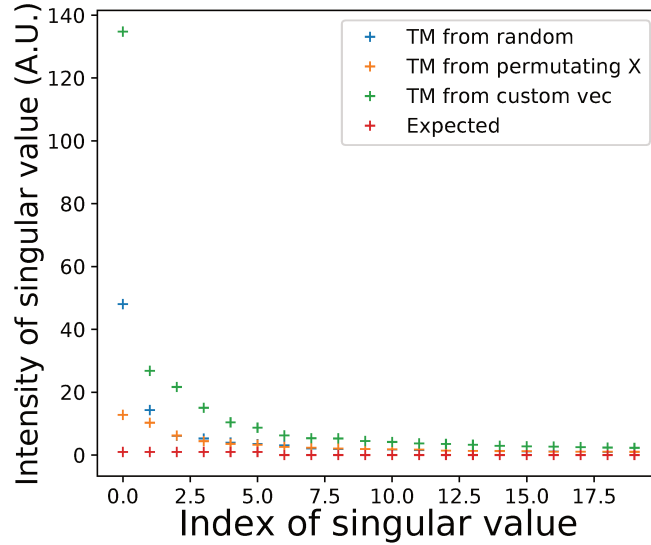


Figure F.1: Singular value distributions of the TM for different input sets without oversampling.

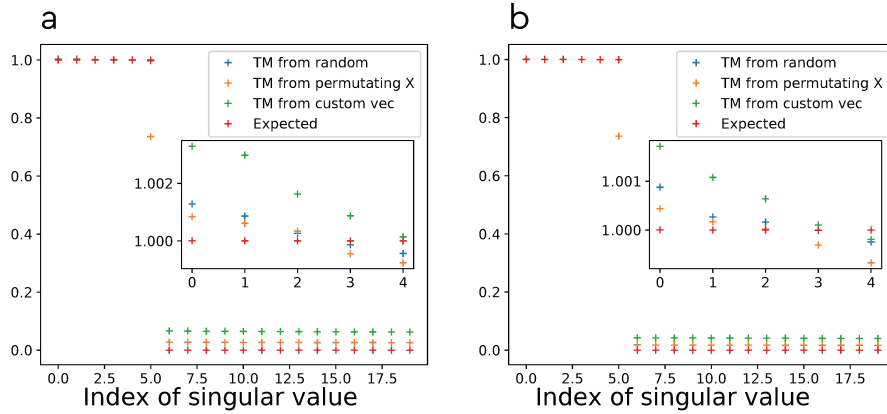


Figure F.2: Singular value distributions of the TM for different input sets and oversampling ratios. **a**, Oversampling ratio of $p/N = 6$. **b**, Oversampling ratio of $p/N = 12$.

We notice that the *random* and *custom vec* produce a TM with an appropriate distribution of singular values compared to the initial TM, whereas the *permutating* inputs produce a TM where the sixth singular value is incorrect. Doubling the oversampling ratio allows a slight increase in the quality of the reconstruction in terms of singular values. Indeed, we observe that the distributions of the reconstructed matrices are closer to the expected distribution.

We select the *custom vec* method that shows good results. To choose the oversampling ratio p/N , a trade-off between reconstruction accuracy and measurement time has to be found.

2 Quantitative assessments of reconstruction

When we record experimental TMs, we want a method to evaluate the quality of the transmission matrix. In simulation, we can evaluate the fidelity of the estimated

reconstructed TM by computing the fidelity defined as:

$$F = \frac{\text{Tr}(|\mathbf{H}_{\text{modes}} \hat{\mathbf{H}}_{\text{modes}}^+|^2)}{\sqrt{\text{Tr}(|\mathbf{H}_{\text{modes}}|^2) \text{Tr}(|\hat{\mathbf{H}}_{\text{modes}}|^2)}}. \quad (\text{F.2})$$

The fidelity is evaluated on the modal TM, after conversion of the estimated canonical TM on the mode basis. Indeed, we want to study the propagation properties of optical fibers.

However, this measure is not possible experimentally as we have no way to access the real TM $\mathbf{H}_{\text{modes}}$ of the system. As a substitute, we measure how outputs generated from the estimated TM are close to experimental outputs. To define a relevant metric for these assessments, we use set of p_{test} input vectors that were not used for the initial reconstruction that we call test vectors \mathbf{X}^{test} and obtain the corresponding outputs $\mathbf{Y}^{\text{simu}} = \hat{\mathbf{H}} \mathbf{X}^{\text{test}}$. We compare these outputs to the experimental measurements \mathbf{Y}^{test} resulting from the measured test inputs. We use the absolute value error:

$$\epsilon_i = \frac{\sum_{j=1}^{p_{\text{test}}} |y_{ij}^{\text{simu}} - y_{ij}^{\text{test}}|}{\sum_{j=1}^{p_{\text{test}}} |y_{ij}^{\text{simu}}|} \text{ for } i \in [1, m] \quad (\text{F.3})$$

The error ϵ_i is computed for each output point i , therefore we can draw maps of the reconstruction error depending on the position with respect to the fiber core.

In the following simulations, the system is perturbed by noise impacting our measurements. Two main sources can be identified. One is the noise from the camera and can be modeled by a complex Gaussian noise added to the theoretical output y^{th} , resulting in a measured field $y^{\text{test}} = y^{\text{th}} + y^{\text{noise}}$ after phase reconstruction. The second one likely to have a significant impact is the phase fluctuations of the off-axis measurements, which can be modeled in the first approximation as a phase added to each measurement so that we have $y^{\text{test}} = y^{\text{th}} * e^{i\phi(t)}$ where $\phi(t)$ is a random Gaussian variable.

In an attempt to draw quantitative comparisons, we use both noise sources under the form $y^{\text{test}} = y^{\text{th}} * e^{i\phi(t)} + y^{\text{noise}}$ and tune their standard deviations $\sigma_{\text{cam}/\text{phase}}$ to be close to the ones experimentally observed. In the next examples, we use $\sigma_{\text{cam}} = 10^{-4}$ and $\sigma_{\text{phase}} = 8 \cdot 10^{-2}$; for reference, we used normalized input vectors of size 35×35 . To draw sensible comparisons, we perform the simulations with an OM2 fiber of 55 modes, like the one in the experiments.

The reconstruction of the TM is performed with different oversampling ratios in the range: $\frac{p}{N} \in [1.2, 10]$. To compute the error, we used $p^{\text{test}} = N$ test samples which were not used for the reconstruction, and both the noisy and clean version of these vectors were used to obtain two values of the error.

We remark that the error values computed for the noisy test vectors seem to reach a plateau at around $p/N \simeq 5$, while with the clean vectors the error keeps on decreasing. It seems that the quality of the reconstructed TM is still improving as shown in the noiseless measurements. The enhancement can not be assessed when we compute the error from the experimental, noisy, measurements. Indeed, the noise imposes an reconstruction error value threshold which is higher than the theoretical reconstruction error.

In Figure F.4, we use an oversampling ratio of 5 and study the reconstruction quality as a function of the pixel noise. We observe in Figure F.4.a, b the error maps for two noise standard deviation values of 10^{-4} and 10^{-3} , in the right part the fidelity in function of the standard deviation. Even though the test error gets very high,

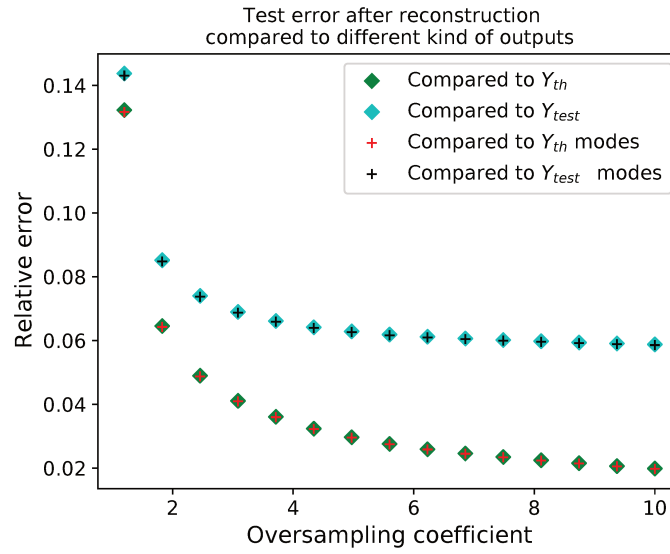


Figure F.3: Reconstruction error as a function of oversampling. Absolute value error (defined in F.3) computed for several oversampling values, and with noisy (y_{test}) and noise-less (y_{th}) test vectors. Both the pixel and the mode basis of the vectors are used.

the fidelity of the TM remains very close to 1, indicating that the reconstruction is correct. When reconstructing experimental matrices, we can compare the obtained test error with the simulated values to roughly estimate the fidelity of the TM. A correct estimation of the sources of noise may allow drawing better results.

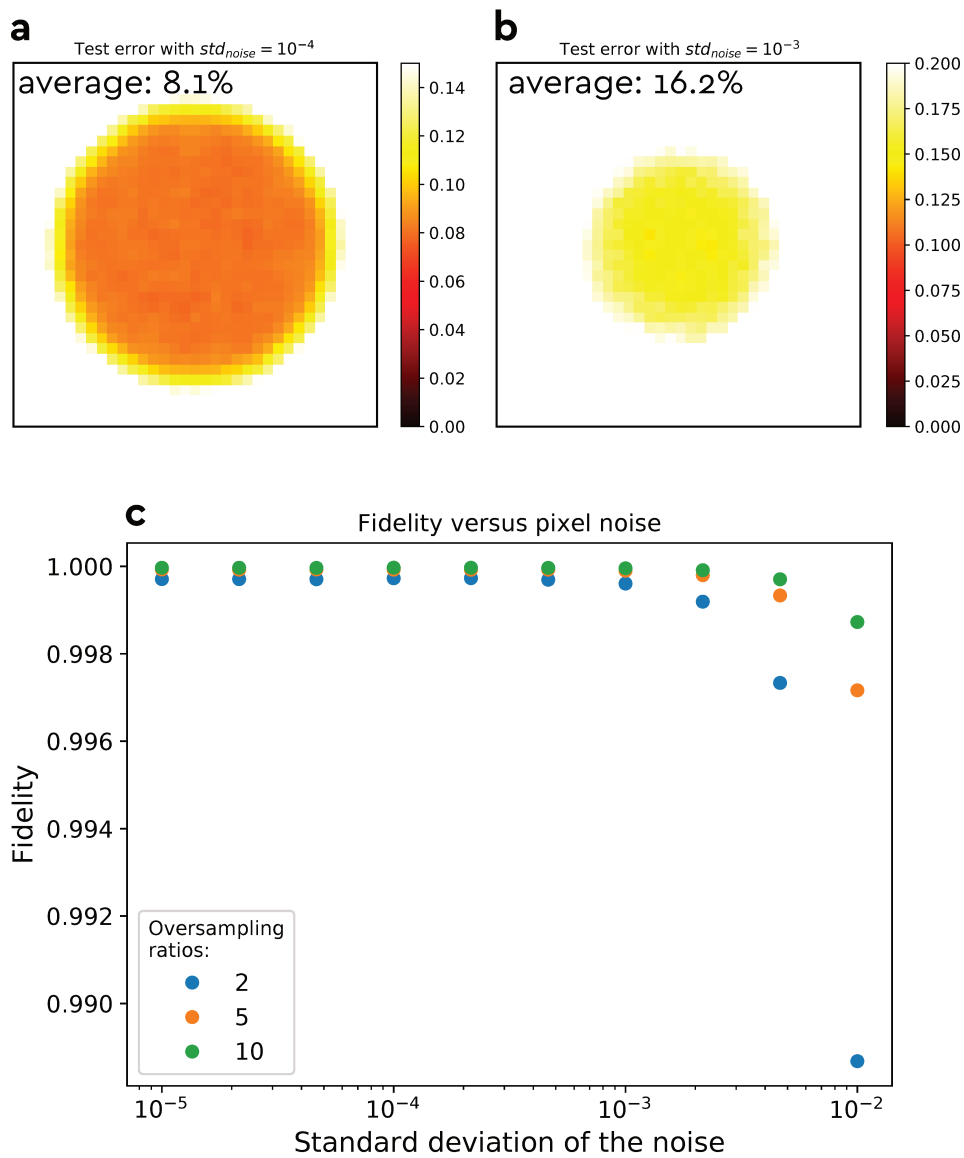


Figure F.4: Reconstruction error for pixel noise of different standard deviation values. **a, b**, Test error computed for noise standard deviations of 10^{-4} and 10^{-3} respectively. **c**, Fidelity of the estimated modal TM as a function of the noise standard deviation. Simulations performed with an oversampling ratio $p/N = 5$.

Appendix G

Numerical computation of the modes

We want to estimate the modes profiles of a perfect straight graded-index fiber under the scalar approximation. Graded-index fiber mode profiles and dispersion relation do not have a closed-form analytical expression. However, approximate analytical expressions can be found, for instance, using perturbation theory or a variational approach [Sharma and Bindal, 1992]. Arguably the most widely used approximation is the Wentzel-Kramers-Brillouin (WKB) approximation. It leads to an analytical dispersion relation when assuming an infinite quadratic spatial profile of the refractive index. While leading to accurate estimations of the propagation constants, it has a limited accuracy for the expression of the spatial mode profiles [Gedeon, 1974; Maksymiuk and Stepniak, 2016]. Finite difference methods are easy to implement numerically, but the 2D discretization of the field leads to high memory requirement and computation time, and could lead to inaccuracies for high order modes. Because we consider axisymmetric index $n(r)$ profiles, we want to simplify the system to solve a 1D problem that only depends on the radial coordinate r , allowing us to increase the accuracy and decrease the computation time.

The 2D scalar Helmholtz equation for a propagating mode can be written in the cylindrical coordinate system as

$$\partial_r^2 \psi(r, \phi) + \frac{1}{r} \partial_r \psi(r, \phi) + \frac{1}{r^2} \partial_\phi^2 \psi(r, \phi) + [k_0^2 n^2(r) - \beta^2] \psi(r, \phi) = 0, \quad (\text{G.1})$$

where ψ is the optical field, ϕ is the azimuthal coordinate, β is the propagation constant, and $k_0 = 2\pi/\lambda$ with λ the wavelength.

Because the refractive index only depends on the radial coordinate r for a perfect graded-index fiber, we can separate the variables r and ϕ . We are then looking for the orbital angular momentum modes of the form:

$$\psi_{ml} = f_l(r) e^{im\phi}. \quad (\text{G.2})$$

With l the radial order and m the azimuthal order, which also corresponds to the orbital angular momentum. Injecting this expression in equation G.1 leads to the 1D equation

$$d_r^2 f_l(r) + \frac{1}{r} d_r f_l(r) + \left[k_0^2 n^2(r) - \beta^2 - \frac{m^2}{r^2} \right] f_l(r) = 0 \quad (\text{G.3})$$

The singularity at $r = 0$ arising from the $\frac{1}{r}$ term makes direct finite difference methods unstable. We can use the transformation:

$$g_l(r) = \frac{1}{f_l(r)} d_r f_l(r), \quad (\text{G.4})$$

and rewrite equation G.3 as a quadratic Riccati equation [Tamil et al., 1991]:

$$d_r g_l(r) + P(r) + Q(r)g_l(r) + g_l^2(r) = 0, \quad (\text{G.5})$$

where

$$Q(r) = \frac{1}{r}, \quad (\text{G.6})$$

$$P(r) = k_0^2 n^2(r) - \beta^2 - \frac{m^2}{r^2}. \quad (\text{G.7})$$

A finite difference approximation of such equation leads to the recursive expression [Tamil et al., 1991; File and Aga, 2016]:

$$1 + h g_l^{n+1} = \frac{1}{1 + h Q_n/2} \left(h^2 P_n - 2 + \frac{1 - h Q_n/2}{1 + h g_l^n} \right), \quad (\text{G.8})$$

where $g_l^n = g_l(r_n)$, $Q_n = Q(r_n)$, $P_n = P(r_n)$, and $h = r_{n+1} - r_n$ is the step size.

The expression G.4 can then be discretized as:

$$f_l^{n+1} = f_l^n (1 + h g_l^n). \quad (\text{G.9})$$

To find the first steps to initialize the iteration, we need to consider the boundary conditions at the center of the fiber core:

$$\left. \frac{df}{dr} \right|_{r=0} = 0 \quad \text{for } m = 0, \quad (\text{G.10})$$

$$f(r = 0) = 0 \quad \text{for } m \neq 0. \quad (\text{G.11})$$

For $m = 0$, we discretize the functions at $r_n = nh - 1/2$, and initialize the functions with $f_l^0 = 1$ and $g_l^0 = 0$. For $m \neq 0$, we discretize the the functions at $r_n = nh$, and initialize the functions with $f_l^0 = 0$, $f_l^1 = h$ and $g_l^1 = (1 - h^2 P_1)/h$. For a given value of m , the propagation constants β_{ml} that satisfy the Helmholtz equation, corresponding to the propagating modes, are the ones for which the field vanishes at large values of r .

The steps to find the modes of the fiber are the following: We start with $m = 0$, and perform a coarse scan of the propagation constant values between $\beta_{min} = k_0 n_{min}$ and $\beta_{max} = k_0 n_{max}$. We choose $r_N > a$ large enough to assume that the field at this point, and thus f_N , should be vanishingly small. The number of times $f_N(\beta)$ changes sign gives us the number of propagation modes for the current value of m . It corresponds to the maximal radial number l admissible for the azimuthal number m . We then use a binary search algorithm to find, at a minimum computational cost, the accurate admissible values of β for each l , i.e. the values that minimize f_N under a given tolerance value. We then increment the value of m , and repeat the procedure. We stop when no solution is found for the current value of m .

This procedure has been implemented in the Python module `pyMMF` [Popoff, 2020] that we developed and share. Sample codes to compute the ideal modes of the MMF are available at: [Github.com/wavefrontshaping/article_MMf_disorder](https://github.com/wavefrontshaping/article_MMf_disorder).

Appendix H

Center detection algorithm for off-axis holography

When we perform off-axis holography, the precise determination of the center of the replica in Fourier domain has to be done before performing its inverse Fourier transform. A wrong estimation of the center of the replica leads to an incorrect phase in the direct real plane. Indeed, this effect can be written as $\tilde{A}_O(u, v) \otimes \delta(u - \epsilon_u, v)$ in the Fourier plane. After inverse Fourier transform, a phase term remains as we obtain $A_O(x, y)e^{-i2\pi\epsilon_u x}$.

It is difficult to measure the angle of incidence of the reference with good precision. To avoid having to manually determine the center of the replicas in the Fourier domain for each experiment, we wrote a compact algorithm to automatically compute it from the stack of Fourier transforms previously obtained from a set of random input excitations. The principle consists in using morphological operations on the Fourier transforms of a stack of interference patterns to determine with precision the center of mass of the replica of interest. Its main steps are presented in algorithm 1 and illustrated in Figure H.1.

Algorithm 1 Find the coordinates of the center of a stack of (complex) images

- 1: Compute the sum of the absolute values of the images in the direction of the stack;
 - 2: Apply a maximum filter on the resulting image;
 - 3: Threshold the resulting image to binarize the image;
 - 4: Perform a distance transform of the binarized image;
 - 5: Identify the local maxima of this map;
 - 6: Select the maximum that corresponds to a given criterion (e.g. amplitude, position...), its coordinates correspond to the sought after center;
 - 7: (Optional) Shift the stack of speckle to the obtained center.
-

The algorithm allows to automatically obtain the center of the replicas for off-axis images of MMF¹. We then have to shift back to replica around center the image in the Fourier domain. The next step consists in filtering the image to only keep the spatial frequencies below $\frac{2NA}{\gamma\lambda}$ ². It amounts to selecting only the replica.

¹Because the signal is localized and bounded in the Fourier space.

²As demonstrated in appendix E in equation E.5 for an MMF of numerical aperture NA, with output magnification of γ .

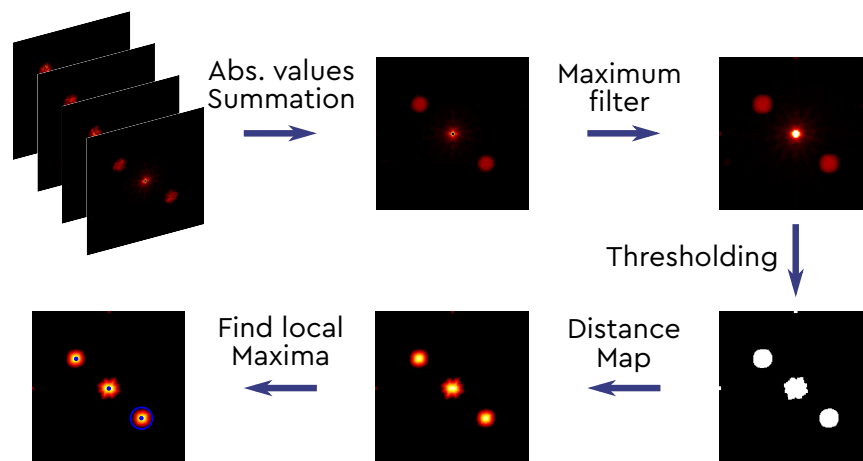


Figure H.1: Operating scheme of the center detection algorithm. Here, the operations are performed on a stack of Fourier transforms of interference images.

Appendix I

Publications and Conferences

Peer-reviewed journal articles

- Optical complex media as universal reconfigurable linear operators, *Optica* 6.4,p. 465, 2019-04, M. W. Matthès, P. del Hougne, J. de Rosny, G. Lerosey, S. M. Popoff.

To be published

- Learning and avoiding disorder in multimode fibers, *arXiv* 2010.14813, M. W. Matthès, Y. Bromberg, J. de Rosny, S. M. Popoff.

Conferences

- Invited talk: Performing Linear Operations Using Optical Complex Media, *IEEE Photonics Society Summer Topical Meeting Series*, 8-10 July 2019, M. W. Matthès, P. del Hougne, J. de Rosny, G. Lerosey, S. M. Popoff.
- Contributed talk: Performing Linear Operations Using Optical Complex Media, *Complex Nanophotonics Science Camp*, 11-14 August 2019, M. W. Matthès, P. del Hougne, J. de Rosny, G. Lerosey, S. M. Popoff.

Bibliography

- Ablowitz, M. A. and P. A. Clarkson (1991). *Solitons, Nonlinear Evolution Equations and Inverse Scattering*. London Mathematical Society Lecture Note Series. Cambridge University Press. DOI: [10.1017/CB09780511623998](https://doi.org/10.1017/CB09780511623998).
- Acton, D. S. and R. C. Smithson (1992). "Solar imaging with a segmented adaptive mirror". In: *Appl. Opt.* 31.16, pp. 3161–3169. DOI: [10.1364/AO.31.003161](https://doi.org/10.1364/AO.31.003161).
- Adaptive Optics in Astronomy* (1999). Cambridge University Press. DOI: [10.1017/CB09780511525179](https://doi.org/10.1017/CB09780511525179).
- Agrawal, Govind P (2002). *Fiber-optic communication systems*. English. New York, NY: Wiley-Interscience.
- Allen, L., M. W. Beijersbergen, R. J. C. Spreeuw, et al. (1992-06). "Orbital angular momentum of light and the transformation of Laguerre-Gaussian laser modes". en. In: *Physical Review A* 45.11, pp. 8185–8189. DOI: [10.1103/PhysRevA.45.8185](https://doi.org/10.1103/PhysRevA.45.8185).
- Ambichl, Philipp, Andre Brandstötter, Julian Böhm, et al. (2017a). "Focusing inside Disordered Media with the Generalized Wigner-Smith Operator". In: *arXiv preprint arXiv:1703.07250*.
- Ambichl, Philipp, Wen Xiong, Yaron Bromberg, et al. (2017b). "Super- and Anti-Principal Modes in Multi-Mode Waveguides". In: *arXiv preprint arXiv:1704.05117*.
- An, Y., L. Huang, J. Li, et al. (2018). "Learning to decompose the modes in few-mode fibers with deep convolutional neural network". In: 1811.00882v1.
- Annoni, A., E. Guglielmi, M. Carminati, et al. (2017). "Unscrambling light - automatically undoing strong mixing between modes". In: *Light Sci. Appl.* 6.12, e17110. DOI: [10.1038/lsa.2017.110](https://doi.org/10.1038/lsa.2017.110).
- Babcock, H. W. (1953-10). "The Possibility of Compensating Astronomical Seeing". In: *Publications of the Astronomical Society of the Pacific* 65, p. 229. DOI: [10.1086/126606](https://doi.org/10.1086/126606).
- Bayvel, Polina, Carsten Behrens, and David S. Millar (2013). "Chapter 5 - Digital Signal Processing (DSP) and Its Application in Optical Communication Systems". In: *Optical Fiber Telecommunications (Sixth Edition)*. Ed. by Ivan P. Kaminow, Tingye Li, and Alan E. Willner. Sixth Edition. Optics and Photonics. Boston: Academic Press, pp. 163–219. DOI: <https://doi.org/10.1016/B978-0-12-396960-6.00005-5>.
- Böhm, Julian, Andre Brandstötter, Philipp Ambichl, et al. (2018-02). "In situ realization of particlelike scattering states in a microwave cavity". en. In: *Physical Review A* 97.2. DOI: [10.1103/PhysRevA.97.021801](https://doi.org/10.1103/PhysRevA.97.021801).
- Bigo, Sébastien, Yann Frignac, Gabriel Charlet, et al. (2001). "10.2Tbit/s (256×42.7Gbit/s PDM/WDM) transmission over 100km TeraLight™ fiber with 1.28bit/s/Hz spectral efficiency". In: *Optical Fiber Communication Conference and International Conference on Quantum Information*. Optical Society of America, PD25. DOI: [10.1364/OFC.2001.PD25](https://doi.org/10.1364/OFC.2001.PD25).
- Bigot-Astruc, Marianne, David Boivin, and Pierre Sillard (2012-07). "Design and fabrication of weakly-coupled few-modes fibers". In: *2012 IEEE Photonics Society*

- Summer Topical Meeting Series*. 2012 IEEE Photonics Society Summer Topical Meeting Series. Seattle, WA, USA: IEEE, pp. 189–190. DOI: [10.1109/PHOSST.2012.6280766](https://doi.org/10.1109/PHOSST.2012.6280766).
- Bill Hammack's Videos & Audio on Engineering*. URL: <http://www.engineerguy.com/> (visited on 11/29/2020).
- Boonzajer Flaes, Dirk E., Jan Stopka, Sergey Turtaev, et al. (2018-06). "Robustness of Light-Transport Processes to Bending Deformations in Graded-Index Multimode Waveguides". en. In: *Physical Review Letters* 120.23. DOI: [10.1103/PhysRevLett.120.233901](https://doi.org/10.1103/PhysRevLett.120.233901).
- Booth, Martin J (2014-04). "Adaptive optical microscopy: the ongoing quest for a perfect image". In: *Light: Science & Applications* 3.4, e165–e165. DOI: [10.1038/lsa.2014.46](https://doi.org/10.1038/lsa.2014.46).
- Borel, P. I., B. Bilenberg, L. H. Frandsen, et al. (2007). "Imprinted silicon-based nanophotonics". In: *Opt. Express* 15.3, pp. 1261–1266.
- Bruck, Roman, Kevin Vynck, Philippe Lalanne, et al. (2016). "All-optical spatial light modulator for reconfigurable silicon photonic circuits". In: *Optica* 3.4, pp. 396–402. DOI: [10.1364/OPTICA.3.000396](https://doi.org/10.1364/OPTICA.3.000396).
- Carolan, Jacques, Christopher Harrold, Chris Sparrow, et al. (2015). "Universal linear optics". In: *Science* 349.6249, pp. 711–716.
- Carpenter, J., B.J. Eggleton, and J. Schroder (2016). "Complete spatiotemporal characterization and optical transfer matrix inversion of a 420 mode fiber". In: *Optics Letters* 41.23.
- Carpenter, J. and T.D. Wilkinson (2012). "Characterization of Multimode Fiber by Selective Mode Excitation". In: *Journal of Lightwave Technology* 30.10.
- Carpenter, Joel, Benjamin J. Eggleton, and Jochen Schroder (2014-01). "110x110 optical mode transfer matrix inversion". en. In: *Optics Express* 22.1, p. 96. DOI: [10.1364/OE.22.000096](https://doi.org/10.1364/OE.22.000096).
- (2015-10). "Observation of Eisenbud Wigner Smith states as principal modes in multimode fibre". In: *Nature Photonics* 9.11, pp. 751–757. DOI: [10.1038/nphoton.2015.188](https://doi.org/10.1038/nphoton.2015.188).
- Choi, Youngwoon, Changhyeong Yoon, Moonseok Kim, et al. (2012). "Scanner-Free and Wide-Field Endoscopic Imaging by Using a Single Multimode Optical Fiber". In: *Phys. Rev. Lett.* 109 (20), p. 203901. DOI: [10.1103/PhysRevLett.109.203901](https://doi.org/10.1103/PhysRevLett.109.203901).
- Chraplyvy, A. R. (1988). "Limitations on lightwave communications imposed by optical fiber nonlinearities". In: *Optical Fiber Communication*. Optical Society of America, TuD3. DOI: [10.1364/OFC.1988.TuD3](https://doi.org/10.1364/OFC.1988.TuD3).
- Cizmar, Tomá and Kishan Dholakia (2012-08). "Exploiting multimode waveguides for pure fibre-based imaging". In: *Nature Communications* 3, p. 1027. DOI: [10.1038/ncomms2024](https://doi.org/10.1038/ncomms2024).
- Cognolato, L. (1995-06). "Chemical Vapour Deposition for Optical Fibre Technology". en. In: *Le Journal de Physique IV* 05.C5, pp. C5–975–C5–987. DOI: [10.1051/jphyscol:19955115](https://doi.org/10.1051/jphyscol:19955115).
- Colladon, Daniel (1884). "La Fontaine Colladon". In: *La Nature*, p. 325.
- Conkey, D.B., A.M. Caravaca-Aguirre, E. Niv, et al. (2013). "High-speed phase-control of wavefronts with binary amplitude DMD for light control through dynamic turbid media". In: *Proc. SPIE* 8617.
- Conkey, Donald B., Antonio M. Caravaca-Aguirre, and Rafael Piestun (2012). "High-speed scattering medium characterization with application to focusing light through turbid media". In: *Optics express* 20.2, pp. 1733–1740.

- Cuche, Etienne, Pierre Marquet, and Christian Depeursinge (2000). "Spatial filtering for zero-order and twin-image elimination in digital off-axis holography". In: *Applied optics* 39.23, pp. 4070–4075.
- Defienne, H., M. Barbieri, B. Chalopin, et al. (2014). "Nonclassical light manipulation in a multiple-scattering medium". In: *Opt. Lett.* 39.21.
- Defienne, H., M. Barbieri, I. A. Walmsley, et al. (2016-01). "Two-photon quantum walk in a multimode fiber". en. In: *Science Advances* 2.1, e1501054–e1501054. DOI: [10.1126/sciadv.1501054](https://doi.org/10.1126/sciadv.1501054).
- Desurvire, E., J. R. Simpson, and P. C. Becker (1987). "High-gain erbium-doped traveling-wave fiber amplifier". In: *Opt. Lett.* 12.11, pp. 888–890. DOI: [10.1364/OL.12.000888](https://doi.org/10.1364/OL.12.000888).
- Diamond, Steven and Stephen Boyd (2016). "CVXPY: A Python-embedded modeling language for convex optimization". In: *Journal of Machine Learning Research* 17.83, pp. 1–5.
- Dong, Jonathan, Mushegh Rafayelyan, Florent Krzakala, et al. (2020-01). "Optical Reservoir Computing using multiple light scattering for chaotic systems prediction". In: *IEEE Journal of Selected Topics in Quantum Electronics* 26.1, pp. 1–12. DOI: [10.1109/JSTQE.2019.2936281](https://doi.org/10.1109/JSTQE.2019.2936281).
- Dong, Zhenhua, Siddarth Hari, Tao Gui, et al. (2015-08-01). "Nonlinear Frequency Division Multiplexed Transmissions Based on NFT". In: *IEEE Photonics Technology Letters* 27.15, pp. 1621–1623. DOI: [10.1109/LPT.2015.2432793](https://doi.org/10.1109/LPT.2015.2432793).
- Dremeau, Angélique, Antoine Liutkus, David Martina, et al. (2015-05). "Referenceless measurement of the transmission matrix of a highly scattering material using a DMD and phase retrieval techniques". en. In: *Optics Express* 23.9, p. 11898. DOI: [10.1364/OE.23.011898](https://doi.org/10.1364/OE.23.011898).
- Dubois, Arnaud, Laurent Vabre, Albert-Claude Boccara, et al. (2002). "High-resolution full-field optical coherence tomography with a Linnik microscope". In: *Appl. Opt.* 41.4, pp. 805–812. DOI: [10.1364/AO.41.000805](https://doi.org/10.1364/AO.41.000805).
- Durand, M., S. M. Popoff, R. Carminati, et al. (2019-12). "Optimizing Light Storage in Scattering Media with the Dwell-Time Operator". In: *Physical Review Letters* 123 (24), pp. –. DOI: [10.1103/physrevlett.123.243901](https://doi.org/10.1103/physrevlett.123.243901).
- (2020). "To be published". In:
- Electric, Sumitomo (2017). "Success of ultra-high capacity optical fiber transmission breaking the world". In: p. 3.
- Emori, Y. and S. Namiki (1999). "100 nm bandwidth flat gain Raman amplifiers pumped and gain-equalized by 12-wavelength-channel WDM high power laser diodes". In: *OFC/IOOC. Technical Digest. Optical Fiber Communication Conference, 1999, and the International Conference on Integrated Optics and Optical Fiber Communication*. Vol. Supplement, PD19/1–PD19/3 Suppl.
- Essiambre, René-Jean, Gerhard Kramer, Peter J. Winzer, et al. (2010-02). "Capacity Limits of Optical Fiber Networks". en. In: *Journal of Lightwave Technology* 28.4, pp. 662–701. DOI: [10.1109/JLT.2009.2039464](https://doi.org/10.1109/JLT.2009.2039464).
- Fan, Shanhui and Joseph Khan (2005-01). "Principal Modes in multimode waveguides". In: *Optics Letters*.
- Farahi, Salma, David Ziegler, Ioannis N Papadopoulos, et al. (2013). "Dynamic bending compensation while focusing through a multimode fiber". In: *Optics express* 21.19, pp. 22504–22514.
- Fickler, R. and R.W. Boyd (2016). "Custom-Tailored Sorting of Structured Light by Controlled Scattering". In: *FiO 2016*.

- File, Gemechis and Tesfaye Aga (2016). "Numerical solution of quadratic Riccati differential equations". In: *Egyptian journal of basic and applied sciences* 3.4, pp. 392–397. DOI: [10.1016/j.ejbas.2016.08.006](https://doi.org/10.1016/j.ejbas.2016.08.006).
- Finch, Michael. *Optical fibre and cable industry review* | CRU. URL: <https://www.crugroup.com/knowledge-and-insights/spotlights/2020/optical-fibre-and-cable-industry-review/> (visited on 10/10/2020).
- Fink, M. (2000). "Time Reversal of Ultrasonic Fields-Part I : Basic Principles". In: Florentin, Raphael, Vincent Kermene, Agnès Desfarges-berthelemot, et al. (2018). "Fast transmission matrix measurement of a multimode fiber with common path reference". In: *arXiv preprint arXiv:1806.09315*.
- Fontaine, Nicolas K., Roland Ryf, Haoshuo Chen, et al. (2020). "Laguerre-Gaussian mode sorters of high spatial mode count". In: *Advances in Optical Astronomical Instrumentation 2019*. Ed. by Simon C. Ellis and Celine d'Orgeville. Vol. 11203. International Society for Optics and Photonics. SPIE, pp. 87–88. DOI: [10.1117/12.2560595](https://doi.org/10.1117/12.2560595).
- Fukuchi, Kiyoshi, Tadashi Kasamatsu, Masao Morie, et al. (2001). "10.92-Tb/s (273 × 40-Gb/s) triple-band/ultra-dense WDM optical-repeated transmission experiment". In: *Optical Fiber Communication Conference and International Conference on Quantum Information*. Optical Society of America, PD24. DOI: [10.1364/OFC.2001.PD24](https://doi.org/10.1364/OFC.2001.PD24).
- Gambling, W. A., D. N. Payne, and H. Matsumura (1975). "Mode conversion coefficients in optical fibers". In: *Applied Optics* 14 (7), pp. –. DOI: [10.1364/AO.14.001538](https://doi.org/10.1364/AO.14.001538).
- Gardner, Clifford S., John M. Greene, Martin D. Kruskal, et al. (1967). "Method for Solving the Korteweg-deVries Equation". In: *Phys. Rev. Lett.* 19 (19), pp. 1095–1097. DOI: [10.1103/PhysRevLett.19.1095](https://doi.org/10.1103/PhysRevLett.19.1095).
- Garito, A. F., J. Wang, and R. Gao (1998). "Effects of Random Perturbations in Plastic Optical Fibers". In: *Science* 281.5379, pp. 962–967. DOI: [10.1126/science.281.5379.962](https://doi.org/10.1126/science.281.5379.962).
- Garnier, J., J. Fatome, and G. Le Meur (2002-09-01). "Statistical analysis of pulse propagation driven by polarization-mode dispersion". In: *Journal of the Optical Society of America B* 19.9, p. 1968. DOI: [10.1364/JOSAB.19.001968](https://doi.org/10.1364/JOSAB.19.001968).
- Gedeon, A. (1974-11). "Comparison between rigorous theory and WKB-analysis of modes in graded-index waveguides". In: *Optics Communications* 12 (3), pp. 329–332. DOI: [10.1016/0030-4018\(74\)90027-3](https://doi.org/10.1016/0030-4018(74)90027-3).
- Gérardin, Benoît, Jérôme Laurent, Philipp Ambichl, et al. (2016-07). "Particlelike wave packets in complex scattering systems". In: *Physical Review B* 94 (1), pp. –. DOI: [10.1103/physrevb.94.014209](https://doi.org/10.1103/physrevb.94.014209).
- Glance, B. (1987). "Polarization independent coherent optical receiver". In: *Journal of Lightwave Technology* 5.2, pp. 274–276.
- Gloge, D. (1971-10-01). "Weakly Guiding Fibers". In: *Applied Optics* 10.10, p. 2252. DOI: [10.1364/AO.10.002252](https://doi.org/10.1364/AO.10.002252).
- Gloge, D. (1972). "Optical power flow in multimode fibers". In: *The Bell System Technical Journal* 51.8, pp. 1767–1783.
- Gloge, D. and E. A. J. Marcatili (1973). "Impulse response of fibers with ring-shaped parabolic index distribution". In: *The Bell System Technical Journal* 52.7, pp. 1161–1168.
- Goetschy, A. and A. D. Stone (2013). "Filtering random matrices: The effect of imperfect channel control in multiple-scattering". In: *Phys. Rev. Lett.* 1304.5562.
- Goodman, Joseph W (2005). "Introduction to Fourier optics". In: *Introduction to Fourier optics, 3rd ed., by JW Goodman*. Englewood, CO: Roberts & Co. Publishers, 2005 1.

- (2007). *Speckle phenomena in optics: theory and applications*. Roberts and Company Publishers.
- Goorden, S.A., J. Bertolotti, and A.P. Mosk (2014). “Superpixel-based spatial amplitude and phase modulation using a digital micromirror device”. In: *Opt. Express* 22.15.
- Gordon, J. P. and H. Kogelnik (2000-04-25). “PMD fundamentals: Polarization mode dispersion in optical fibers”. In: *Proceedings of the National Academy of Sciences* 97.9, pp. 4541–4550. DOI: [10.1073/pnas.97.9.4541](https://doi.org/10.1073/pnas.97.9.4541).
- Gurobi Optimization, Inc. (2018). *Gurobi Optimizer Reference Manual*. misc.
- Han, Lu, Zhen-Jia Cheng, Yang Yang, et al. (2017). “Double-channel angular multiplexing polarization holography with common-path and off-axis configuration”. In: *Opt. Express* 25.18, pp. 21877–21886. DOI: [10.1364/OE.25.021877](https://doi.org/10.1364/OE.25.021877).
- Hari, S., M. I. Yousefi, and F. R. Kschischang (2016). “Multieigenvalue Communication”. In: *Journal of Lightwave Technology* 34.13, pp. 3110–3117.
- Hasegawa, Akira and Frederick Tappert (1973-08-01). “Transmission of stationary nonlinear optical pulses in dispersive dielectric fibers. I. Anomalous dispersion”. In: *Applied Physics Letters* 23.3, pp. 142–144. DOI: [10.1063/1.1654836](https://doi.org/10.1063/1.1654836).
- Hecht, Jeff (1999). *City of light: the story of fiber optics*. en. The Sloan technology series. New York: Oxford University Press.
- Hicks, Jr John W., Snitzer Elias, and Osterberg Harold (1964-11). “Optical energy transmitting devices and method of making same”. Pat. US3157726A.
- Hirano, M., T. Haruna, Y. Tamura, et al. (2013). “Record low loss, record high FOM optical fiber with manufacturable process”. In: *2013 Optical Fiber Communication Conference and Exposition and the National Fiber Optic Engineers Conference (OFC/NFOEC)*, pp. 1–3.
- Hirano, M., Y. Yamamoto, Y. Tamura, et al. (2012). “Aeff-enlarged pure-silica-core fiber having ring-core profile”. In: *OFC/NFOEC*, pp. 1–3.
- Hitz, Breck (2009-07). “Intel turns to photonics to extend Moore’s law”. In: *Physics World* 22.7, pp. 12–13. DOI: [10.1088/2058-7058/22/07/22](https://doi.org/10.1088/2058-7058/22/07/22).
- Ho, Keang-Po and Joseph M. Kahn (2011-11). “Statistics of Group Delays in Multimode Fiber with Strong Mode Coupling”. en. In: *J. Lightwave Technol.* 29.21, pp. 3119–3128. DOI: [10.1109/JLT.2011.2165316](https://doi.org/10.1109/JLT.2011.2165316).
- (2013). “Mode Coupling and its Impact on Spatially Multiplexed Systems”. In: *Optical Fiber Telecommunications*. Elsevier, pp. 491–568. DOI: [10.1016/B978-0-12-396960-6.00011-0](https://doi.org/10.1016/B978-0-12-396960-6.00011-0).
- (2014-02). “Linear Propagation Effects in Mode-Division Multiplexing Systems”. In: *Journal of Lightwave Technology* 32.4, pp. 614–628. DOI: [10.1109/JLT.2013.2283797](https://doi.org/10.1109/JLT.2013.2283797).
- Horodynski, Michael, Matthias Kühmayer, Andre Brandstötter, et al. (2020-03). “Optimal wave fields for micromanipulation in complex scattering environments”. en. In: *Nature Photonics* 14.3, pp. 149–153. DOI: [10.1038/s41566-019-0550-z](https://doi.org/10.1038/s41566-019-0550-z).
- Hougue, Philipp del and Geoffroy Lerosey (2018-11). “Leveraging Chaos for Wave-Based Analog Computation: Demonstration with Indoor Wireless Communication Signals”. In: *Phys. Rev. X* 8.4, p. 041037. DOI: [10.1103/PhysRevX.8.041037](https://doi.org/10.1103/PhysRevX.8.041037).
- Hui, Rongqing (2019). *Introduction to fiber-optic communications*. 1st edition. Cambridge, CA: Elsevier.
- Huisman, S.R., T.J. Huisman, S.A. Goorden, et al. (2014). “Programming balanced optical beam splitters in white paint”. In: *arxiv* 1401.4349.
- Huisman, S.R., T.J. Huisman, T.A.W. Wolterink, et al. (2015). “Programmable multiport optical circuits in opaque scattering materials”. In: *Opt. Express* 3.23.

- Ingerslev, Kasper, Patrick Gregg, Michael Galili, et al. (2018b-08). "12 mode, WDM, MIMO-free orbital angular momentum transmission". In: *Optics Express*. DOI: [10.1364/OE.26.020225](https://doi.org/10.1364/OE.26.020225).
- Ingerslev, Kasper, Patrick Gregg, Michael Galili, et al. (2018a). "12 mode, WDM, MIMO-free orbital angular momentum transmission". In: *Opt. Express* 26. DOI: [10.1364/OE.26.020225](https://doi.org/10.1364/OE.26.020225).
- Jasion, Gregory T, Thomas D Bradley, Kerriane Harrington, et al. (2020). "Hollow Core NANF with 0.28 dB/km Attenuation in the C and L Bands". In: *Optical Fiber Communication Conference Postdeadline Papers 2020*. Optical Society of America, Th4B.4. DOI: [10.1364/OFC.2020.Th4B.4](https://doi.org/10.1364/OFC.2020.Th4B.4).
- Jensen, J. S. and O. Sigmund (2011). "Topology optimization for nano-photonics". In: *Laser Photonics Rev.* 5.2, pp. 308–321.
- Jiao, Yang, Shanhui Fan, and David A. B. Miller (2005-01). "Demonstration of systematic photonic crystal device design and optimization by low-rank adjustments: an extremely compact mode separator". en. In: *Optics Letters* 30.2, p. 141. DOI: [10.1364/OL.30.000141](https://doi.org/10.1364/OL.30.000141).
- Jones, M. W. and K. C. Kao (1969-04). "Spectrophotometric studies of ultra low loss optical glasses II: double beam method". In: *Journal of Physics E: Scientific Instruments* 2.4, pp. 331–335. DOI: [10.1088/0022-3735/2/4/307](https://doi.org/10.1088/0022-3735/2/4/307).
- Kao, K C (1966). "Dielectric-fibre surface waveguides for optical frequencies". In: 113.7, p. 8.
- Kerr, John (1875). "XL. A new relation between electricity and light: Dielectrified media birefringent". In: *The London, Edinburgh, and Dublin Philosophical Magazine and Journal of Science* 50.332, pp. 337–348. DOI: [10.1080/14786447508641302](https://doi.org/10.1080/14786447508641302).
- Kim, Moonseok, Wonjun Choi, Youngwoon Choi, et al. (2015-05-18). "Transmission matrix of a scattering medium and its applications in biophotonics". In: *Optics Express* 23.10, p. 12648. DOI: [10.1364/OE.23.012648](https://doi.org/10.1364/OE.23.012648).
- Kingma, Diederik P. and Jimmy Ba (2017-01). "Adam: A Method for Stochastic Optimization". en. In: *arXiv:1412.6980 [cs]*.
- Kitayama, K., S. Seikai, and N. Uchida (1980). "Impulse response prediction based on experimental mode coupling coefficient in a 10-km long graded-index fiber". In: *IEEE Journal of Quantum Electronics* 16.3, pp. 356–362.
- koshi, Takanori (1982). *Optical fibers*. New York: Academic Press. 299 pp.
- Labroille, G., B. Denolle, P. Jian, et al. (2014). "Efficient and mode selective spatial mode multiplexer based on multi-plane light conversion". In: *Opt. Express* 22.13, pp. 15599–15607.
- Lee, Wai-Hon (1978). "Computer-generated holograms techniques and applications". en. In: p. 114.
- Leite, Ivo T., Sergey Turtaev, Xin Jiang, et al. (2017-12). "Three-dimensional holographic optical manipulation through a high-numerical-aperture soft-glass multimode fibre". en. In: *Nature Photonics*. DOI: [10.1038/s41566-017-0053-8](https://doi.org/10.1038/s41566-017-0053-8).
- Li, Guifang, Neng Bai, Ningbo Zhao, et al. (2014). "Space-division multiplexing: the next frontier in optical communication". en. In: *Advances in Optics and Photonics*, p. 75.
- Li, Shuhui, Charles Saunders, Daniel J. Lum, et al. (2020). "Compressively sampling the optical transmission matrix of a multimode fibre". In: *arxiv*.
- Ma, Zelin and Siddharth Ramachandran (2020-10). "Propagation stability in optical fibers: role of path memory and angular momentum". en. In: *Nanophotonics* 0.0. DOI: [10.1515/nanoph-2020-0404](https://doi.org/10.1515/nanoph-2020-0404).
- Main, Douglas (2015-02). *Undersea Cables Transport 99 Percent of International Data*.

- Maksymiuk, L. and G. Stepniak (2016-01). "On the precision of mode delays derivation with the use of the WKB method". In: *Optical and Quantum Electronics* 48 (1). DOI: [10.1007/s11082-015-0269-0](https://doi.org/10.1007/s11082-015-0269-0).
- Marcenko, V. A. and L. Andreevich Pastur (1967). "Distribution of eigenvalues for some sets of random matrices". In: *Math. USSR-Sb.* 1.4, p. 457.
- Marcuse, Dietrich (1972). *Light transmission optics*.
- (1974). *Theory of dielectric optical waveguides*. Academic Press.
- (1976-04). "Field deformation and loss caused by curvature of optical fibers". In: *Journal of the Optical Society of America* 66 (4), p. 311. DOI: [10.1364/josa.66.000311](https://doi.org/10.1364/josa.66.000311).
- Matthès, Maxime W., Yaron Bromberg, Julien de Rosny, et al. (2020-10-28). "Learning and avoiding disorder in multimode fibers". In: *arXiv:2010.14813 [physics]*.
- Matthès, Maxime W., Philipp del Hougne, Julien de Rosny, et al. (2019-04). "Optical complex media as universal reconfigurable linear operators". en. In: *Optica* 6.4, p. 465. DOI: [10.1364/OPTICA.6.000465](https://doi.org/10.1364/OPTICA.6.000465).
- McNab, Sharee J, Nikolaj Moll, and Yurii A Vlasov (2003). "Ultra-low loss photonic integrated circuit with membrane-type photonic crystal waveguides". In: *Optics express* 11.22, pp. 2927–2939.
- Mears, R, L Reekie, I. Jauncey, et al. (1987-08). *Low-noise erbium doped fibre amplifier operating at 1.54um*.
- Mennea, P. L., W. R. Clements, D. H. Smith, et al. (2018). "Modular linear optical circuits". In: *Optica* 5.9, pp. 1087–1090. DOI: [10.1364/OPTICA.5.001087](https://doi.org/10.1364/OPTICA.5.001087).
- Meron, Eado, Meir Feder, and Mark Shtauf (2012-12-20). "On the Achievable Communication Rates of Generalized Soliton Transmission Systems". In: *arXiv:1207.0297 [cs, math]*.
- Metzler, Christopher A., Manoj K. Sharma, Sudarshan Nagesh, et al. (2017). "Coherent inverse scattering via transmission matrices: Efficient phase retrieval algorithms and a public dataset". In: *Computational Photography (ICCP), 2017 IEEE International Conference on*. IEEE, pp. 1–16.
- Mie, Gustav (1908). "Beitrage zur Optik truber Medien, speziell kolloidaler Metallosungen". In: *Annalen der Physik* 330.3, pp. 377–445. DOI: <https://doi.org/10.1002/andp.19083300302>.
- Miller, David A. B. (2013a-03-11). "Self-aligning universal beam coupler". In: *Optics Express* 21.5, p. 6360. DOI: [10.1364/OE.21.006360](https://doi.org/10.1364/OE.21.006360).
- (2013b-06). "Self-configuring universal linear optical component [Invited]". en. In: *Photonics Research* 1.1, p. 1. DOI: [10.1364/PRJ.1.000001](https://doi.org/10.1364/PRJ.1.000001).
- Miller, David AB (2017). "Attojoule optoelectronics for low-energy information processing and communications". In: *Journal of Lightwave Technology* 35.3, pp. 346–396.
- Miya, T., Y. Terunuma, T. Hosaka, et al. (1979). "Ultimate low-loss single-mode fibre at 1.55 um". In: *Electronics Letters* 15.4, pp. 106–108.
- Morizur, J-F., L. Nicholls, P. Jian, et al. (2010). "Programmable unitary spatial mode manipulation". In: *Journal of the Optical Society of America A* 27.11.
- Mounaix, M., D. Andreoli, H. Defienne, et al. (2015). "Spatiotemporal coherent control of light through a multiply scattering medium with the Multi-Spectral Transmission Matrix". In: *arxiv* 1512.07753.
- Mounaix, Mickaël (2017). "Matricial approaches for spatio-temporal control of light in multiple scattering media". In:
- Nejad, R. M., K. Allahverdyan, P. Vaity, et al. (2016). "Mode Division Multiplexing Using Orbital Angular Momentum Modes Over 1.4-km Ring Core Fiber". In: *Journal of Lightwave Technology* 34.18, pp. 4252–4258.

- Nicholson, J. W., A. D. Yablon, S. Ramachandran, et al. (2008-05). "Spatially and spectrally resolved imaging of modal content in large-mode-area fibers". en. In: *Optics Express* 16.10, p. 7233. DOI: [10.1364/OE.16.007233](https://doi.org/10.1364/OE.16.007233).
- Noll, Robert J. (1976-03-01). "Zernike polynomials and atmospheric turbulence". In: *Journal of the Optical Society of America* 66.3, p. 207. DOI: [10.1364/JOSA.66.000207](https://doi.org/10.1364/JOSA.66.000207).
- Ohta, Atsunobu, Daisuke Tanimura, Tomohiko Kyakuno, et al. (2008). "43-Gbps RZ-DQPSK transponder for long-haul optical transmission system". In: 46, p. 4.
- Okamoto, Katsunari, Takanori Okoshi, and Kazuo Hotate (1979). "A closed-form approximate dispersion formula for $\hat{\text{I}}\text{s}$ -power graded-core fibers". In: *Fiber and Integrated Optics* 2.2, pp. 127–143. DOI: [10.1080/01468037908202100](https://doi.org/10.1080/01468037908202100).
- Olshansky, Robert (1975-04-01). "Mode Coupling Effects in Graded-Index Optical Fibers". In: *Applied Optics* 14.4, p. 935. DOI: [10.1364/AO.14.000935](https://doi.org/10.1364/AO.14.000935).
- Oyamada, K. and T. Okoshi (1980). "High-Accuracy Numerical Data on Propagation Characteristics of alpha-Power Graded-Core Fibers". In: *IEEE Transactions on Microwave Theory and Techniques* 28.10, pp. 1113–1118.
- Padilla Michel, Yazmin, Massimiliano Lucci, Mauro Casalboni, et al. (2015). "Mechanical Characterisation of the Four Most Used Coating Materials for Optical Fibres:" in: *Proceedings of the 3rd International Conference on Photonics, Optics and Laser Technology*. International Conference on Photonics, Optics and Laser Technology. Berlin, Germany: SCITEPRESS - Science, and Technology Publications, pp. 96–102. DOI: [10.5220/0005336700960102](https://doi.org/10.5220/0005336700960102).
- Papadopoulos, Ioannis N, Salma Farahi, Christophe Moser, et al. (2012). "Focusing and scanning light through a multimode optical fiber using digital phase conjugation". In: *Optics express* 20.10, pp. 10583–10590.
- Paschotta, Dr Rüdiger (2017a). *Differential Mode Delay*. en.
- Paschotta, Rüdiger (2017b). "V Number". en. In:
- Paszke, Adam, Sam Gross, Francisco Massa, et al. (2019). "PyTorch: An Imperative Style, High-Performance Deep Learning Library". In: *Advances in Neural Information Processing Systems* 32. Ed. by H. Wallach, H. Larochelle, A. Beygelzimer, et al. Curran Associates, Inc., pp. 8024–8035.
- Pfau, Timo, Sebastian Hoffmann, and Reinhold Noe (2009-04). "Hardware-Efficient Coherent Digital Receiver Concept With Feedforward Carrier Recovery for M^2M -QAM Constellations". In: *Journal of Lightwave Technology* 27.8, pp. 989–999. DOI: [10.1109/JLT.2008.2010511](https://doi.org/10.1109/JLT.2008.2010511).
- Piggott, Alexander Y., Jan Petykiewicz, Logan Su, et al. (2017-05). "Fabrication-constrained nanophotonic inverse design". En. In: *Scientific Reports* 7.1, p. 1786. DOI: [10.1038/s41598-017-01939-2](https://doi.org/10.1038/s41598-017-01939-2).
- Ploschner, Martin, Tomá Tyc, and Tomá Cizmar (2015-07). "Seeing through chaos in multimode fibres". In: *Nature Photonics* 9.8, pp. 529–535. DOI: [10.1038/nphoton.2015.112](https://doi.org/10.1038/nphoton.2015.112).
- Poole, CD and RE Wagner (1986). "Phenomenological approach to polarisation dispersion in long single-mode fibres". In: *Electronics Letters* 22.19, pp. 1029–1030.
- Popoff, S. M., A. Goetschy, S. F. Liew, et al. (2014a). "Coherent Control of Total Transmission of Light through Disordered Media". In: *Phys. Rev. Lett.* 112 (13), p. 133903. DOI: [10.1103/PhysRevLett.112.133903](https://doi.org/10.1103/PhysRevLett.112.133903).
- (2014b). "Coherent Control of Total Transmission of Light through Disordered Media". In: *Phys. Rev. Lett.* 112 (13), p. 133903. DOI: [10.1103/PhysRevLett.112.133903](https://doi.org/10.1103/PhysRevLett.112.133903).

- Popoff, S. M., G. Lerosey, R. Carminati, et al. (2010a-03). "Measuring the Transmission Matrix in Optics: An Approach to the Study and Control of Light Propagation in Disordered Media". en. In: *Physical Review Letters* 104.10. DOI: [10.1103/PhysRevLett.104.100601](https://doi.org/10.1103/PhysRevLett.104.100601).
- Popoff, S M, G Lerosey, M Fink, et al. (2011-12). "Controlling light through optical disordered media: transmission matrix approach". In: *New Journal of Physics* 13.12, p. 123021. DOI: [10.1088/1367-2630/13/12/123021](https://doi.org/10.1088/1367-2630/13/12/123021).
- Popoff, Sébastien M. (2020). *pyMMF: a simple module in Python for numerically finding multimode fiber modes under the scalar approximation*. Version 0.4. DOI: [10.5281/zenodo.4075298](https://doi.org/10.5281/zenodo.4075298).
- Popoff, Sebastien, Geoffroy Lerosey, Mathias Fink, et al. (2010b-09). "Image transmission through an opaque material". In: *Nature Communications* 1.6, pp. 1–5. DOI: [10.1038/ncomms1078](https://doi.org/10.1038/ncomms1078).
- Randel, Sebastian, Stephen Corteselli, Damiano Badini, et al. (2015-10). "First real-time coherent MIMO-DSP for six coupled mode transmission". In: *2015 IEEE Photonics Conference (IPC)*. 2015 IEEE Photonics Conference (IPC). Reston, VA: IEEE, pp. 1–2. DOI: [10.1109/IPCon.2015.7323761](https://doi.org/10.1109/IPCon.2015.7323761).
- Rayleigh, Lord (1899). "XXXIV. On the transmission of light through an atmosphere containing small particles in suspension, and on the origin of the blue of the sky". In: *The London, Edinburgh, and Dublin Philosophical Magazine and Journal of Science* 47.287, pp. 375–384. DOI: [10.1080/14786449908621276](https://doi.org/10.1080/14786449908621276).
- Reck, M., A. Zeilinger, H. J. Bernstein, et al. (1994). "Experimental realization of any discrete unitary operator". In: *Phys. Rev. Lett.* 73.1, p. 58.
- Redding, Brandon, Sebastien M. Popoff, and Hui Cao (2013). "All-fiber spectrometer based on speckle pattern reconstruction". In: *Optics Express* 21.5, p. 6584. DOI: [10.1364/oe.21.006584](https://doi.org/10.1364/oe.21.006584).
- Ribeiro, A., A. Ruocco, L. Vanacker, et al. (2016). "Demonstration of a 4×4 -port universal linear circuit". In: *Optica* 3.12, pp. 1348–1357.
- Richardson, D. J., J. M. Fini, and L. E. Nelson (2013-05). "Space-division multiplexing in optical fibres". en. In: *Nature Photonics* 7.5, pp. 354–362. DOI: [10.1038/nphoton.2013.94](https://doi.org/10.1038/nphoton.2013.94).
- Roberts, P. J., F. Couny, H. Sabert, et al. (2005). "Ultimate low loss of hollow-core photonic crystal fibres". In: *Optics Express* 13.1, p. 236. DOI: [10.1364/OPEX.13.000236](https://doi.org/10.1364/OPEX.13.000236).
- Rothe, Stefan, Qian Zhang, Nektarios Koukourakis, et al. (2020-02). "Deep Learning for Computational Mode Decomposition in Optical Fibers". en. In: *Applied Sciences* 10.4, p. 1367. DOI: [10.3390/app10041367](https://doi.org/10.3390/app10041367).
- Rotter, Stefan, Philipp Ambichl, and Florian Libisch (2011-03). "Generating Particle-like Scattering States in Wave Transport". In: *Physical Review Letters* 106 (12), pp. –. DOI: [10.1103/physrevlett.106.120602](https://doi.org/10.1103/physrevlett.106.120602).
- Rotter, Stefan and Sylvain Gigan (2017-03). "Light fields in complex media: mesoscopic scattering meets wave control". en. In: *Reviews of Modern Physics* 89.1. DOI: [10.1103/RevModPhys.89.015005](https://doi.org/10.1103/RevModPhys.89.015005).
- Ruder, Sebastian (2016-01-19). *An overview of gradient descent optimization algorithms*. Sebastian Ruder. URL: <https://ruder.io/optimizing-gradient-descent/> (visited on 11/13/2020).
- Russell, J. S. (1844). "Report on Wave". In: *Report of the 14th Meeting of the British Association for the Advancement of Science*, pp. XLVII–LVII.
- Russell, Philip St.J. (2006-12). "Photonic-Crystal Fibers". In: *Journal of Lightwave Technology* 24.12, pp. 4729–4749. DOI: [10.1109/JLT.2006.885258](https://doi.org/10.1109/JLT.2006.885258).

- Ryf, R., N. K. Fontaine, H. Chen, et al. (2015). "Mode-multiplexed transmission over conventional graded-index multimode fibers". In: *Optics Express* 23 (1), pp. –. DOI: [10.1364/OE.23.000235](https://doi.org/10.1364/OE.23.000235).
- Ryf, Roland, Nicolas K. Fontaine, Haoshuo Chen, et al. (2018-09). "Mode-Multiplexed Transmission Over 36 Spatial Modes of a Graded-Index Multimode Fiber". In: *2018 European Conference on Optical Communication (ECOC)*. 2018 European Conference on Optical Communication (ECOC). Rome: IEEE, pp. 1–3. DOI: [10.1109/ECOC.2018.8535431](https://doi.org/10.1109/ECOC.2018.8535431).
- Ryf, Roland, Sebastian Randel, Alan H. Gnauck, et al. (2012). "Mode-Division Multiplexing Over 96 km of Few-Mode Fiber Using Coherent 6×6 MIMO Processing". In: *J. Lightwave Technol.* 30.4, pp. 521–531.
- Saade, A., F. Caltagirone, I. Carron, et al. (2015). "Random Projections through multiple optical scattering: Approximating kernels at the speed of light". In: *arxiv* 1510.06664.
- Savage, Neil (2009-03). "Digital spatial light modulators". In: *Nature Photonics* 3.3, pp. 170–172. DOI: [10.1038/nphoton.2009.18](https://doi.org/10.1038/nphoton.2009.18).
- Schimpf, D. N., R. A. Barankov, and S. Ramachandran (2011-07). "Cross-correlated (C^2) imaging of fiber and waveguide modes". en. In: *Optics Express* 19.14, p. 13008. DOI: [10.1364/OE.19.013008](https://doi.org/10.1364/OE.19.013008).
- Sebbah, Patrick, ed. (2001). *Waves and Imaging through Complex Media*. Dordrecht: Springer Netherlands. DOI: [10.1007/978-94-010-0975-1](https://doi.org/10.1007/978-94-010-0975-1).
- Shannon, C. E. (1948). "A mathematical theory of communication". In: *The Bell System Technical Journal* 27.3, pp. 379–423.
- Sharma, A and P Bindal (1992). "Solutions of the 2-D Helmholtz Equation for Optical Waveguides: Semi-Analytical and Numerical Variational Approaches". In: *LAMP Series Report, LAMP/92 2*, pp. –.
- Shen, B., P. Wang, R. Polson, et al. (2015). "An integrated-nanophotonics polarization beamsplitter with $2.4 \times 2.4 \mu\text{m}^2$ footprint". In: *Nat. Photonics* 9.6, p. 378.
- Shen, Y., N. C. Harris, S. Skirlo, et al. (2017a). "Deep learning with coherent nanophotonic circuits". In: *Nat. Photonics* 11.7, p. 441.
- Shen, Yichen, Nicholas C. Harris, Scott Skirlo, et al. (2017b-07). "Deep learning with coherent nanophotonic circuits". In: *Nature Photonics* 11.7, pp. 441–446. DOI: [10.1038/nphoton.2017.93](https://doi.org/10.1038/nphoton.2017.93).
- Sillard, P, D Molin, and M Bigot-Astruc (2015). "Low-Differential-Mode-Group-Delay 9-LP-Mode Fiber". In: p. 3.
- Sillard, P, D. Molin, M. Bigot-Astruc, et al. (2014). "Low-DMGD 6-LP-Mode Fiber". In: *Optical Fiber Communication Conference*. Optical Fiber Communication Conference. San Francisco, California: OSA, M3F.2. DOI: [10.1364/OFC.2014.M3F.2](https://doi.org/10.1364/OFC.2014.M3F.2).
- Sillard, Pierre, Marianne Bigot-Astruc, David Boivin, et al. (2011). "Few-Mode Fiber for Uncoupled Mode-Division Multiplexing Transmissions". en. In: *37th European Conference and Exposition on Optical Communications*. Geneva: OSA, Tu.5.LeCervin.7. DOI: [10.1364/ECOC.2011.Tu.5.LeCervin.7](https://doi.org/10.1364/ECOC.2011.Tu.5.LeCervin.7).
- Silva, Alexandre and Nader Engheta (2014). "Performing Mathematical Operations with Metamaterials". en. In: *Science*.
- Skipetrov, S. E. and A. Goetschy (2011-02). "Eigenvalue distributions of large Euclidean random matrices for waves in random media". en. In: *Journal of Physics A: Mathematical and Theoretical* 44.6, p. 065102. DOI: [10.1088/1751-8113/44/6/065102](https://doi.org/10.1088/1751-8113/44/6/065102).
- Smith, Felix T. (1960-04). "Lifetime Matrix in Collision Theory". In: *Physical Review* 118 (1), pp. 349–356. DOI: [10.1103/physrev.118.349](https://doi.org/10.1103/physrev.118.349).

- Stolen, R. H. and Chinlon Lin (1978-04-01). "Self-phase-modulation in silica optical fibers". In: *Physical Review A* 17.4, pp. 1448–1453. DOI: [10.1103/PhysRevA.17.1448](https://doi.org/10.1103/PhysRevA.17.1448).
- Sévigny, Benoit, Guillaume Le Cocq, Geraud Bouwmans, et al. (2016). "Advanced S2 imaging spatial mode analysis: furthering modal characterization". In: *Next-Generation Optical Communication: Components, Sub-Systems, and Systems V*. Ed. by Guifang Li and Xiang Zhou. Vol. 9774. International Society for Optics and Photonics. SPIE, pp. 136–142. DOI: [10.1117/12.2210851](https://doi.org/10.1117/12.2210851).
- Tamil, Lakshman S., S. S. Mitra, R. Dutta, et al. (1991-03). "Finite difference solution for graded-index cylindrical dielectric waveguides: a scalar wave approximation". In: *Applied Optics* 30 (9), p. 1113. DOI: [10.1364/ao.30.001113](https://doi.org/10.1364/ao.30.001113).
- Tamura, Y., H. Sakuma, K. Morita, et al. (2018). "The First 0.14-dB/km Loss Optical Fiber and its Impact on Submarine Transmission". In: *Journal of Lightwave Technology* 36.1, pp. 44–49.
- TeleGeography (2020-04). *Submarine Cable Map*.
- Trinel, Jean-Baptiste, Guillaume Le Cocq, Esben Ravn Andresen, et al. (2017). "Latest results and future perspectives on Few-Mode Erbium Doped Fiber Amplifiers". In: *Optical Fiber Technology* 35, pp. 56–63. DOI: <https://doi.org/10.1016/j.yofte.2016.09.004>.
- Trischitta, P., M. Colas, M. Green, et al. (1996). "The TAT-12/13 Cable Network". In: *IEEE Communications Magazine* 34.2, pp. 24–28.
- Tyson, Robert K (2015). *Principles of adaptive optics*. CRC press.
- Vellekoop, I.M. and A.P. Mosk (2007). "Focusing coherent light through opaque strongly scattering media". In: *Opt. Lett.* 32.16.
- Vellekoop, Ivo Micha (2008). "Controlling the propagation of light in disordered scattering media". In: *arXiv preprint arXiv:0807.1087*.
- Wang, Xuyang, Shuangyi Yan, Jiangbo Zhu, et al. (2017). "3.36-Tbit/s OAM and Wavelength Multiplexed Transmission over an Inverse-Parabolic Graded Index Fiber". In: *Conference on Lasers and Electro-Optics*. Optical Society of America, SW4I.3. DOI: [10.1364/CLEO_SI.2017.SW4I.3](https://doi.org/10.1364/CLEO_SI.2017.SW4I.3).
- Wierzba, P and B B Kosmowski (2003). "Application of polarisation-maintaining side-hole fibres to direct force measurement". In: 4, p. 9.
- Wigner, Eugene P. (1955-04). "Lower Limit for the Energy Derivative of the Scattering Phase Shift". In: *Physical Review* 98 (1), pp. 145–147. DOI: [10.1103/physrev.98.145](https://doi.org/10.1103/physrev.98.145).
- Winzer, P.J. and R.-J. Essiambre (2006-05). "Advanced Optical Modulation Formats". In: *Proceedings of the IEEE* 94.5, pp. 952–985. DOI: [10.1109/JPROC.2006.873438](https://doi.org/10.1109/JPROC.2006.873438).
- Wolterink, T.A.W., R. Uppu, G. Ctistis, et al. (2015). "Programmable two-photon quantum interference in 3 channels in opaque scattering media". In: *arxiv* 1511.00897.
- Xiong, W., P. Ambichl, Y. Bromberg, et al. (2017a). "Principal modes in multimode fibers: exploring the crossover from weak to strong mode coupling". In: *Opt. Express* 25.3, pp. 2709–2724.
- Xiong, Wen, Philipp Ambichl, Yaron Bromberg, et al. (2016-07). "Spatiotemporal Control of Light Transmission through a Multimode Fiber with Strong Mode Coupling". en. In: *Physical Review Letters* 117.5. DOI: [10.1103/PhysRevLett.117.053901](https://doi.org/10.1103/PhysRevLett.117.053901).
- (2017b-02). "Principal modes in multimode fibers: exploring the crossover from weak to strong mode coupling". en. In: *Optics Express* 25.3, p. 2709. DOI: [10.1364/OE.25.002709](https://doi.org/10.1364/OE.25.002709).
- Xiong, Zhongfei, Weijin Chen, Peng Wang, et al. (2017c-11). "Classification of symmetry properties of waveguide modes in presence of gain/ losses, anisotropy/

- bianisotropy, or continuous/ discrete rotational symmetry". en. In: *Optics Express* 25.24, p. 29822. DOI: [10.1364/OE.25.029822](https://doi.org/10.1364/OE.25.029822).
- Yamada, E, H Takara, T Ohara, et al. (2001). "A high SNR, 150 ch supercontinuum CW optical source with precise 25 GHz spacing for 10 Gbit/s DWDM systems". In: p. 3.
- Yammine, J., A. Tandjè, Michel Dossou, et al. (2019-02). "Time-dependence of the transmission matrix of a specialty few-mode fiber". en. In: *APL Photonics* 4.2, p. 022904. DOI: [10.1063/1.5047578](https://doi.org/10.1063/1.5047578).
- Yousefi, Mansoor I. and Xianhe Yangzhang (2018-04). "Linear and Nonlinear Frequency-Division Multiplexing". en. In: *arXiv:1603.04389 [cs, math]*.
- Zabusky, N. J. and M. D. Kruskal (1965). "Interaction of "Solitons" in a Collisionless Plasma and the Recurrence of Initial States". In: *Phys. Rev. Lett.* 15 (6), pp. 240–243. DOI: [10.1103/PhysRevLett.15.240](https://doi.org/10.1103/PhysRevLett.15.240).
- Zhu, B., B. J. Mangan, T. Kremp, et al. (2020). "First Demonstration of Hollow-Core-Fiber Cable for Low Latency Data Transmission". In: *Optical Fiber Communication Conference Postdeadline Papers 2020*. Optical Society of America, Th4B.3. DOI: [10.1364/OFC.2020.Th4B.3](https://doi.org/10.1364/OFC.2020.Th4B.3).
- Zhu, B., T.F. Taunay, M. Fishteyn, et al. (2011-08). "112-Tb/s Space-division multiplexed DWDM transmission with 14-b/s/Hz aggregate spectral efficiency over a 768-km seven-core fiber". en. In: *Optics Express* 19.17, p. 16665. DOI: [10.1364/OE.19.016665](https://doi.org/10.1364/OE.19.016665).
- Zuo, Ying, Bohan Li, Yujun Zhao, et al. (2019-09-20). "All-optical neural network with nonlinear activation functions". In: *Optica* 6.9, p. 1132. DOI: [10.1364/OPTICA.6.001132](https://doi.org/10.1364/OPTICA.6.001132).
- Zyskind, John and Atul Srivastava (2011). *Optically amplified WDM networks*. 1st ed. Burlington, MA: Elsevier/Academic Press. 464 pp.

RÉSUMÉ

Ce projet de doctorat vise à utiliser des techniques de modulation du front d'onde pour étudier le contenu modal des fibres multimodes. Cette étude est cruciale pour l'implémentation du multiplexage spatial dans le domaine télécommunications fibrées.

Récemment, de nouvelles méthodes de caractérisation de la propagation des modes à l'intérieur des fibres multimodes ont été mises au point. Elles s'appuient sur des techniques de modulation spatiale du front d'onde pour mesurer la matrice de transmission donnant la relation spatiale entre le champ entrant d'un côté d'un milieu et celui sortant de l'autre. Cette mesure est particulièrement intéressante pour examiner comment les perturbations extérieures affectent le couplage entre les différents modes propagatifs d'une fibre. Nous présentons l'approche que nous avons développée pour réaliser une acquisition rapide et fiable de ces matrices avec un système léger, dans le cas des fibres multimodes. Nous réalisons la caractérisation de l'effet provoqué par des déformations appliquées sur des fibres optiques grâce à un grand nombre de mesures de matrices de transmission. Cela nous permet de concevoir des canaux spatiaux robustes au désordre. De plus, nous réalisons l'étude des mécanismes de couplage des modes.

Enfin, nous exploitons le caractère aléatoire de la propagation de la lumière dans les fibres fortement perturbées pour concevoir une approche originale pour générer des opérateurs linéaires optiques reconfigurables.

MOTS CLÉS

Fibres Multimodes, Modulation du Front d'Onde, Matrices de Transmission, Télécommunications, Calculs Optique

ABSTRACT

This Ph.D. project aims at using wavefront shaping techniques to probe the modal content of multimode fibers. Doing so is a crucial stepping stone for the implementation of space division multiplexing for telecommunication applications.

Recently, new methods to characterize the propagation of modes inside multimode fibers were introduced. They leverage wavefront shaping techniques to measure the transmission matrix, which gives the spatial relationship between the fields entering from one side and exiting from the other side of the medium. This measure is of particular interest to examine how external perturbations affect the coupling between the different propagating modes of a fiber. We present the approach we developed to perform fast and reliable acquisition of these matrices with a lightweight system.

Because we can perform numerous measurements in a short time, we characterize the effect of induced deformations and successfully design spatial channels that are robust to disorder. A study of the mechanisms of mode coupling is also performed.

Finally, we take advantage of the randomness of the propagation of light in perturbed fibers to design an original approach to generate optical reconfigurable linear operators.

KEYWORDS

Multimode Fibers, Wavefront Shaping, Transmission Matrices, Telecommunications, Optical Computations